

UNIVERSITY OF CALIFORNIA  
SANTA BARBARA

**Growth Optimization of Metal-polar III-Nitride High-electron-mobility Transistor  
Structures by Molecular Beam Epitaxy**

A dissertation submitted in partial satisfaction of the  
requirements for the degree of

Doctor of Philosophy

in

Materials

by

Stephen William Kaun

Committee in charge:

Prof. James S. Speck, Chair

Prof. Umesh K. Mishra

Prof. Steven P. DenBaars

Prof. Shuji Nakamura

June 2014

The dissertation of Stephen William Kaun is approved.

---

Umesh K. Mishra

---

Steven P. DenBaars

---

Shuji Nakamura

---

James S. Speck, Committee Chair

March 2014

**Growth Optimization of Metal-polar III-Nitride High-electron-mobility Transistor  
Structures by Molecular Beam Epitaxy**

Copyright © 2014

by

Stephen William Kaun

## Acknowledgements

None of this work would have been possible without the help of John English, the MBE lab manager. John runs the lab with a religious fervor. His hands have picked from the Tree of Life. Through his mind's eye, he scans the past, present, and future. System malfunctions are anticipated and corrected with extreme prejudice.

I was also fortunate to have my graduate studies overlap with those of Dr. Man Hoi Wong. Man Hoi taught me how to grow, characterize, fabricate, and measure. He is relentless in his pursuit of scientific truth. His wisdom and patience are unmatched. To speak about Man Hoi is to drain the vocabulary of superlatives.

Along with Man Hoi, I had the pleasure of working with several talented Nitride MBE growers. I would like to thank Sansaptak, Soojeong, Brian, Elaheh, Karine, and Hiro for being great co-workers on the Gen-II. I would also like to thank Erin K, Erin Y, Dave, Christophe, and Jordan for their help on the 930.

Peter, Min-Ying, Chad, Mark, and Trevor were excellent officemates. Peter and I adopted Guinea pigs, which we named Min-Ying and Man Hoi (after Min-Ying and Man Hoi). Unlike Human Min-Ying and Human Man Hoi, they were despicable garbage animals. We gave them our love, but they did not reciprocate. After about 3 months, we decided that their reign of terror was finally over, and we gave them to a rodent sanctuary. We never attempted to reconnect. I hope they're burning in hell right now.

Having friends like Jack, Lindsey, HJ, Po, Ben C, Anne, Lou, Ben B, Peter, Claire, John, Erin, Brian, Howard, Elaheh, and Karine, made the time fly by. Philosophically, we followed the 3 Fs (food, fun, and frivolity), the 3 Bs (brews, boats, and buds), and the 1 T (trampolines).

I am grateful for the support of my committee members: my advisor, Prof. Jim Speck; Prof. Umesh Mishra; Prof. Steve DenBaars; and Prof. Shuji Nakamura. Jim is a great teacher and mentor. His passion concerning the SuperHEMT project helped me shake off early failures and move forward with studies that consistently yielded interesting data. My committee members have established UCSB as a leading university for materials science. UCSB is a great place to work. The facilities at UCSB are incredible, and the collaboration between groups is truly unique.

I owe a debt of gratitude to my parents, Tom and Wendy; my brother, Benjamin; my sister-in-law, Megan; my nephew, Jonas; and my niece, Wrenna. I would not have pursued a PhD without their encouragement.

**Curriculum Vitae  
Stephen William Kaun  
March 2014**

**Education**

***University of California, Santa Barbara***

- Doctor of Philosophy, Materials Sept 08 – present
- PhD Advisor: Prof. James S. Speck
- PhD Committee: Prof. James S. Speck, Prof. Umesh K. Mishra,  
Prof. Steven P. DenBaars, and Prof. Shuji Nakamura
- Dissertation Topic: Molecular beam epitaxy and fabrication of metal-polar  
(Al,Ga,In)N/GaN high-electron-mobility transistors

***University of Illinois, Urbana-Champaign***

- Bachelor of Applied Science, Aug 04 – May 08  
Materials Science and Engineering,  
High Honors

**Work Experience**

- Research Assistant Sept 08 - present  
Materials Department, University of California, Santa Barbara  
*Molecular beam epitaxy of III-Nitrides, fabrication of high-electron mobility  
transistors*
- Teaching Assistant  
University of California, Santa Barbara
  - MATRL 209B- X-Ray Diffraction II: Advanced Methods Mar 12 – Jun 12
  - ECE 124 B- Semiconductor Device Processing Dec 11 – Mar 11
  - MATRL 188- Alternative Energy Materials Dec 10 – Mar 10
  - MATRL 209A- Crystallography and Diffraction Fundamentals Sept 09 – Dec 09
- Technician May 04 – Aug 08  
InvenTek Corporation, New Lenox, IL  
*Design and operation of assembly systems for Li-ion rolled-ribbon batteries*

## Journal Publications

- **S. W. Kaun**, E. Ahmadi, B. Mazumder, F. Wu, E. C. H. Kyle, P. G. Burke, U. K. Mishra, and J. S. Speck, “GaN-based high-electron-mobility transistor structures with homogeneous lattice-matched InAlN barriers grown by plasma-assisted molecular beam epitaxy,” *Semicond. Sci. Technol.* *29*, 045011 (2014). – Included in IOPselect
- **S. W. Kaun**, M. H. Wong, J. Lu, U. K. Mishra, and J. S. Speck, “Reduction of carbon proximity effects by including AlGaIn back barriers in HEMTs on free-standing GaN,” *Electron. Lett.* *49*, 893 (2013). – Featured Article
- **S. W. Kaun**, M. H. Wong, U. K. Mishra, and J. S. Speck, “Molecular beam epitaxy for high-performance Ga-face GaN electron devices,” *Semicond. Sci. Technol.* *28*, 074001 (2013). – Included in SST Highlights of 2013
- **S. W. Kaun**, B. Mazumder, J. Lu, S. Keller, U. K. Mishra, and J. S. Speck, “Atom probe analysis of AlN interlayers in AlGaIn/AlN/GaN heterostructures,” *Appl. Phys. Lett.* *102*, 111603 (2013). – S. W. Kaun and B. Mazumder contributed equally
- **S. W. Kaun**, P. G. Burke, M. H. Wong, E. C. H. Kyle, U. K. Mishra, and J. S. Speck, “Effect of dislocations on electron mobility in AlGaIn/GaN and AlGaIn/AlN/GaN heterostructures,” *Appl. Phys. Lett.* *101*, 262102 (2012).
- **S. W. Kaun**, M. H. Wong, U. K. Mishra, and J. S. Speck, “Correlation between threading dislocation density and sheet resistance of AlGaIn/AlN/GaN heterostructures grown by plasma-assisted molecular beam epitaxy,” *Appl. Phys. Lett.* *100*, 262102 (2012).
- **S. W. Kaun**, M. H. Wong, S. Dasgupta, S. Choi, R. Chung, U. K. Mishra, J. S. Speck, “Effects of Threading Dislocation Density on the Gate Leakage of AlGaIn/GaN Heterostructures for High Electron Mobility Transistors,” *Appl. Phys. Express* *4*, 4101 (2011).
- M. Tapajna, **S. W. Kaun**, M. H. Wong, F. Gao, T. Palacios, U. K. Mishra, J. S. Speck, and M. Kuball, “Influence of threading dislocation density on early degradation in AlGaIn/GaN high electron mobility transistors,” *Appl. Phys. Lett.* *99*, 223501 (2011).
- C. Hodges, N. Killat, **S. W. Kaun**, M. H. Wong, F. Gao, T. Palacios, U. K. Mishra, J. S. Speck, T. Palacios, and M. Kuball, “Optical investigation of degradation mechanisms in AlGaIn/GaN high electron mobility transistors: Generation of non-radiative recombination centers,” *Appl. Phys. Lett.* *100*, 112106 (2012).

- D. W. Cardwell, A. Sasikumar, A. R. Arehart, **S. W. Kaun**, J. Lu, S. Keller, J. S. Speck, U. K. Mishra, and S. Ringel, “Spatially-resolved spectroscopic measurements of  $E_c-0.57$  eV traps in AlGa<sub>N</sub>/Ga<sub>N</sub> high electron mobility transistors,” *Appl. Phys. Lett.* *102*, 193509 (2013).
- F. Gao, B. Lu, L. Li, **S. W. Kaun**, J. S. Speck, C. Thompson, and T. Palacios, “Role of oxygen in the OFF-state degradation of AlGa<sub>N</sub>/Ga<sub>N</sub> high electron mobility transistors,” *Appl. Phys. Lett.* *99*, 223506 (2011).
- E. Ahmadi, R. Shivaraman, F. Wu, S. Wienecke, **S. W. Kaun**, S. Keller, J. S. Speck, and U. K. Mishra, “Elimination of columnar microstructure in N-face InAlN, lattice-matched to GaN, grown by plasma-assisted molecular beam epitaxy in the N-rich regime,” *Appl. Phys. Lett.* *104*, 072107 (2014).
- J. Chen, Y. S. Puzyrev, C. X. Zhang, E. X. Zhang, M. W. McCurdy, D. M. Fleetwood, R. D. Schrimpf, S. T. Pantelides, **S. W. Kaun**, E. C. H. Kyle, and J. S. Speck, “Proton-Induced Dehydrogenation of Defects in AlGa<sub>N</sub>/Ga<sub>N</sub> HEMTs,” *IEEE Trans. Nucl. Sci.* *60*, 4080 (2013).

#### **Conference Presentations (First Author Only)**

- **S. W. Kaun**, M. H. Wong, B. Mazumder, U. K. Mishra, and J. S. Speck, “Materials Issues in Ga<sub>N</sub>-based HEMTs for Power Electronics,” TMS Annual Meeting, February 17-19, 2014 (San Diego, CA)
- **S. W. Kaun**, B. Mazumder, M. H. Wong, U. K. Mishra, and J. S. Speck, “Dislocation scattering in AlGa<sub>N</sub>/Ga<sub>N</sub> and AlGa<sub>N</sub>/AlN/Ga<sub>N</sub> Heterostructures,” MRS Spring Meeting, April 1-5, 2013 (San Francisco, CA).
- **S. W. Kaun**, P. G. Burke, B. Mazumder, M. H. Wong, U. K. Mishra, and J. S. Speck, “Dislocation scattering in AlGa<sub>N</sub>/Ga<sub>N</sub> and AlGa<sub>N</sub>/AlN/Ga<sub>N</sub> Heterostructures grown by plasma-assisted molecular beam epitaxy,” IWN, October 14-19, 2012 (Sapporo, Japan).
- **S. W. Kaun**, M. H. Wong, S. Dasgupta, S. Choi, U. K. Mishra, and J. S. Speck, “Effects of Threading Dislocation Density on the Gate Leakage of AlGa<sub>N</sub>/Ga<sub>N</sub> Heterostructures for High Electron Mobility Transistors,” EMC, June 22-24, 2011 (Santa Barbara, CA).
- **S. W. Kaun**, M. H. Wong, S. Dasgupta, S. Choi, U. K. Mishra, and J. S. Speck, “Effects of Threading Dislocations on the Performance of Al<sub>0.25</sub>Ga<sub>0.75</sub>N/Ga<sub>N</sub> HEMTs Grown by PAMBE,” IWN, September 19-24, 2010 (Tampa, FL).

## Awards

- Outstanding Graduate Student Research Award 2013  
Solid State Lighting and Energy Center, University of California, Santa Barbara
- GAANN Fellowship 2008  
University of California, Santa Barbara
- Larry D. and Carol Rakers Scholarship 2007  
University of Illinois, Urbana-Champaign
- Kimberly-Clark Scholarship 2006  
University of Illinois, Urbana-Champaign
- Cullen W. Parmalee Scholarship 2005  
University of Illinois, Urbana-Champaign
- Alfred W. Allen Award 2005  
University of Illinois, Urbana-Champaign



## Abstract

### Growth Optimization of Metal-polar III-Nitride High-electron-mobility Transistor Structures by Molecular Beam Epitaxy

by

Stephen William Kaun

GaN-based high-electron-mobility transistors (HEMTs) will play an important role in the next generation of high-frequency amplifiers and power-switching devices. Since parasitic conduction (leakage) through the GaN buffer layer and (Al,Ga,In)N barrier reduces the efficiency of operation, HEMT performance hinges on the epitaxial quality of these layers. Increasing the sheet charge density and mobility of the two-dimensional electron gas (2DEG) is also essential for reducing the channel resistance and improving output. The growth conditions applied in plasma-assisted molecular beam epitaxy (PAMBE) and ammonia-based molecular beam epitaxy (NH<sub>3</sub>-MBE) that result in high-quality metal-polar HEMT structures are described.

The effects of threading dislocations on the gate leakage and channel conductivity of AlGa<sub>x</sub>N/GaN HEMTs were studied in detail. For this purpose, a series of HEMT structures were grown on GaN templates with threading dislocation densities (TDDs) that spanned three orders of magnitude. There was a clear trend of reduced gate leakage with reduced TDD for HEMTs grown by Ga-rich PAMBE; however, a reduction in TDD also entailed an increase in buffer leakage. By reducing the unintentionally doped (UID) GaN buffer thickness and including an AlGa<sub>x</sub>N back barrier, a HEMT regrown by Ga-rich

PAMBE on low-TDD free-standing (FS) GaN ( $\sim 5 \times 10^7 \text{ cm}^{-2}$  TDD) yielded a three-terminal breakdown voltage greater than 50 V and a power output (power-added efficiency) of 6.7 W/mm (50 %) at 4 GHz with a 40 V drain bias. High TDD was then shown to severely degrade the 2DEG mobility of  $\text{Al}_x\text{Ga}_{1-x}\text{N}/\text{GaN}$  ( $x = 0.24, 0.12, 0.06$ ) and  $\text{AlGaIn}/\text{AlN}/\text{GaN}$  heterostructures grown by Ga-rich PAMBE. By regrowing on low-TDD FS GaN and including a 2.5 nm AlN interlayer, an  $\text{Al}_{0.24}\text{Ga}_{0.76}\text{N}/\text{AlN}/\text{GaN}$  heterostructure achieved a room temperature (RT) 2DEG sheet resistance of  $169 \text{ } \Omega/\square$ . As evidenced by atom probe tomography, the AlN interlayer grown by Ga-rich PAMBE was pure with abrupt interfaces. The pure AlN interlayer greatly reduced alloy-related scattering.

When  $\text{AlGaIn}/\text{AlN}/\text{GaN}$  heterostructures were grown by  $\text{NH}_3$ -MBE at  $820 \text{ }^\circ\text{C}$ , the 2DEG sheet density was lower than expected. These AlN interlayers were shown to have a significant concentration of Ga impurities by atom probe tomography. The source of these impurities was most likely the decomposition of the underlying GaN layers, as reduction of the growth temperature below  $750 \text{ }^\circ\text{C}$  yielded a much lower concentration of Ga impurities. Flux optimization and application of an In surfactant was necessary to reduce the interface roughness in  $\text{AlGaIn}/\text{AlN}/\text{GaN}$  heterostructures grown by  $\text{NH}_3$ -MBE at low temperature, yielding sheet resistances below  $300 \text{ } \Omega/\square$ .

The growth of  $\text{InAlN}/(\text{GaIn})/(\text{AlN})/\text{GaN}$  heterostructures with lattice-matched  $\text{In}_{0.17}\text{Al}_{0.83}\text{N}$  barriers by N-rich PAMBE is also described. Through flux optimization, the columnar microstructure previously observed in N-rich PAMBE-grown InAlN layers was eliminated. By including a 3 nm AlN interlayer and 2 nm GaN interlayer, an

$\text{In}_{0.17}\text{Al}_{0.83}\text{N}/\text{GaN}/\text{AlN}/\text{GaN}$  heterostructure regrown on low-TDD FS GaN achieved an exceptionally low RT 2DEG sheet resistance of  $145 \Omega/\square$ .

# Contents

<b>1. Introduction</b> .....	1
1.1 Figures of Merit for GaN-based Electron Devices .....	1
1.2 Metal-polar GaN-based HEMT Basics .....	4
1.3 Epitaxy of Metal-polar GaN HEMT Structures .....	11
1.3.1 MBE vs. MOCVD .....	11
1.3.2 Heteroepitaxy by Ga-rich PAMBE.....	14
1.3.3 Heteroepitaxy by NH <sub>3</sub> -MBE.....	26
1.4 Synopsis .....	28
<b>2. Ga-rich PAMBE AlGaN/GaN HEMT TDD Series: Leakage</b> .....	31
2.1 Introduction.....	31
2.2 Experimental Procedure.....	31
2.2.1 Regrowth on GaN Templates.....	31
2.2.2 Growth of TDD Series .....	34
2.2.3 Device Fabrication .....	36
2.3 Results and Discussion .....	37
2.3.1 Structural Properties.....	37
2.3.2 2DEG Characteristics.....	40
2.3.3 Buffer Breakdown.....	40
2.3.4 DC and Small-signal Performance.....	41
2.3.5 Schottky Contact Leakage .....	44
2.3.6 Three-terminal Breakdown .....	46
<b>3. Optimization of Ga-rich PAMBE AlGaN/GaN HEMTs on FS GaN</b> .....	47
3.1 Introduction.....	47
3.2 Device Design and Fabrication.....	47
3.3 Results and Discussion .....	50
3.3.1 Improved Breakdown on FS GaN.....	50
3.3.2 Improved Large-signal Performance on FS GaN .....	52
<b>4. AlN Interlayer Optimization by Ga-rich PAMBE</b> .....	55
4.1 Introduction.....	55
4.2 Growth of AlGaN/AlN/GaN with Interruption.....	56
4.3 Results and Discussion .....	59
4.3.1 Purity of Ga-rich PAMBE-grown AlN Interlayer .....	59
4.3.2 Structural Properties.....	52
4.3.3 2DEG Characteristics.....	60
4.3.4 Mechanism for Mobility Improvement with Thick AlN .....	63

<b>5. Ga-rich PAMBE <math>\text{Al}_x\text{Ga}_{1-x}\text{N}/(\text{AlN})/\text{GaN}</math> TDD Series: Mobility</b>	64
5.1 Introduction	64
5.2 Experiment Design	66
5.3 Results and Discussion	68
5.3.1 Structural Properties	68
5.3.2 Surface Morphologies	69
5.3.3 Temperature-dependent Hall Measurements	70
<b>6. <math>\text{NH}_3</math>-MBE <math>\text{AlGaIn}/\text{GaN}</math> TDD Series: Leakage</b>	77
6.1 Introduction	77
6.2 Experimental Procedure	77
6.2.1 Regrowth by $\text{NH}_3$ -MBE	77
6.2.2 Growth of TDD Series	78
6.3 Results and Discussion	80
6.3.1 Structural Properties	80
6.3.2 2DEG Characteristics	81
6.3.3 Buffer Breakdown	81
6.3.4 Schottky Contact Leakage	82
<b>7. AlN Interlayer Optimization by <math>\text{NH}_3</math>-MBE</b>	84
7.1 Introduction	84
7.2 Ga Impurities in $\text{NH}_3$ -MBE and MOCVD AlN Interlayers	86
7.3 Source of Ga Impurities in $\text{NH}_3$ -MBE AlN Interlayers	91
7.3.1 Ga Residency Time	91
7.3.2 Decomposition of Underlying GaN Layers	93
7.4 LT $\text{NH}_3$ -MBE AlN Interlayers with In Surfactant	96
<b>8. Homogeneous Lattice-matched InAlN by N-rich PAMBE</b>	101
8.1 Introduction	101
8.2 Experimental Procedure	103
8.2.1 Growth of Interlayer Series	103
8.2.2 Growth of InAlN/GaN/AlN/GaN HEMT Structure on FS GaN	106
8.3 Results and Discussion	107
8.3.1 Structural Properties of Interlayer Series	107
8.3.2 In-plane Compositional Homogeneity of InAlN	109
8.3.3 Verification of Interlayer Thickness and Purity	112
8.3.4 Surface Morphologies of Interlayer Series	115
8.3.5 Temperature-dependent Mobility of Interlayer Series	116
8.3.6 Structural Properties of InAlN/GaN/AlN/GaN HEMT on FS GaN	122
8.3.7 Surface Morphology of InAlN/GaN/AlN/GaN HEMT on FS GaN	126
8.3.8 Temperature-dependent Mobility of InAlN/GaN/AlN/GaN HEMT on FS GaN	127
8.3.9 DC-IV Measurement of InAlN/GaN/AlN/GaN HEMT on FS GaN	130

<b>9. Summary and Future Work .....</b>	<b>133</b>
<b>Appendix A. Metal-polar HEMT Fabrication .....</b>	<b>149</b>
<b>Appendix B. OFF-state Stress Tests on Passivated Slant-gate .....</b>	<b>158</b>
<b>and Passivated Rectangular-gate HEMTs</b>	

# Chapter 1. Introduction

## 1.1 Figures of Merit for GaN-based Electron Devices

GaN and its alloys with InN and AlN will be the subjects of intense research for years to come, owing to the wide range of direct bandgaps that enables applications in electronics and optoelectronics. The band gaps of the  $\text{In}_x\text{Ga}_{1-x}\text{N}$  alloys cross the entire visible spectrum (Fig. 1.1), facilitating GaN-based lighting and display technologies. With a large bandgap ( $E_g$ ) of 3.42 eV, GaN is a suitable semiconductor for high-power electronics since avalanche breakdown requires a large electric field.

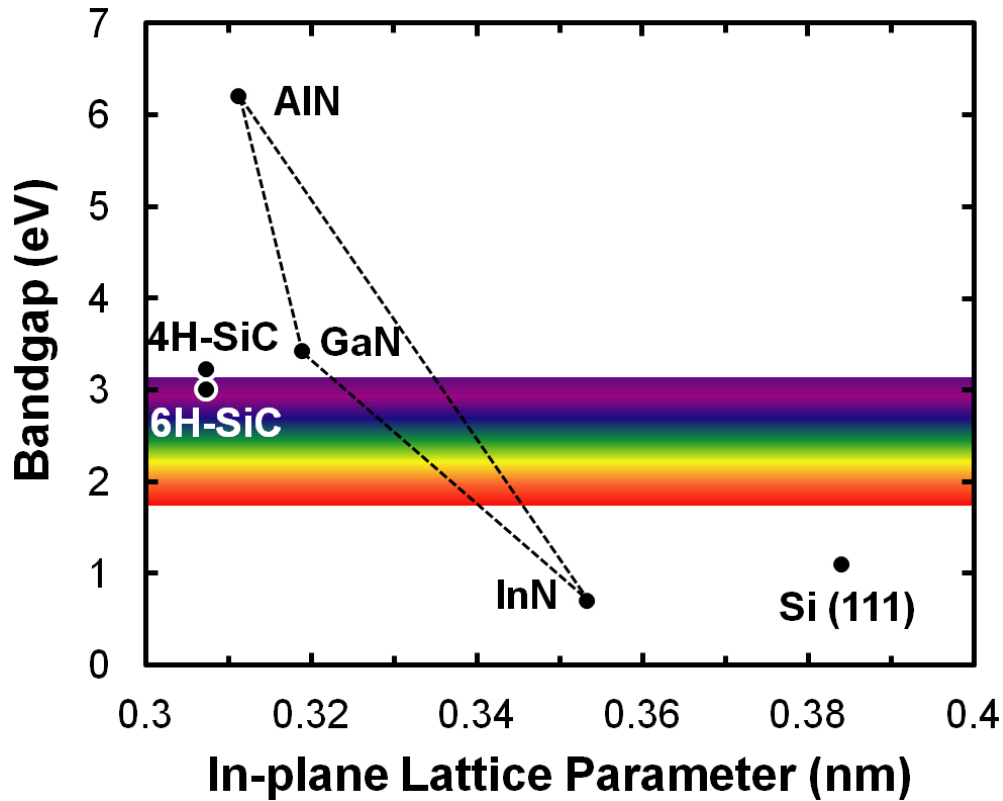


Figure 1.1: In-plane lattice parameters and band gaps for GaN (0001) and its related alloys. The lattice parameters and band gaps for common substrates, 4H-SiC (0001), 6H-SiC (0001) and Si (111), are also included.

The two most often cited figures of merit concerning a material's applicability to unipolar power electronics are the Johnson Figure of Merit (JFOM) [1] and the Baliga Figure of Merit (BFOM) [2]. The formulas for these figures of merit are as follows:

$$JFOM = \frac{E_C v_s}{2\pi} \quad (1.1)$$

$$BFOM = \epsilon_r \mu_n E_C^3 \quad (1.2)$$

where  $E_C$  is the critical breakdown electric field,  $v_s$  is the electron saturation velocity,  $\epsilon_r$  is the relative permittivity, and  $\mu_n$  is the low-field electron mobility (majority carrier mobility).

**Table 1.1: Material properties at room temperature and figures of merit (relative to Si) related to unipolar power performance [3].**

Material	Si	InP	GaAs	6H-SiC	4H-SiC	GaN
$E_g$ (eV)	1.11	1.34	1.42	3.02	3.26	3.42
$\epsilon_r$	11.8	12.5	12.9	9.7	9.7	9.5
$\mu_n$ (cm <sup>2</sup> /Vs)	1350	5400 *9000	8500 *9000	350	700	1250 *2000
$v_s$ (10 <sup>7</sup> cm/s)	1.0	0.8	0.7	1.0	1.4	1.5
$E_C$ (MV/cm)	0.3	0.5	0.4	2.5	3.0	3.3
<b>JFOM</b>	1	1.3	0.93	8.3	14	17
<b>BFOM</b>	1	20 *33	16 *17	120	430	990 *1600
<b>HMFOM</b>	1	3.3 *4.3	3.4 *3.4	4.3	7.2	10.6 *13.4

\*HEMT structure

The formula for the JFOM is the product of the theoretical current-gain-cutoff frequency ( $f_T$ ),  $f_T = v_s/2\pi L_G$  ( $L_G$  is the gate length), and the critical breakdown voltage



( $V_C$ ),  $V_C = L_G \times E_C$ . Because of its large breakdown electric field (3.3 MV/cm) and high saturation electron velocity ( $\sim 1.5 \times 10^7$  cm/s), GaN yields a JFOM higher than Si, GaAs, InP, and SiC, suggesting GaN as a superior semiconductor for high-frequency power amplification (Table 1.1) [4]. The JFOM gives a sense of a material's high-frequency power performance, but is not entirely accurate for device comparison. The formula presented above for the current-gain-cutoff frequency is only applicable in the absence of parasitics. This formula for  $f_T$  also stipulates that the electric field under the gate is uniform, and all electrons in the channel are traveling at the saturation velocity. This is an oversimplification of device operation, as the electric field varies greatly along the channel and is highly dependent on gate geometry, passivation, etc. It should also be noted that measurements of the saturation velocity vary significantly in the literature, and the low-field electron mobility is much easier to measure.

The BFOM is based on the low-field electron mobility, but it is only applicable if the device's power losses are dominated by conduction losses. The BFOM is inversely proportional to the ideal specific on-resistance ( $R_{sp,on}$ ),  $R_{sp,on} = \frac{4V_C^2}{\epsilon_r \mu_n E_C^3}$ , of the drift region. Comparison of the normalized values for the BFOM, presented in Table 1.1, promotes GaN for power-switching applications. Power-switching devices generally operate at 50 kHz - 1 MHz, while power amplifiers are often required to operate beyond X-band (8-12 GHz), where switching losses are more important.

The formula for the Huang Material Figure of Merit (HMFOM) [5] is as follows:

$$HMFOM = E_C \sqrt{\mu_n} \quad (1.3)$$

The HMFOM is inversely proportional to a field-effect transistor's minimum power loss

$$(P_{\text{loss,min}}), P_{\text{loss,min}} = \frac{4I_{\text{rms}} (V_C V_D)^{3/4} \sqrt{kI_D f / i_{g,av}}}{E_C \sqrt{\mu_n}},$$

where  $I_{\text{rms}}$  represents the root-mean-square channel current,  $V_D$  is the drain/bus voltage,  $k$  represents the ratio of the gate-to-drain overlap area over the whole chip area,  $I_D$  is the turn-on/turn-off current,  $f$  is the switching frequency, and  $i_{g,av}$  is the average gate current. This formula for the minimum power loss considers losses from conduction and gate charge transients (switching). The HMFOM is the most complete for comparison of the high-frequency power losses in different material systems.

Although 4H-SiC and 6H-SiC have HFOMs nearly as high as GaN (Table 1.1), 4H-SiC and 6H-SiC suffer from inferior transistor characteristics. 4H-SiC and 6H-SiC can only be used in the fabrication of metal-semiconductor field-effect transistors (MESFETs) [6] and metal-oxide field-effect transistors (MOSFETs) [7] whereas GaN heterostructures can be used to fabricate high-electron-mobility transistors (HEMTs) [4].

## 1.2 Metal-polar GaN-based HEMT Basics

HEMTs incorporate a heterojunction between (at least) two semiconductors with different bandgaps and electron affinities. As electrons are drawn from the larger bandgap (lower electron affinity) semiconductor to the smaller band gap (higher electron affinity) semiconductor, a triangular electrostatic potential well forms at the heterointerface. A two-dimensional electron gas (2DEG) forms within the triangular well and serves as the channel of the transistor. Since the 2DEG is confined to an ordered epitaxial interface that is free of ionized dopants, the conductivity is very high.

The two most popular HEMT structures are those based on the AlGaAs/GaAs system (in development since the early 1980s) and the metal-polar AlGaN/GaN system (in development since the mid-1990s). In the case of zinc-blende AlGaAs/GaAs, Si-doping (modulation doping) in the AlGaAs barrier provides the electrons that constitute the 2DEG. The Si-doped layer of the AlGaAs barrier is spatially separated from the 2DEG by an undoped AlGaAs layer to minimize charged impurity scattering.

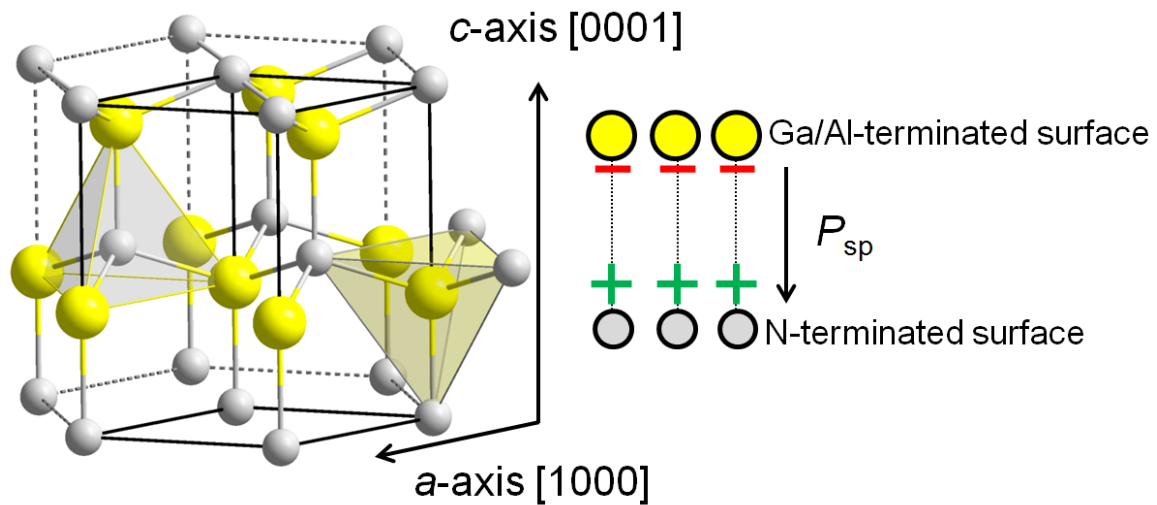


**Figure 1.2: GaN/AlN wurtzite crystal structure showing the  $c$ -axis,  $a$ -axis, and direction of spontaneous polarization ( $P_{sp}$ ).**

Modulation doping is not required in an (0001)-oriented AlGaN/GaN heterostructure. Instead, the AlGaN/GaN heterostructure employs polarization doping to create a 2DEG at the heterointerface. GaN and AlN are polar materials due to their non-centrosymmetric crystal structure (wurtzite, space group:  $P6_3mc$ ), as shown in Fig. 1.2. In an ideal wurtzite cell, where the ratio between the  $c$ -lattice parameter ( $c_0$ ) and  $a$ -lattice parameter ( $a_0$ ) is 1.6330 (i.e.  $c_0/a_0 = 1.6330$ ), the resultant polarization of the nitride

bonds not directed along the  $c$ -axis negate the  $c$ -axis polarization. When  $c_0/a_0$  is less than 1.6330, the non- $c$ -axis covalent bonds are angled farther from the  $c$ -axis, and their resultant polarization is insufficient to compensate the  $c$ -axis polarization. GaN and AlN do not have ideal wurtzite cells, and the degree of divergence from the ideal  $c_0/a_0$  ratio determines the strength of polarization. The  $c_0/a_0$  ratios for GaN and AlN are shown in Table 1.2.

**Table 1.2: Lattice parameters and  $c_0/a_0$  ratios for GaN, AlN, and InN [8].**

Parameter	GaN	AlN	InN
$a_0$ (nm)	0.3189	0.3112	0.3548
$c_0$ (nm)	0.5185	0.4982	0.5760
$c_0/a_0$	1.6259	1.6010	1.6234

Since AlN (AlGaN) has a  $c_0/a_0$  ratio that diverges farther from the ideal ratio than GaN, it has a larger spontaneous polarization. When a thin AlGaN layer is coherently grown on  $c$ -plane GaN, it is under equibiaxial tensile stress, and a piezoelectric component ( $P_{pe}$ ) must be added to the spontaneous polarization in the AlGaN layer. The equibiaxial tensile stress further reduces the resultant  $c$ -axis polarization of the other three nitride bonds, increasing polarization in the AlGaN layer. The discontinuity in total polarization, which is the sum of spontaneous and piezoelectric

polarization between AlGa<sub>x</sub>N and GaN, determines the theoretical charge density at the heterointerface ( $\sigma_{int}$ ). This charge density is given by the following equation:

$$\begin{aligned}\sigma_{int} &= (P_{sp})_{GaN} - (P_{sp} + P_{pe})_{AlGaN} \\ &= P_{sp}(0) - P_{sp}(x) - 2 \frac{a(0) - a(x)}{a(x)} (e_{31}(x) - e_{33}(x) \frac{C_{13}(x)}{C_{33}(x)})\end{aligned}\quad (1.4)$$

where  $P_{sp}(0)$  is the spontaneous polarization of GaN,  $P_{sp}(x)$  is the spontaneous polarization of Al<sub>x</sub>Ga<sub>1-x</sub>N,  $a(0)$  is GaN's  $a$ -lattice parameter,  $a(x)$  is Al<sub>x</sub>Ga<sub>1-x</sub>N's  $a$ -lattice parameter,  $e_{31}(x)$  and  $e_{33}(x)$  are piezoelectric constants for Al<sub>x</sub>Ga<sub>1-x</sub>N, and  $C_{13}(x)$  and  $C_{33}(x)$  are elastic constants for Al<sub>x</sub>Ga<sub>1-x</sub>N. The relevant values for Al<sub>x</sub>Ga<sub>1-x</sub>N are generally estimated as a linear combination of its constituents' parameters (Table 1.2).

**Table 1.2: Spontaneous polarization, piezoelectric constants, and elastic constants for GaN, AlN, and InN [8,9].**

Material	$P_{sp}$ (C/m <sup>2</sup> )	$e_{31}$ (C/m <sup>2</sup> )	$e_{33}$ (C/m <sup>2</sup> )	$C_{13}$ (10 <sup>12</sup> N/m <sup>2</sup> )	$C_{33}$ (10 <sup>12</sup> N/m <sup>2</sup> )
GaN	-0.029	-0.49	0.73	1.03	3.55
AlN	-0.081	-0.6	1.46	1.08	3.95
InN	-0.032	-0.57	0.97	0.96	2.58

Using Eq. 1.4 for an Al<sub>0.3</sub>Ga<sub>0.7</sub>N/GaN heterostructure, the total discontinuity in polarization is 0.0277 C/m<sup>2</sup>, which results in a sheet charge (2DEG) density of 1.7 x 10<sup>13</sup> cm<sup>-2</sup> at the heterointerface. This density of sheet charges would fully compensate the electric field in the AlGa<sub>x</sub>N barrier (Fig. 1.3). As identified by Ibbetson *et al.* [10], the

source of the electrons in the 2DEG is a surface donor state(s). As the thickness of the AlGaN barrier increases, the Fermi level eventually reaches the surface donor level and is pinned (Fig. 1.4). Surface donors are then ionized and balanced by the 2DEG. The surface donor level defines the surface barrier height ( $\Phi_B$ ), and an electric field remains in the AlGaN layer; thus, the 2DEG density predicted by Eq. 1.4 is far less than what is measured. As the  $\text{Al}_{0.3}\text{Ga}_{0.7}\text{N}$  barrier thickness reaches  $\sim 15$  nm, the 2DEG density plateaus. Whether the surface donor state is a discrete level or a distribution of levels is the subject of ongoing debate, but recent studies suggest the donor state is related to surface oxidation of Al dangling bonds [11]. As the Al mole fraction of the AlGaN barrier increases, the polarization discontinuity and sheet charge density increase. However, due to a trade-off between charge and mobility (explained later on), the Al mole fraction of the AlGaN/GaN heterostructure is generally kept between 0.2 and 0.3, yielding a mobility of 1000-2000  $\text{cm}^2/\text{Vs}$ .

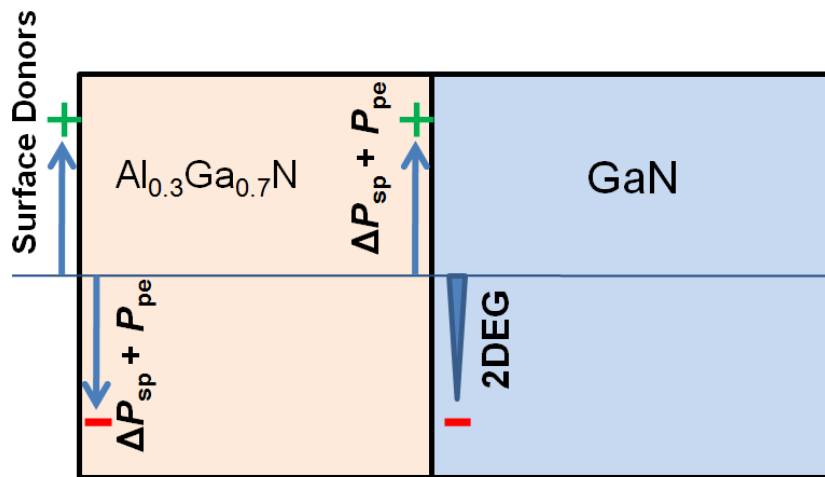


**Figure 1.3: Schematic of polarization charges and compensating charges in an  $\text{Al}_{0.3}\text{Ga}_{0.7}\text{N}/\text{GaN}$  heterostructure.**

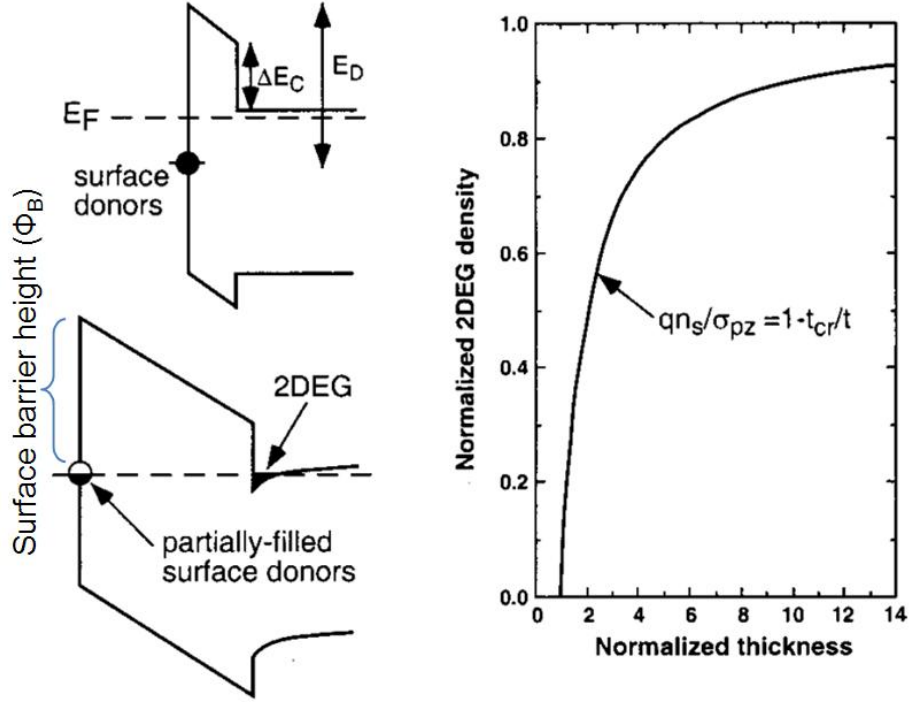


**Figure 1.4: Schematic of surface donor state in an  $\text{Al}_{0.3}\text{Ga}_{0.7}\text{N}/\text{GaN}$  heterostructure and the critical thickness for 2DEG formation. From Ref. [10].**

Piezoelectric polarization is not necessary for the formation of a 2DEG in a GaN-based HEMT structure. The lattice-matched  $\text{In}_{0.17}\text{Al}_{0.83}\text{N}/\text{GaN}$  heterostructure, in which the polarization discontinuity evolves solely from a discontinuity in spontaneous polarization, is of significant interest. Using the values from Table 1.2 and Eq. 1.4, the polarization discontinuity at the heterointerface of the  $\text{In}_{0.17}\text{Al}_{0.83}\text{N}/\text{GaN}$  heterostructure is  $0.0437 \text{ C/m}^2$ , resulting in a high theoretical 2DEG sheet density of  $2.7 \times 10^{13} \text{ cm}^{-2}$ .

Since the 2DEG is present without an applied voltage, *c*-plane metal-polar (In,Al,Ga)N/GaN HEMTs are normally-on (depletion-mode), unless the barrier beneath the gate is etched. The HEMT is turned off when a negative gate voltage (pinch-off

voltage) achieves flat band conditions in the GaN channel (Fig. 1.5). The pinch-off voltage ( $V_{PO}$ ), which is a negative, is found using the equation:

$$-eV_{PO} + \Phi_B = eE_{pol}t_b + \Delta E_C + (E_C - E_F) \quad (1.5)$$

$$V_{PO} = \Phi_B - E_{pol}t_b - \frac{\Delta E_C + (E_C - E_F)}{e}$$

where  $e$  is the charge of a single electron,  $\Phi_B$  is the surface barrier height of the (In,Al,Ga)N barrier,  $E_{pol}$  is the polarization-induced electric field in the (In,Al,Ga)N barrier,  $t_b$  is the thickness of the (In,Al,Ga)N barrier,  $\Delta E_C$  is the conduction band offset between (In,Al,Ga)N and GaN,  $E_C$  is GaN's conduction band energy, and  $E_F$  is the Fermi level. If we neglect the aforementioned Fermi surface pinning, the surface barrier height is the difference between the work function of the metal contact ( $\Phi_M$ ) and the barrier electron affinity ( $\chi_{(In,Ga,Al)N}$ ).

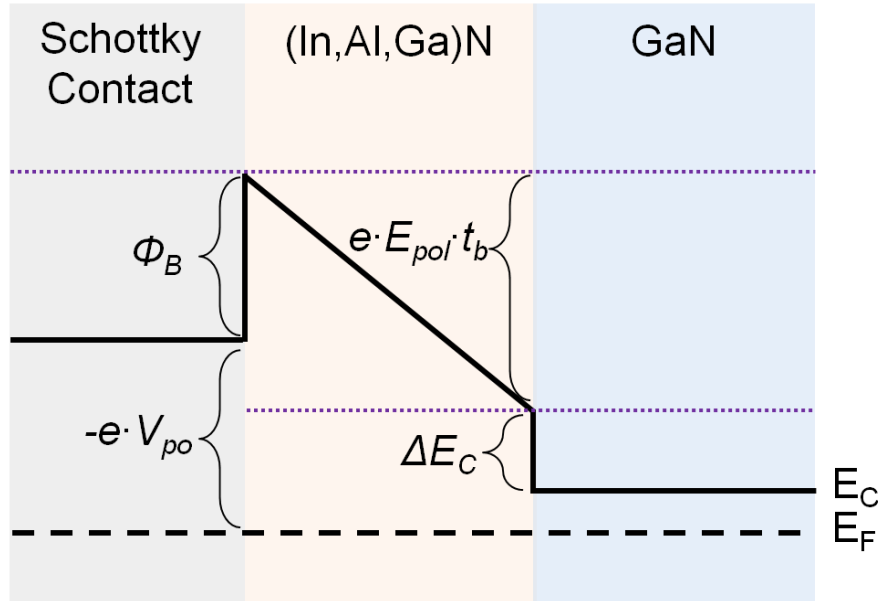


**Figure 1.5: Schematic showing flat-band conditions in an (In,Al,Ga)N/GaN heterostructure.**



## 1.3 Epitaxy of Metal-polar GaN HEMT Structures

### 1.3.1 MBE vs. MOCVD

With high-quality growth through molecular beam epitaxy (MBE) -- both plasma-assisted MBE (PAMBE) and ammonia-based MBE (NH<sub>3</sub>-MBE) -- and metal-organic chemical vapor (MOCVD), GaN-based HEMT structures have been realized with low on-resistance and high output power, which are essential for high-performance power-switching devices and microwave amplifiers [12].

MOCVD is the epitaxial technique of choice for the GaN electronics industry, despite similar operational costs between MOCVD and MBE. GaN growth consumes expensive metal-organic precursors in MOCVD (trimethylgallium (TMG), trimethylindium (TMI), trimethylaluminum (TMA)), and constant cooling of the growth chamber with expensive liquid nitrogen is necessary for MBE. However, MOCVD's higher growth rates and throughput make it much more attractive for industry (especially for LED production). Notwithstanding cost issues, MBE offers several advantages over MOCVD, including highly abrupt interfaces, low point defect concentrations, and very low carbon and hydrogen impurity concentrations. To date, the high-frequency performance of state-of-the-art (SOA) MBE-grown HEMTs has tracked well with MOCVD-grown HEMTs [13–15], despite higher-quality heteroepitaxy with MOCVD (discussed later on). With the optimization of growth parameters that would bring about higher growth rates and better material, MBE may prove to be the best growth option for reliable, high-performance HEMTs. Regardless, MBE is a valuable technique for research. The growth surface can be monitored through *in situ* diagnostic techniques like

reflection high energy electron diffraction (RHEED) [16], and desorbing atomic and molecular species can be identified through line-of-sight quadrupole mass spectrometry (QMS) [17]. Carefully controlled growth is important for proof-of-concept device structures, and successful band engineering with MBE can often translate to MOCVD.

In PAMBE, the N source consists of high-purity  $N_2$  gas that is activated by an RF plasma power source, typically operating at a forward power of 250-350 W. With  $NH_3$ -MBE, however, active nitrogen is introduced to the growth surface as  $NH_3$ , which is then thermally cracked and incorporated.  $NH_3$ -MBE provides a growth environment with some growth characteristics similar to MOCVD, including highly N-rich conditions and higher growth temperatures than PAMBE. PAMBE generally involves tightly controlled, low-temperature Ga-rich growth, though there have been developments in high-temperature (HT) N-rich PAMBE growth [18].  $NH_3$ -MBE has a much larger growth parameter space than PAMBE for high-quality GaN. Even so,  $NH_3$ -MBE is a less common growth technique, and publications concerning devices grown by  $NH_3$ -MBE are infrequent.

Successful growth of GaN-based HEMTs yields smooth surface morphology and one high-conductivity channel, the 2DEG. Limiting the concentration of trap states that can be charged during device operation is another key aspect. However, much of the improvement in HEMT performance over the past decade was the result of complex fabrication methods (discussed in detail elsewhere). Fabrication of sub-100 nm gates brought about power-gain ( $f_{max}$ ) and current-gain cutoff frequencies ( $f_T$ ) far beyond 100 GHz [19]. The addition of multiple field plates increased breakdown voltage and helped

improve the continuous wave output power ( $P_{out}$ ) [20,21]. Soon, performance will be limited by the crystallinity and purity of the device epistructure and the passivation layers [22]. The following sections focus on PAMBE and  $NH_3$ -MBE growth procedures that result in HEMT structures with low on-resistance and few leakage pathways, specifically those that increase the gate and buffer current. Maximizing output resistance (sharp pinch-off) is crucial to device performance. Power-added efficiency (PAE) is very sensitive to buffer and gate leakage, as well as charged surface and buffer states that lead to capacitive coupling and current collapse [23,24].

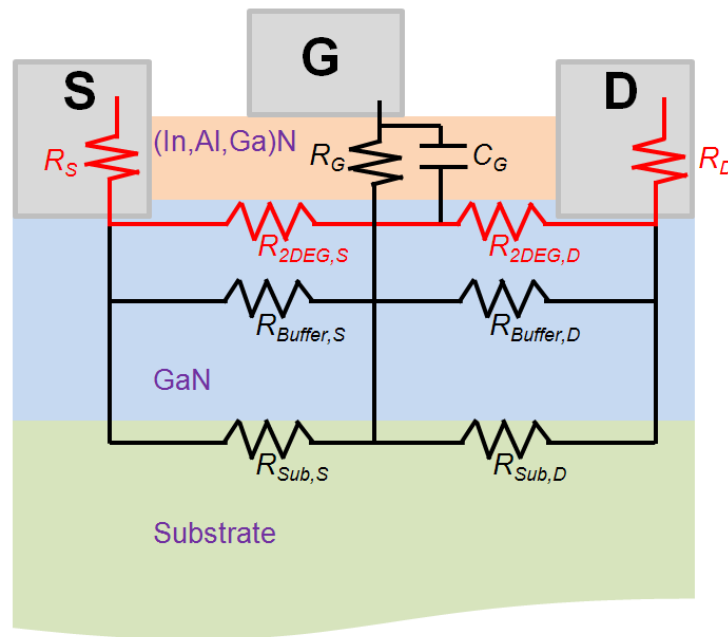


**Figure 1.5: Equivalent circuit for an (In,Al,Ga)N/GaN HEMT during DC operation, showing the parasitic resistance elements (red). Resistances in black are to be maximized.**

An equivalent circuit for an unpassivated metal-polar GaN-based HEMT under DC operation is presented in Figure 1.5. The source and drain resistances ( $R_S, R_D$ ) should be minimized, but are generally determined by *ex situ* processing (e.g. metal deposition

and annealing). The growth experiments in the following sections detail the MBE growth parameters that yield HEMTs with low 2DEG resistances ( $R_{2\text{DEG}}$ ) and very high substrate resistances ( $R_{\text{Sub}}$ ), buffer resistances ( $R_{\text{Buffer}}$ ), and gate resistances ( $R_{\text{G}}$ ). An equivalent circuit for a HEMT under high-frequency operation would have far greater complexity. It would include source-pad, gate-pad, and drain-pad parasitic capacitances, as well as gate-source and gate-drain parasitic capacitances through passivation layers. Performance limitations from pad capacitances will also be addressed.

### 1.3.2 Heteroepitaxy by Ga-rich PAMBE

Seeing that FS  $c$ -plane GaN substrates are currently cost-prohibitive and lack wide availability, GaN-based HEMTs are commonly grown on either 6H-SiC, 4H-SiC, sapphire, or Si. Early studies eliminated sapphire as a viable substrate for high-power HEMTs.

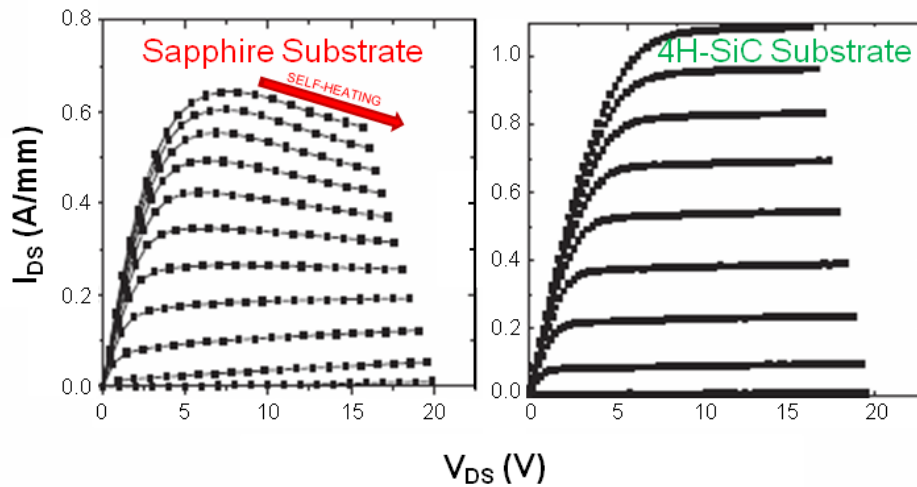


**Figure 1.6: DC-IV curves showing heat dispersion in HEMTs grown by Ga-rich PAMBE on sapphire. Heat dispersion is evident when HEMTs are grown on 4H-SiC. From Ref. [25].**

Sapphire's poor thermal conductivity (0.42 W/cmK) leads to self-heating of HEMTs, which results in lower saturation current and heat dispersion at high biases (Fig. 2) [25]. 4H-SiC, 6H-SiC, and Si, on the other hand, have rather high thermal conductivity (4.9 W/cmK for 6H-SiC, 3.7 W/cmK for 4H-SiC, and 1.3 W/cmK for Si), and 4H-SiC and 6H-SiC act as effective heat sinks for GaN (1.5-2.5 W/cmK) [26,27] electron devices. Yet, these substrates are not lattice-matched to (0001)-oriented GaN, which can lead to significant threading dislocation densities (TDDs) in the range of  $\sim 10^{10}$  cm<sup>-2</sup> by PAMBE [28].

High-performance GaN-based HEMTs on SiC were developed before HEMTs on Si because heteroepitaxy on SiC is much less difficult. The lattice mismatch (thermal mismatch) between SiC and GaN is -3.9% (25%), which is far less than the lattice mismatch (thermal mismatch) of 16.9% (-56%) between Si (111) and GaN. The schematic in Fig. 1.7 is a general depiction of the material stack needed to make a high-performance HEMT on a SiC substrate. All layers on top of the substrate are grown epitaxially, except for the passivation layer. The following sections will refer back to Fig. 1.7, noting the similarities and differences between HEMT heteroepitaxy by Ga-rich PAMBE and NH<sub>3</sub>-MBE.

As shown in Fig. 1.7, growth on 4H-SiC or 6H-SiC begins with an AlN initiation layer. When GaN is grown directly on SiC, a rough, islanded GaN layer results, due to poor surface wetting [29]. The AlN initiation layer promotes surface wetting and reduces the lattice mismatch from -3.9% to -2.4%. By means of its large band gap (6.2 eV), the AlN initiation layer also provides a barrier between the GaN buffer layer and donor

impurities (Si and O) at the substrate surface. -2.4% is still relatively high lattice mismatch, so GaN-on-AlN grows in the Volmer-Weber three-dimensional (3D) mode, and the GaN islands grow until they coalesce into a consistent film. Threading dislocations (TDs) form at the island peripheries due to island-island misorientation, which itself is a result of the relaxation of lattice mismatch between the 3D GaN islands in the AlN via misfit dislocations. These TDs persist through the buffer layer and intersect the 2DEG.

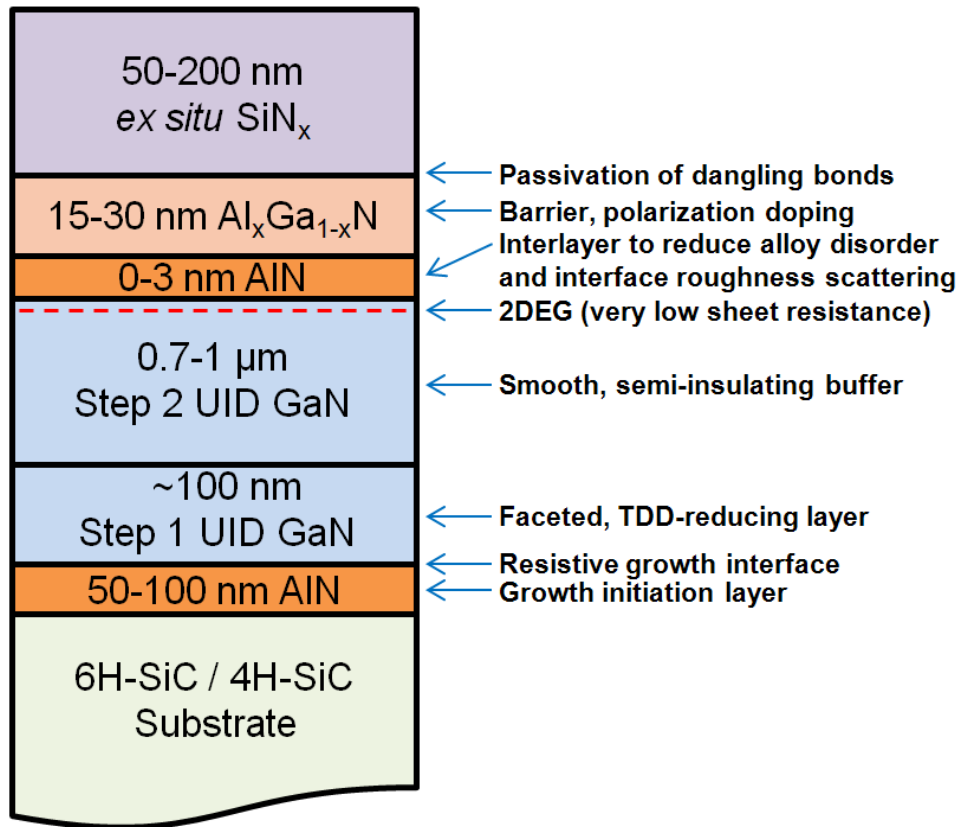


**Figure 1.7: Schematic of a general HEMT material stack with epitaxial layers grown by Ga-rich PAMBE on a 6H-SiC or 4H-SiC substrate. Layer and interface functions are noted. UID stands for ‘unintentionally doped.’**

In MOCVD, with growth temperatures above 1000 °C, there is a lower thermodynamic driving force for island nucleation, so larger islands grow at the expense of smaller islands before coalescence [30]. With Ga-rich PAMBE, low growth temperatures and lack of an MOCVD-like boundary layer limit island size upon coalescence. For growth on SiC, Ga-rich PAMBE yields TDDs in the low  $10^{10}$  cm<sup>-2</sup> range [31], while MOCVD yields TDDs nearly two orders of magnitude lower ( $\sim 5 \times 10^8$  cm<sup>-2</sup>) [30]. Lower TDDs in GaN layers grown on foreign substrates is another incentive for industry's use of MOCVD over PAMBE.

Early growths of AlGaN/GaN/AlN/SiC HEMT structures by Ga-rich PAMBE included AlN initiation layers grown Al-rich. Under Al-rich conditions, an initiation layer with smooth surface morphology and lower TDD was realized, but buffer leakage was significant [32,33]. Through a systematic study, Poblenz *et al.* [33] demonstrated that a higher Al/N flux ratio yielded a GaN buffer layer with unexpectedly high conductivity. Comparisons in buffer quality are commonly made through buffer breakdown measurements with the buffer breakdown voltage defined as the voltage necessary to reach 1 mA/mm of buffer current between the source and drain. To facilitate buffer breakdown measurements, a 1  $\mu$ m-long segment of the AlGaN barrier was etched between the source and drain, eliminating the 2DEG. As shown in Fig. 1.8(a), with Al/N flux ratios higher than 1, buffer breakdown voltages were in the range of 1 V, which is unsuitable for HEMT operation. To understand the origin of these results, secondary ion mass spectroscopy (SIMS) was performed. When Al/N flux ratios were  $\geq 1$ , a high concentration of Si was observed at the GaN/AlN interface (Fig. 1.8(b)).

Liquid Al reacts with SiC. Namely, in the ternary Al-Si-C phase diagram, there is no tie-line between Al and SiC, thus reaction of Al with SiC is expected. The reaction of excess Al with SiC results in dissolution of  $\sim 1$  ML equivalent Si, which primarily floats on the growing AlN layer and subsequently incorporates in the GaN layer. As a result, the initial GaN layer is doped heavily n-type.

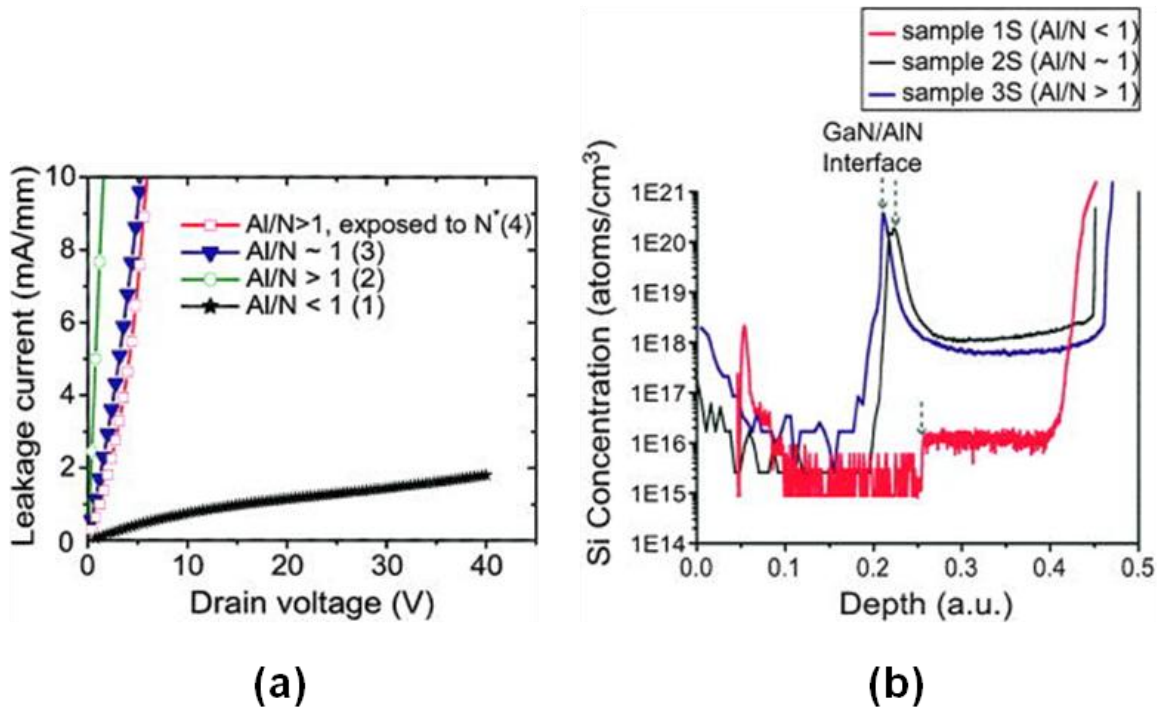


**Figure 1.8: (a) Buffer DC-IV curves for a HEMT grown on 4H-SiC by Ga-rich PAMBE, showing increased buffer leakage current with higher Al/N flux ratios. (b) SIMS profiles of Si concentration in the AlN initiation layers and GaN buffers. From Ref. [33].**

After this discovery, the AlN initiation layers in AlGaIn/GaN/AlN/SiC HEMT structures were grown N-rich at  $\sim 745$  °C. The N-rich AlN initiation layers proceed in the Volmer-Weber growth mode, as evidenced by a spotty RHEED pattern. As the AlN growth is N-rich, there is no excess Al metal on the surface to react with SiC. Though it



results in rough surface morphology, N-rich growth of the AlN initiation layer provides the resistive GaN growth interface highlighted in Fig. 1.7. This yields a high substrate resistance (Fig. 1.5) that reduces parasitic substrate conduction to negligible values. Without a resistive GaN growth interface, there are two highly conductive channels, and this leakage path is too far from the gate contact to be pinched off during HEMT operation.

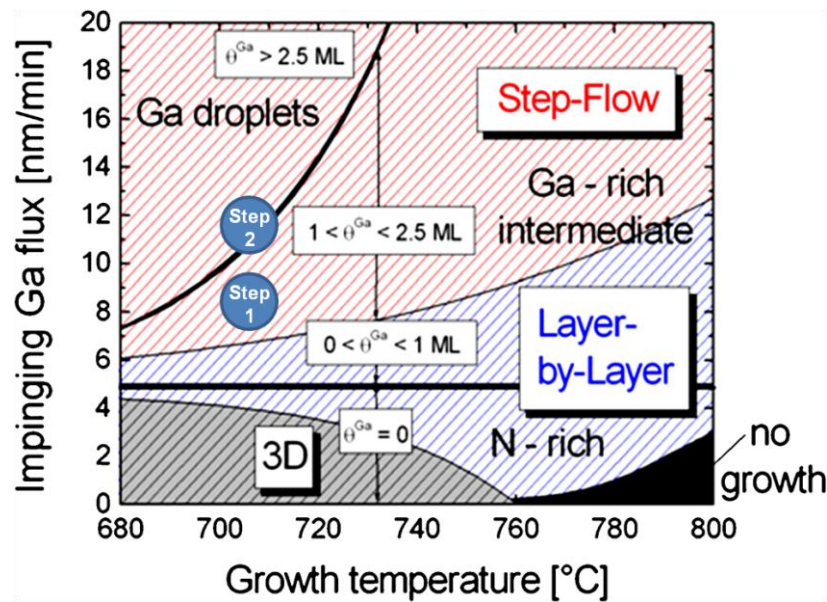


**Figure 1.9: PAMBE growth diagram for Ga-face GaN as a function of Ga flux and growth temperature, showing the growth regimes, growth modes, and liquid Ga surface coverage ( $\theta^{Ga}$ ). From Ref. [34].**

Upon completion of the AlN initiation layer, a two-step GaN buffer is usually grown at temperatures near 700 °C to smooth the surface [35] and reduce TDD by up to a factor of 4 [36]. The GaN growth modes as a function of Ga flux and temperature are shown in Fig. 1.9. Figure 1.9 shows the three characteristic growth regimes for GaN: N-rich, Ga-rich intermediate, and Ga-rich droplets. The growth regimes depicted are based

on an N flux yielding a GaN growth of ~4 nm/hr. Over the range of N fluxes (up to ~20 nm/hr) from currently available N plasma sources, Fig. 1.9 is considered the universal GaN growth diagram for PAMBE (shifting the N-rich regime with the N flux). Figure 1.9 also shows three distinct growth modes: step-flow, layer-by-layer, and 3D.

The ‘Step 1’ UID GaN layer in Fig. 1.7 is usually grown in the Ga-rich intermediate regime. In the intermediate regime, GaN growth is faceted, bending threading dislocations off-axis. This angled propagation of threading dislocations leads to fusion and annihilation reactions that reduce TDD. The Ga/N flux ratio for ‘Step 1’ is ~2, so Ga adlayer coverage of the surface is between 1 and 2.5 monolayers (MLs). In ‘Step 2’ (shown in Fig. 1.9) of the two-step buffer, GaN is grown in the droplet regime, in which a complete Ga adlayer (> 2.5 ML) acts as an autosurfactant. The complete Ga adlayer enables high growth surface mobility and helps recover smooth morphology, which is indicated by a streaky RHEED pattern. If droplet accumulation is left unchecked, clusters of unknown composition (presumably a  $\text{GaN}_x$  compound) form, and buffer breakdown voltage suffers. Growth in the droplet regime is commonly modulated with 15 minutes of growth, followed by 3 minutes of thermal desorption. Complete desorption of the Ga bilayer is evidenced through RHEED intensity transients before growth resumes. The RHEED intensity during thermal desorption is characterized by two distinct peaks. Desorption does not occur favorably at the droplet surfaces, but rather at the surface of the wetting layer. The amount of liquid Ga in excess of 2 ML is fed by the droplets as it desorbs. During thermal desorption, RHEED intensity peaks are

observed when there is exactly 1 ML of liquid Ga on the surface and when the surface is bare.

As buffer layer thickness increases, there are more opportunities for fusion and annihilation reactions of TDs, but dislocation inclination often leads to cracking with buffers thicker than 2  $\mu\text{m}$  [37]. Buffer layers in AlGaN/GaN/AlN/SiC HEMT structures are generally  $\sim 1 \mu\text{m}$  thick. Upon completion of the buffer layer, the 2DEG is then commonly formed through growth of an AlGaN or AlGaN/AlN barrier (Fig. 1.7); the growth parameters for homogeneous InAlN by PAMBE were only recently discovered (discussed in Chapter 8) [38,39]. The high TDD that results from heteroepitaxy on SiC results in an (In,Al,Ga)N surface morphology dominated by spiral hillocks with ML step height, terminated by screw-component dislocations (Fig. 1.10) [40].

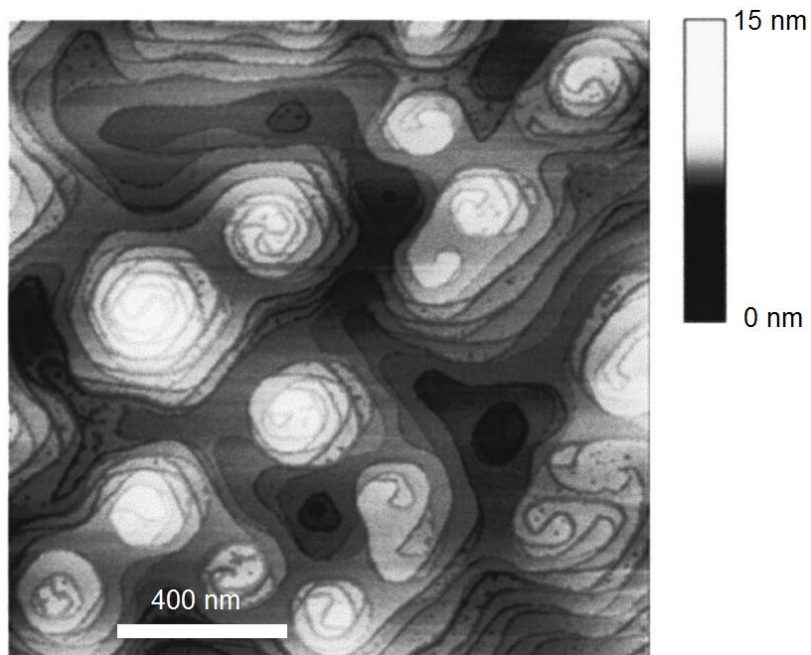


**Figure 1.10: AFM micrograph showing dislocation-mediated spiral hillocks on the surface of an AlGaN/GaN heterostructure grown by Ga-rich PAMBE. From Ref. [40].**

Plan-view transmission electron microscope (PV-TEM), high resolution x-ray diffraction (HRXRD), and monochromatic cathodoluminescence (mono-CL) data show that ~1-2  $\mu\text{m}$ -thick Ga-rich PAMBE GaN buffer layers grown on SiC (with an AlN initiation layer) have TDDs of  $\sim 10^{10} \text{ cm}^{-2}$ . Despite having high TDD, Ga-rich PAMBE AlGaN/GaN/AlN/SiC HEMTs have been fabricated with excellent DC and RF performance. These performance metrics are dependent on SOA processing techniques, including gate design and *ex situ* material deposition (passivation layers, gate dielectrics, etc); however, this performance could not be accomplished with trap-ridden or leaky epistuctures.

Even though the MBE chamber pressure is at ultrahigh vacuum ( $\sim 10^{-10}$  Torr) before growth begins, background concentrations for O and Si near  $\sim 1 \times 10^{17} \text{ cm}^{-3}$  have been detected with SIMS in UID buffers. Considering that the chamber pressure during growth is  $\sim 10^{-5}$  Torr and that the atomic density GaN is  $\sim 10^{22} \text{ cm}^{-3}$ , this background impurity concentration should be expected  $((10^{-5} \text{ Torr})/(10^{-10} \text{ Torr}) \times (10^{22} \text{ cm}^{-3})) = 10^{17} \text{ cm}^{-3}$ . There could also be a non-negligible concentration of nitrogen vacancies ( $V_N$ ), which are intrinsic donors, assuming that their formation is favorable in a Ga-rich environment. The UID GaN buffer would be relatively conductive if it were not for dislocation-associated traps. It has been proposed that there is an electron trap for every  $c/2$  translation (0.259 nm) of each TD [41]. With a TDD of  $\sim 2 \times 10^{10} \text{ cm}^{-2}$ , there is a TD-associated trap density of  $\sim 7.7 \times 10^{17} \text{ cm}^{-2}$ , which is greater than the background doping concentration. Thus, GaN buffers in AlGaN/GaN/AlN/SiC HEMTs grown by Ga-rich PAMBE show semi-insulating behavior.

When the sample exits the growth chamber, the surface is covered with O, Si, and C from the atmosphere. Surface states have a significant impact on device performance at high-frequency if they are not a substantial distance from the channel. In typical Ga-face HEMTs, devices have no additional capping layers on top of the AlGa<sub>N</sub> barrier, so the surface states are 20-30 nm from the channel. Since the c-plane of GaN appears not to have a native oxide, thin GaN caps ( $\leq 2$  nm) have been grown on top of the AlGa<sub>N</sub> barrier to reduce surface traps that might aid in gate leakage.

Without thick GaN caps or *ex situ* passivation, high-frequency operation AlGa<sub>N</sub>/GaN HEMTs is impossible. Current collapses as surface traps on the drain-side of the gate become negatively charged [24]. These surface states are effectively removed through *ex situ* deposition of a dielectric passivation layer (Fig. 1.7). SiN<sub>x</sub>, HfO<sub>2</sub> [42], Al<sub>2</sub>O<sub>3</sub> [43], and other low-K dielectrics have been deposited with e-beam evaporation, pulsed laser deposition (PLD), atomic layer deposition (ALD), and plasma-enhanced chemical vapor (PECVD). Yet, the impact of passivation material quality on device performance has yet to be thoroughly investigated.

Material degradation, manifested as pits near the peak electric field during HEMT operation, has been observed when devices are passivated *ex situ* (Fig. 1.11) [44,45]. The pit formation at a critical gate-to-drain voltage is supposedly the result of O<sup>2-</sup> or ionized water molecule diffusion to the AlGa<sub>N</sub> surface and subsequent electrochemical etching [46]. The native oxide on the AlGa<sub>N</sub> surface has also been implicated as a factor in the electrical stress-induced pit formation.

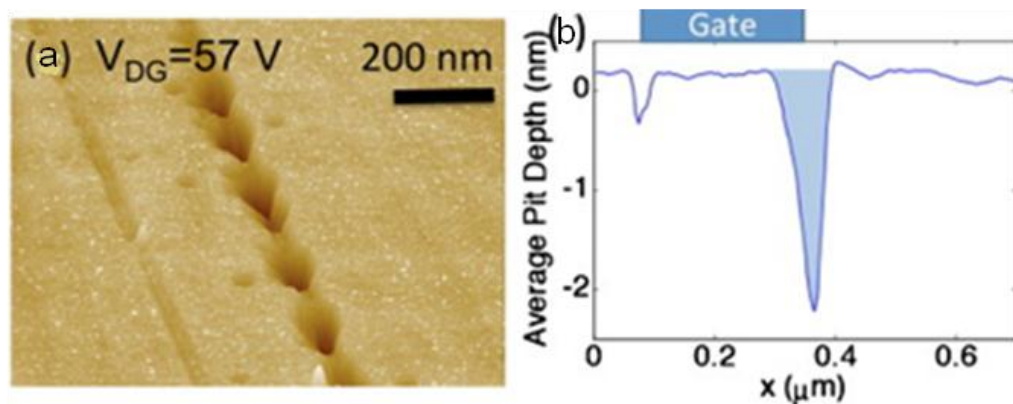


**Figure 1.11: (a) SEM image of pit formation in a HEMT stressed at a drain-gate voltage ( $V_{DG}$ ) of 57 V and (b) average pit depth at this bias measured by AFM. From Ref. [45].**

Bypassing the need for *ex situ* passivation could be an important step in improving the reliability of GaN-based HEMTs. In the deep-recess HEMT structure, a thick (100+ nm) GaN cap is included, and surface states are too far from the channel to effect device performance at high frequency. To prevent the formation of a two-dimensional hole gas (2DHG) at the top GaN/AlGaN interface, the GaN cap is Si-doped [13,47]. The gate also needs to be recessed down to the AlGaN surface, otherwise the channel cannot be modulated. Processing of the deep-recess HEMT structure was simplified with the discovery of the  $\text{BCl}_3/\text{SF}_6$  dry etch with high selectivity of GaN over AlGaN [48]. Fluorine reacts with Al to form the nonvolatile compound  $\text{AlF}_3$  that increases the etch rate differential of GaN to AlGaN (80:1) [13]. High PAE (63% at 28 V drain bias) and  $P_{\text{out}}$  (10.5 W/mm at 48 V drain bias) have been achieved at 10 GHz with the unpassivated deep-recess HEMT structure, suggesting minimal effects from charged surface states and charged trap states in the thick GaN cap. Further studies of the deep-

recess HEMT structure will determine how defects in the thick GaN cap affect device performance and reliability.

Though high-quality heteroepitaxy can be achieved for GaN growth on 4H-SiC and 6H-SiC, large-area SiC substrates are expensive (4" diameter substrates are currently used in SOA fabrication facilities). Si (111) presents an attractive alternative to 4H-SiC and 6H-SiC since inexpensive, high-quality Si substrates are widely available, due to the well-established Si electronics industry [49–52]. Currently, 12" diameter Si substrates are used in SOA fabrication facilities, and plans to move on to 18" diameter substrates have been announced. With such large substrates, Si fabrication facilities have throughput far beyond those for SiC electronics.

The three main challenges for GaN growth on Si (111) substrates are as follows: minimizing interfacial reactions; managing high TDDs and the resulting stress gradients; and managing thermal stresses. The in-plane lattice constant for Si (111) is  $0.384 \text{ nm}$  ( $a_{\text{Si}(100)}/\sqrt{2}$ ). As stated earlier, there is a lattice mismatch (thermal mismatch) of 16.9% (-56%) between Si (111) and GaN. The reactivity of Si with an impinging active N flux increases the probability of  $\text{SiN}_x$  growth, so initiation layers are grown at low temperatures to suppress the formation of  $\text{SiN}_x$ . Since growth initiation temperatures are low, island size upon coalescence is very small, and this produces high TDD. The large thermal mismatch between GaN and Si often leads to extreme wafer bowing and cracking upon cool-down. Reports of crack-free GaN on Si (111) have increased rapidly over the past decade through initiation layer optimization, and detailed explanations of these initiation layers can be found in the literature. Even with initiation layer optimization, the

highest quality heteroepitaxy by Ga-rich PAMBE on Si (111) yields TDDs from  $10^9$  to  $10^{10}$   $\text{cm}^{-2}$  [52].

Heteroepitaxy on AlN substrates has also been considered, and GaN layers grown on AlN have the lowest TDD amongst GaN grown on foreign substrates. Though there have been advances in the growth of AlN boules [53], AlN substrates are still expensive and have low distribution. If AlN substrates are a viable option, it would be more sensible to forego heteroepitaxy and grow directly on FS GaN.

### **1.3.3 Heteroepitaxy by $\text{NH}_3$ -MBE**

In an effort to combine a low-impurity, ultrahigh vacuum environment with the growth rates of MOCVD,  $\text{NH}_3$ -MBE was developed with high flows of  $\text{NH}_3$  impinging on the surface. Growth rates of 8.3 nm/min (500 nm/hr) and greater are commonly realized with  $\text{NH}_3$ -MBE – far greater than those for conventional Ga-rich PAMBE. With group III-limited growth (Ga/N: 0.001), the “growth window” is also much wider, and tight temperature control is not as important [54–56].

Many of the issues discussed for heteroepitaxy with Ga-rich PAMBE apply to  $\text{NH}_3$ -MBE. The epistucture for a HEMT grown by  $\text{NH}_3$ -MBE on SiC is essentially the same as the one depicted in Fig. 1.7. The AlN initiation layer is generally grown at ~800-850 °C with a high  $\text{NH}_3$  overpressure to yield a smooth surface morphology. High  $\text{NH}_3$  overpressure appears to suppress decomposition, while the high growth temperature enhances the surface diffusion of adatoms. A two-step buffer is included in HEMT structures grown by  $\text{NH}_3$ -MBE to reduce TDD. Though the growth kinetics of  $\text{NH}_3$ -MBE are not fully understood, a growth map has been developed (Fig. 1.12(a)) that



depicts the parameter space of the three main growth modes: unstable layer-by-layer, quasi-stable step flow, and dislocation-mediated pitting.

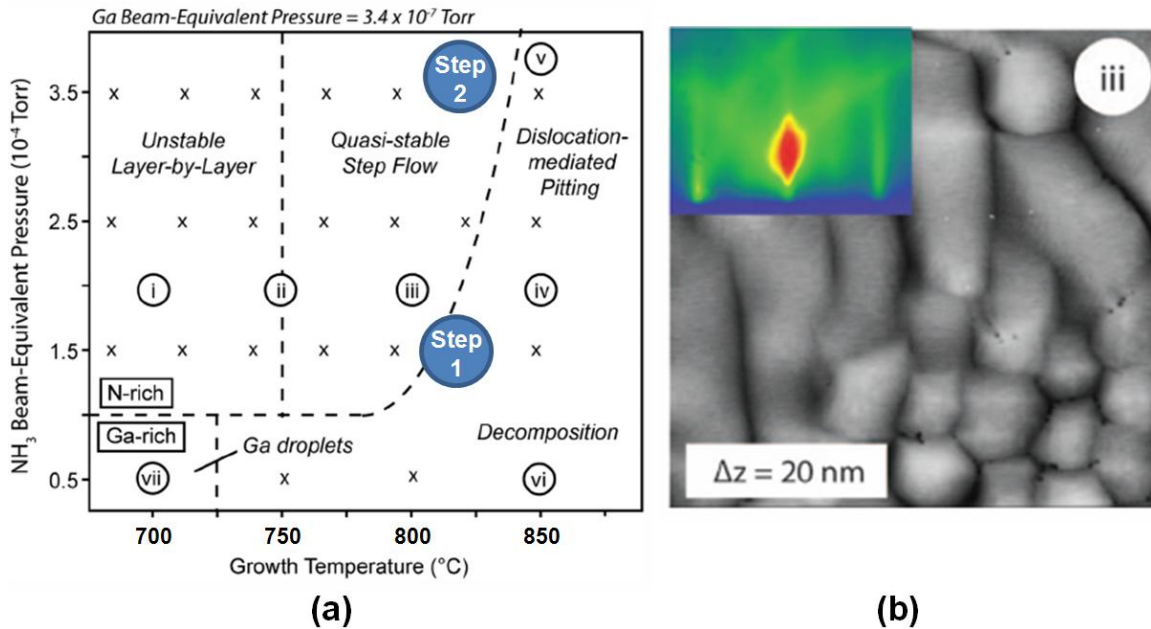


**Figure 1.12: (a) Growth diagram for NH<sub>3</sub>-MBE, showing the conditions used for ‘Step 1’ and ‘Step 2’ of the GaN buffer. (b) AFM micrograph showing the smooth mounds that form in the quasi-stable step flow regime and a streaky RHEED pattern (inset). From Ref. [56].**

The growth parameters for ‘Step 1’ of the two-step buffer are shown in Fig. 1.12(a) [56]. In ‘Step 1,’ there is a slight overpressure of NH<sub>3</sub>. The growth temperature is above that for the thermal decomposition of GaN, so there is pitting at threading dislocations, where exposed facets balance dislocation line tension. The faceted surface promotes the formation of closed TD loops. Smooth surface morphology is recovered with ‘Step 2,’ in which a high NH<sub>3</sub> overpressure effectively suppresses decomposition, yielding quasi-stable step flow growth. The step flow growth mode is deemed “quasi-stable” because surface morphology is initially dominated by spiral hillocks (like those

shown in Fig. 1.10 for Ga-rich PAMBE). As buffer thickness increases beyond 500 nm, the spiral hillocks transition into truncated pyramidal mounds (Fig. 1.12(b)). PV-TEM, HRXRD, and mono-CL have shown that GaN grown on SiC by NH<sub>3</sub>-MBE has similar TDD to Ga-rich PAMBE ( $\sim 10^{10}$  cm<sup>-2</sup>) [54].

There are very few reports of large-signal performance for AlGaN/GaN HEMTs grown directly on SiC by NH<sub>3</sub>-MBE. The highest reported P<sub>out</sub> (PAE) at 10 GHz for an NH<sub>3</sub>-MBE-grown HEMT is 11.2 W/mm (58%) at an unspecified drain bias [54]. This excellent load-pull performance indicates that NH<sub>3</sub>-MBE has great potential in the realm of X-band power amplification.

The first crack-free AlGaN/GaN HEMT grown on a 3" Si(111) substrate by NH<sub>3</sub>-MBE was also recently demonstrated [57]. Using an AlN(50 nm)/GaN(200 nm)/AlN(200 nm) initiation layer, a TDD of  $\sim 2.1 \times 10^9$  cm<sup>-2</sup> was achieved. A high 2DEG mobility (sheet density) of 1350 cm<sup>2</sup>/Vs ( $1.2 \times 10^{13}$  cm<sup>-2</sup>) was also measured, but large-signal measurements have yet to be reported.

## 1.4 Synopsis

This dissertation builds upon the research of C. Poblenz (Ga-rich PAMBE) and A. Corriou (NH<sub>3</sub>-MBE). Their work identified and corrected many important growth issues for AlGaN/GaN heterostructures on SiC, resulting in high-quality HEMTs. However, it was clear that heteroepitaxy by molecular beam epitaxy yields GaN layers with unacceptably high TDD. The principal objective of this dissertation is to determine the benefits and detriments of growing low-TDD HEMT structures on FS GaN.

Chapter 1 gave a brief overview of HEMT operation and performance metrics. The advancements in MBE growth technology (mainly from UCSB) for GaN-based HEMT structures on SiC were also detailed. Much of the information in Chapter 1 was reviewed in Ref. [58].

In Chapter 2, the effects of threading dislocations on the gate leakage and buffer leakage of AlGaN/GaN heterostructures are investigated with growth by Ga-rich PAMBE. Most of the data presented in Chapter 2 was published in Ref. [59]. Threading dislocation density is then correlated to the three-terminal breakdown of Ga-rich PAMBE-grown HEMTs in Chapter 3. Chapter 3 also includes the structural modification of Ga-rich PAMBE-grown HEMTs on FS GaN for the purpose of reducing DC-RF dispersion. The large-signal measurements in Chapter 3 were reported in Ref. [60].

In Chapter 4, a growth procedure for the inclusion of pure AlN interlayers in AlGaN/AlN/GaN heterostructures is developed with Ga-rich PAMBE. This growth procedure was published in Ref. [61]. A correlation between TDD and the sheet resistance of these AlGaN/AlN/GaN heterostructures is also identified. The concept of dislocation-related scattering is expanded upon in Chapter 5.  $\text{Al}_x\text{Ga}_{1-x}\text{N}/\text{GaN}$  heterostructures yielding a wide range of 2DEG sheet densities are grown on substrates that provide TDDs from  $\sim 5 \times 10^7$  to  $\sim 2 \times 10^{10} \text{ cm}^{-2}$ . Temperature-dependent Hall measurements then aid in assessing the effects of threading dislocations on the 2DEG mobility in these heterostructures. These results were reported in Ref. [62].

In Chapter 6,  $\text{NH}_3$ -MBE is used to grow a series of heterostructures similar to that presented in Chapter 2. The effects of threading dislocations on the leakage of  $\text{NH}_3$ -

MBE-grown AlGaN/GaN heterostructures are then determined. In Chapter 7, issues concerning the purity of NH<sub>3</sub>-MBE-grown AlN interlayer are discussed, and a procedure to improve their purity is outlined.

Moving away from AlGaN/GaN heterostructures, a growth procedure for homogeneous In<sub>0.17</sub>Al<sub>0.83</sub>N layers, lattice-matched to GaN, is developed using N-rich PAMBE in Chapter 8. This growth procedure was published in Ref. [38]. These barriers are then incorporated into HEMT structures that yield extremely low sheet resistances.

The salient findings are then summarized in Chapter 9, and future work is proposed.

## **Chapter 2. Ga-rich PAMBE AlGaN/GaN HEMT TDD Series: Leakage**

### **2.1 Introduction**

Threading dislocations are known to facilitate reverse leakage in MOCVD-grown GaN p-n junctions [63], and first-principles calculations predict that pure screw dislocations are Ga-decorated in Ga-rich PAMBE-grown GaN [64,65]. If threading dislocations are decorated with Ga, they could be highly conductive. It is known that TDs introduce mid-gap trap levels along the TD core or in the surrounding material, so leakage may be facilitated through trap hopping. Recent studies with conductive-AFM suggest that dislocation type may not be as important to leakage as III/V ratio since higher III/V ratios lead to an increase in leakage pathways [66].

Seeing that heteroepitaxy by Ga-rich PAMBE yields GaN layers with significant TDDs, a HEMT series was developed to determine the benefits of growth on native substrates. To assess the correlation between TDD and various HEMT performance metrics, regrowths of HEMT structures on GaN templates spanning nearly three orders of magnitude in TDD were performed, including regrowth on FS GaN.

### **2.2 Experimental Procedure**

#### **2.2.1 Regrowth on GaN Templates**

Parasitic conductive channels at the regrowth interface must be eliminated in GaN homoepitaxy. Whereas the AlN initiation layer in GaN heteroepitaxy on SiC provides a natural barrier to impurities on substrate surface, growth on GaN templates requires

intentional doping at the regrowth interface or *in situ* cleaning techniques to ensure low buffer conductivity. The regrowth interface is plagued by high O and Si content on the template surface (Fig. 2.1).

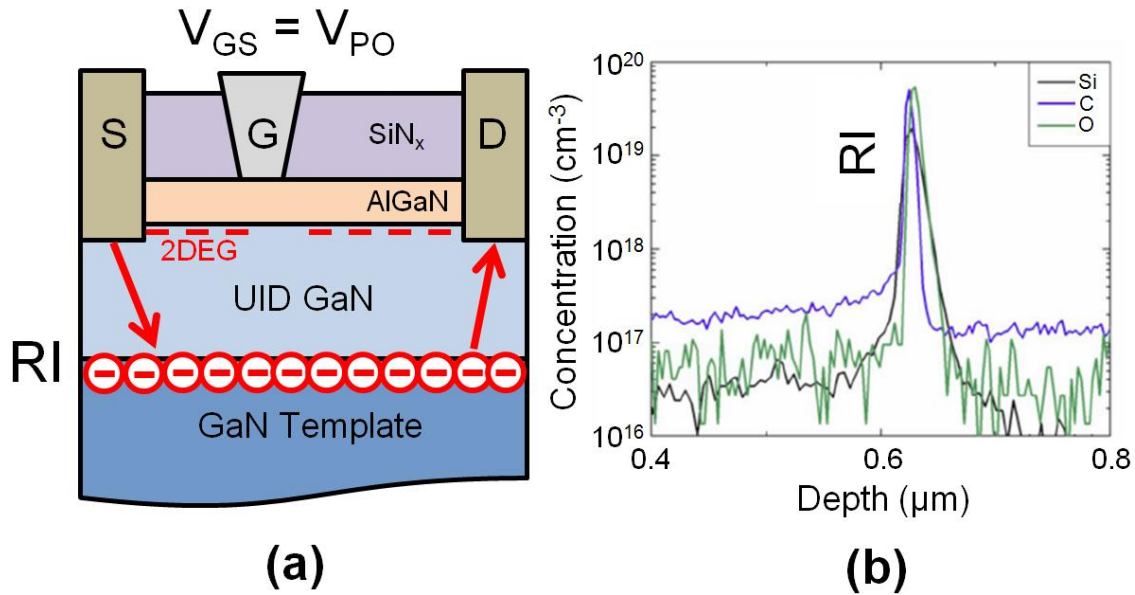


**Figure 2.1:** (a) Schematic showing the mechanism for buffer leakage at pinch-off. (b) SIMS analysis showing high Si, O, and C concentration at the regrowth interface (RI). SIMS from Ref. [18].

Subjecting the template surface to a long high-power N plasma treatment [67] has been shown to decompose the impurity-rich layers of the template and improve buffer breakdown voltage. The N plasma treatment may also introduce roughness that is not easily recovered during GaN regrowth. Depositing an ultrathin AlN layer at the regrowth interface to introduce a polarization dipole barrier has also been effective at improving buffer breakdown voltage [68]. Intentional doping that introduces deep-level traps and compensates residual impurities that may float in the Ga adlayers is the most common method for achieving semi-insulating buffers. In MOCVD growth, Fe-doping provides semi-insulating buffers [69], but Fe-doping in PAMBE has only had limited success [70].

C-doping with  $\text{CBr}_4$  at the regrowth interface has been established as effective in creating highly resistive buffer layers in Ga-rich PAMBE [71]. Theoretical calculations suggest that C impurities in GaN are self-compensating and amphoteric, and these predictions are consistent with recent deep-level optical spectroscopy (DLOS) studies in both p- and n-type GaN [72]. When GaN is co-doped with C and Si, semi-insulating behavior results, attributed to the free-carrier compensation of the deep-level C impurity [73].

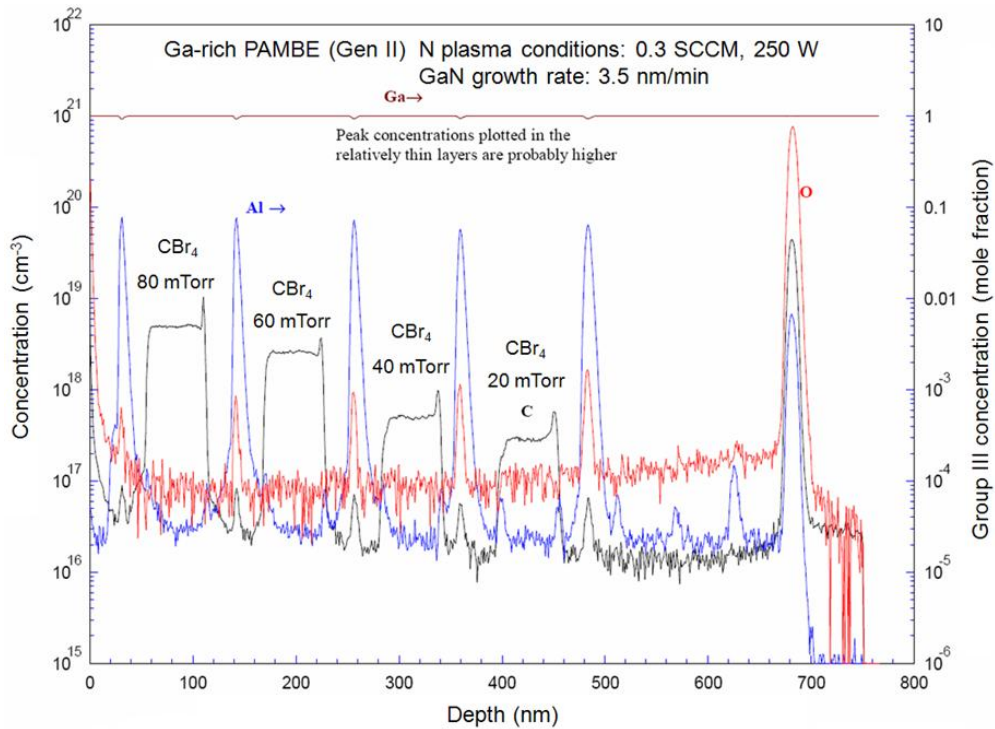


**Figure 2.2: SIMS analysis of C concentration in Ga-rich PAMBE GaN layers grown on the Varian Gen-II MBE with various  $\text{CBr}_4$  foreline pressures.**

C-doping was employed in all Ga-rich PAMBE regrowths presented in this thesis. The C concentration for various  $\text{CBr}_4$  foreline pressures was calibrated with SIMS (Fig. 2.2). Since the  $\text{CBr}_4$  delivery system cannot maintain a steady foreline pressure above 100 mTorr, the highest foreline pressure used was 80 mTorr, which resulted in a C

concentration of  $\sim 5 \times 10^{18} \text{ cm}^{-2}$  for a growth rate of 3.5 nm/min. The leak valve on the  $\text{CBr}_4$  system can be adjusted to introduce higher  $\text{CBr}_4$  fluxes, but a C concentration one order of magnitude higher than the background donor concentration generally yields semi-insulating GaN.

## 2.2.2 Growth of TDD Series

All  $\text{AlGaN}/\text{GaN}$  heterostructures (Fig. 2.3) were grown in a Varian Gen-II MBE system, equipped with conventional Ga and Al effusion cells and an RF-plasma nitrogen source. The nitrogen source consisted of ultrahigh purity (99.9995%)  $\text{N}_2$  gas flowing at 0.3 SCCM through the gas input to the RF-plasma source with 250 W RF power. This flow rate and RF power combination corresponded to a growth rate of  $\sim 3 \text{ nm/min}$  for Ga-rich GaN layers. The 4H-SiC substrate and GaN templates were solvent-cleaned and degassed in ultrahigh vacuum prior to growth.

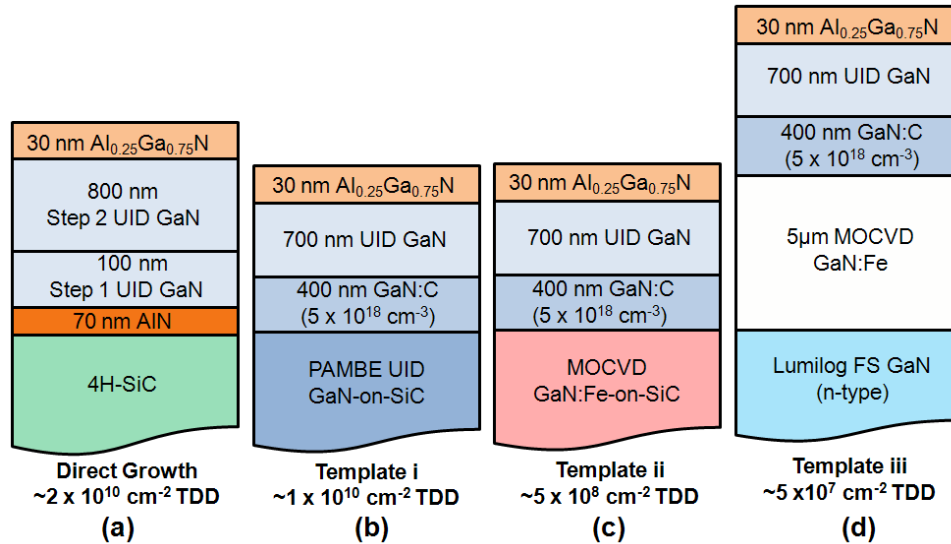


**Figure 2.3: Layer schematics for  $\text{Al}_{0.25}\text{Ga}_{0.75}\text{N}/\text{GaN}$  HEMT structures (a) grown directly on 4H-SiC, (b) regrown on Template i, (c) regrown on Template ii, and (d) regrown on Template iii by Ga-rich PAMBE.**



Direct growth on 4H-SiC was initiated with an AlN layer grown at 745 °C with an Al/N flux ratio of ~0.65, resulting in a growth rate of ~2 nm/min. The growth temperature was measured with an optical pyrometer that was calibrated to the melting point of Al (660 °C). A spotty reflection high energy electron diffraction (RHEED) pattern indicated the Volmer-Weber growth mode for the AlN. Subsequently, 900 nm of two-step GaN buffer was grown to reduce TDD. To control Ga droplet accumulation, the growth was modulated with 15 minutes of growth followed by 3 minutes of thermal desorption. RHEED intensity transients showed complete desorption of Ga droplets before growth resumed. Upon completion of the GaN buffer layer, a 30 nm  $\text{Al}_{0.25}\text{Ga}_{0.75}\text{N}$  barrier was grown to complete the AlGaIn/GaN heterostructure.

Regrowths on template i, template ii, and template iii were also performed in the Ga-rich regime. Template i ( $\sim 2 \times 10^{10} \text{ cm}^{-2}$  TDD) consisted of 900 nm GaN grown by PAMBE on a 4H-SiC substrate. Template ii ( $\sim 5 \times 10^8 \text{ cm}^{-2}$  TDD) consisted of 1  $\mu\text{m}$  GaN:Fe grown by MOCVD on a 4H-SiC substrate, and 5  $\mu\text{m}$  GaN:Fe grown by MOCVD on Lumilog n-type FS GaN comprised Template iii ( $\sim 5 \times 10^7 \text{ cm}^{-2}$  TDD). Only n-type FS GaN was available at the time of this study, and the thick GaN:Fe layer was included to reduce the parasitic pad capacitance. PAMBE regrowth on these templates started with 400 nm GaN:C. The GaN:C layer was grown in the Ga droplet regime with a Ga/N flux ratio of ~3 at 715 °C, employing modulated growth as described above.  $\text{CBr}_4$  flow was interrupted during the thermal desorption interval. A subsequent UID 700 nm GaN layer was grown under the same conditions, followed by a 30 nm  $\text{Al}_{0.25}\text{Ga}_{0.75}\text{N}$  barrier.

### 2.2.3 Device Fabrication

Van der Pauw Hall structures (Fig. 2.2(a)), Schottky diodes (Fig. 2.2(b)), and HEMTs (Fig. 2.2(c)) were fabricated using optical lithography on the Ga-rich PAMBE TDD Series. Ohmic contacts (Ti/Al/Ni/Au - 20/120/30/50 nm) were deposited by e-beam evaporation and annealed at 820 °C in an N<sub>2</sub> environment for 30 s. For the Schottky diode structures, Schottky contacts (Ni/Au/Ni - 30/250/50 nm) were subsequently deposited by e-beam evaporation. Mesa isolation was then performed with a BCl<sub>3</sub>/Cl<sub>2</sub> reactive ion etch (RIE). This etch (~60 nm deep) was also employed for the removal of the AlGaN barriers in the buffer breakdown test patterns. After mesa isolation, the AlGaN surface in the HEMT structures was passivated with SiN<sub>x</sub> deposited by PECVD. Slant-gate contacts (Ni/Au/Ni - 30/250/50 nm) were then deposited by e-beam evaporation following a self-aligned SiN<sub>x</sub> recess process using a CF<sub>4</sub> RIE [74]. The HEMTs had a 0.7 μm gate length (L<sub>G</sub>), 2x75 μm gate width (L<sub>W</sub>), 0.5 μm gate-source spacing (L<sub>GS</sub>), and 2 μm gate-drain spacing (L<sub>GD</sub>). Extensive description of the HEMT fabrication process is presented in Appendix A. The circular Schottky diodes had a radius of 100 μm, and the van der Pauw Hall.

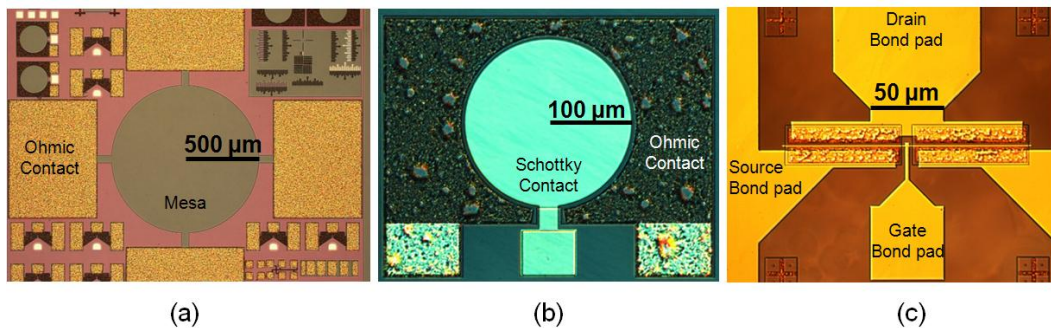


**Figure 2.4: Nomarski microscope images of (a) van der Pauw Hall structure, (b) Schottky diode, and (c) HEMT.**

## 2.3 Results and Discussion

### 2.3.1 Structural Properties

HRXRD  $\omega$ - $2\theta$  scans (Fig. 2.5) of the GaN (0002) reflection indicated the following AlGaN barrier thicknesses (Al mole fractions) of the AlGaN/GaN heterostructures: 28 nm (0.28) for the direct growth on 4H-SiC, 27 nm (0.24) for the regrowth on template i, 28.8 nm (0.23) for the regrowth on template ii, and 30 nm (28 %) for the regrowth on template iii. The barrier thicknesses were calculated from the spacing of Pendellösung fringes, and Al mole fractions were determined through the spacing of the GaN (0002) and AlGaN (0002) peaks.

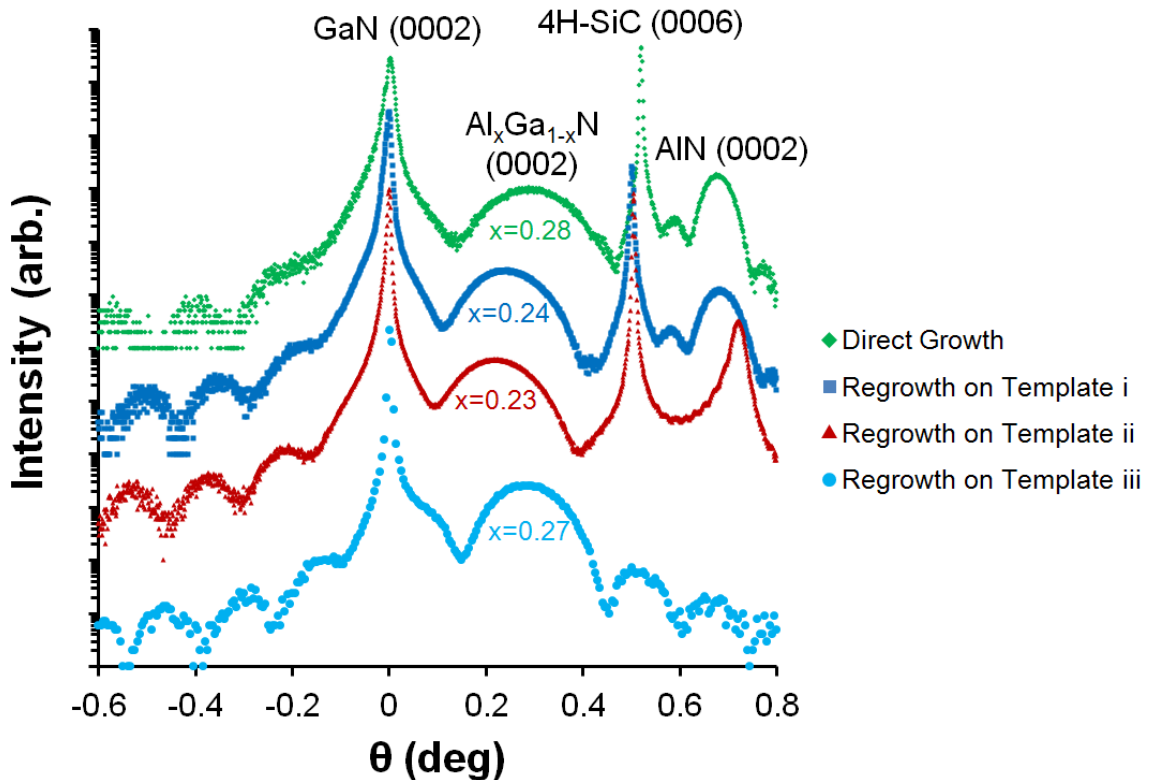
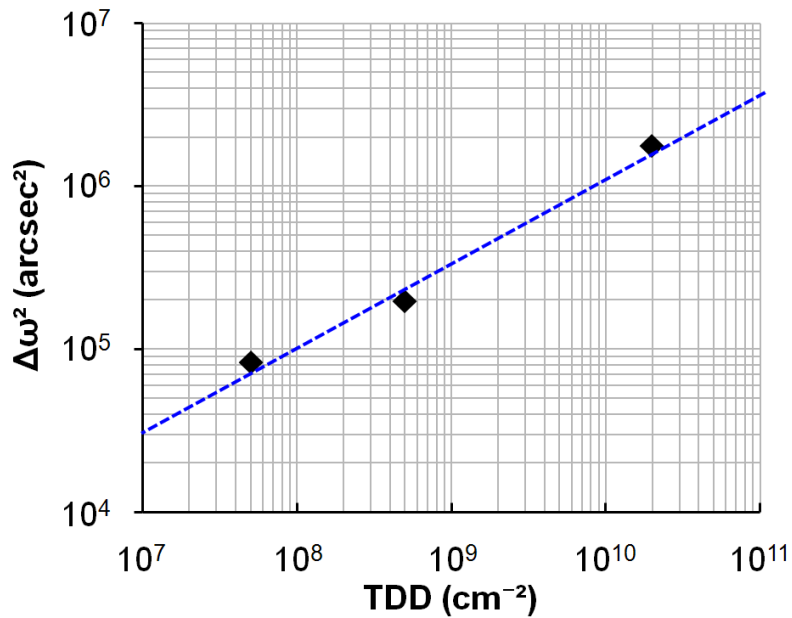


Figure 2.5: HRXRD  $\omega$ - $2\theta$  scans of the GaN (0002) reflections in the Ga-rich PAMBE TDD Series.

The rocking curve full width half maximums of  $\omega$ -scans ( $\Delta\omega$ ) for the GaN (20 $\bar{2}$ 1) reflection (measured in a skew symmetric geometry) were 1332, 1319, 324, and 288 arcsec, for the direct growth, regrowth on template i, regrowth on template ii, and regrowth on template iii, respectively. The rocking curve width for the nearly in-plane (20 $\bar{2}$ 1) reflection is primarily affected by edge-component TDDs, and  $\Delta\omega^2$  is proportional to edge-component TDD. Using the calibration curve (Fig. 2.6) developed with plan-view transmission electron microscopy (PV-TEM), these  $\Delta\omega$  values are in close agreement with the presumed TDD of each sample [75–77].



**Figure 2.6: Calibration curve for TDD with HRXRD  $[\Delta\omega (20\bar{2}1)]^2$  created from PV-TEM data.**

Although the screw-component TDD can generally be estimated from the relative values of  $[\Delta\omega (0002)]^2$ , the direct growth and regrowth on template i gave very low  $[\Delta\omega (0002)]^2$  values. This was in contrast to AFM scans (Fig. 2.7), which suggested that the

direct growth and regrowth on template i had very high screw-component TDDs. The origin of the discrepancy between the HRXRD and AFM data was unclear. AFM scans indicated the presence of spiral hillocks, which form about screw-component dislocations [40], on the surface of the AlGaIn barriers for the direct growth and regrowths on templates i and ii (Fig. 2.6). The density of spiral hillocks and the roughness of the standard growth and regrowth on template i were very similar, with spiral hillock density of  $1.3 \times 10^9 \text{ cm}^{-2}$  and surface root-mean-square (rms) roughness of  $\sim 0.6 \text{ nm}$ . The density of spiral hillocks on the template ii regrowth was markedly lower at  $3.2 \times 10^8 \text{ cm}^{-2}$ , and the surface rms roughness of this sample was slightly lower at  $\sim 0.5 \text{ nm}$ . Since spiral hillocks are connected to screw-component dislocations, spiral hillock density can be used as an approximation of screw-component TDD. No spiral hillocks were seen in the regrowth on template iii. It can be inferred that the screw-component TDD of template iii is lower than that of template ii. Spiral hillock density correlated positively with the total TDD, as expected.

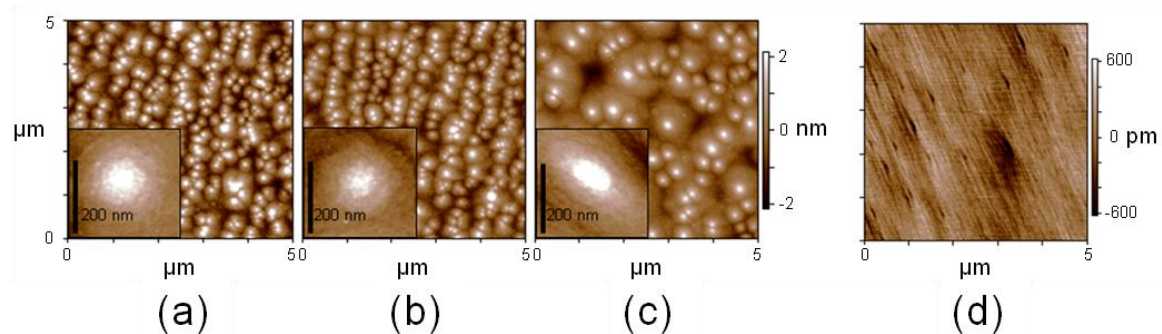


**Figure 2.7: AFM micrographs showing AlGaIn surface morphology from HEMT structures (a) directly grown on 4H-SiC, (b) regrown on template i, (c) regrown on template ii, and (d) regrown on template iii, with insets focusing on single spiral hillocks.**

### 2.3.2 2DEG Characteristics

Hall measurements were performed on four van der Pauw Hall structures on each sample. Averaging the measurements from the four Hall structures, the mobility (2DEG density) of the direct growth, regrowth on template i, regrowth on template ii, and regrowth on template iii, were  $1550 \text{ cm}^2/\text{Vs}$  ( $1.1 \times 10^{13} \text{ cm}^{-2}$ ),  $1450 \text{ cm}^2/\text{Vs}$  ( $1.0 \times 10^{13} \text{ cm}^{-2}$ ),  $1850 \text{ cm}^2/\text{Vs}$  ( $7.5 \times 10^{12} \text{ cm}^{-2}$ ), and  $1700 \text{ cm}^2/\text{Vs}$  ( $1.1 \times 10^{13} \text{ cm}^{-2}$ ), respectively. There appeared to be a slight increase in 2DEG mobility with a reduction in TDD. These measurements agree with the literature for AlGaIn/GaN heterostructures and indicated that HEMTs with low resistance channels ( $350 - 425 \text{ } \Omega/\square$ ) could be fabricated.

### 2.3.3 Buffer Breakdown

Buffer leakage currents were measured on test structures with a source-to-drain spacing of  $1 \text{ } \mu\text{m}$ . Figure 2.8 shows that a drain-source bias ( $V_{\text{DS}}$ ) of  $\sim 77 \text{ V}$  for the direct growth,  $\sim 69 \text{ V}$  for the regrowth on template i,  $\sim 57 \text{ V}$  for the regrowth on template ii, and  $\sim 21 \text{ V}$  to the regrowth on template iii was necessary to reach  $1 \text{ mA/mm}$  of buffer current. C-doping at the regrowth interface effectively compensated residual impurities, as evidenced by the high  $V_{\text{DS}}$  needed to reach  $1 \text{ mA/mm}$  of buffer current. The lower  $V_{\text{DS}}$  to reach  $1 \text{ mA/mm}$  in the regrowths on template ii and template iii can be attributed to a significant reduction in TD-associated electron traps. As mentioned previously, it has been proposed that there is an electron trap for every  $c/2$  translation of each TD. At low TDD the background donor impurity concentration exceeds the dislocation-associated trap concentration, and there is an increase in buffer carrier concentration.

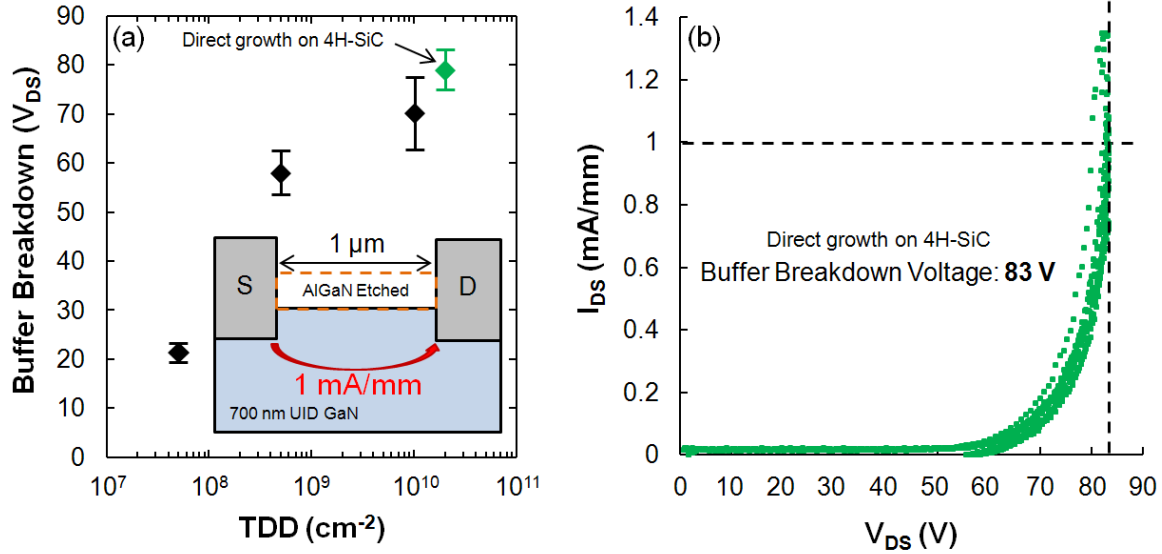


**Figure 2.8: (a) Buffer breakdown voltage with respect to TDD for Ga-rich PAMBE-grown AlGaN/GaN heterostructures (error bars represent standard deviation). (b) Buffer DC-IV curve (continuous measurement) for the heterostructure grown directly on 4H-SiC.**

### 2.3.4 DC and Small-signal Performance

Pulsed DC-IV measurements for the TDD series are shown in Fig. 2.9. As evidenced by a lack of dispersion with a 100 ns pulse width for all heterostructures, passivation with PECVD  $\text{SiN}_x$  was effective. Since bulk GaN has roughly half the thermal conductivity of 4H-SiC, increased dispersion from heating is shown for the DC measurements on the FS GaN regrowth. This heat dispersion was also more pronounced for the regrowth on FS GaN because of the higher current density, which was a result of lower contact resistance and higher 2DEG sheet density and mobility.

Although all DC-IV curves in Fig. 2.9 display sharp pinch-off, the majority of HEMTs fabricated on templates with mid-range ( $\sim 5 \times 10^8 \text{ cm}^{-2}$ ) or low ( $\sim 5 \times 10^7 \text{ cm}^{-2}$ )

TDD could not be fully pinched off. This was the result of a strong leakage pathway, which was likely associated with the  $\text{SiN}_x/\text{AlGaN}$  interface since most of the unpassivated HEMTs were effectively modulated. Further discussion of PECVD-related leakage will be presented in the next chapter.

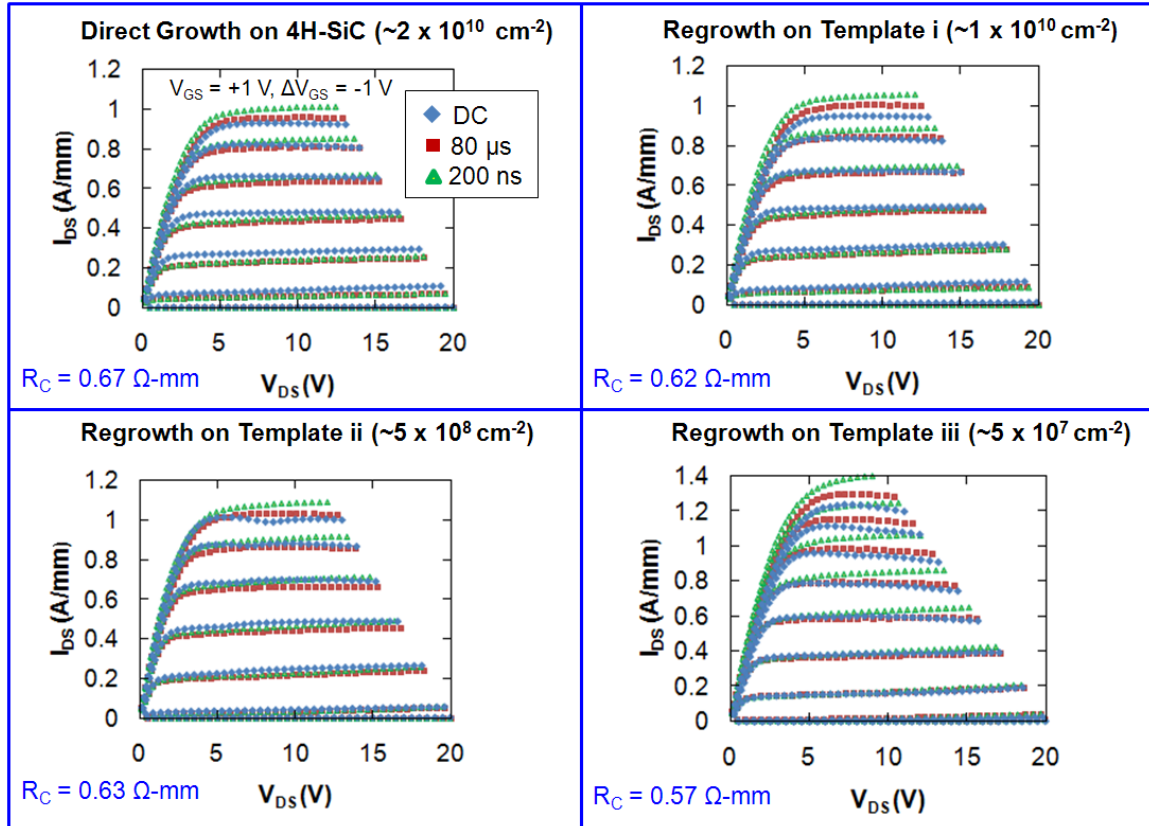


**Figure 2.9: Pulsed DC-IV measurements (10% duty cycle, 50  $\Omega$  load line) from  $V_{GS} = -7$  V to  $V_{GS} = +1$  V on the Ga-rich PAMBE-grown HEMT TDD Series.**

Small-signal measurements (Fig. 2.10) were performed on the passivated slant-gate HEMTs in the TDD Series with an Agilent E8361A precision network analyzer. The extrinsic current-gain-cutoff frequencies ( $f_T$ ) and power-gain-cutoff frequencies ( $f_{max}$ ) determined through  $s$ -parameters were typical for HEMTs with an  $L_G$  of 700 nm. The  $f_T$  and  $f_{max}$  for the regrowth on FS GaN (template iii) were slightly lower than those of the



other heterostructures in the TDD Series, and this was attributed to parasitic pad capacitance. The gate pad capacitance ( $C_{pg}$ ) was an order of magnitude higher for the regrowth on template iii in comparison to the other heterostructures, and the drain pad capacitance ( $C_{pd}$ ) showed a 4-fold increase.

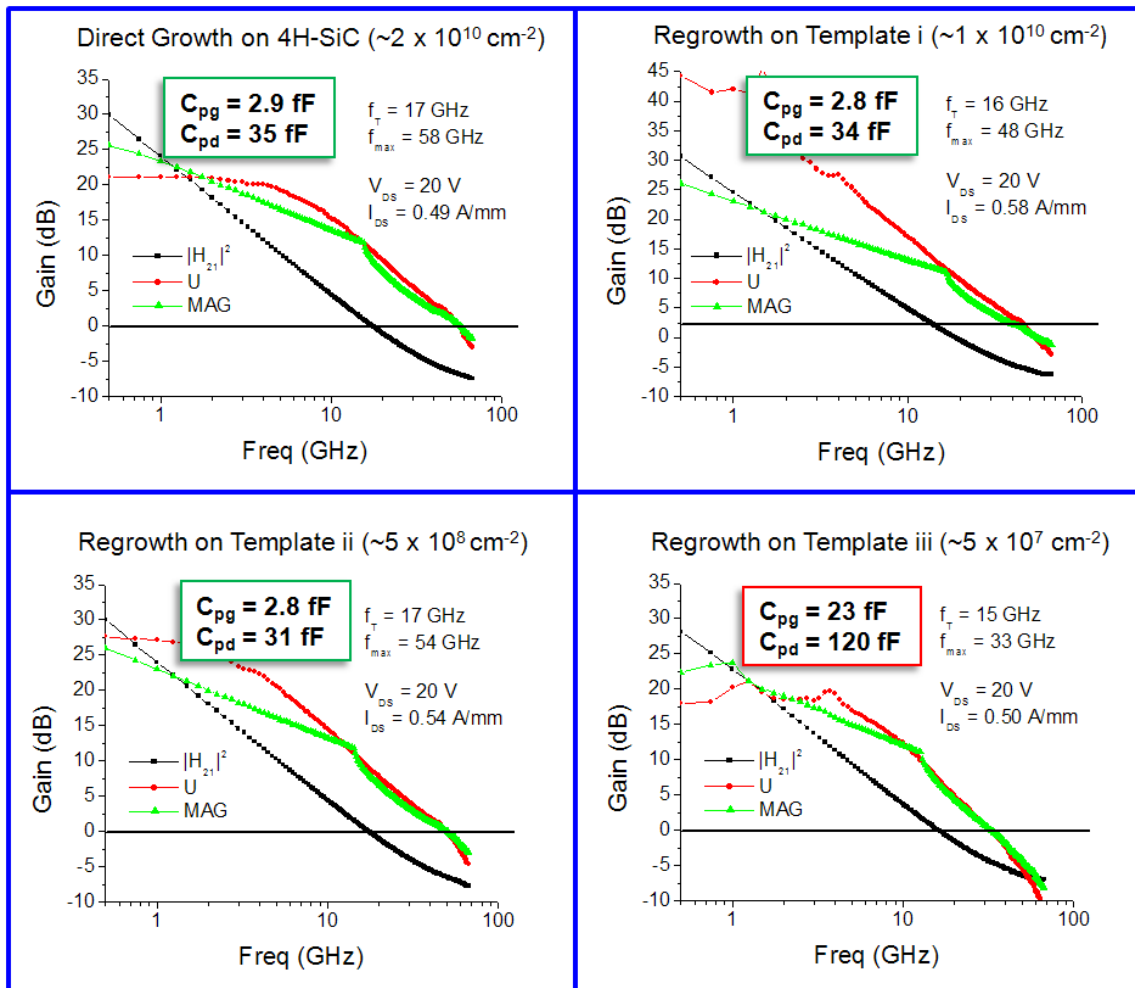
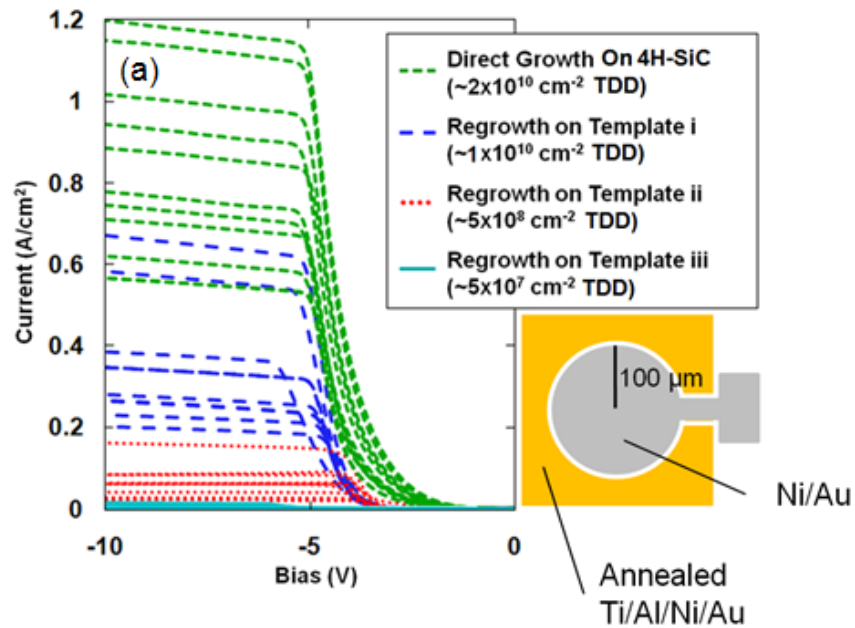


**Figure 2.10: Small-signal measurements, including extrinsic values for  $f_T$  and  $f_{max}$ , in the Ga-rich PAMBE-grown TDD series with  $V_{GS} = -2 \text{ V}$ , showing increased parasitic pad capacitance in the regrowth on template iii.**

### 2.3.5 Schottky Contact Leakage

The DC-IV curves in Fig. 2.11 depict the reverse current of Schottky diodes from the 10 lowest leakage dies of each heterostructure. The average reverse current density at -10 V was 0.85 A/cm<sup>2</sup> for the direct growth on 4H-SiC, 0.40 A/cm<sup>2</sup> for the regrowth on template i, 0.067 A/cm<sup>2</sup> for the regrowth on template ii, and 0.019 A/cm<sup>2</sup> for the regrowth on template iii. Decreasing the TDD or spiral hillock density was connected to a decrease in the reverse current of Schottky diodes. Decreasing the TDD from  $\sim 2 \times 10^{10}$  to  $\sim 5 \times 10^7$  cm<sup>-2</sup> produced up to a 45-fold decrease in average reverse current density. Leakage measurements using large-area Schottky diodes eliminated high-field effects in HEMT geometries. Thus, reverse leakage measurements of large-area Schottky diodes provide a general indication of the true gate leakage that accompanies an increase in TDD. No conclusions can be made about the character of TDs responsible for leakage, however.

Although the directly grown heterostructure and the regrowth on template i were assumed to have the same dislocation density, the regrowth had a thicker GaN layer, which provided more opportunities for fusion and annihilation reactions of TDs. This is seen in the lower FWHM of the GaN (20 $\bar{2}$ 1) rocking curve. The reduction in TDD likely explains the lower average reverse Schottky diode current measured on the template i regrowth.



10 Lowest Leakage Dies on each quarter wafer

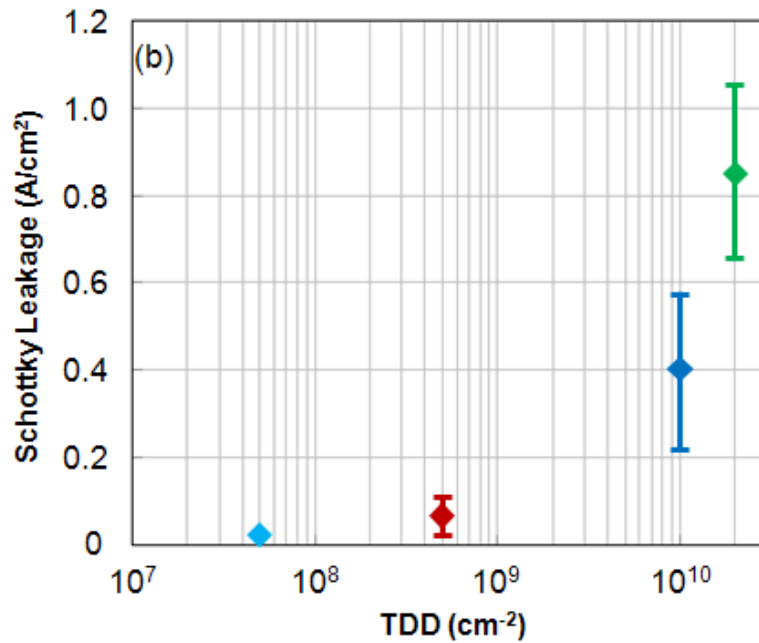


**Figure 2.11: (a) Reverse bias Schottky DC-IV measurements, showing lower reverse leakage current with reduced TDD. (b) Average Schottky leakage current density at -10 V bias for the 10 lowest leakage dies on each heterostructure as a function of TDD (error bars represent standard deviation).**

### 2.3.5 Three-terminal Breakdown

The three-terminal breakdown voltage is defined as the  $V_{DS}$  necessary to reach 1 mA/mm of drain current with  $V_{GS}$  at 1 V below the pinch-off voltage. Assuming that buffer conduction was negligible for the passivated slant-gate HEMTs with TDDs above  $\sim 5 \times 10^8 \text{ cm}^{-2}$ , this drain current was dominated by gate leakage. As shown in Fig. 2.12, the trend in three-terminal breakdown voltage with TDD followed that of reverse Schottky leakage until the TDD was lowered to  $\sim 5 \times 10^7 \text{ cm}^{-2}$ . As mentioned previously, the buffer breakdown voltage of the regrowth on FS GaN was handicapped by a lower concentration of TD-associated electron traps. Therefore, the three-terminal breakdown voltage of the regrowth on FS GaN was limited by buffer conductivity. To yield high three-terminal breakdown voltages with low-TDD HEMTs, the buffer breakdown voltage needs to be increased to values similar to those for high-TDD HEMTs.

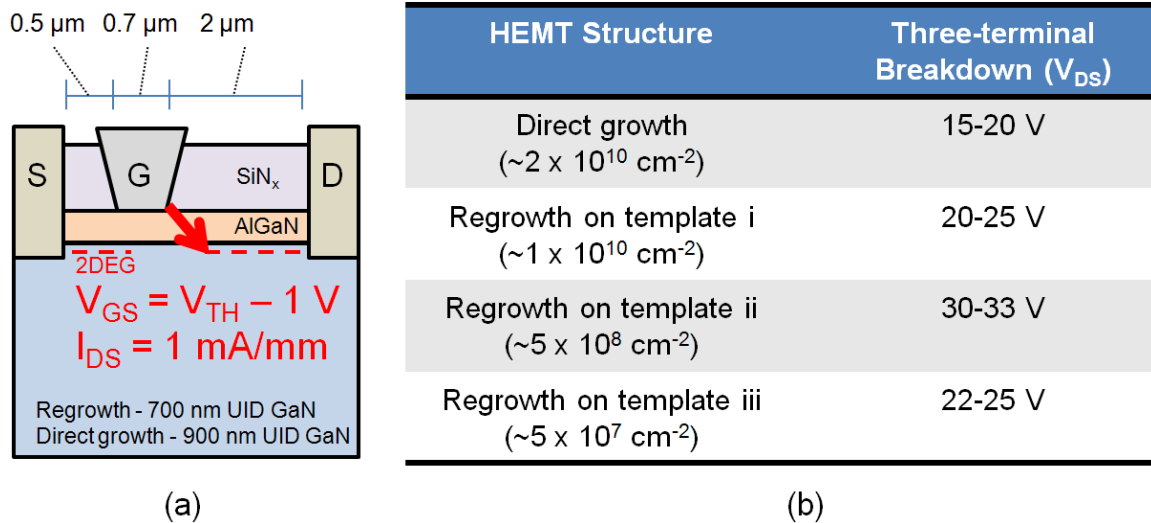


**Figure 2.12: (a) Schematic of the mechanism for three-terminal breakdown, assuming a high buffer breakdown voltage. (b) Three-terminal breakdown voltages for the Ga-rich PAMBE HEMT TDD Series.**

## Chapter 3. Optimization of Ga-rich PAMBE AlGaN/GaN HEMTs on FS GaN

### 3.1 Introduction

In the previous section, C-doping provided deep-level traps at the regrowth interface (RI) to create a highly resistive layer between the channel and the RI. The UID GaN buffer layer thickness,  $t_{UID}$ , was held at 700 nm for regrown heterostructures. The reverse leakage of Schottky diodes fabricated on HEMT structures was shown to correlate with TDD, but the trend in three-terminal breakdown voltage of passivated slant-gate HEMTs with TDD was unclear due to unacceptably high buffer leakage with low TDD. Decreasing  $t_{UID}$  is paramount for the regrowth of high-quality HEMT structures on FS GaN substrates with very low TDD. Previous efforts in HEMT regrowth on FS GaN by PAMBE included beryllium-doped layers in the buffer [78], and beryllium-related traps in close proximity to the channel were shown to have a detrimental effect on output conductance [79]. Simulations have also suggested that carbon-related traps near the channel may introduce significant DC-RF dispersion [23].

### 3.2 Device Design and Fabrication

$Al_{0.25}Ga_{0.75}N/GaN$  HEMT structures (Fig. 3.1) were regrown by Ga-rich PAMBE on semi-insulating GaN-on-SiC templates with TDDs of  $\sim 1 \times 10^{10} \text{ cm}^{-2}$  (Sample A) and  $\sim 5 \times 10^8 \text{ cm}^{-2}$  (Sample B) and n-type FS GaN substrates with TDDs of  $\sim 5 \times 10^7 \text{ cm}^{-2}$  (Sample C) and  $\sim 1 \times 10^7 \text{ cm}^{-2}$  (Sample D). The FS GaN substrate with a TDD of  $\sim 5 \times 10^{17} \text{ cm}^{-2}$  was produced by Lumilog, and the FS GaN substrate with a TDD of  $\sim 1 \times 10^{17}$

cm<sup>-2</sup> was produced by Mitsubishi Chemical Company. To mitigate the effects of parasitic gate pad and drain pad capacitance, 5 μm of semi-insulating GaN:Fe was deposited by MOCVD before PAMBE regrowths on the conductive FS GaN substrates. Assuming a background donor concentration of ~5 x 10<sup>16</sup> cm<sup>-3</sup>, a two-step carbon-doped buffer was included in the regrowths on FS GaN (400 nm GaN:C with C-doping of ~5 x 10<sup>18</sup> cm<sup>-2</sup> followed by 400 nm GaN:C with C-doping ~5 x 10<sup>17</sup> cm<sup>-2</sup>), reducing the  $t_{UID}$  to 200 nm. To prevent C-related traps from causing current collapse during RF operation, two HEMT structures regrown on FS GaN included 10 nm Al<sub>0.1</sub>Ga<sub>0.9</sub>N and 5 nm Al<sub>0.3</sub>Ga<sub>0.7</sub>N back barriers at the UID GaN/GaN:C interface. Sample C and D did not include back barriers.

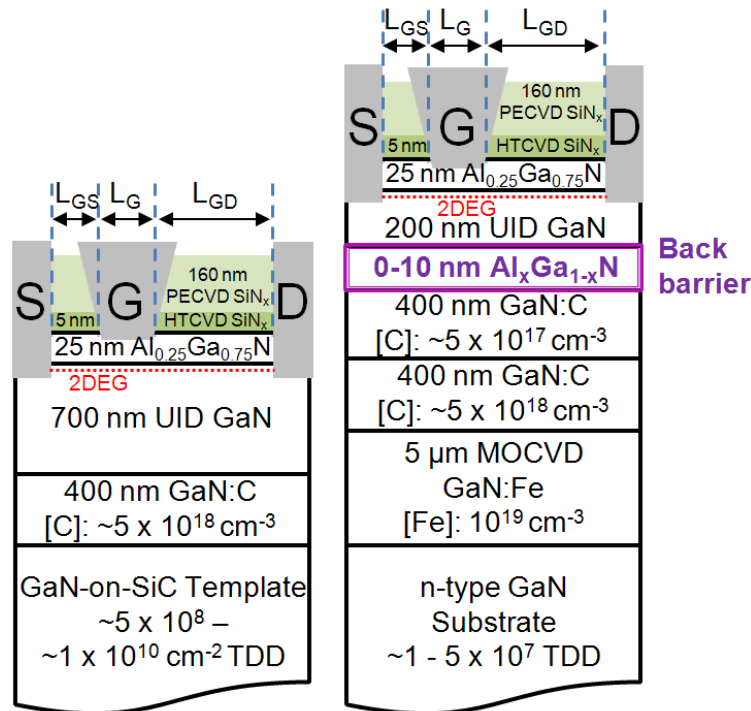


**Figure 3.1: HEMT structures with variable-TDD to determine the correlation between TDD and three-terminal breakdown. Regrowths on FS GaN also included 0-10 nm Al<sub>x</sub>Ga<sub>1-x</sub>N back barriers.**

As mentioned previously, the majority of devices fabricated on low-TDD templates showed high leakage currents after PECVD SiN<sub>x</sub> deposition. Prior to fabrication in this study, 5 nm SiN<sub>x</sub> passivation layers were deposited by high-temperature chemical vapor deposition (HTCVD) to protect the AlGaN surfaces during the subsequent processing steps.

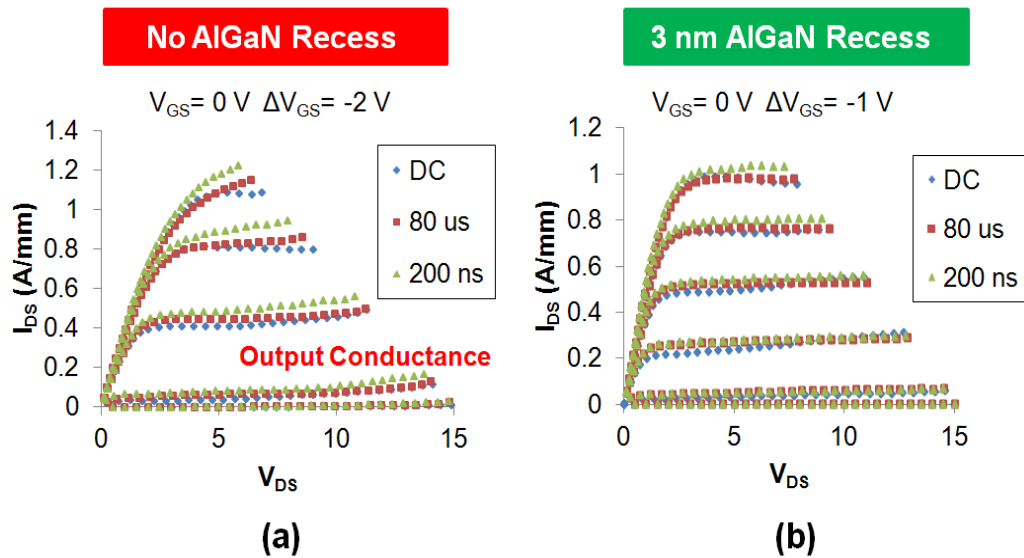


**Figure 3.2: Pulsed DC-IV measurements showing output conductance when the AlGaN is not recessed in HTCVD SiN<sub>x</sub> passivated HEMTs. (b) Elimination of this output conductance with a 3 nm AlGaN recess.**

Ohmic source and drain contacts (Ti/Al/Ni/Au – 20/120/30/50 nm) were deposited by e-beam evaporation and alloyed at 820 °C. Mesas were formed by BCl<sub>3</sub>/Cl<sub>2</sub> RIEs. 160 nm SiN<sub>x</sub> passivation layers were then deposited by PECVD. Before depositing the gates (Ni/Au/Ni – 30/250/50 nm), self-aligned SiN<sub>x</sub> recess processes were performed with CF<sub>4</sub>/O<sub>2</sub> RIEs, and the AlGaN surfaces were etched (~2-3 nm) with low-power BCl<sub>3</sub>/Cl<sub>2</sub> RIEs. This AlGaN recess etch was necessary to prevent output conductance related to surface residue associated with HTCVD SiN<sub>x</sub> (Fig. 3.2). Like the

study in the previous chapter, the devices were  $2 \times 75 \mu\text{m}$  wide with a gate-source spacing of  $0.5 \mu\text{m}$ , gate length of  $0.7 \mu\text{m}$ , and gate-drain spacing of  $2 \mu\text{m}$ .

### 3.3 Results and Discussion

#### 3.3.1 Improved Breakdown on FS GaN

Hall measurements yielded sheet resistances of  $375\text{-}425 \Omega/\text{sq}$  for Sample A and B. Sheet resistances of  $325\text{-}350 \Omega/\text{sq}$  were measured for Sample C and D. 200 ns pulsed DC-IV curves with a 10% duty cycle and  $50 \Omega$  load line are shown in Fig. 3.3 for HEMTs fabricated on Sample A, B, C, and D. The pulsed IV measurements indicated effective passivation of surface states on the drain-side of the gate, sharp pinch-off, and SOA maximum  $I_{\text{DS}}$  ( $\sim 1 \text{ A/mm}$  at  $V_{\text{GS}} = 0 \text{ V}$ ) for all HEMTs.

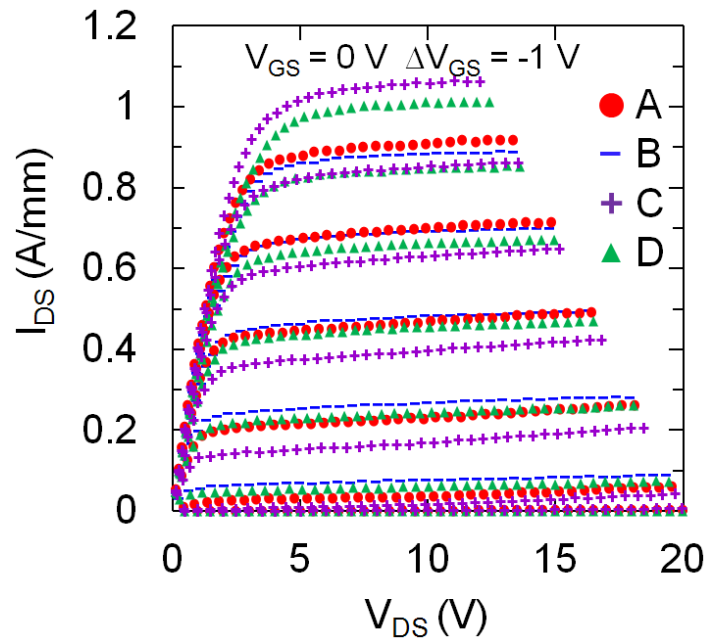


**Figure 3.3: 200 ns pulsed IV measurements (10% duty cycle,  $50 \Omega$  load line) for Sample A, B, C, and D.**



Sample A, B, C, and D yielded buffer breakdown voltages of 60-70 V. Three-terminal breakdown measurements were also performed on Sample A, B, C, and D. The five highest three-terminal breakdown voltages of the passivated slant-gate HEMTs on Sample A, B, C, and D are plotted against their TDDs in Fig. 3.3. Lower TDD yielded higher three-terminal breakdown voltages, with the highest three-terminal breakdown voltage (52 V) measured on Sample D ( $\sim 1 \times 10^7 \text{ cm}^{-2}$  TDD). Though HEMT structures with lower TDD produced devices with higher breakdown voltages, the structures also had a smaller  $t_{\text{UID}}$ . With traps in the GaN:C layer of the buffer closer to the 2DEG, there was a higher probability of trapping hot electrons during high-power operation. These negatively charged traps would “back gate” the device and cause current collapse.

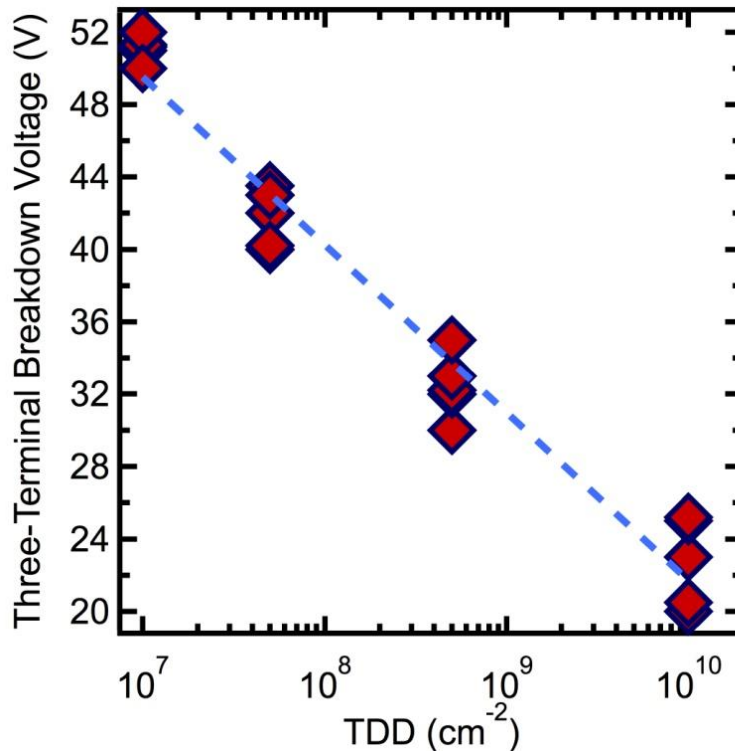


**Figure 3.4: Three-terminal breakdown voltage (5 highest breakdown dies) as a function of TDD for passivated slant-gate HEMTs regrown by Ga-rich PAMBE.**

### 3.3.2 Improved Large-signal Performance on FS GaN

To determine if carbon-related deep-level traps near the channel cause DC-RF dispersion, continuous-wave power measurements were performed at 4 GHz using a Focus microwave load-pull system. A HEMT fabricated on Sample D and HEMTs fabricated on FS GaN regrowths with AlGa<sub>n</sub>N back barriers were biased at 20 V, 30 V, and 40 V, and matched for PAE. The HEMTs with AlGa<sub>n</sub>N back barriers yielded similar pulsed IV curves to those shown for the HEMT fabricated on Sample D in Fig. 3.3. Without a back barrier, DC-RF dispersion was evident, as the PAE fell steadily from 60% to 37% with an increase in drain bias from 20 V to 40 V (Fig. 3.5(a)), and the  $P_{\text{out}}$  reached a plateau at ~4 W/mm. With a 10 nm Al<sub>0.1</sub>Ga<sub>0.9</sub>N back barrier, there were only slight improvements in PAE over the HEMT with no back barrier. Although the output power at 4 GHz rose steadily from 20 V to 40 V (Fig. 3.5(b)), the PAE dropped to 38% at 40 V. Inclusion of a 5 nm Al<sub>0.3</sub>Ga<sub>0.7</sub>N back barrier appeared to block hot electrons far more effectively, with PAE falling from 63% to only 50% as  $V_{\text{DS}}$  increased from 20 V to 40 V (Fig. 3.5(c)). The HEMT with the Al<sub>0.3</sub>Ga<sub>0.7</sub>N back barrier achieved the highest  $P_{\text{out}}$ , 6.7 W/mm, at a drain bias of 40 V. The power measurements on these 3 HEMT structures are summarized in Fig. 3.6.

The higher blocking potential of the 5 nm Al<sub>0.3</sub>Ga<sub>0.7</sub>N back barrier is shown in the band simulations in Fig. 3.7. Further optimization of the back barrier, such as increasing the Al mole fraction or including a digital barrier, will presumably aid PAE and  $P_{\text{out}}$  at high biases, but there is also greater likelihood of creating a parallel parasitic channel.

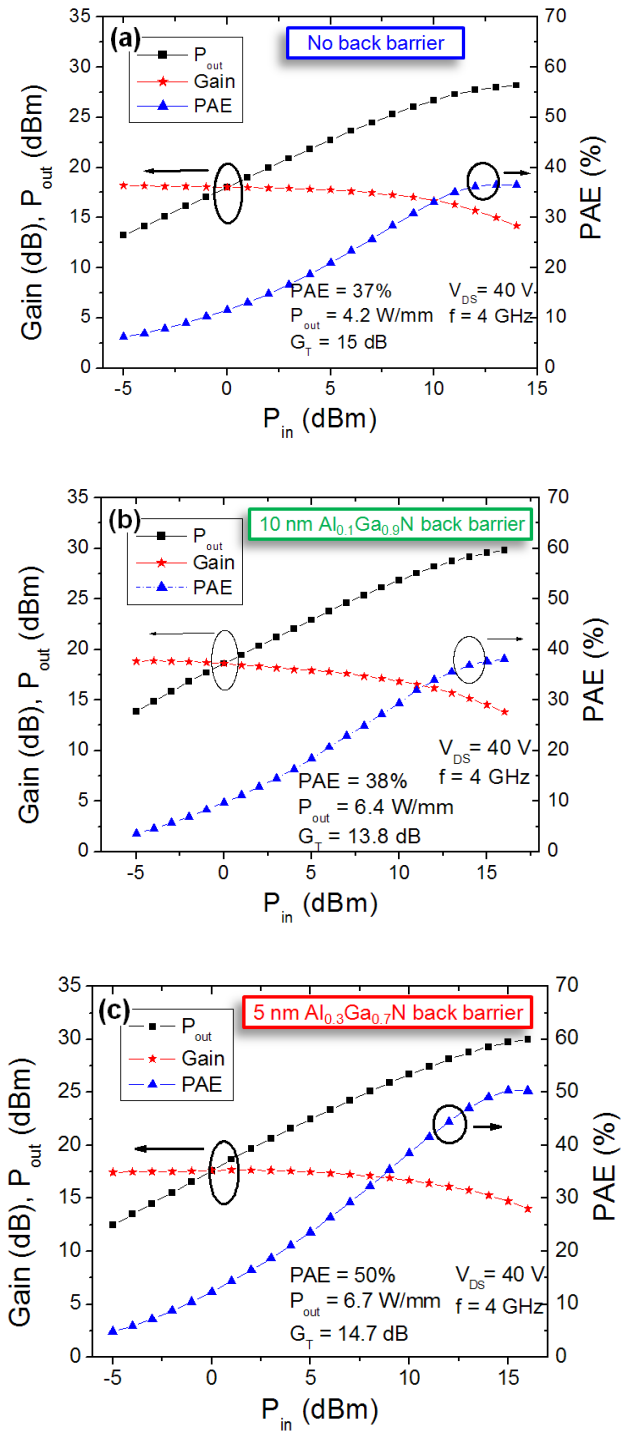


**Figure 3.5: Large-signal measurements at 4 GHz and  $V_{DS} = 40$  V for passivated slant-gate HEMTs regrown by Ga-rich PAMBE on FS GaN (a) without a back barrier, (b) with a 10 nm  $Al_{0.1}Ga_{0.9}N$  back barrier, and (c) a 5 nm  $Al_{0.3}Ga_{0.7}N$  back barrier.**

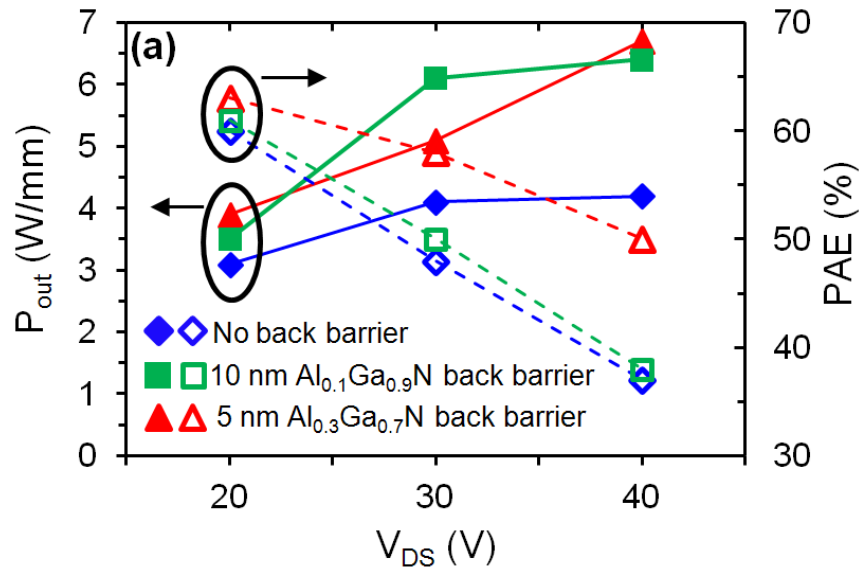


Figure 3.6: Summary of 4 GHz large-signal measurements for passivated slant-gate HEMTs regrown on FS GaN by Ga-rich PAMBE.

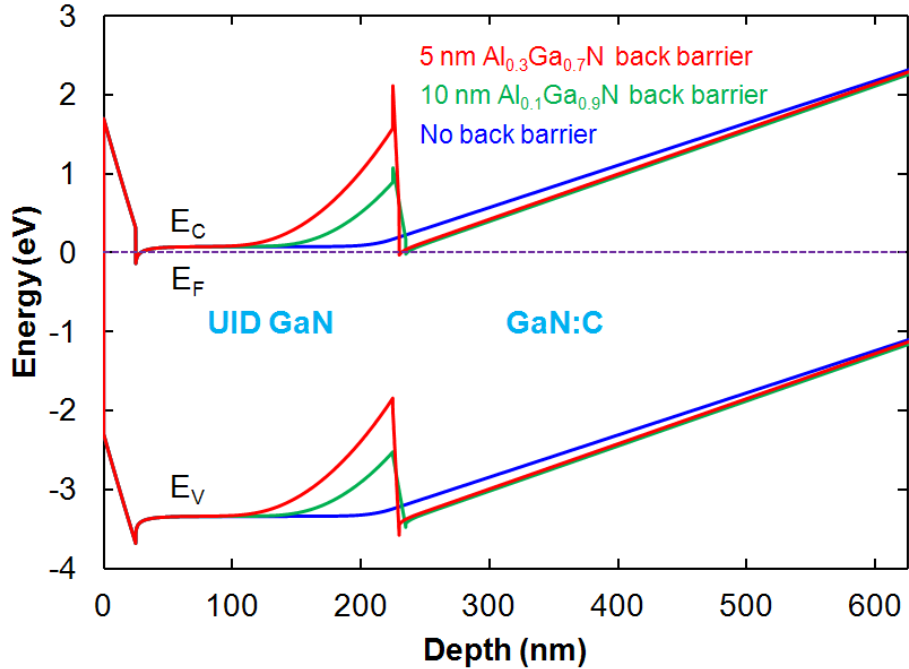


Figure 3.7: Band diagrams for HEMT structures with 0-10 nm  $Al_xGa_{1-x}N$  back barriers at the UID GaN/GaN:C interface.

## Chapter 4. AlN Interlayer Optimization by Ga-rich PAMBE

### 4.1 Introduction

With the inclusion of a coherent AlN interlayer (IL) at the AlGaN/GaN heterointerface, the 2DEG density and mobility can be significantly increased. The AlN barrier reduces the effects of alloy scattering by restricting carrier penetration into the AlGaN layer. AlGaN/AlN/GaN heterostructures with approximately 1 nm of AlN have been grown with MOCVD, resulting in room temperature (RT) sheet resistances of  $\sim 250 \Omega/\square$  [3,80], but reports of AlN ILs successfully grown with molecular beam epitaxy are limited [81]. MOCVD and  $\text{NH}_3$ -MBE growth involve V/III ratios in excess of 1000, and no change in TMA flow or Al flux is necessary to grow AlN and AlGaN in succession. With Ga-rich PAMBE, however, growing AlN and AlGaN sequentially without a growth interruption is more complicated.

In Ga-rich PAMBE, the Al flux during growth of the AlN IL must be equivalent to the active N flux, as Al is preferentially incorporated into the crystal. The Al flux must then be reduced far below the active N flux during growth of the AlGaN barrier. If AlN is grown N-rich, growth proceeds in the Volmer-Weber growth mode, and the AlN interlayer will not fully coalesce. Growing an AlGaN/AlN/GaN heterostructure without interruption and without digitally grown AlGaN would require two Al effusion cells, occupying two upward-facing cell ports. The MBE system used in this study has only one Al effusion cell, and a unique Ga flux sequence following the growth of the AlN

interlayer was used to eliminate the impurity incorporation that accompanies a growth interruption.

The first AlN/GaN and (Al,Ga)N/AlN/GaN heterostructures were grown with Ga-rich PAMBE without interruption. An Al<sub>0.37</sub>Ga<sub>0.63</sub>/AlN/GaN heterostructure with a 1 nm AlN interlayer and digitally grown (Al,Ga)N achieved a RT sheet resistance of 194  $\Omega/\square$  [81]. Ultrashallow single AlN/GaN heterojunctions have also yielded very low RT sheet resistances. After flux optimization, a record-low RT sheet resistance of  $\sim 128 \Omega/\square$  for a single III-nitride heterojunction was obtained for an AlN/GaN structure with a 3.5 nm AlN cap [82,83]. These heterostructures were regrown on MOCVD GaN:Fe-on-sapphire templates that had TDDs of  $\sim 5 \times 10^8 \text{ cm}^{-2}$ . Little work has been done to experimentally confirm the effect of dislocation scattering on electron transport in 2DEGs. Theoretical calculations predict that strain fields and Coulombic scattering from charged dislocation lines have a considerable impact on 2DEG mobility, even at high sheet charge concentrations [84–88].

## 4.2 Growth of AlGaN/AlN/GaN with Interruption

All AlGaN/AlN/GaN heterostructures (Fig. 3.1) were grown in a Varian Gen-II MBE system, equipped with conventional Ga and Al effusion cells and an RF-plasma N source. The N source consisted of ultrahigh-purity (99.9995%) N<sub>2</sub> gas flowing at 0.4 SCCM through the gas input to the RF-plasma source with 300 W RF power. This flow rate and RF power corresponded to a growth rate of  $\sim 3.7 \text{ nm/min}$ . The 6H-SiC substrate, GaN:Fe-on-sapphire (Lumilog STINS) template, and FS GaN template (MOCVD-grown

GaN:Fe on Lumilog FS GaN) were solvent-cleaned and degassed in ultrahigh vacuum prior to growth.

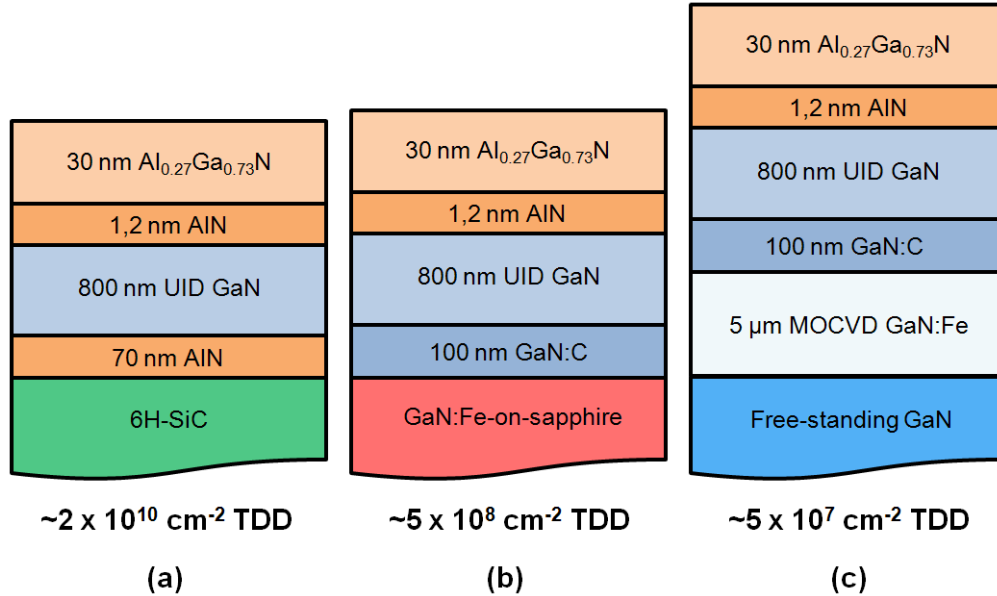


**Figure 4.1: Schematics of AlGaN/AlN/GaN heterostructures (a) directly grown on 6H-SiC, (b) regrown on GaN:Fe-on-sapphire, and regrown on FS GaN.**

Direct growth on 6H-SiC was initiated in the manner described previously for direct growth on 4H-SiC. Nearing completion of the GaN buffer layer, the growth temperature was increased to  $\sim 735^\circ\text{C}$  in preparation for growth of the AlN IL. With the Ga shutter remaining open to maintain the Ga adlayers (acting as a surfactant), the Al shutter was opened for 17 s, which corresponded to  $\sim 1$  nm of AlN. Growing heterostructures with  $\sim 2$  nm AlN interlayers required the Al shutter be opened for 34 s. Upon completion of the AlN interlayer, all shutters were closed, the Al cell was cooled for 240 s, and the growth temperature was reduced to  $715^\circ\text{C}$ . Prior to growth it was determined that the Al flux stabilized 240 s after the effusion cell was rapidly cooled. During the growth interruption, RHEED intensity was monitored. When the Ga adlayers

began to desorb, which was indicated by an increase in RHEED intensity, the Ga shutter was opened for 2 s, and this flux pattern was continued until the AlGa<sub>0.27</sub>N capping layer was grown (Fig. 4.2). Maintaining the Ga adlayers during the growth interruption provided a protective layer against impurity incorporation. When the Ga adlayers were allowed to desorb during the growth interruption, there was a severe degradation of 2DEG mobility. However, the sample in which the Ga adlayers were desorbed included only a ~1 nm AlN IL, and thicker ILs may mitigate these effects.

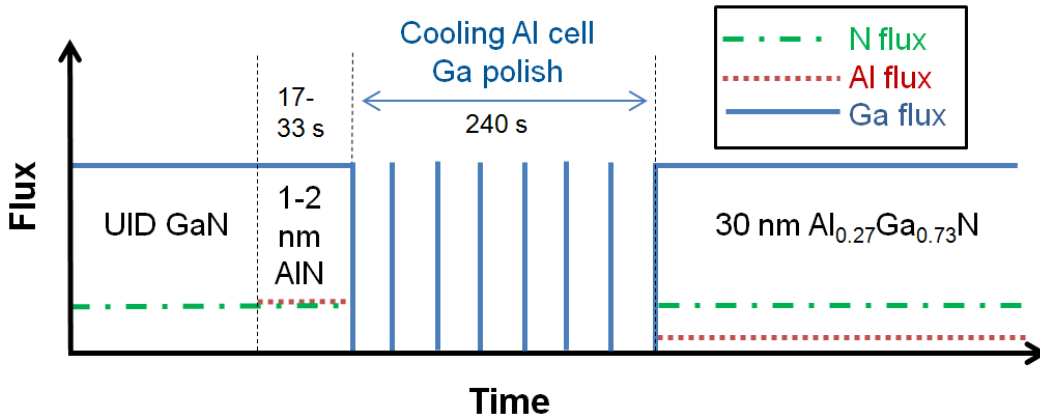


**Figure 4.2: Flux pattern used during the growth of the AlN interlayer, growth interruption, and growth of the AlGa<sub>0.27</sub>N barrier by Ga-rich PAMBE.**

Regrowths on GaN:Fe-on-sapphire and FS GaN templates were also performed in the Ga-rich regime. 5 μm GaN:Fe was grown by MOCVD on the n-type Lumilog FS GaN before entering the MBE system. Regrowth on these templates started with 100 nm GaN:C ([C]:  $\sim 5 \times 10^{18} \text{ cm}^{-3}$ ), having C-doping provided by CBr<sub>4</sub>. Although previous regrowths included 400- nm- thick GaN:C layers, it was determined that GaN:C layers thicker than 50 nm were sufficient in blocking the leakage pathway at the regrowth interface (especially for Hall studies with very low applied biases). The GaN:C layer was



grown in the Ga droplet regime with a Ga/N flux ratio of  $\sim 3$  at  $715\text{ }^\circ\text{C}$ , employing modulated growth. The  $\text{CBr}_4$  flow was interrupted during the thermal desorption interval. A subsequent unintentionally doped  $800\text{ nm}$  GaN layer was grown under the same conditions, followed by  $\sim 1\text{-}2\text{ nm}$  AlN and a  $25\text{ nm}$  AlGaN barrier, using the flux pattern shown in Fig. 4.2.

## 4.3 Results and Discussion

### 4.3.1 Purity of Ga-rich PAMBE AlN Interlayer

The growth rate of the AlN IL was calibrated well, as confirmed by atom probe tomography (APT) of an AlGaN/AlN( $2\text{ nm}$ )/GaN heterostructure regrown on GaN:Fe-on-sapphire, shown in Fig. 4.3. The AlN interlayer was pure, as shown in Fig. 4.3, and the surrounding interfaces were abrupt. Leaving the Ga shutter open during growth of the AlN interlayer did not introduce Ga impurities. The Al flux was effectively matched to the active N flux.

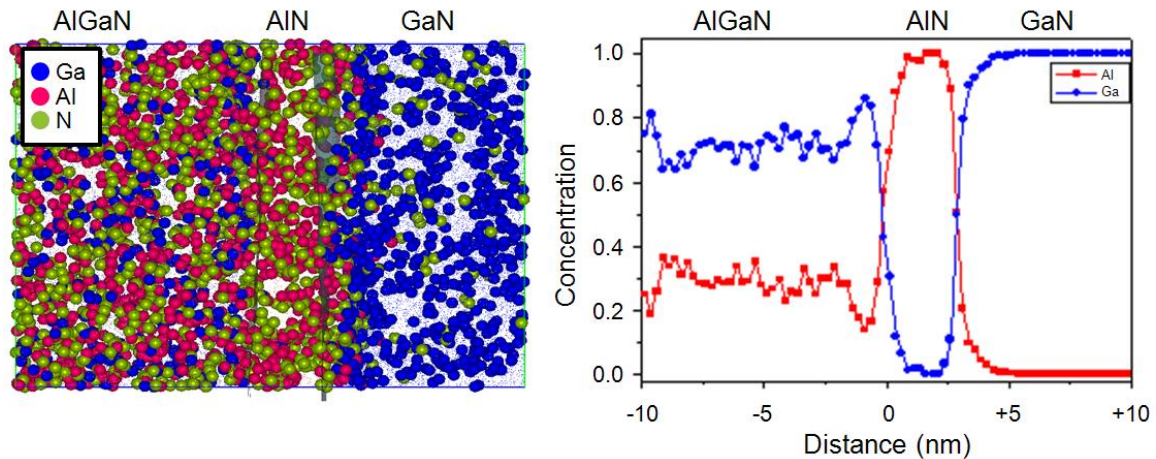


**Figure 4.3: 3D reconstruction and 1D concentration profile by APT of a Ga-rich PAMBE-grown AlGaN/AlN( $2\text{ nm}$ )/GaN heterostructure on GaN:Fe-on-sapphire. APT performed by Baishakhi Mazumder.**

### 4.3.2 Structural Properties

HRXRD  $\omega$ - $2\theta$  scans of the GaN (0002) reflection indicated the following AlGaIn barrier thicknesses (Al content) of the AlGaIn/AlN/GaN heterostructures: 25 nm (27%) for the direct growths on 6H-SiC, 25 nm (26%) for the regrowths on Lumilog STINS GaN, and 23 nm (28%) for the regrowths on Lumilog FS GaN. The rocking curve full widths at half maximum of  $\omega$ -scans ( $\Delta\omega$ ) for the GaN (20 $\bar{2}$ 1) reflection (measured in a skew symmetric geometry) are reported in Table 4.1, as well as those for the GaN (0002) reflection. Using the calibration curve developed from PV-TEM data, the GaN (20 $\bar{2}$ 1)  $\Delta\omega$  values yield TDDs of  $\sim 2 \times 10^{10} \text{ cm}^{-2}$  for the direct growths on 6H-SiC,  $\sim 5 \times 10^8 \text{ cm}^{-2}$  for the regrowths on GaN:Fe-on-sapphire, and  $\sim 5 \times 10^7 \text{ cm}^{-2}$  for the regrowths on FS GaN, thus verifying the anticipated TDDs.

**Table 4.1: HRXRD  $\omega$ -rocking curve FWHMs of the GaN (0002) and GaN (20 $\bar{2}$ 1) reflections for all AlGaIn/AlN/GaN heterostructures.**

Substrate/ Template	AlN Interlayer Thickness (nm)	GaN (0002) FWHM (arcsec)	GaN (20 $\bar{2}$ 1) FWHM (arcsec)
6H-SiC	~1	498	1483
	~2	547	1447
GaN:Fe-on-sapphire	~1	335	527
	~2	354	572
FS GaN	~1	174	281
	~2	162	259

### 4.3.3 2DEG Characteristics

Hall measurements were performed on ten van der Pauw test patterns on each sample. There was little variation of the sheet resistance measured on different patterns,

and the mobility and 2DEG sheet density of those patterns with the lowest RT sheet resistance are reported in Table 4.2.

**Table 4.2: 2DEG sheet density ( $n_s$ ), mobility ( $\mu$ ), sheet resistance ( $R_{sh}$ ) measured at RT and 77 K of AlGaN/AlN/GaN heterostructures grown by Ga-rich PAMBE.**

Substrate/ Template	AlN Interlayer Thickness (nm)	$n_s$ ( $\times 10^{13} \text{ cm}^{-2}$ )		$\mu$ ( $\text{cm}^2/\text{V}\cdot\text{s}$ )		$R_{sh}$ ( $\Omega/\square$ )	
		RT	77 K	RT	77 K	RT	77 K
6H-SiC	~1	1.63	1.59	1200	2080	320	198
	~2	1.81	1.81	1240	2330	278	154
GaN:Fe-on-sapphire	~1	1.56	1.56	1720	6240	233	67
	~2	1.65	1.65	2030	9400	188	42
FS GaN	~1	1.72	1.70	1710	8910	214	43
	~2	1.75	1.75	2020	10640	175	35

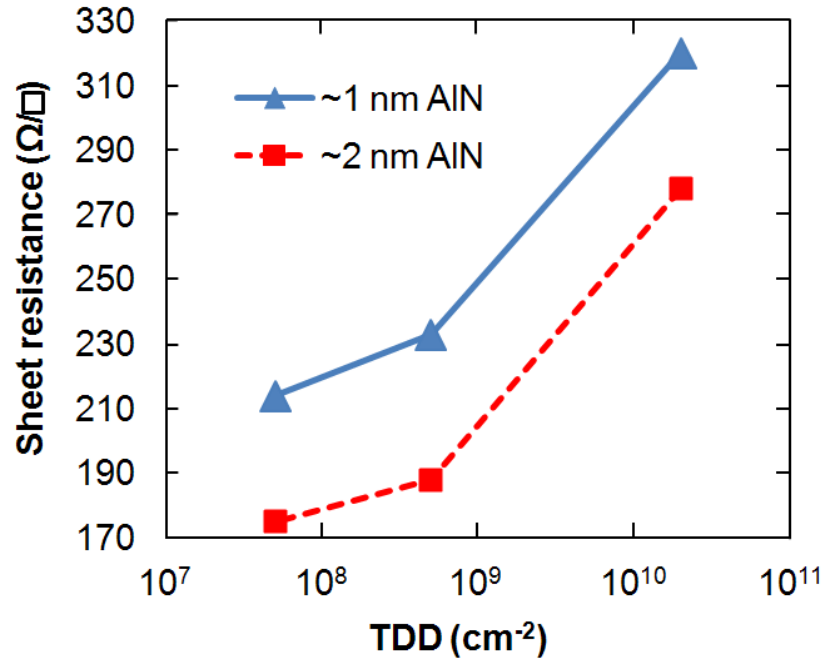


**Figure 4.4. Trend of RT sheet resistance with TDD at RT for Ga-rich PAMBE-grown AlGaN/AlN/GaN heterostructures with ~1 nm and ~2 nm AlN interlayers.**

For similar TDDs, heterostructures with 2 nm AlN ILs yielded higher 2DEG mobilities and lower sheet densities than heterostructures with 1 nm AlN ILs. There was also a clear trend of reduced sheet resistance with reduced TDD at RT and 77K, regardless of AlN interlayer thickness. There was also a trend of increased mobility at 77 K with reduced TDD. With polar optical phonon scattering greatly reduced at low temperature, dislocation scattering and interface roughness are the dominant scattering mechanisms [87,88]. Although RT sheet resistance correlated positively with TDD, only modest improvements were made when TDD was reduced below  $\sim 5 \times 10^8 \text{ cm}^{-2}$ . At some TDD above  $\sim 5 \times 10^8 \text{ cm}^{-2}$ , for sheet densities on the order of  $10^{13} \text{ cm}^{-2}$ , there is a transition where dislocation scattering becomes a significant RT scattering mechanism. RT 2DEG mobilities are very similar with  $\sim 5 \times 10^7 \text{ cm}^{-2}$  and  $\sim 5 \times 10^8 \text{ cm}^{-2}$  TDD. By taking into account the effects of interface roughness scattering, it can be inferred that the RT 2DEG mobilities of  $\sim 5 \times 10^7 \text{ cm}^{-2}$  TDD samples would be higher than those of the  $\sim 5 \times 10^8 \text{ cm}^{-2}$  TDD samples if they had the same sheet density.

#### **4.3.4 Mechanism for Mobility Improvement with Thicker AlN Interlayers**

Band diagrams for AlGa<sub>N</sub>/Ga<sub>N</sub> and AlGa<sub>N</sub>/AlN/Ga<sub>N</sub> heterostructures were calculated using a 1-D Schrödinger-Poisson solver and are shown in Fig. 4.5 [89]. The calculated 2DEG sheet densities were similar to those found through Hall measurements. For the Al<sub>0.25</sub>Ga<sub>0.75</sub>N/Ga<sub>N</sub> heterostructures in Chapter 2, there was little variation in RT sheet resistance with TDD (350 – 425  $\Omega/\square$ ). For RT transport, dislocation-associated scattering appeared to be less significant than alloy disorder scattering. When alloy

disorder scattering was reduced with AlN ILs, having a high TDD significantly degraded the 2DEG mobility at RT and 77 K.

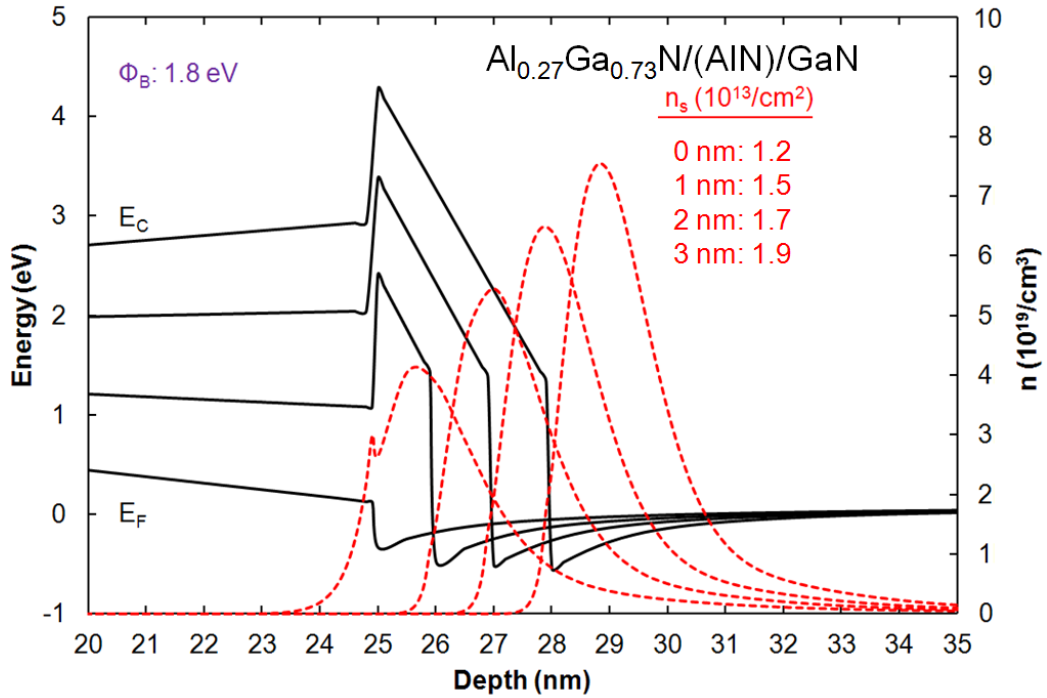


**Figure 4.5: Band diagrams of AlGaN/(AlN)/GaN heterostructures with 0-3 nm AlN, including calculated 2DEG sheet density ( $n_s$ ).**

The trend of increased mobility with a thicker AlN IL identified in the previous section is counterintuitive. The thicker AlN IL increases the polarization discontinuity, increasing the 2DEG sheet density. As the 2DEG sheet density increases, the centroid of the 2DEG wavefunction moves closer to the heterojunction, and interface roughness scattering increases. As shown in Fig. 4.5, the 2DEG wavefunction does not penetrate the alloy barrier with a 1 nm AlN IL, so the effect of reduced alloy disorder scattering with a thicker AlN IL is negligible. It appears that the thicker AlN ILs shields the 2DEG from potential fluctuations in the alloy barrier caused by AlN clustering, which has been

identified by APT. With a thicker AlN IL, there is a deeper quantum well at the heterointerface, and the effects of potential fluctuations in the alloy barrier on the ground state energy of the 2DEG are lessened (Fig. 4.6). Calculations of “alloy cluster scattering” are currently underway.

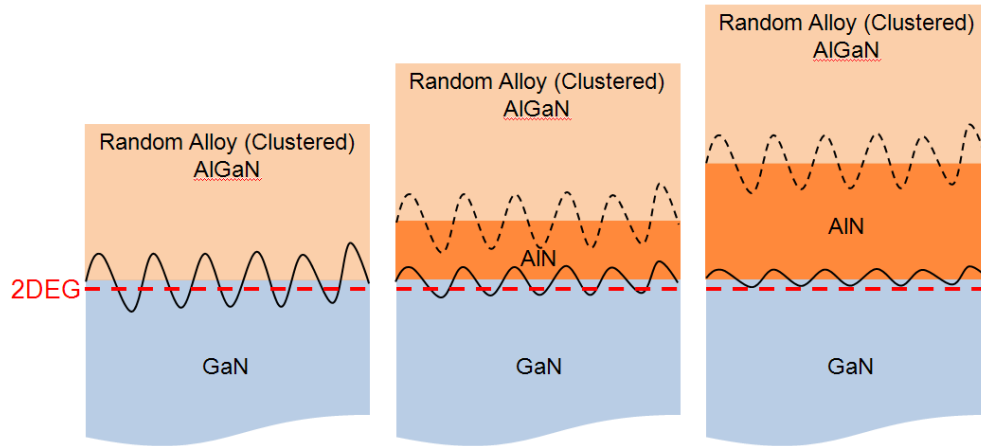


**Figure 4.6: Schematic showing lower fluctuation of the 2DEG ground state energy with thicker AlN ILs.**

Increasing the AlN interlayer thickness and the Al mole fraction of the AIGaN barrier beyond the values studied in this chapter will yield further reduction of the sheet resistance. An  $\text{Al}_{0.24}\text{Ga}_{0.76}\text{N}/\text{AlN}(\sim 2.5 \text{ nm})/\text{GaN}$  heterostructure was also regrown on FS GaN and achieved a sheet resistance of  $169 \text{ } \Omega/\square$  ( $n_s: 1.72 \times 10^{13} \text{ cm}^{-2}$ ,  $\mu: 2160 \text{ cm}^2/\text{Vs}$ ) at RT and  $29 \text{ } \Omega/\square$  ( $n_s: 1.77 \times 10^{13} \text{ cm}^{-2}$ ,  $\mu: 12232 \text{ cm}^2/\text{Vs}$ ) at 77K. This is the lowest reported RT sheet resistance for an AIGaN/AlN/GaN heterostructure, and this RT sheet resistance is lower than the best reported for InAlN/AlN/GaN ( $182 \text{ } \Omega/\square$ ) [90]. The AlN interlayer thickness can be increased to  $\sim 5 \text{ nm}$  before the onset of biaxial stress relief by cracking, and the Al mole fraction of the AIGaN barrier can be pushed beyond 0.3, providing 2DEG sheet densities above  $2 \times 10^{13} \text{ cm}^{-2}$ .

## Chapter 5. Ga-rich PAMBE $\text{Al}_x\text{Ga}_{1-x}\text{N}/(\text{AlN})/\text{GaN}$ TDD Series: Mobility

### 5.1 Introduction

In Chapter 4, dislocation scattering was shown to be significant mechanism for high TDDs (greater than  $\sim 10^9 \text{ cm}^{-2}$ ), even when the charged dislocation lines should be screened to a great extent by the high 2DEG sheet density. Dislocation scattering in an AlGa<sub>x</sub>N/GaN 2DEG has been treated theoretically by Jena *et al.* [91], Joshi *et al.* [92], Gurusinghe *et al.* [87], and recently Asgari *et al.* [88], but a thorough experimental study had yet to be completed.

In addition to dislocation scattering, alloy disorder scattering, interface roughness scattering, and phonon scattering are generally considered to limit the 2DEG mobility. Polar optical phonon (OP) scattering is inelastic (electron energy is absorbed by high-energy polar optical phonons) and plays an important role at high temperatures. According to accepted theory, OP-scattering-limited mobility ( $\mu_{\text{OP}}$ ) has an Arrhenius dependence on temperature ( $\mu_{\text{OP}} \propto \exp(1/T)$ ) [88]. Acoustic phonon scattering, on the other hand, is essentially elastic (acoustic phonons have very low energy) and has a much weaker contribution at high temperatures. Coupling of electron transport to acoustic phonons tied to the deformation potential (DP) and piezoelectric components (PE) has been considered. The DP-scattering-limited mobility ( $\mu_{\text{DP}}$ ) and PE-scattering-limited mobility ( $\mu_{\text{PE}}$ ) have been calculated to have an inverse temperature dependence ( $\mu_{\text{DP,PE}} \propto 1/T$ ) [88]. Since sheet carrier concentrations are often very high ( $\sim 10^{13} \text{ cm}^{-2}$ ) in AlGa<sub>x</sub>N/GaN heterostructures, penetration of the 2DEG wave function into the AlGa<sub>x</sub>N

barrier is to be expected. As the centroid of the 2DEG wave function moves closer to the heterointerface, there is greater scattering from the randomly varying barrier potential (alloy disorder scattering) and fluctuations in well width (interface roughness scattering), as mentioned previously. Alloy disorder (AD) scattering, interface roughness (IR) scattering, and dislocation scattering have been calculated to be temperature-independent.

The study presented in this chapter aims to identify the dominant 2DEG scattering mechanisms through a range of TDDs and sheet concentrations, and with the inclusion of an AlN IL. This will be accomplished mainly through qualitative analysis of temperature-dependent Hall measurements.

## 5.2 Experiment Design

AlGaN/(AlN)/GaN heterostructures (Fig. 5.1) were grown in a Varian Gen-II MBE system on 6H-SiC, GaN:Fe-on-sapphire, and FS GaN. The N source consisted of ultrahigh-purity (99.9995%) N<sub>2</sub> gas flowing at 0.4 SCCM through the RF-plasma source with 300 W RF power. This flow rate and RF power corresponded to a growth rate of ~3.5 nm/min, similar to that of the study in Chapter 4. The heterostructures were grown under Ga-rich conditions in a similar manner as those described in previous chapters and included AlGaN barriers with Al mole fractions of 0.06, 0.12, 0.24, and 0.27. The heterostructures with Al<sub>0.27</sub>Ga<sub>0.73</sub>N barriers incorporated 2 nm AlN ILs. With this wide range of barrier compositions, 2DEG sheet densities spanning an order of magnitude were predicted by band simulations (Fig. 5.2).



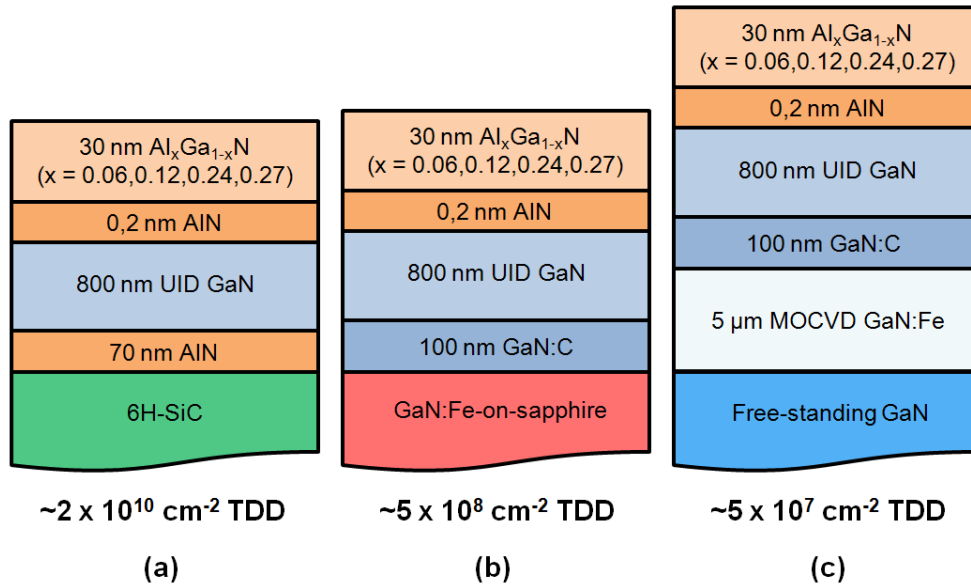


**Figure 5.1: Schematics of AlGaN/(AlN)/GaN heterostructures (a) directly grown on 6H-SiC, (b) regrown on GaN:Fe-on-sapphire, and (c) regrown on FS GaN by Ga-rich PAMBE.**

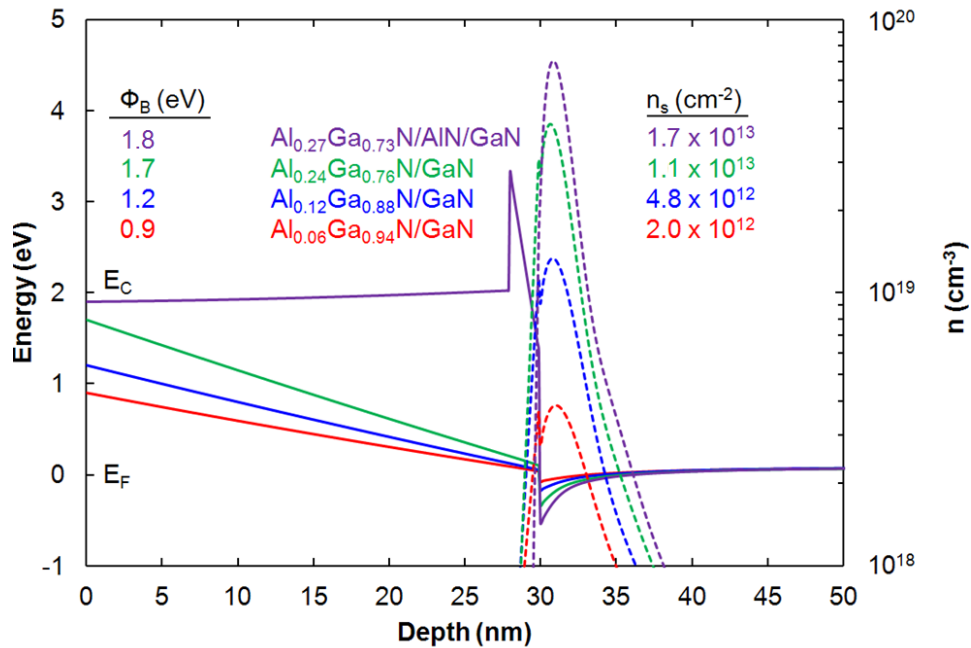


**Figure 5.2: Band simulations AlGaN/(AlN)/GaN heterostructures, including the 2DEG sheet density (n<sub>s</sub>) and surface barrier height (Φ<sub>B</sub>).**

## 5.3 Results and Discussion

### 5.3.1 Structural Properties

The rocking curve full widths at half maximum (FWHMs) of HRXRD  $\omega$ -scans for the GaN (20 $\bar{2}$ 1) reflection (measured in a skew symmetric geometry) are reported in Table 5.1, as well as those for the GaN (0002) reflection. Using the calibration curve developed from PV-TEM data, the FWHMs of the GaN (20 $\bar{2}$ 1) reflections yielded the expected TDDs of  $\sim 2 \times 10^{10} \text{ cm}^{-2}$  for the growths on 6H-SiC,  $\sim 5 \times 10^8 \text{ cm}^{-2}$  for the regrowths on GaN-on-sapphire, and  $\sim 5 \times 10^7 \text{ cm}^{-2}$  for the regrowths on FS GaN.

**Table 5.1: HRXRD  $\omega$ -rocking curve FWHMs of the GaN (0002) and GaN (20 $\bar{2}$ 1) reflections for all AlGa<sub>x</sub>N/(AlN)/GaN heterostructures.**

Substrate/ Template	Al <sub>0.06</sub> Ga <sub>0.94</sub> N/GaN		Al <sub>0.12</sub> Ga <sub>0.88</sub> N/GaN		Al <sub>0.24</sub> Ga <sub>0.76</sub> N/GaN		AlGa <sub>x</sub> N/AlN/GaN	
	GaN (0002) FWHM (arcsec)	GaN (20 $\bar{2}$ 1) FWHM (arcsec)	GaN (0002) FWHM (arcsec)	GaN (20 $\bar{2}$ 1) FWHM (arcsec)	GaN (0002) FWHM (arcsec)	GaN (20 $\bar{2}$ 1) FWHM (arcsec)	GaN (0002) FWHM (arcsec)	GaN (20 $\bar{2}$ 1) FWHM (arcsec)
6H-SiC	514	1580	523	1659	453	1598	547	1447
GaN-on- sapphire	344	356	356	390	359	394	366	412
FS GaN	180	256	223	247	224	256	178	252

HRXRD  $\omega$ -2 $\theta$  scans of the AlGa<sub>x</sub>N and GaN (0002) reflection indicated the Al mole fractions of the AlGa<sub>x</sub>N barriers and their thicknesses, shown in Table 5.2, for the Al<sub>0.24</sub>Ga<sub>0.76</sub>N/GaN and AlGa<sub>x</sub>N/AlN/GaN heterostructures. AlGa<sub>x</sub>N thicknesses were determined by analyzing the spacing of Pendellösung fringes. As it is difficult to resolve the separation of the GaN (0002) and Al<sub>x</sub>Ga<sub>1-x</sub>N (0002) peaks with  $x < 0.15$ , scans of the GaN (0004) reflection were performed for the Al<sub>0.12</sub>Ga<sub>0.88</sub>N/GaN heterostructures, and

scans of the GaN (0006) reflection were performed for the  $\text{Al}_{0.06}\text{Ga}_{0.94}\text{N}/\text{GaN}$  heterostructures. The AlGaN barrier compositions and thicknesses for the  $\text{Al}_{0.12}\text{Ga}_{0.88}\text{N}/\text{GaN}$  and  $\text{Al}_{0.06}\text{Ga}_{0.94}\text{N}/\text{GaN}$  heterostructures are also reported in Table 5.2. For all heterostructures, AlGaN barrier compositions were determined by analyzing the separation of the GaN and AlGaN peaks.

**Table 5.2: Al mole fractions and thicknesses ( $t$ ) of the AlGaN barriers for all AlGaN/(AlN)/GaN heterostructures.**

Substrate/ Template	$\text{Al}_{0.06}\text{Ga}_{0.94}\text{N}/\text{GaN}$		$\text{Al}_{0.12}\text{Ga}_{0.88}\text{N}/\text{GaN}$		$\text{Al}_{0.24}\text{Ga}_{0.76}\text{N}/\text{GaN}$		AlGaN/AlN/GaN	
	Al mole fraction	$t$ (nm)	Al mole fraction	$t$ (nm)	Al mole fraction	$t$ (nm)	Al mole fraction	$t$ (nm)
6H-SiC	0.065	32	0.115	29	0.243	28	0.273	26
GaN-on-sapphire	0.062	33	0.118	29	0.231	27	0.242	26
FS GaN	0.061	32	0.116	29	0.233	27	0.247	24

### 5.3.2 Surface Morphologies

AFM micrographs (Fig. 5.3) indicated the presence of spiral hillocks, which form about screw-component dislocations, for the growths on 6H-SiC and regrowths on GaN-on-sapphire. Straight (meandering) step edges were observed on the surfaces of the FS GaN regrowths. Root mean square (rms) roughness ( $a_{\text{rms}}$ ) values are included in Fig. 5.3. Reduction of TDD entailed a slight decrease in rms roughness. Surprisingly, the Al mole fraction of the AlGaN barrier had a negligible impact on the rms roughness.

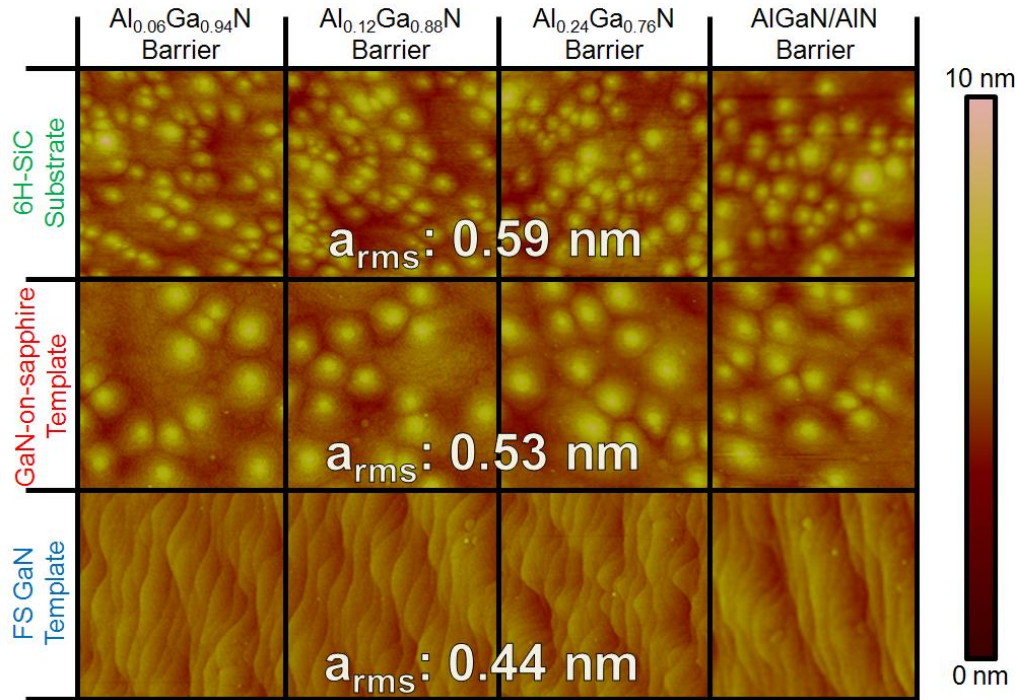


**Figure 5.3:**  $2 \times 2 \mu\text{m}^2$  AFM micrographs for all AlGaN/(AlN)/GaN heterostructures.

### 5.3.3 Temperature-dependent Hall Measurements

RT Hall measurements showed a significant deviation between the 2DEG sheet density of AlGaN/GaN heterostructures with high ( $\sim 2 \times 10^{10} \text{ cm}^{-2}$ ) TDD and those with mid-range ( $\sim 5 \times 10^8 \text{ cm}^{-2}$ ) or low ( $\sim 5 \times 10^7 \text{ cm}^{-2}$ ) TDD (Table 5.3). The sheet concentration was possibly affected by TD-associated electron traps. For all mid-range and low-TDD heterostructures, there was a modest increase in sheet density as temperature was reduced (shown for  $\text{Al}_{0.24}\text{Ga}_{0.76}\text{N}/\text{GaN}$  in Fig. 5.4); thus, an increase in buffer layer carrier concentration with lower TDD could not account for the increase in sheet density. Though piezoelectric polarization and spontaneous polarization are nonlinear with regard to strain states, residual stress in the GaN buffer would produce

minimal effects on the electrical characteristics. It is generally assumed that the electric fields surrounding charged dislocations are fully screened by high-density 2DEGs. We suspect that the charged dislocations lines are not fully screened (Fig. 5.5), and the depletion regions surrounding them had an impact on the sheet concentration. Variation in the RT sheet density of the AlGaN/AlN/GaN heterostructures was most likely the result of differences in the AlGaN barrier composition and slight differences in the AlN thickness.

**Table 5.3: RT 2DEG sheet density for all AlGaN/(AlN)/GaN heterostructures.**

	$\text{Al}_{0.06}\text{Ga}_{0.94}\text{N}/\text{GaN}$	$\text{Al}_{0.12}\text{Ga}_{0.88}\text{N}/\text{GaN}$	$\text{Al}_{0.24}\text{Ga}_{0.76}\text{N}/\text{GaN}$	$\text{AlGaN}/\text{AlN}/\text{GaN}$
Substrate/ Template	RT $n_s$ ( $10^{12}/\text{cm}^2$ )	RT $n_s$ ( $10^{12}/\text{cm}^2$ )	RT $n_s$ ( $10^{13}/\text{cm}^2$ )	RT $n_s$ ( $10^{13}/\text{cm}^2$ )
6H-SiC	1.59	2.77	1.18	1.83
GaN-on-sapphire	1.72	4.37	1.38	1.62
FS GaN	1.83	4.71	1.40	1.72

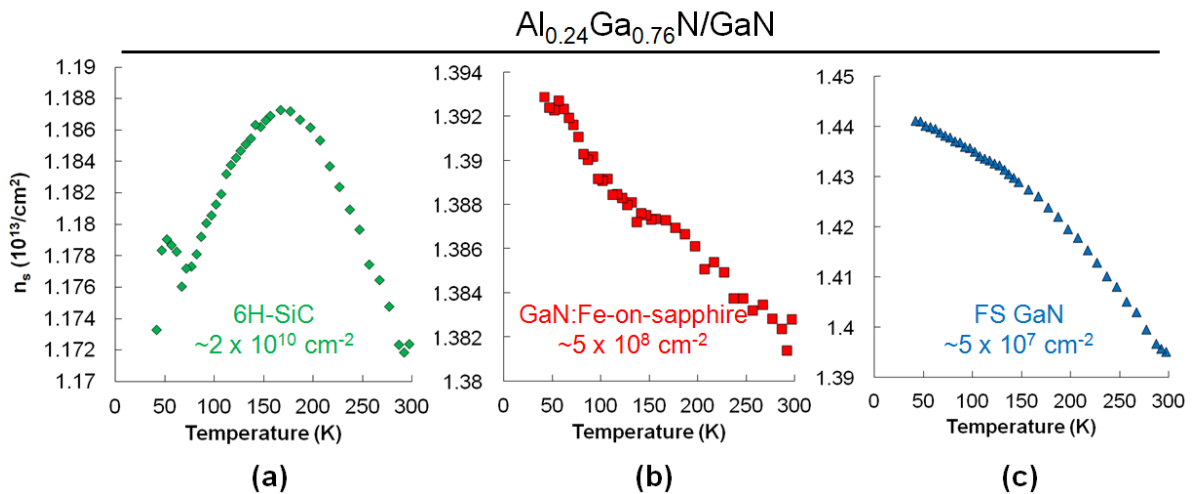


**Figure 5.4: Temperature-dependent 2DEG sheet densities for  $\text{Al}_{0.24}\text{Ga}_{0.76}\text{N}/\text{GaN}$  heterostructures (a) grown directly on 6H-SiC, (b) regrown on GaN:Fe-on-sapphire, and (c) regrown on FS GaN.**

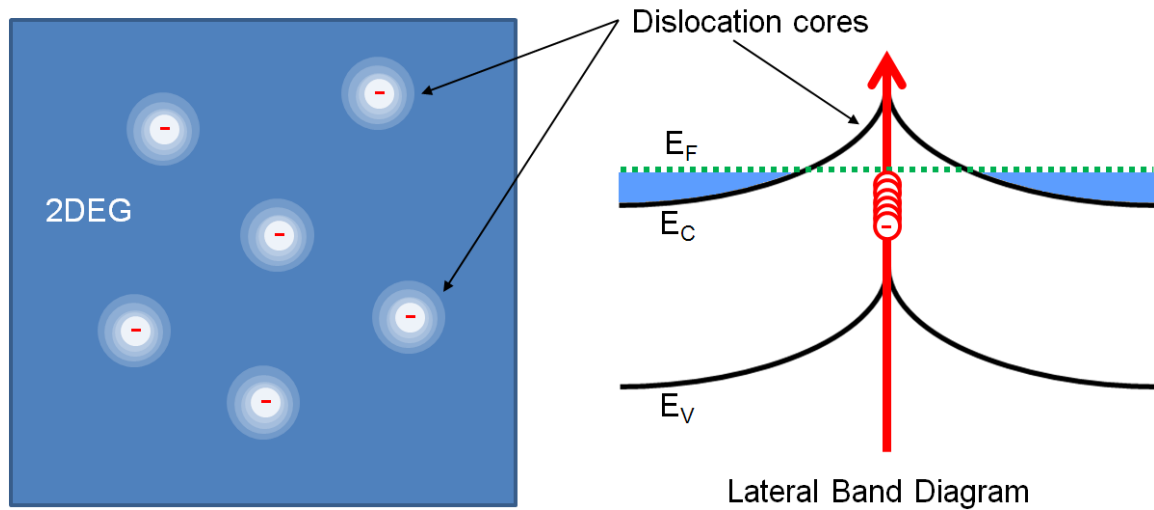


**Figure 5.5: Schematic showing the depletion regions surrounding charged dislocation lines in the plane of the 2DEG.**

Temperature-dependent Hall measurements were performed for the  $\text{Al}_x\text{Ga}_{1-x}\text{N}/\text{GaN}$  heterostructures, and the results are shown in Fig. 5.6. Based on the theoretical temperature-dependences of scattering rates, the dominant scattering mechanisms with the TDDs and Al mole fractions of  $\text{AlGaN}/\text{GaN}$  heterostructure presented here can be inferred. OP scattering is the dominant scattering mechanism in the high-temperature (HT) range. The diminishment of OP scattering with decreasing temperature contributed to the mobility increase observed for all heterostructures from 300 K to  $\sim 150$  K. In the low-temperature (LT) range ( $< 150$  K), the mobilities of 2DEGs in the  $\text{Al}_{0.24}\text{Ga}_{0.76}\text{N}/\text{GaN}$  heterostructures were found to be temperature-independent. This was most likely due to the dominance of alloy disorder and interface roughness scattering, which have been calculated to be temperature-independent.

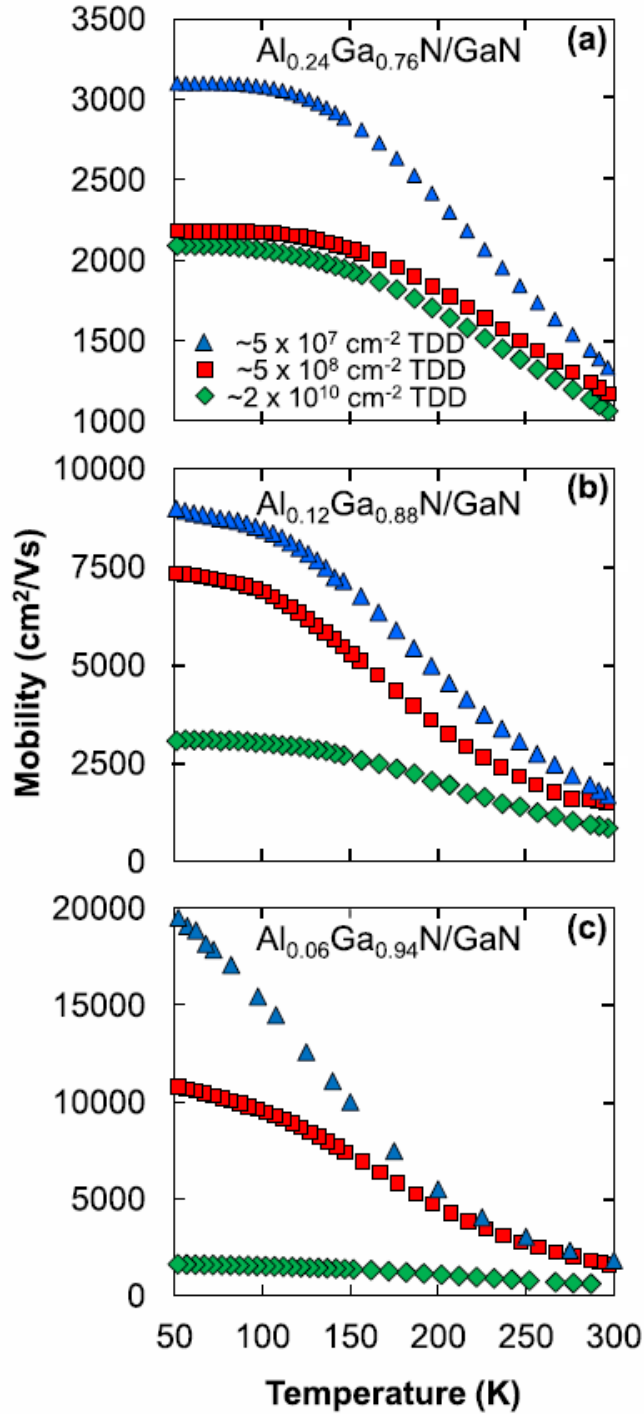


Figure 5.4: Temperature dependences of the 2DEG mobilities in  $\text{Al}_x\text{Ga}_{1-x}\text{N}/\text{GaN}$  heterostructures with (a)  $x = 0.24$ , (b)  $x = 0.12$ , and (c)  $x = 0.06$  with TDDs of  $\sim 2 \times 10^{10} \text{ cm}^{-2}$ ,  $\sim 5 \times 10^8 \text{ cm}^{-2}$ , and  $\sim 5 \times 10^7 \text{ cm}^{-2}$ .

Temperature-independence has also been calculated for dislocation scattering. Since TDD was the only quality varied between the  $\text{Al}_{0.24}\text{Ga}_{0.76}\text{N}/\text{GaN}$  heterostructures, changes in TDD determined the separation between mobility curves in Fig. 5.4(a). The contribution of dislocation-related scattering to mobility reduction, as seen at mid-range and high TDD for the  $\text{Al}_{0.24}\text{Ga}_{0.76}\text{N}/\text{GaN}$  samples, was masked by the additional alloy disorder scattering in the heterostructure with mid-range TDD. The  $\text{Al}_{0.24}\text{Ga}_{0.76}\text{N}/\text{GaN}$  sample with mid-range TDD had a higher 2DEG sheet density than the sample with high TDD; therefore, there was additional overlap of the 2DEG wave function with the AlGaN barrier. This higher 2DEG sheet density would also enhance the effects of interface roughness scattering.

As 2DEG sheet density was reduced, the importance of dislocation scattering to 2DEG mobility became clearer. The separation between mobility curves increased as the Al mole fraction of the AlGaN barrier was lowered from 0.24 to 0.12 (Fig. 5.4(b)) and then 0.06 (Fig. 5.4(c)). Whereas sheet density correlated negatively with mobility at mid-range and low TDD, as a result of increased 2DEG overlap with the AlGaN barrier, the opposite was observed with high TDD. With reduced screening of charged dislocation lines, the 2DEG mobility at high TDD was seen to be significantly degraded, even at RT. The RT mobilities with high TDD for the  $\text{Al}_{0.12}\text{Ga}_{0.88}\text{N}/\text{GaN}$  and  $\text{Al}_{0.06}\text{Ga}_{0.94}\text{N}/\text{GaN}$  heterostructures were 847 and 612  $\text{cm}^2/\text{Vs}$ , respectively. The 2DEG mobility with high TDD was constant in the LT range because of the dominance of temperature-independent dislocation scattering. The LT 2DEG mobility in the  $\text{Al}_{0.12}\text{Ga}_{0.88}\text{N}/\text{GaN}$  and  $\text{Al}_{0.06}\text{Ga}_{0.94}\text{N}/\text{GaN}$  heterostructures with mid-range and low TDD had an inverse



relationship with temperature, suggesting the greater importance of DP or PE scattering over dislocation scattering. DP and PE scattering have been calculated to have an inverse relationship with temperature.

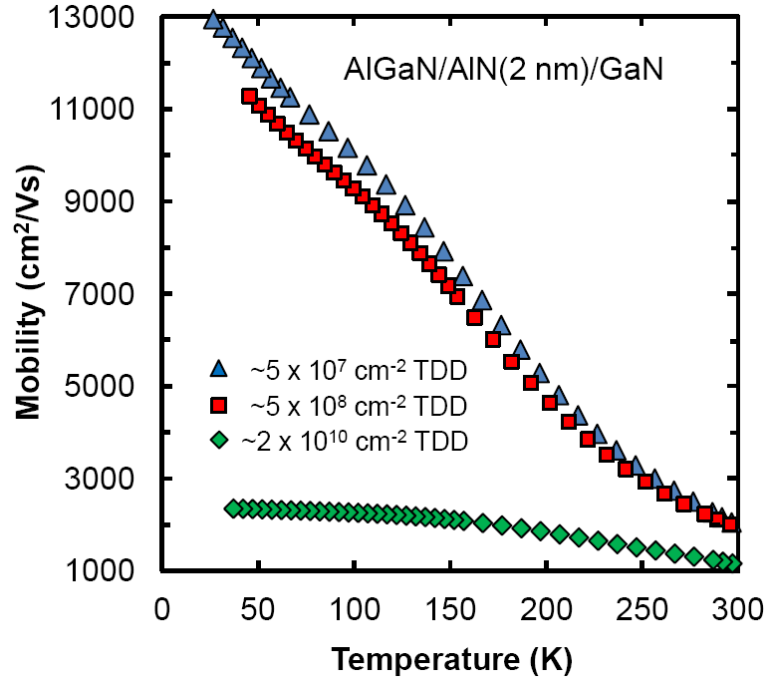


**Figure 5.5: Temperature-dependences of the 2DEG mobilities for AlGaIn/AlN(2 nm)/GaIn heterostructures with TDDs of  $\sim 2 \times 10^{10} \text{ cm}^{-2}$ ,  $\sim 5 \times 10^8 \text{ cm}^{-2}$ , and  $\sim 5 \times 10^7 \text{ cm}^{-2}$ .**

Including an AlN IL at the heterointerface minimizes alloy disorder scattering. Carrier penetration into the AlGaIn barrier is limited by the AlN barrier, which also increases polarization charge. To determine the effect of dislocation scattering on a high-density 2DEG, temperature-dependent Hall measurements were performed on AlGaIn/AlN(2 nm)/GaIn heterostructures grown directly on 6H-SiC, regrown on GaN-on-sapphire, and regrown on FS GaIn (Fig. 5.5). Dislocation scattering was seen to severely reduce the 2DEG mobility of the AlGaIn/AlN(2 nm)/GaIn heterostructure with high TDD.

A 2DEG mobility of 2333 cm<sup>2</sup>/Vs was recorded at 42 K for the AlGa<sub>N</sub>/AlN(2 nm)/Ga<sub>N</sub> with a TDD of  $\sim 2 \times 10^{10}$  cm<sup>-2</sup>. 2DEG mobilities higher than 2333 cm<sup>2</sup>/Vs were measured at 273 K and 277K for the samples with mid-range and low TDD, respectively. The LT mobilities of the AlGa<sub>N</sub>/AlN/Ga<sub>N</sub> heterostructures with TDDs of  $\sim 5 \times 10^8$  and  $\sim 5 \times 10^7$  cm<sup>-2</sup> appeared to be far less affected by dislocation scattering, as evidenced by their inverse temperature dependence. Decreasing the TDD of AlGa<sub>N</sub>/AlN(2 nm)/Ga<sub>N</sub> heterostructures below  $\sim 5 \times 10^8$  cm<sup>-2</sup> yielded incremental improvements in mobility. At 46 K, a mobility of 11,251 cm<sup>2</sup>/Vs was recorded for the AlGa<sub>N</sub>/AlN/Ga<sub>N</sub> heterostructure with mid-range TDD, and a mobility of 12,107 cm<sup>2</sup>/Vs was measured for the heterostructure with low TDD.

Calculations by Asgari *et al.* [88] concerning AlGa<sub>N</sub>/AlN/Ga<sub>N</sub> heterostructures predicted mobility limitation in the LT range by temperature-independent interface roughness scattering, which is most likely the case in our study. However, the influence of interface roughness appeared to be significantly reduced by the incorporation of an AlN IL. The increased separation of the 2DEG from potential fluctuations in the AlGa<sub>N</sub> barrier with a relatively thick AlN interlayer may also play a role in the improved LT mobility.

## **Chapter 6. NH<sub>3</sub>-MBE AlGa<sub>n</sub>/Ga<sub>n</sub> HEMT TDD Series: Leakage**

### **6.1 Introduction**

Ga-rich conditions, which are standard in PAMBE, were implicated as an important factor in the vertical leakage of PAMBE-grown HEMT structures. It has been hypothesized that this vertical leakage is facilitated by Ga-decorated threading dislocations (specifically, screw dislocations). Standard growth conditions for NH<sub>3</sub>-MBE are highly N-rich, so Ga-decoration of threading dislocations during GaN grown by NH<sub>3</sub>-MBE is unlikely. In this chapter, AlGa<sub>n</sub>/Ga<sub>n</sub> heterostructures with a large range of TDDs are grown by NH<sub>3</sub>-MBE. This chapter presents a similar to that which was presented in Chapter 4. This study is far less extensive though, as the thermal conductivity of the substrate was not taken into consideration, and HEMTs were not fabricated.

### **6.2 Experimental Procedure**

#### **6.2.1 Regrowth by NH<sub>3</sub>-MBE**

Unlike for Ga-rich PAMBE regrowths, CBr<sub>4</sub> does not appear to be an effective conveyance for C-doping at the regrowth interface in NH<sub>3</sub>-MBE. SIMS analysis yielded only a background C concentration on samples with varied CBr<sub>4</sub> flow rates and growth temperatures. Some groups have had success using ionized methane sources for C doping in GaN with NH<sub>3</sub>-MBE [93], but the only demonstrated method for effective NH<sub>3</sub>-MBE regrowth of HEMT structures is through p-GaN back barriers with Mg-

doping. Hybrid Ga-rich PAMBE/NH<sub>3</sub>-MBE regrowths with C-doping at the regrowth interface have also been successful. The following study included p<sup>+</sup>-i-p<sup>-</sup> structures at the regrowth interface. The p<sup>+</sup>-i-p<sup>-</sup> structure was developed specifically for bulk layer Hall measurements, as it minimized the depletion width into the active region and reduced the roughening associated with high Mg-doping.

## 6.2.2 Growth of TDD Series

The AlGaN/GaN TDD Series (Fig. 6.1) was grown in a Veeco 930 MBE system, equipped with conventional Ga and Al effusion cells. The N source consisted of NH<sub>3</sub> flowing through a custom-built showerhead injector.

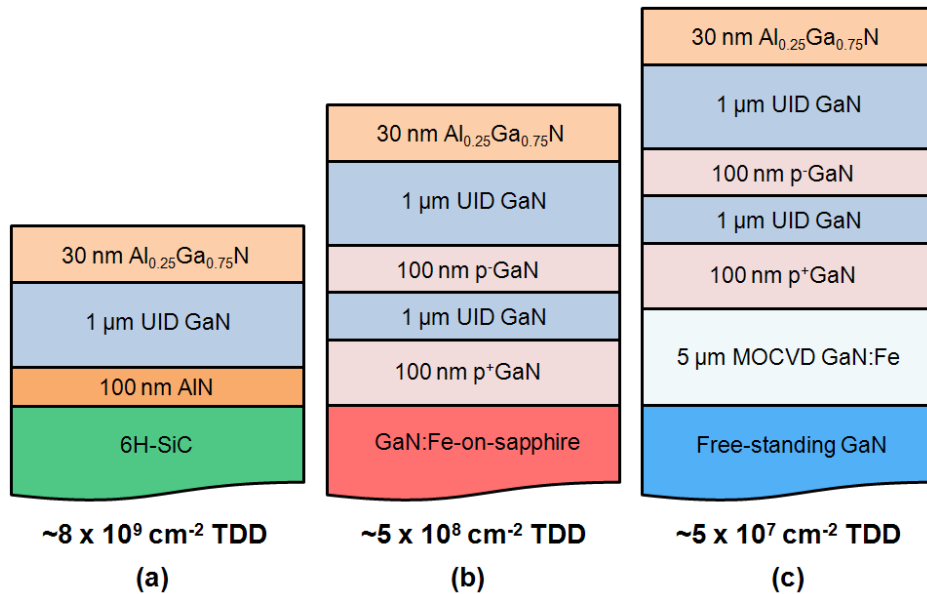


**Figure 6.1: Schematics of AlGaN/GaN heterostructures (a) directly grown on 6H-SiC, (b) regrown on GaN:Fe-on-sapphire, and regrown on FS GaN by NH<sub>3</sub>-MBE.**

Direct growth on 6H-SiC was initiated with a 100 nm AlN layer grown with an NH<sub>3</sub> flow rate of 200 SCCM at 820 °C. These conditions resulted in an AlN growth rate

of  $\sim 8$  nm/min. The RHEED pattern was initially spotty but transitioned to streaks after 10 nm of AlN growth. Subsequently, a 1  $\mu\text{m}$  two-step GaN buffer was grown at 820  $^{\circ}\text{C}$  to reduce TDD. Step 1 was grown with an  $\text{NH}_3$  flow rate of 25 SCCM, and Step 2 was grown with an  $\text{NH}_3$  flow rate of 200 SCCM ( $\sim 9$  nm/min). Upon completion of the GaN buffer layer, a 30 nm AlGaIn barrier was grown with an  $\text{NH}_3$  flow rate of 200 SCCM.

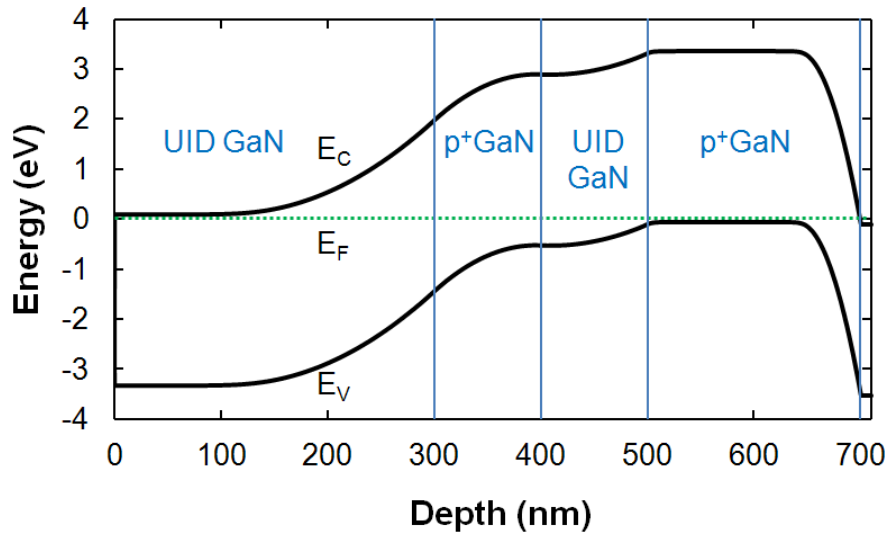


**Figure 6.2: Band structure of p<sup>+</sup>-i-p<sup>-</sup> isolation structure used in NH<sub>3</sub>-MBE regrowths.**

To isolate the active region from donor impurities at the regrowth interface, a p<sup>+</sup>-i-p<sup>-</sup> structure was included in the regrowths on GaN:Fe-on-sapphire and FS GaN. The p<sup>+</sup>GaN and p<sup>-</sup>GaN layers were grown at 790  $^{\circ}\text{C}$  with Mg-doping concentrations of  $\sim 1 \times 10^{19}$  and  $\sim 1 \times 10^{18} \text{ cm}^{-3}$ , respectively, which were determined by SIMS. Assuming that 1% of the Mg dopants were activated and that the UID GaN had a background donor concentration of  $\sim 5 \times 10^{16} \text{ cm}^{-3}$ , the band structure near the regrowth interface would be similar to the one depicted in Fig. 6.2. This band structure also assumes 10 nm of highly n-type ( $\sim 10^{20} \text{ cm}^{-3}$  donor concentration) GaN as the template surface. After completion

of the isolation structure, a 1  $\mu\text{m}$  UID GaN buffer layer ( $\sim 9$  nm/min) and 30 nm AlGaIn barrier ( $\sim 6$  nm/min) were grown at 820  $^{\circ}\text{C}$  with an  $\text{NH}_3$  flow rate of 200 SCCM.

## 6.3 Results and Discussion

### 6.3.1 Structural Properties

HRXRD  $\omega$ -2 $\theta$  scans of the AlGaIn and GaN (0002) reflection indicated the Al mole fractions of the AlGaIn barriers and their thicknesses shown in Table 6.1 for the all heterostructures. The rocking curve FWHMs of HRXRD  $\omega$ -scans for the GaN (20 $\bar{2}$ 1) reflection (measured in a skew symmetric geometry) are also reported in Table 6.1, as well as those for the GaN (0002) reflection. Using the calibration curve developed from PV-TEM data, the FWHMs of the GaN (20 $\bar{2}$ 1) reflections yielded TDDs of  $\sim 8 \times 10^9 \text{ cm}^{-2}$  for the direct growth on 6H-SiC,  $\sim 5 \times 10^8 \text{ cm}^{-2}$  for the regrowth on GaN-on-sapphire, and  $\sim 5 \times 10^7 \text{ cm}^{-2}$  for the regrowth on FS GaN.

**Table 6.1: Al mole fractions and thicknesses ( $t$ ) of the AlGaIn barriers and HRXRD  $\omega$ -rocking curve FWHMs of the GaN (0002) and GaN (20 $\bar{2}$ 1) reflections for the  $\text{NH}_3$ -MBE AlGaIn/GaN TDD Series.**

Substrate/ Template	Al mole fraction	$t$ (nm)	GaN (0002) FWHM (arcsec)	GaN (20 $\bar{2}$ 1) FWHM (arcsec)
6H-SiC	0.268	28	476	911
GaN-on- sapphire	0.266	30	395	404
FS GaN	0.252	28	152	188

### 6.3.2 2DEG Characteristics

Hall measurements were performed on three van der Pauw Hall structures on each AlGaIn/GaN heterostructure. Averaging the measurements from the three Hall structures, the 2DEG mobility (sheet density) of the direct growth, regrowth on GaN:Fe-on-sapphire, and regrowth on FS GaN were  $1360 \text{ cm}^2/\text{Vs}$  ( $1.0 \times 10^{13} \text{ cm}^{-2}$ ),  $1526 \text{ cm}^2/\text{Vs}$  ( $1.1 \times 10^{13} \text{ cm}^{-2}$ ), and  $1607 \text{ cm}^2/\text{Vs}$  ( $1.1 \times 10^{13} \text{ cm}^{-2}$ ), respectively. There was a modest increase in 2DEG mobility when the TDD was reduced, which was similar to the results from AlGaIn/GaN heterostructures grown by Ga-rich PAMBE in Chapter 2. Without an AlN interlayer, it was assumed that alloy disorder scattering was an important scattering mechanism at RT.

### 6.3.3 Buffer Breakdown

Buffer leakage currents were measured on test structures with a source-to-drain spacing of  $1 \mu\text{m}$ . Figure 6.3 shows that a  $V_{\text{DS}}$  of  $\sim 82 \text{ V}$  for the direct growth on 6H-SiC,  $\sim 80 \text{ V}$  for the regrowth on GaN:Fe-on-sapphire, and  $\sim 79 \text{ V}$  for the regrowth on FS GaN was necessary to reach  $1 \text{ mA/mm}$  of buffer current. The  $\text{p}^+\text{-i-p}^-$  effectively blocked the leakage path at the regrowth interface, as evidenced by the high  $V_{\text{DS}}$  needed to reach  $1 \text{ mA/mm}$  of buffer current. Unlike in HEMT structures grown by Ga-rich PAMBE, TDD did not appear to impact the buffer breakdown voltage in  $\text{NH}_3$ -MBE-grown AlGaIn/GaN heterostructures. This suggests that a high intrinsic acceptor concentration (possibly  $V_{\text{Ga}}$ ) is compensating the background donor concentration. In Ga-rich PAMBE, C-doped GaN was in close proximity to the channel to facilitate a high buffer breakdown voltage, and

this had a detrimental effect on large-signal performance. The intrinsic compensation of background donor impurities in NH<sub>3</sub>-MBE may enable much simpler HEMT structures with low-TDD than those necessary for Ga-rich PAMBE.

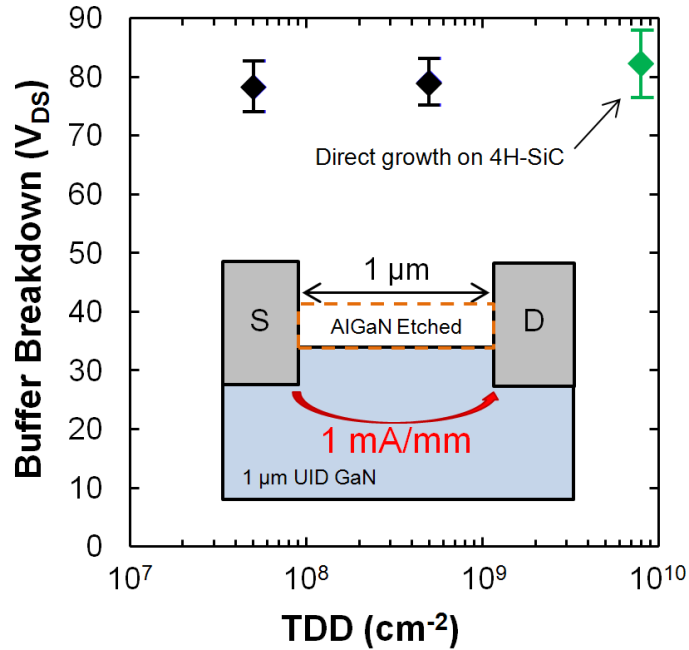


**Figure 6.3: Buffer breakdown voltage with respect to TDD for NH<sub>3</sub>-MBE-grown AlGaN/GaN heterostructures (error bars represent standard deviation).**

### 6.3.4 Schottky Contact Leakage

The average Schottky diode reverse current density (Fig. 6.4(a)) at -10 V was 23 mA/cm<sup>2</sup> for the direct growth on 6H-SiC, 40 mA/cm<sup>2</sup> for the regrowth on template ii, and 22 mA/cm<sup>2</sup> for the regrowth on template iii. Unlike the Ga-rich PAMBE-grown HEMT TDD Series, there was no discernible trend of Schottky leakage with TDD in the NH<sub>3</sub>-MBE-grown heterostructures. However, the average Schottky reverse current at -10 V for the NH<sub>3</sub>-MBE direct growth on 6H-SiC was nearly a factor of 38 less than the reverse current for the Ga-rich PAMBE direct growth on 4H-SiC. Presumably, the N-rich



conditions of  $\text{NH}_3$ -MBE reduced the number of leakage paths associated with threading dislocations. It is unlikely that TDD has no effect on gate leakage, but rather the effect is masked by more dominant leakage mechanisms. Percolative transport has recently been identified as a strong leakage pathway [94]. Fabrication procedures may also need refinement for  $\text{NH}_3$ -MBE-grown HEMT structures, as surface traps may be facilitating another leakage pathway. Nevertheless, the low leakage of the  $\text{NH}_3$ -MBE direct growth on 6H-SiC presents  $\text{NH}_3$ -MBE as a promising growth technique for SOA HEMTs.

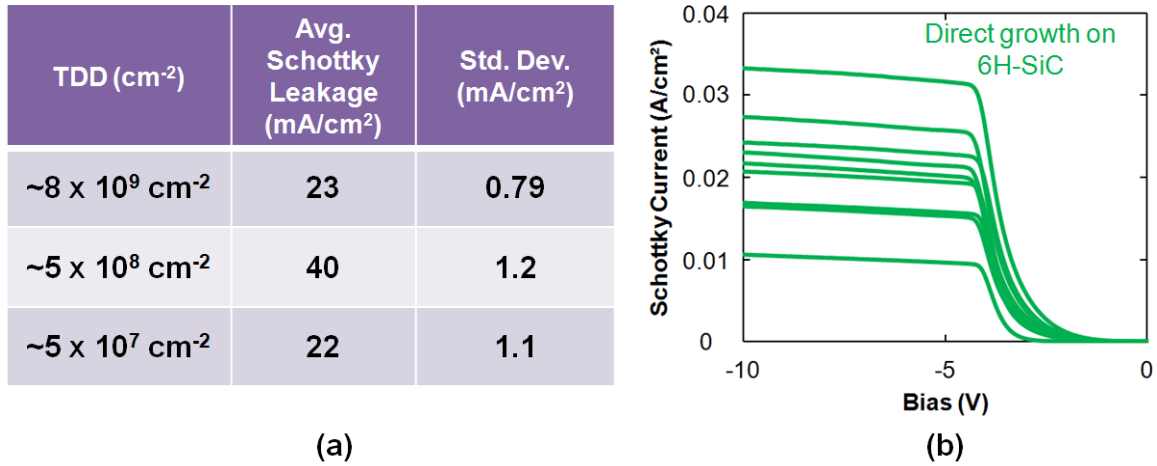


**Figure 6.4. (a) Average Schottky diode reverse current density with respect to TDD for  $\text{NH}_3$ -MBE-grown AlGaIn/GaN heterostructures. (b) Schottky diode IV curves for the 10 lowest leakage dies on the heterostructure grown directly on 6H-SiC by  $\text{NH}_3$ -MBE.**

## Chapter 7. AlN Interlayer Optimization by NH<sub>3</sub>-MBE

### 7.1 Introduction

As described in Chapter 4, AlN ILs are often included at the heterointerface of AlGa<sub>x</sub>N/GaN heterostructures to reduce or eliminate the overlap of the 2DEG wave function with the alloy (AlGa<sub>x</sub>N) barrier. The AlN ILs also reduce the effects of alloy barrier potential fluctuations. In addition to improving the 2DEG mobility, the AlN interlayer increases polarization discontinuity and, thus, the 2DEG sheet density. The growth procedure for AlGa<sub>x</sub>N/AlN/GaN heterostructures is simplified, in comparison with Ga-rich PAMBE, under N-rich conditions. With NH<sub>3</sub>-MBE and MOCVD (III/V: ~0.001), a growth interruption is unnecessary since the Al flux does not need to be changed.

The 2DEG characteristics of AlGa<sub>x</sub>N/AlN/GaN are curiously different between the three aforementioned growth techniques. With MOCVD, the optimized AlN interlayer thickness is under 1 nm (typically 0.7 nm). The 2DEG mobility of MOCVD-grown AlGa<sub>x</sub>N/AlN(0.7 nm)/GaN is generally very high ( $> 2000 \text{ cm}^2/\text{Vs}$ ), but the 2DEG sheet density is rarely greater than  $1.0 \times 10^{13} \text{ cm}^{-2}$ . As the AlN IL thickness grown by MOCVD is increased beyond 1 nm, the 2DEG mobility degrades drastically (Fig. 7.1). This was thought to be the result of structural degradation of thicker AlN ILs, possibly associated with threading dislocations. Although a systematic study is not presented in this thesis, the Hall measurements of AlGa<sub>x</sub>N/AlN/GaN heterostructures grown by NH<sub>3</sub>-MBE (non-sequentially with unisolated system conditions) show similar AlN IL

thickness limitations to those identified with MOCVD. In the case of  $\text{NH}_3$ -MBE, 2DEG mobility degraded with AlN ILs thicker than  $\sim 2$  nm. The ideal range for  $\text{NH}_3$ -MBE-grown interlayers was 1 – 2 nm, as mobilities in excess of  $2000 \text{ cm}^2/\text{Vs}$  were consistently measured with these AlN IL thicknesses.

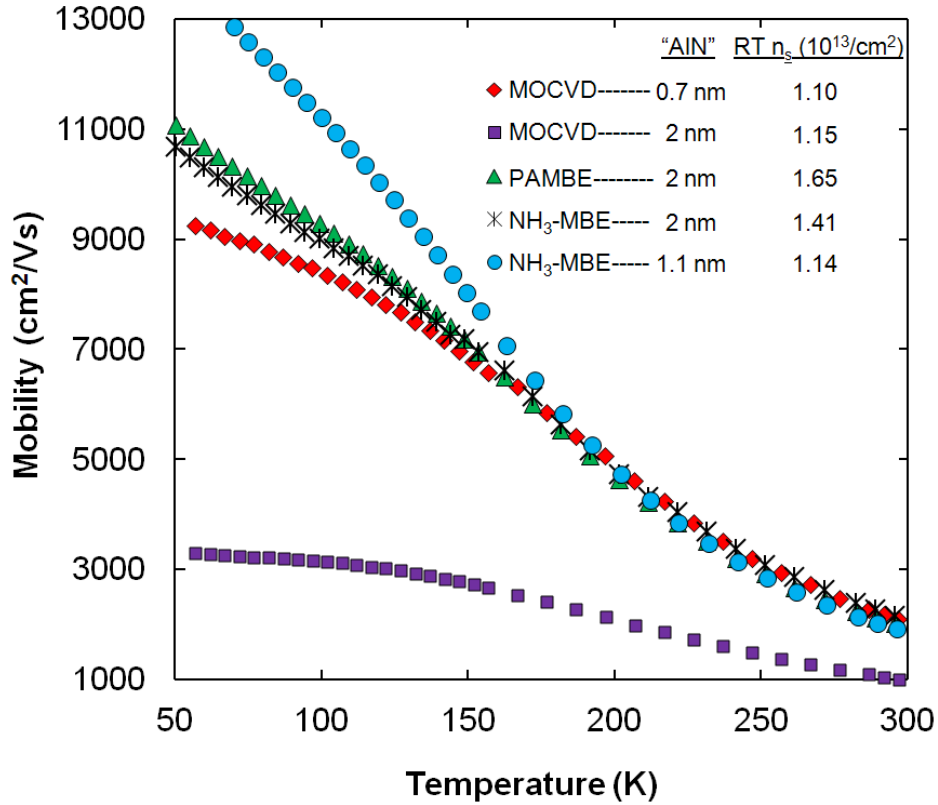


**Figure 7.1: Temperature-dependent 2DEG mobilities of AlGaN/AlN/GaN heterostructures grown by MOCVD,  $\text{NH}_3$ -MBE, and Ga-rich PAMBE with various AlN IL thicknesses ( $\sim 5 \times 10^8 \text{ cm}^{-2}$  TDD).**

The limitations for AlN interlayer thicknesses in MOCVD-grown and  $\text{NH}_3$ -MBE-grown heterostructures are in stark contrast with results from Ga-rich PAMBE-grown AlGaN/AlN/GaN heterostructures. In Chapter 4, the highest RT mobility was achieved with a 2.5 nm AlN interlayer, and several studies in the literature describe low-resistance AlN/GaN heterostructures with AlN barriers thicker than 4 nm grown by Ga-

rich PAMBE. The different growth conditions of MOCVD,  $\text{NH}_3$ -MBE, and Ga-rich PAMBE result in heterostructures with significantly different interfacial and chemical qualities.

## 7.2 Ga Impurities in $\text{NH}_3$ -MBE and MOCVD AlN Interlayers

$\text{AlGaN}/\text{AlN}(2\text{ nm})/\text{GaN}$  heterostructures (Fig. 7.2) were grown on GaN:Fe-on-sapphire by Ga-rich PAMBE,  $\text{NH}_3$ -MBE, and MOCVD for analysis by atom probe tomography.

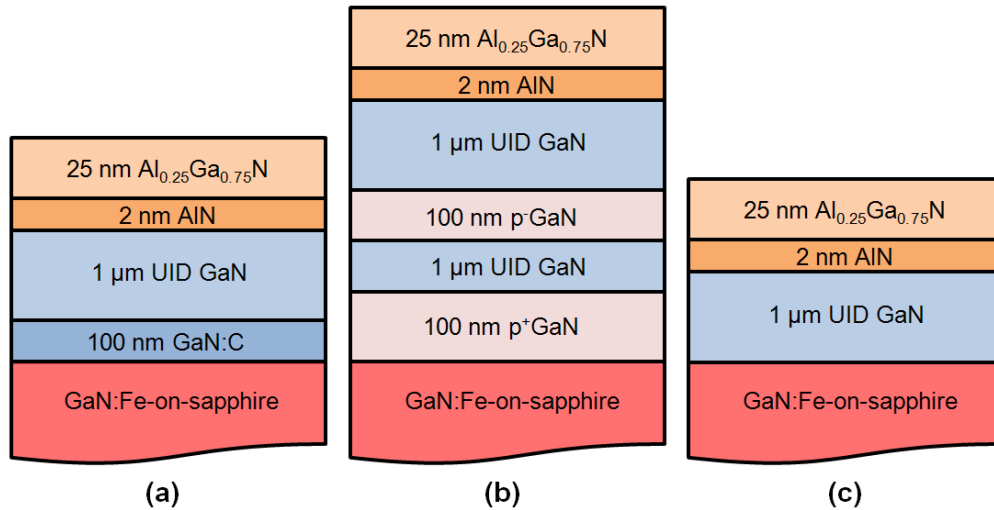


**Figure 7.2: Schematics of  $\text{AlGaN}/\text{AlN}(2\text{ nm})/\text{GaN}$  heterostructures grown by (a) Ga-rich PAMBE, (b)  $\text{NH}_3$ -MBE, and (c) MOCVD. MOCVD heterostructure was provided by Jing Lu.**

The growth parameters for the Ga-rich PAMBE heterostructure were described in Chapter 4, and the noteworthy growth parameters used for the  $\text{NH}_3$ -MBE heterostructure were described in Chapter 6. The AlN interlayer of the  $\text{NH}_3$ -MBE heterostructure was grown at  $820\text{ }^\circ\text{C}$  with an  $\text{NH}_3$  flow rate of 200 SCCM ( $\sim 1.5\text{ nm/min}$

AlN). The MOCVD growth was performed in a Veeco P-75 vertical reactor. All MOCVD-grown layers were deposited at 1100 °C with an NH<sub>3</sub> flow of 0.04 mol/min and a chamber pressure of 100 Torr. The TMG flow during GaN growth was 29 μmol/min. The MOCVD AlN interlayer was grown with a TMA flow of 0.9 μmol/min, and the AlGaIn layers were grown using TMG and TMA flows of 1 and 1.1 μmol/min, respectively.

Hall measurements at RT and 77 K were performed on the heterostructures shown in Fig. 7.2, and the results are displayed in Table 7.1.

**Table 7.1: Hall measurements at RT and 77 K including 2DEG sheet density ( $n_s$ ), mobility ( $\mu$ ), and sheet resistance ( $R_{sh}$ ) for AlGaIn/AlN/GaN heterostructures grown by PAMBE, NH<sub>3</sub>-MBE, and MOCVD.**

		$n_s$ ( $\times 10^{13} \text{ cm}^{-2}$ )		$\mu$ ( $\text{cm}^2/\text{V}\cdot\text{s}$ )		$R_{sh}$ ( $\Omega/\square$ )	
Growth Technique	Attempted AlN interlayer thickness (nm)	RT	77 K	RT	77 K	RT	77 K
PAMBE	~2	1.65	1.65	2030	9400	188	42
NH <sub>3</sub> -MBE	~2	1.41	1.45	2107	8740	209	49
MOCVD	~2	1.15	1.10	1280	3316	425	171

From the APT 1D concentration profiles (Fig. 7.3), it was clear that Ga impurities in the AlN ILs were the source of the discrepancy in 2DEG characteristics between the growth techniques. As AlN purity increased, the 2DEG sheet density increased. The AlN IL grown by MOCVD had a far greater concentration of Ga impurities than the AlN IL grown by NH<sub>3</sub>-MBE. The carry-over of Ga into thin AlN layers in the MOCVD samples is most likely related to the much higher growth temperatures used in the MOCVD growth process (> 1100 °C). This leads to evaporation of Ga species not only

from the underlying GaN layer prior to full coverage with AlN or AlGaN, but also from GaN deposits on hot reactor parts.

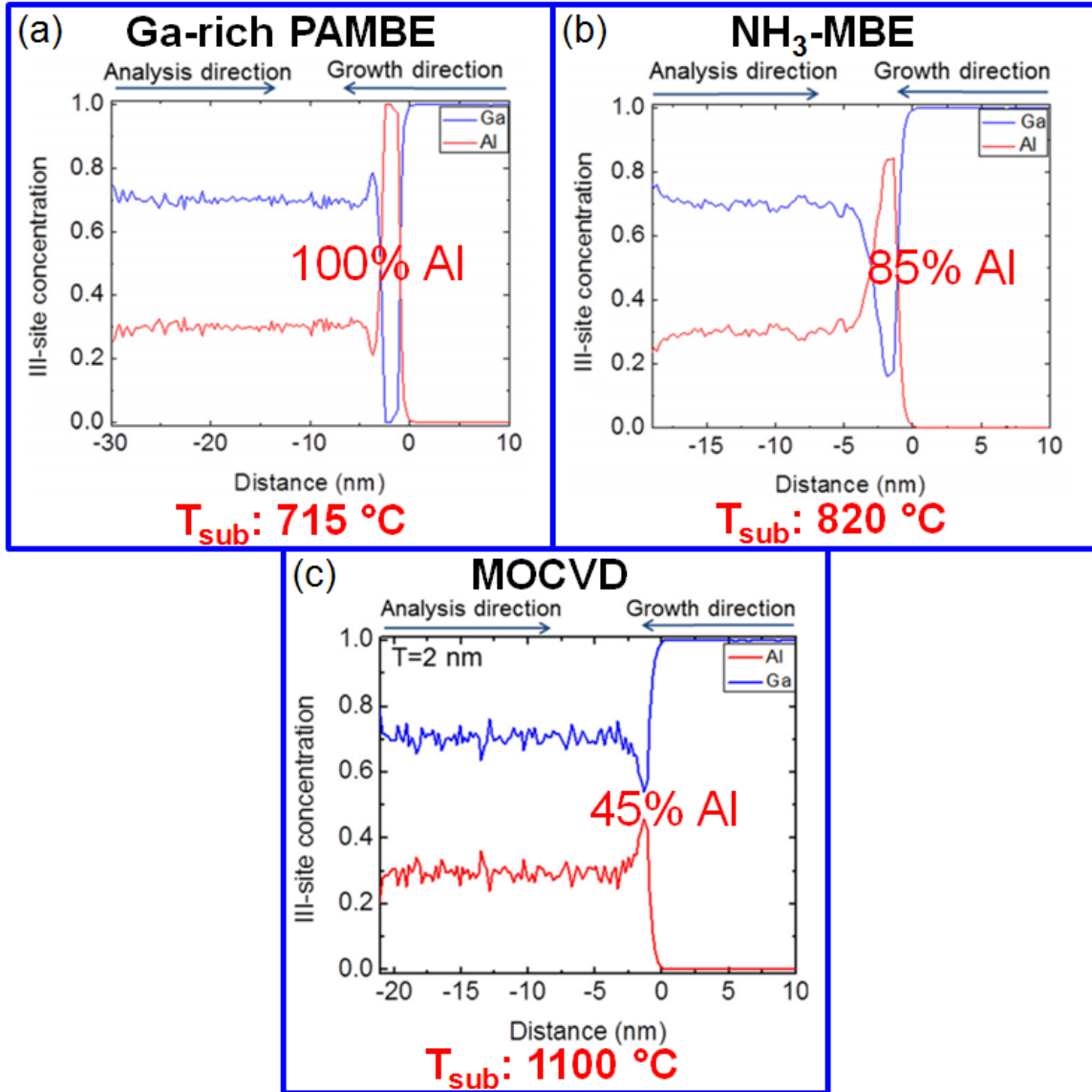


**Figure 7.3: 1D concentration profiles from APT on AlGaN/AlN(2 nm)/GaN heterostructures grown by (a) Ga-rich PAMBE, (b) NH<sub>3</sub>-MBE, and (c) MOCVD. APT was performed by Baishakhi Mazumder.**

The growth mechanics of NH<sub>3</sub>-MBE are not well understood. The unintended Ga present in the NH<sub>3</sub>-MBE-grown AlN IL most likely arises from Ga adatoms that were not

incorporated during GaN layer growth. Whether this is due to Ga residency time or decomposition of the underlying GaN layers will be evaluated in the following sections.

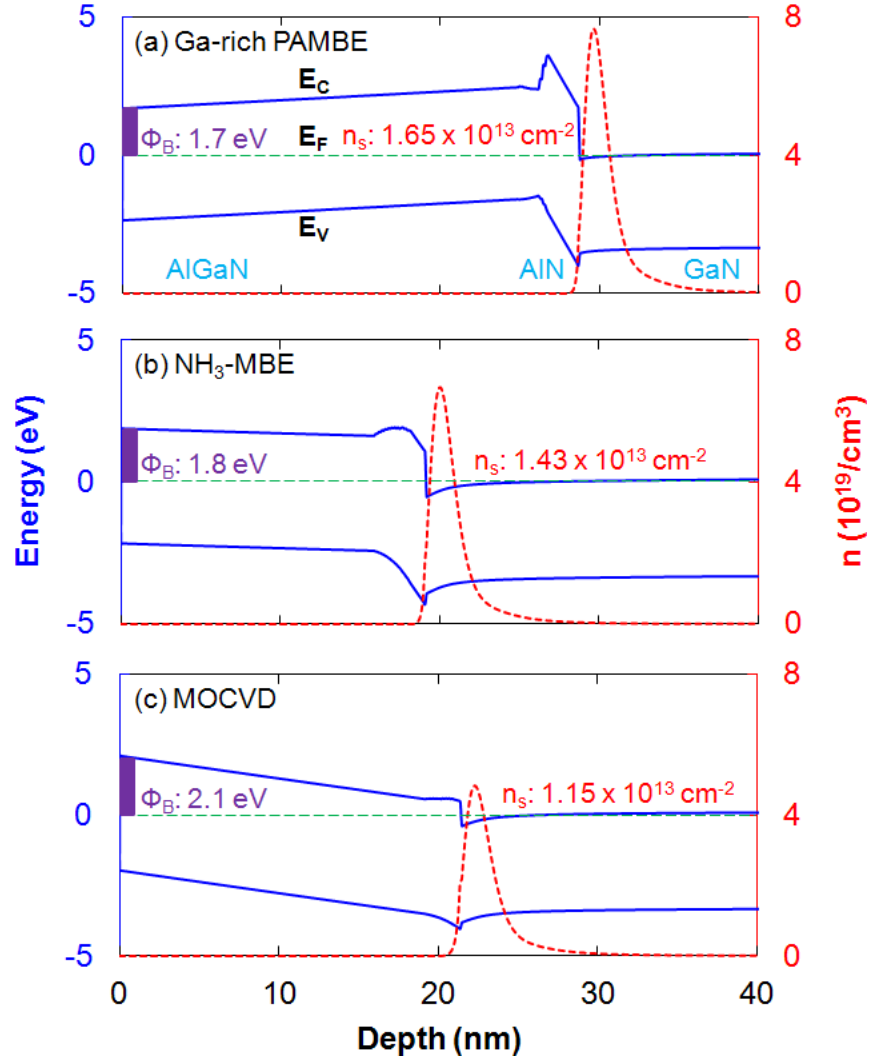


**Figure 7.4: Band diagrams of AlGaN/AlN(2 nm)/GaN heterostructures grown by (a) Ga-rich PAMBE, (b) NH<sub>3</sub>-MBE, and (c) MOCVD. Compositions and thicknesses for each layer are taken directly from APT data. Sheet concentrations ( $n_s$ ) and surface barrier heights ( $\Phi_B$ ) are included.**

Band diagrams (Fig. 7.4) were created using the APT 1D concentration profiles with the measured 2DEG sheet concentration (Table 7.1) as a fixed parameter to determine the surface barrier height ( $\Phi_B$ ). Since SIMS was not performed on these

structures, background donor concentrations are inexact. A background donor concentration of  $1 \times 10^{17} \text{ cm}^{-3}$  was used for all layers. There was stark contrast between the surface barrier heights of samples grown by MBE and those grown by MOCVD. The surface barrier heights of the MBE-grown heterostructures were closer to the barrier height of  $\sim 1.65 \text{ eV}$  determined by Ibbetson *et al.* [10]. Recently, Higashiwaki *et al.* [11] used x-ray photoelectron spectroscopy (XPS) to determine the surface barrier heights of MOCVD-grown AlGaIn/GaN samples annealed in a variety of environments. After annealing in a  $\text{N}_2$  environment at  $800 \text{ }^\circ\text{C}$  for 1 min, similar to the annealing conditions used in this study, a surface barrier height of  $2.1 \text{ eV}$  was measured, and this matched perfectly with our Hall measurements on MOCVD-grown samples. Although a similar study using XPS analysis has yet to be performed on MBE-grown samples, the data presented here suggests a barrier height below  $2 \text{ eV}$  would be measured. The origin of the disparity between surface barrier heights for MBE-grown and MOCVD-grown material is unclear at this point, but one could speculate that different oxide surface structures are involved.

The simulated band diagrams in Fig. 7.4 may not be entirely accurate. The compositional grading identified at the negative polarization interface of the “AlN” IL in the MOCVD-grown and  $\text{NH}_3$ -MBE-grown samples is likely an artifact of APT. A rough interface would likely result in grading of the 1D composition. Al adatom diffusivity below  $900 \text{ }^\circ\text{C}$  is very low without use of a surfactant, so the AlGaIn with very high Al content develops facets as the thickness increases. This would explain the poor 2DEG mobility measured on  $\text{NH}_3$ -MBE-grown heterostructures with AlN ILs thicker than  $2 \text{ nm}$ .



The increased roughness of the negative polarization interface would result in large fluctuations of the 2DEG ground state energy (Fig. 7.5), which would scatter electrons.

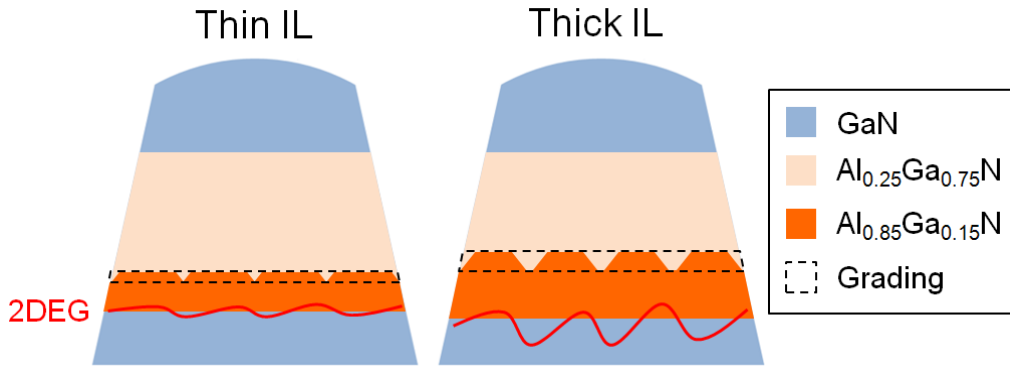


**Figure 7.5:** Schematic showing increased roughness (manifested as grading in APT) of the “AlN” IL grown by NH<sub>3</sub>-MBE (820 °C, 200 SCCM) with increased thickness.

### 7.3 Source of Ga Impurities in NH<sub>3</sub>-MBE AlN Interlayers

#### 7.3.1 Ga Residency Time

To evaluate the effect of Ga adatom residency time on AlN IL purity, a growth interruption was included in a series of samples grown by NH<sub>3</sub>-MBE. Using the standard growth temperature of 820 °C, Al<sub>0.3</sub>Ga<sub>0.7</sub>N(30 nm)/AlN(2 nm)/GaN heterostructures (~1.5 nm/min AlN) including pauses of 30 s, 60 s, and 180 s before AlN deposition were grown. The 2DEG characteristics of these heterostructures are shown in Table 7.2.

**Table 7.2:** Hall measurements at RT and 77 K including 2DEG sheet density ( $n_s$ ), mobility ( $\mu$ ), and sheet resistance ( $R_{sh}$ ) for AlGaN/AlN(2 nm)/GaN heterostructures grown NH<sub>3</sub>-MBE with growth interruptions before AlN deposition.

Growth Interruption Duration	RT $n_s$ ( $10^{13}/\text{cm}^2$ )	RT $\mu$ ( $\text{cm}^2/\text{V}\cdot\text{s}$ )	RT $R_{sh}$ ( $\Omega/\square$ )
30 s	2.43	717	338
60 s	1.84	731	465
180 s	2.40	733	336

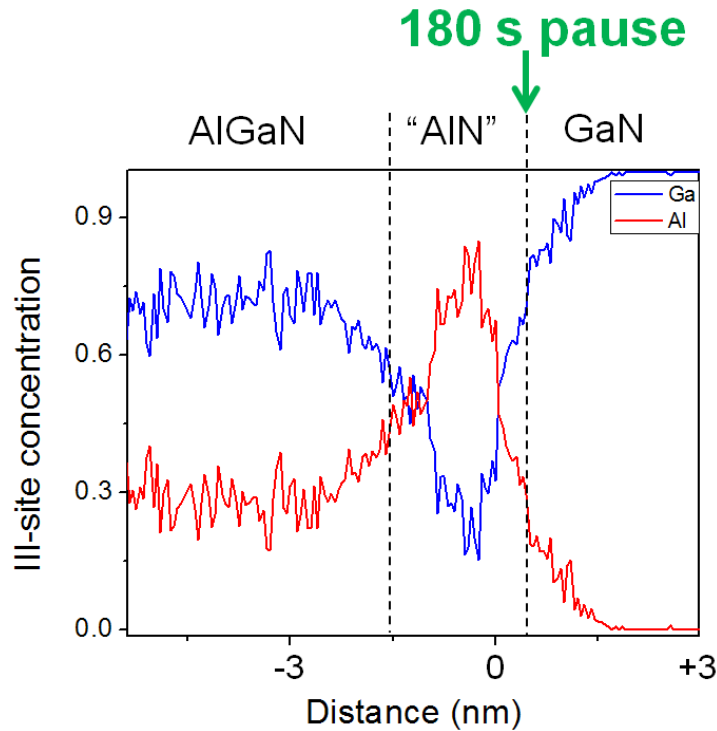


**Figure 7.6: 1D concentration profile of an AlGaN/AIN(2 nm)/GaN heterostructure grown at 820 °C by NH<sub>3</sub>-MBE with a 180 s growth interrupt before AlN deposition. APT was performed by Baishakhi Mazumder.**

The heterostructures with growth interruptions yielded relatively poor 2DEG characteristics. During a growth interruption, it is assumed that impurities from the ambient aggregate on the surface. An increased concentration of donor impurities may have led to the higher 2DEG sheet densities measured on these samples. As evidenced by the 1D concentration profile (Fig. 7.6) of the AlGaN/AIN/GaN heterostructure with a 180 s growth pause, the Ga impurities in the AlN IL were not caused by a long Ga residency time. The AlN IL in this heterostructure was impure (15-20% Ga impurities) and highly graded (rough), resulting in poor 2DEG mobility.

### 7.3.2 Decomposition of Underlying GaN Layers

The decomposition temperature of GaN in vacuum is  $\sim 745$  °C. The standard  $\text{NH}_3$ -MBE GaN growth temperature (HT, 820 °C) is far beyond the GaN decomposition temperature, so  $\text{NH}_3$ -MBE GaN growth involves competition between the forward and reverse reactions. The high  $\text{NH}_3$  overpressure is expected to greatly reduce the reverse reaction rate, but a very low reverse reaction rate can still introduce a significant concentration of Ga in the “AlN” ILs. The growth rate for AlN is generally kept below 2 nm/min because AlN and AlGaN are grown sequentially without an interruption. Before coalescence of the first ML of AlN, GaN bonds are presumably broken, and the Ga species may re-adsorb. This process is schematized in Fig. 7.7.

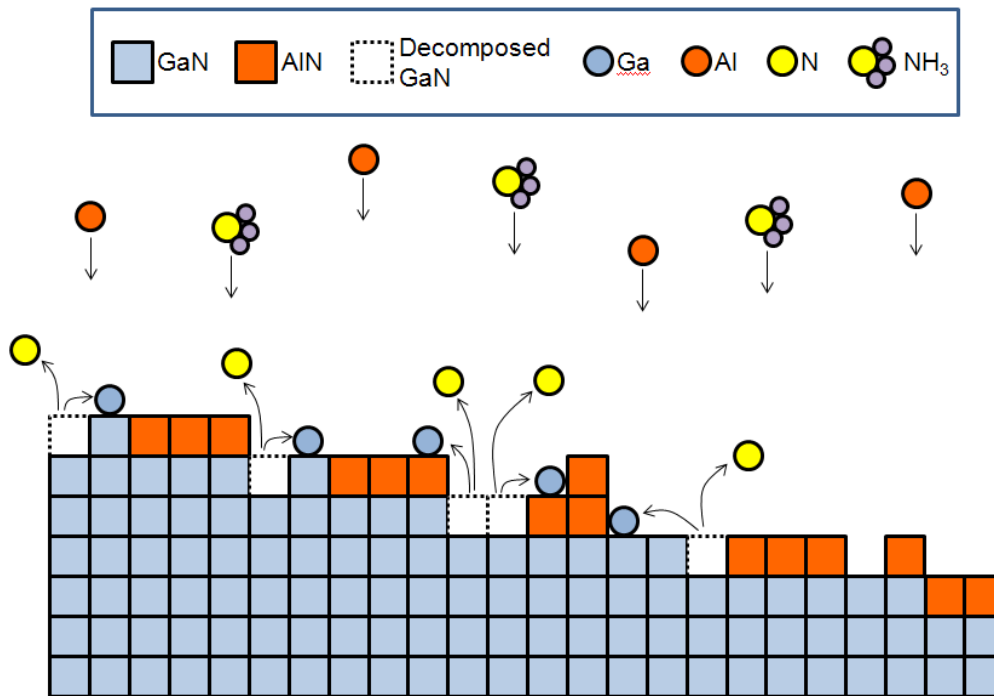


**Figure 7.7: Schematic of GaN decomposition in HT  $\text{NH}_3$ -MBE before coalescence of the first monolayer of AlN in an AlGaN/AlN/GaN heterostructure.**

To determine the effects of growth temperature and  $\text{NH}_3$  overpressure on the concentration of Ga impurities in the AlN IL, two APT structures (Fig. 7.8) were grown. One structure was grown with an  $\text{NH}_3$  flow rate of 200 SCCM (standard), and the other was grown with an  $\text{NH}_3$  flow rate of 1000 SCCM. In both structures, the growth temperature was lowered to 735 °C before deposition of the AlN IL and subsequently raised to 820 °C during deposition of the AlGaN barrier.

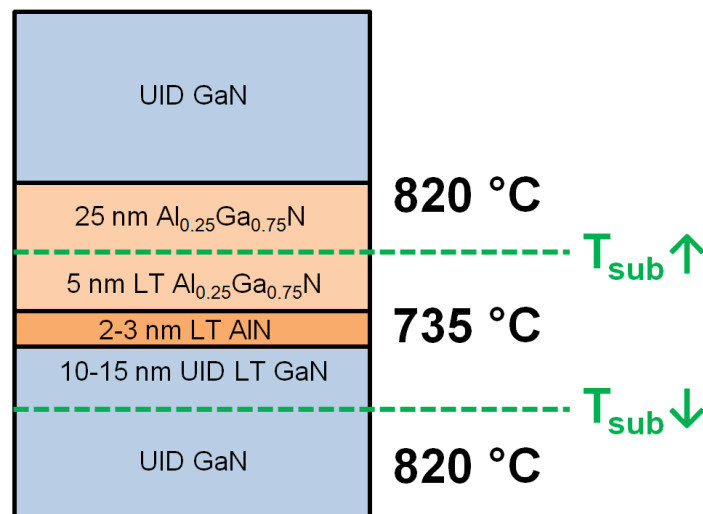


**Figure 7.8: Growth temperature sequence for deposition of low-temperature (LT) AlN ILs by  $\text{NH}_3$ -MBE, noting positions of substrate temperature ( $T_{\text{sub}}$ ) change. During temperature ramps (50 °C/min), Group III shutters were closed.**

The 1D concentration profiles of these structures indicated that the source of Ga impurities in the AlN IL was decomposition of the underlying GaN layers. By growing at a low temperature (LT), below the GaN decomposition temperature, and with a higher  $\text{NH}_3$  flow rate (1000 SCCM), Ga impurities occupied only 4% of the Group III sites in the AlN IL. The growth temperature may have been too close to the GaN decomposition temperature, however, since an appreciable concentration of Ga impurities was still

detected. This may also point to poor calibration of the pyrometer, seeing that the chosen growth temperature was only 10 °C below the GaN decomposition temperature.

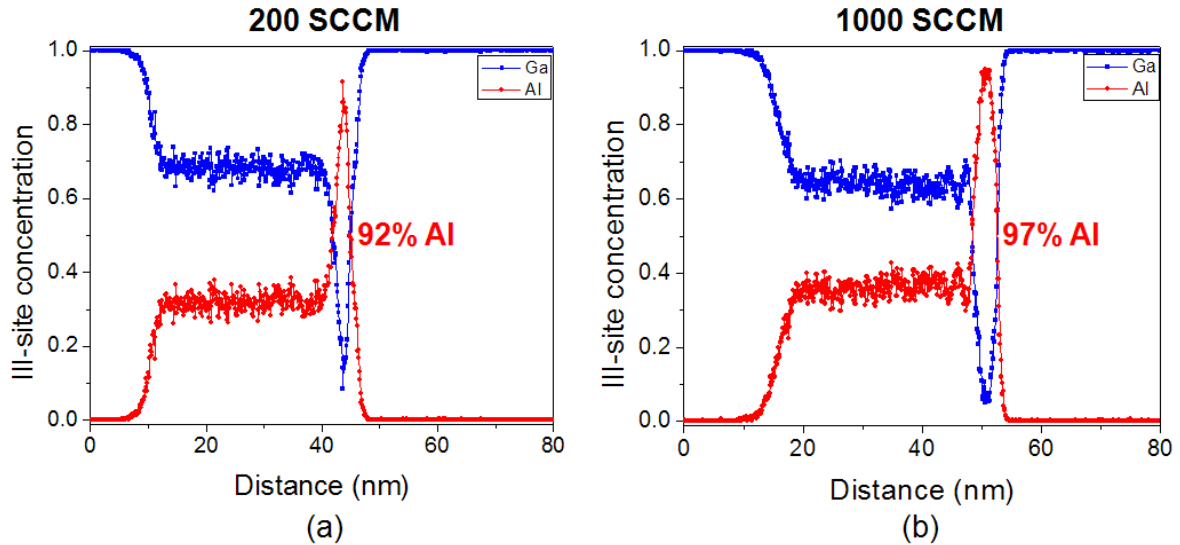


**Figure 7.9: 1D concentration profiles of AlGaN/AlN/GaN heterostructures with low-temperature (735 °C) AlN ILs grown by NH<sub>3</sub>-MBE with NH<sub>3</sub> flow rates of (a) 200 SCCM and (b) 1000 SCCM. APT was performed by Baishakhi Mazumder.**

Growth of GaN at 735 °C by NH<sub>3</sub>-MBE was previously shown to yield a rough, pitted surface morphology [56]. Though the RHEED pattern remained streaky during the growth of both samples in Fig. 7.9, there may have been significant roughening of the GaN surface before the deposition of the AlN IL. If this is the case, and the pyrometer reading was accurate, the higher Ga impurity concentration in the AlN IL grown at 735 °C with 200 SCCM was likely due to imperfection in the APT reconstruction. Since the AlN IL grown with 1000 SCCM NH<sub>3</sub> was slightly thicker, a higher peak Al mole fraction was able to be resolved by APT (Fig. 7.10).

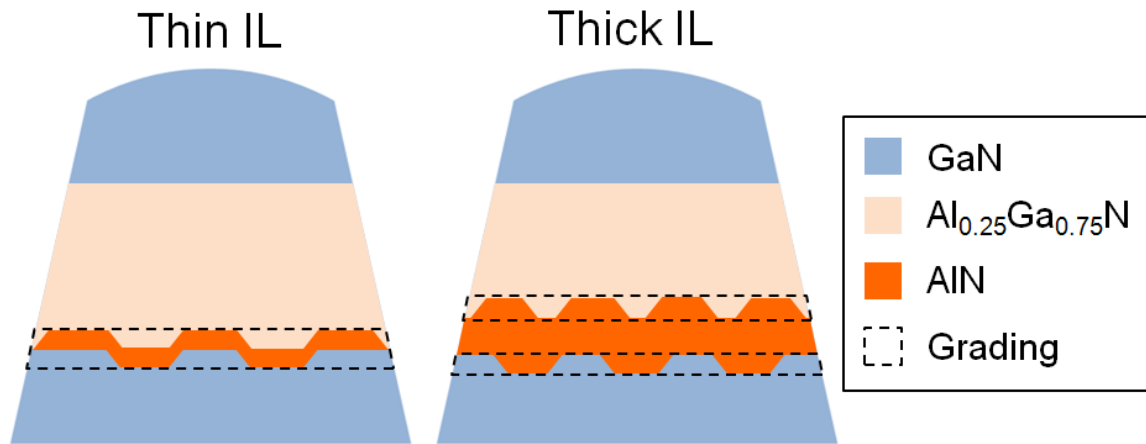


**Figure 7.10: Schematics of APT specimens grown by NH<sub>3</sub>-MBE at LT with thin and thick AlN ILs, showing the rough interfaces that may be identified as compositional grading during analysis.**

#### 7.4 LT NH<sub>3</sub>-MBE AlN Interlayers with In Surfactant

The surface diffusion of Group III adatoms in NH<sub>3</sub>-MBE is thermally enhanced with growth temperatures above the GaN decomposition temperature. When the growth temperature is lowered to ~700 °C, adatom diffusion is severely impacted (especially Al, which has a sticking coefficient of 1 at 700 °C), and surface roughness increases. Increased surface roughness strengthens the effects of interface roughness scattering and negatively influences the 2DEG mobility. In NH<sub>3</sub>-MBE, a low AlN IL growth temperature is necessary to yield pure AlN ILs and achieve the high 2DEG sheet densities measured in Ga-rich PAMBE-grown AlGaN/AlN/GaN heterostructures. Yet, the increase in 2DEG sheet density will also strengthen the effects of interface roughness scattering.

## AlN(3 nm)/GaN

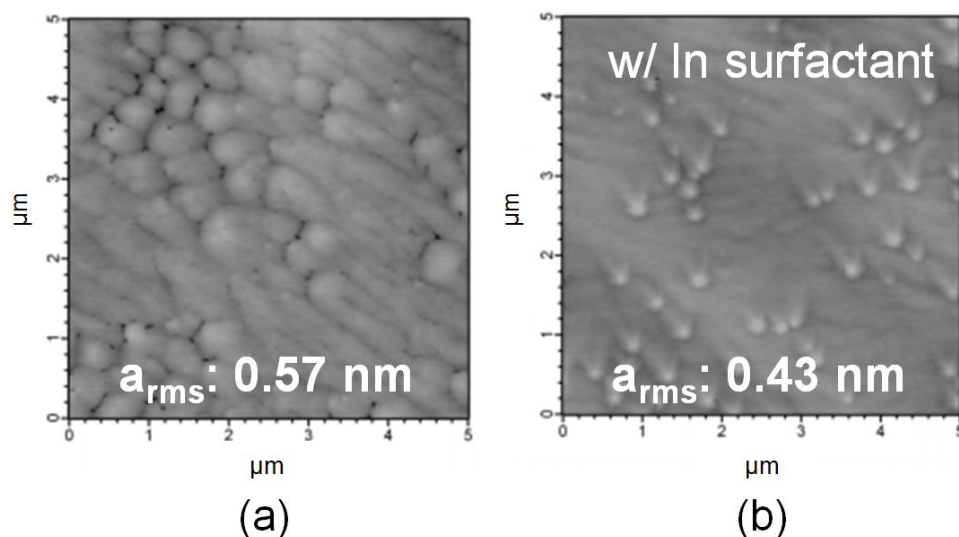


**Figure 7.11: 5 x 5  $\mu\text{m}^2$  AFM micrographs of AlN layers grown by  $\text{NH}_3$ -MBE (700  $^\circ\text{C}$ , 200 SCCM  $\text{NH}_3$  flow) without (a) and with (b) an In surfactant. The rms surface roughness ( $a_{\text{rms}}$ ) is included.**

To smooth the surface morphology of layers grown at low-temperature, an In surfactant with a beam equivalent pressure (BEP) of  $8 \times 10^{-8}$  Torr was applied (Fig. 7.11). The impinging In atoms increase the energy of the Al adatoms, lower the surface barrier for diffusion, and increase the surface mean-free-path. The growth temperature of 700  $^\circ\text{C}$  is far above the decomposition temperature of InN ( $\sim 450$   $^\circ\text{C}$ ), so the sticking coefficient of In is extremely small, and a negligible concentration of In impurities would be found in the AlN layer. As shown in Fig. 7.11, the low-temperature AlN layer without an In surfactant had a high density of pits. With an In surfactant, the AlN layer was very smooth, and the mounded surface morphology faded. Further investigation of the In

surfactant (range of In fluxes and growth temperatures) will be necessary to understand how the presence of In alters the growth mechanics.

**Table 7.3: RT Hall measurements including 2DEG sheet density ( $n_s$ ), mobility ( $\mu$ ), and sheet resistance ( $R_{sh}$ ) for AlGaN/AlN(3 nm)/GaN heterostructures grown by  $NH_3$ -MBE with (shaded in purple) and without In surfactant at LT.**

Structure	AlN IL Growth Temperature (°C)	RT $n_s$ ( $10^{13}/cm^2$ )	RT $\mu$ ( $cm^2/Vs$ )	RT $R_{sh}$ ( $\Omega/\square$ )
$Al_{0.22}Ga_{0.78}N/GaN$	--	1.01	1558	395
$Al_{0.22}Ga_{0.78}N/AlN(3\text{ nm})/GaN$	820	1.66	572	655
$Al_{0.22}Ga_{0.78}N/AlN(3\text{ nm})/GaN$	700	2.03	717	427
$Al_{0.22}Ga_{0.78}N/AlN(3\text{ nm})/GaN$	700*	2.10	978	303

\*In surfactant (BEP:  $8 \times 10^{-8}$  Torr)

A preliminary Hall study involving AlN ILs grown at low temperature by  $NH_3$ -MBE (GaN:Fe-on-sapphire templates) is presented in Table 7.3. AlN and GaN growth rates (were similar to those for the HT and LT  $NH_3$ -MBE-grown APT samples presented earlier. It was mentioned previously that AlN ILs thicker than 2 nm yielded poor 2DEG characteristics in  $NH_3$ -MBE-grown heterostructures, so this study focused on 3 nm AlN ILs. By growing the AlN IL at 700 °C, there was a sharp increase in the 2DEG sheet density, suggesting that a pure AlN IL was grown. When an In surfactant was applied at low temperature, the mobility rose slightly. This was possibly the result of decreased interface roughness scattering. The lowest sheet resistance achieved was 303  $\Omega/\square$ , which is much higher than the sheet resistances of similar heterostructures grown by Ga-rich PAMBE.



Another series of samples involving AlN ILs grown at LT by NH<sub>3</sub>-MBE (GaN:Fe-on-sapphire templates) is presented in Table 7.4. In this series, the growth rates of GaN and AlN were reduced to ~2.4 nm/min and ~0.9 nm/min, respectively. With a lower growth rate, there is lower likelihood of faceting from kinetic constraints, so it is assumed a smoother layer is grown. With a low AlN growth rate and application of an In surfactant at LT, a RT mobility above 1200 cm<sup>2</sup>/Vs was measured.

**Table 7.4: RT Hall measurements including 2DEG sheet density ( $n_s$ ), mobility ( $\mu$ ), and sheet resistance ( $R_{sh}$ ) for AlGaN/AlN(2.5 nm)/GaN heterostructures grown by NH<sub>3</sub>-MBE with reduced growth rates.**

Structure	AlN IL Growth Temperature (°C)	RT $n_s$ ( $10^{13}/\text{cm}^2$ )	RT $\mu$ ( $\text{cm}^2/\text{Vs}$ )	RT $R_{sh}$ ( $\Omega/\square$ )
Al <sub>0.28</sub> Ga <sub>0.72</sub> N/AlN(2.5 nm)/GaN	820	1.21	662	778
Al <sub>0.28</sub> Ga <sub>0.72</sub> N/AlN(2.5 nm)/GaN	735	1.72	995	365
Al <sub>0.28</sub> Ga <sub>0.72</sub> N/AlN(2.5 nm)/GaN	735*	1.78	1241	285

\*In surfactant (BEP:  $8 \times 10^{-8}$  Torr)

Although ionized defect scattering may be an important source of mobility degradation with LT growth, SIMS analysis (Fig. 7.12) showed little difference between the background impurity incorporation at standard (820 °C) and low (720 °C) temperature. It should be noted that heterostructures with low-temperature AlN ILs grown by NH<sub>3</sub>-MBE with 1000 SCCM NH<sub>3</sub> flow yielded extremely high sheet resistances, well beyond 1 k  $\Omega/\square$ . The 2DEG in these heterostructures is being fully compensated. Investigation of the trap states in AlGaN/AlN/GaN grown by NH<sub>3</sub>-MBE at low-temperature will help determine if intrinsic defects are limiting the 2DEG sheet density

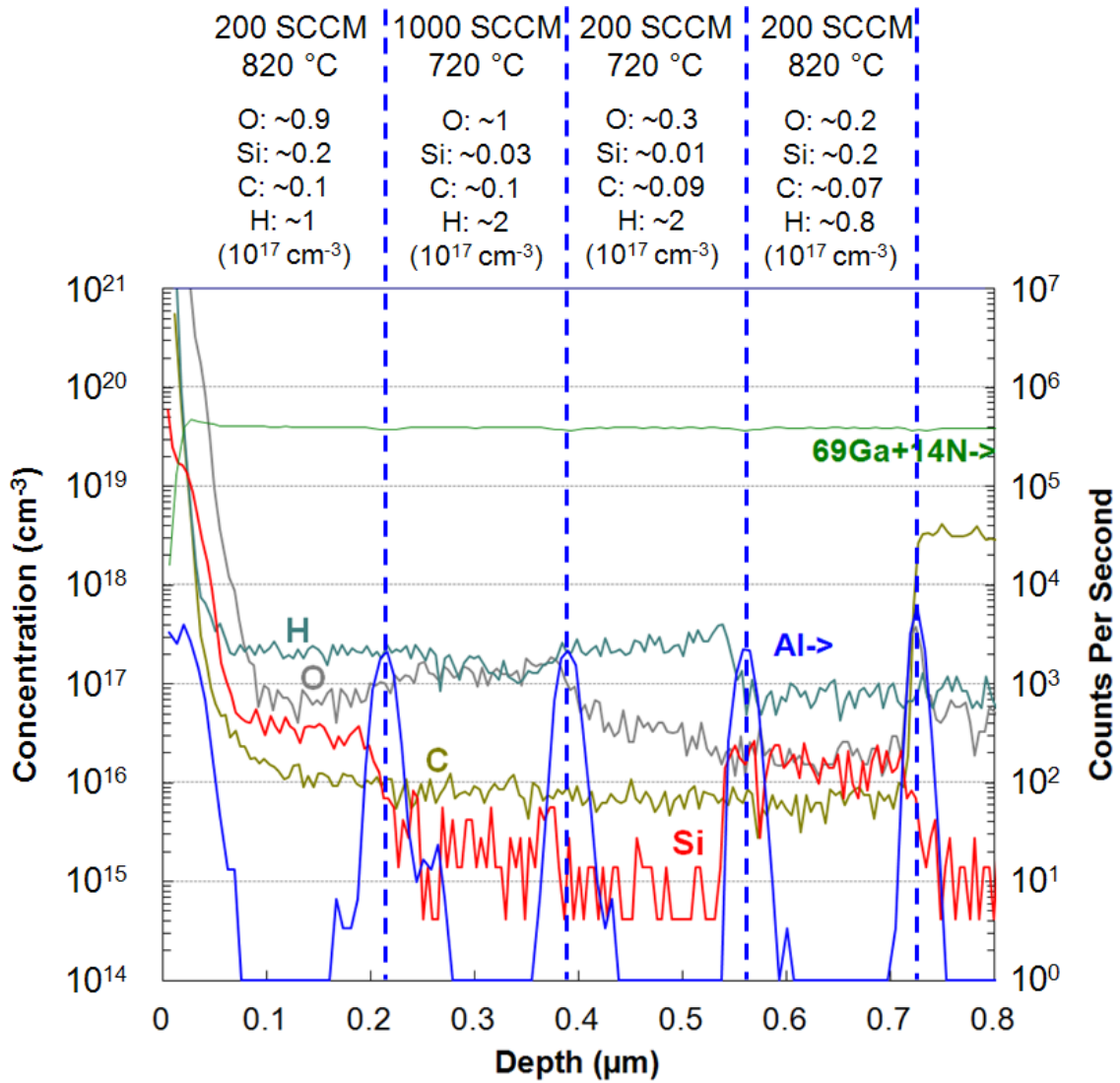


**Figure 7.12: Concentrations of background impurities (Si, C, O, and H) determined by SIMS in  $\text{NH}_3$ -MBE-grown GaN layers. Two layers were grown at 820 °C with an  $\text{NH}_3$  flow of 200 SCCM. Two layers was grown at 720 °C with  $\text{NH}_3$  flows of 200 SCCM and 1000 SCCM.**

## Chapter 8. Homogeneous Lattice-matched InAlN by N-rich PAMBE

### 8.1 Introduction

One of the main challenges in the epitaxy of depletion-mode metal-polar HEMT structures for high-frequency, high-power applications is to maintain high channel conductivity as the (In,Ga,Al)N barrier thickness ( $t_b$ ) is minimized. As the fabricated gate length ( $L_G$ ) is scaled down to facilitate efficient ultrahigh-frequency operation beyond the mm-wave regime,  $t_b$  needs to be reduced to maintain a high aspect ratio ( $L_G/t_b$ ) and avoid short-channel effects [95,96]. When the  $t_b$  of an  $\text{Al}_{0.3}\text{Ga}_{0.7}\text{N}/\text{GaN}$  structure is reduced below 15 nm, the sheet density is lowered well below  $1 \times 10^{13} \text{ cm}^{-2}$  since a significant concentration of surface donors remain neutral [10]. The need for aggressive scaling was not addressed in the previous chapters, as all heterostructures included 20-30 nm AlGaN barriers.

Metal-polar AlN/GaN structures may be applied to ultrathin barrier HEMTs, and extremely low sheet resistances have been measured with AlN barrier thicknesses below 5 nm [82,83]. However, the design space of AlN/GaN structures is severely limited, as the critical AlN thickness for biaxial stress relief through cracking is  $\sim 6$  nm. Stress in the barrier may also increase the favorability of point defect formation, and the inverse piezoelectric effect has been implicated as a key factor in the poor reliability of (Al,Ga)N/GaN HEMTs [97].

Lattice-matched heterostructures with InAlN barriers are an attractive option for the next generation of high-frequency, high-power HEMTs since they relieve design constraints and reduce the likelihood for defect formation observed in heterostructures with strained barriers. According to Vegard's law, InAlN layers are lattice-matched to GaN when they have an In mole fraction of  $\sim 0.17$ .  $\text{In}_{0.17}\text{Al}_{0.83}\text{N}$  has a wide bandgap ( $\sim 4.7$  eV) and large conduction-band-offset ( $\sim 1.2$  eV) relative to GaN. In 2001, Kuzmík [98] suggested  $\text{In}_{0.17}\text{Al}_{0.83}\text{N}/\text{GaN}$  as a superior HEMT structure to AlGaN/GaN, mainly due to the high charge density ( $\sim 3 \times 10^{13} \text{ cm}^{-2}$ ) induced at the heterointerface through a discontinuity in spontaneous polarization. Since then, reports of high-quality metal-polar  $\text{In}_{0.17}\text{Al}_{0.83}\text{N}/\text{GaN}$  structures grown by metalorganic chemical vapor deposition (MOCVD) have increased rapidly, showing that even with a  $t_b$  as low as 5 nm, a sheet density above  $1 \times 10^{13} \text{ cm}^{-2}$  is maintained [99]. Recently, a HEMT with an ultrathin  $\text{In}_{0.17}\text{Al}_{0.83}\text{N}$  barrier grown by MOCVD yielded a very high current-gain-cutoff frequency of 400 GHz [100]. While the performance of AlGaN/GaN HEMTs grown by plasma-assisted molecular beam epitaxy (PAMBE) tracked well with those grown by MOCVD, InAlN/GaN HEMTs grown by PAMBE have lagged behind.

The strong disparity in bond strengths between Al-N (2.88 eV), Ga-N (2.20 eV), and In-N (1.98 eV) necessitates that, with PAMBE, In-containing alloys are grown at lower temperatures ( $< 650$  °C) than AlGaN and GaN [101]. This low growth temperature severely limits the surface diffusion of Al adatoms, which could lead to inhomogeneity in the InAlN layer [102]. Detailed microstructural analyses of InAlN layers grown under metal-rich and N-rich conditions by PAMBE have revealed lateral phase separation

[103,104]. Eliminating this phase separation and the resulting strong potential fluctuations is essential to the improvement of 2DEG characteristics in PAMBE-grown InAlN/GaN structures.

## 8.2 Experimental Procedure

### 8.2.1 Growth of Interlayer Series

All heterostructures were grown in a Veeco Gen 930 molecular beam epitaxy system equipped with conventional In, Ga, and Al thermal effusion cells. The N source consisted of ultrahigh-purity (99.9995%) N<sub>2</sub> gas that was activated by an RF plasma. The growth temperature ( $T_{\text{sub}}$ ) was measured with an optical pyrometer that was calibrated to the melting point of Al (660 °C).

In the IL Series (Fig. 8.1), Structures i-v were regrown on 1- cm<sup>2</sup> Lumilog MOCVD-grown semi-insulating GaN:Fe-on-sapphire templates that had a specified TDD of  $\sim 5 \times 10^8$  cm<sup>-2</sup>. With a small template area,  $T_{\text{sub}}$  was uniform across the template. Regrowth on these templates began with 200 nm GaN:C, having C doping provided by CBr<sub>4</sub>. The C concentration was determined to be  $\sim 2 \times 10^{19}$  cm<sup>-3</sup> by SIMS. The GaN:C layers and subsequent layers before the growth interruption (GI) were grown in the Ga-rich regime at a  $T_{\text{sub}}$  of 720 °C with plasma conditions of 300 W and 1.0 SCCM N<sub>2</sub> flow. These conditions corresponded to an N-limited GaN growth rate of  $\sim 6$  nm/min. With an active N beam equivalent pressure (BEP) of  $1.7 \times 10^{-7}$  Torr (based on metal-rich growth rates), the Ga/N flux ratio ( $F_{\text{Ga}}/F_{\text{N}}$ ) was  $\geq 2$ . A streaky RHEED pattern indicated the

step-flow growth mode for the layers before the GI. Ga-rich growth was modulated as previously described.

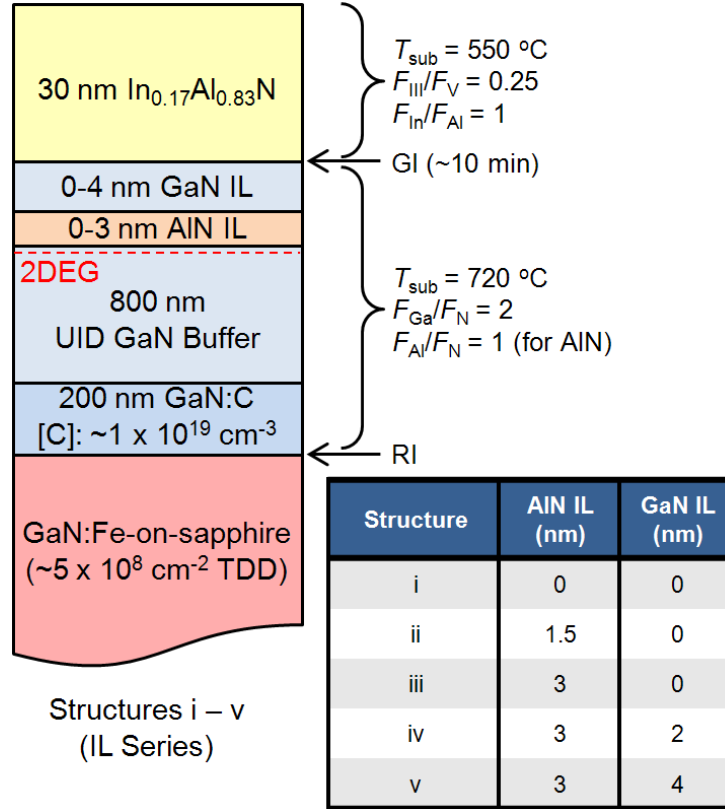


**Figure 8.1: Layer schematics for Structures i-v (IL Series), in which a range of AlN/GaN IL thicknesses were included. Positions of the regrowth interface (RI) and growth interruption (GI) are noted.**

The IL Series included a structure with no ILs (Structure i), structures with only AlN ILs (Structure ii and Structure iii), and structures with AlN and GaN ILs (Structure iv and Structure v). Structure ii and Structure iii had AlN IL thicknesses of 1.5 nm and 3 nm, respectively. Structure iv and Structure v had AlN/GaN IL thicknesses of 3/2 nm and 3/4 nm, respectively. Since Al is preferentially incorporated into the crystal during Ga-rich growth, the Ga shutter remained open during deposition of the AlN ILs ( $F_{Al}/F_N = 1$ ). The growth conditions for the GaN ILs were the same as those for the UID GaN

buffer layers. Prior to the deposition of the  $\text{In}_{0.17}\text{Al}_{0.83}\text{N}$  barrier, growth was interrupted, and the Ga bilayer was thermally desorbed. The substrate temperature was then lowered to 550 °C. During the GI, the N shutter was closed, and the RF plasma was tuned for 350 W with 1.5 SCCM  $\text{N}_2$  flow. The GI lasted approximately 10 min.

From a previous study of metal-polar  $\text{In}_{0.17}\text{Al}_{0.83}\text{N}/\text{GaN}$  structures grown by MOCVD with a range of  $\text{In}_{0.17}\text{Al}_{0.83}\text{N}$  thicknesses, it was shown that the 2DEG sheet density is essentially constant with an  $\text{In}_{0.17}\text{Al}_{0.83}\text{N}$  thickness greater than 20 nm [99]. Since the goal of the IL Series was to isolate the impact of the AlN and GaN ILs on 2DEG characteristics, 30 nm  $\text{In}_{0.17}\text{Al}_{0.83}\text{N}$  barriers were included. Although the large  $t_b$  of the IL Series made the structures unsuitable for HEMT fabrication, slight variations in the  $\text{In}_{0.17}\text{Al}_{0.83}\text{N}$  thickness had little effect on the 2DEG sheet density. The 30 nm  $\text{In}_{0.17}\text{Al}_{0.83}\text{N}$  barriers were grown in the N-rich regime with plasma conditions of 350 W and 1.5 SCCM  $\text{N}_2$  flow, corresponding to an active N BEP of  $2.4 \times 10^{-7}$  Torr. The group III-limited growth ( $F_{\text{III}}/F_{\text{V}} = 0.25$ ,  $F_{\text{In}}/F_{\text{Al}} = 1$ ) rate of the  $\text{In}_{0.17}\text{Al}_{0.83}\text{N}$  barriers was 1.2 nm/min. Throughout the growth of the  $\text{In}_{0.17}\text{Al}_{0.83}\text{N}$  barrier, the RHEED pattern remained streaky, indicating the step-flow growth mode.

Along with Structures i-v, metal-polar  $\text{GaN}/\text{In}_{0.17}\text{Al}_{0.83}\text{N}/\text{GaN}$  and  $\text{GaN}/\text{In}_{0.17}\text{Al}_{0.83}\text{N}/\text{GaN}(2 \text{ nm})/\text{AlN}(3 \text{ nm})/\text{GaN}$  samples were grown on 1-  $\text{cm}^2$  Lumilog GaN:Fe-on-sapphire templates for interfacial and structural analysis by APT. Thick (~200 nm) GaN capping layers were included in these samples to facilitate the APT experiments.

## 8.2.2 Growth of In<sub>0.17</sub>Al<sub>0.83</sub>N/GaN/AlN/GaN HEMT Structure on FS GaN

Structure vi, a metal-polar In<sub>0.17</sub>Al<sub>0.83</sub>N/GaN(2 nm)/AlN(3 nm)/GaN HEMT structure (Fig. 8.2(a)), was regrown under similar conditions to the IL Series on a quarter 2" low-TDD semi-insulating GaN template. The low-TDD template consisted of 5 μm GaN:Fe grown by MOCVD on n-type Lumilog FS GaN, which had a specified TDD of ~5 x 10<sup>7</sup> cm<sup>-2</sup>. To accommodate the fabrication of HEMTs on this structure, the thickness of the GaN:C layer was increased to 600 nm, and the thickness of the UID GaN buffer was reduced to 200 nm.

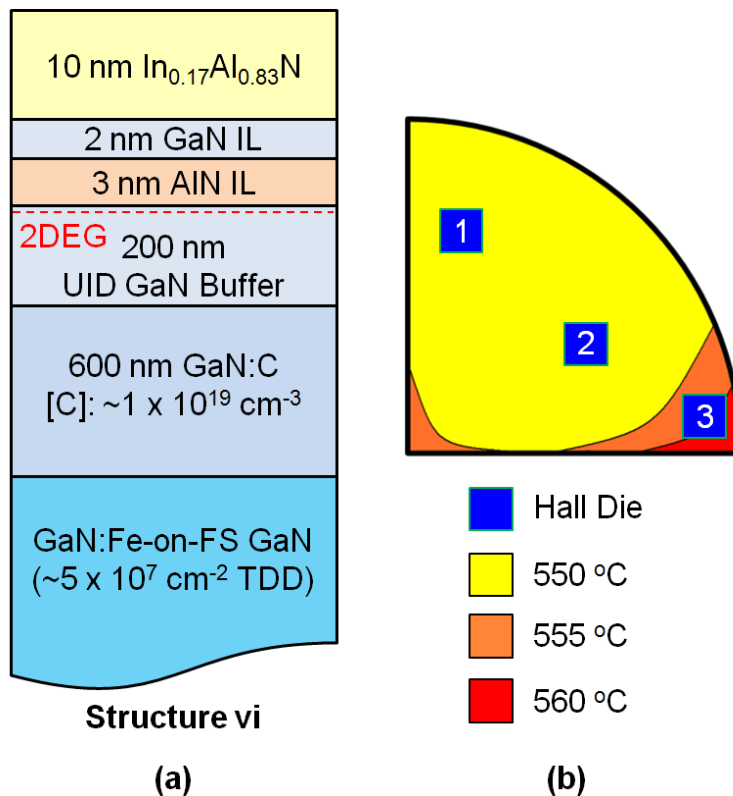


**Figure 8.2:** (a) Layer schematic for an In<sub>0.17</sub>Al<sub>0.83</sub>N/GaN/AlN/GaN HEMT structure grown by PAMBE. (b) Areal variation of growth temperature measured by optical pyrometer during the deposition of the In<sub>0.17</sub>Al<sub>0.83</sub>N barrier. The placement of the three Hall dies is also shown.



With a TDD of  $\sim 5 \times 10^7 \text{ cm}^{-2}$  (assuming the TDD of the grown layers mirrors that of the template), the background donor concentration is not fully compensated by dislocation-associated electron traps [41], and the UID GaN buffer conductivity is non-negligible. The UID GaN buffer thickness was reduced to 200 nm to minimize parasitic buffer conduction during HEMT operation [58,60]. Additionally, the thickness of the  $\text{In}_{0.17}\text{Al}_{0.83}\text{N}$  barrier was reduced to 10 nm. With a total  $t_b$  ( $t_{\text{InAlN}} + t_{\text{GaN IL}} + t_{\text{AlN IL}}$ ) of 15 nm, the channel of Structure vi could be effectively modulated by a sub- $\mu\text{m}$  gate. Since Structure vi was regrown on a quarter 2" template, there was noticeable variation in  $T_{\text{sub}}$  across the template. The areal variation of  $T_{\text{sub}}$ , identified by an optical pyrometer during the deposition of the  $\text{In}_{0.17}\text{Al}_{0.83}\text{N}$  barrier of Structure vi, is shown in Fig. 2(b). The majority of the surface had the intended  $T_{\text{sub}}$  of 550 °C.

## 8.3 Results and Discussion

### 8.3.1 Structural Properties of Interlayer Series

Symmetric HRXRD  $\omega$ - $2\theta$  scans (Fig. 8.3), directed at the center of each IL Series structure, were matched to dynamical simulations from Rigaku Globalfit software to determine the layer thicknesses and the InN mole fractions of the InAlN barriers. Rigaku Globalfit assumes the applicability of Vegard's law. Although a slight deviation from Vegard's law has been identified for InAlN alloys through comparisons between HRXRD and Rutherford backscattering data, bowing parameters for InAlN lattice constants have yet to be established [99,105].

As reported in Table 8.1, the thicknesses of the AlN and GaN ILs, determined through Rigaku Globalfit simulations, were essentially the intended thicknesses. The InN mole fractions and thicknesses of the InAlN barriers, also determined through Rigaku Globalfit simulations, were close to 0.17 and 30 nm, respectively, for all structures in the IL Series. The FWHMs of HRXRD  $\omega$  rocking curves for the GaN (0002) and GaN (20 $\bar{2}$ 1) reflections were consistent for the IL Series and indicative of structures with TDDs of  $\sim 5 \times 10^8 \text{ cm}^{-2}$ , which was the specified TDD of the GaN-on-sapphire template.

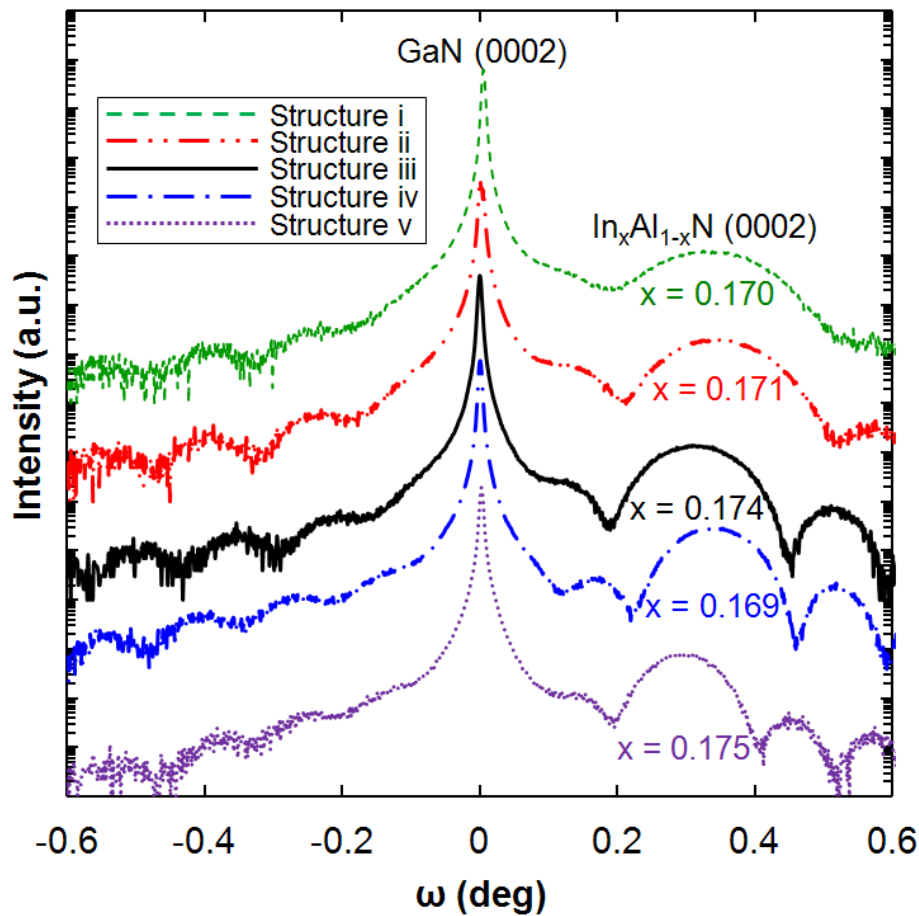


**Figure 8.3: Symmetric HRXRD  $\omega$ - $2\theta$  scans around the GaN (0002) reflection for the IL Series, including the compositions of the InAlN barriers.**

**Table 8.1: Relevant structural parameters of the IL Series determined through HRXRD  $\omega$ -2 $\theta$  scans, including the In mole fraction ( $x$ ) and thickness ( $t$ ) of the  $\text{In}_x\text{Al}_{1-x}\text{N}$  barrier and the thicknesses of the GaN/AlN ILs. FWHMs ( $\Delta\omega$ ) of rocking curve  $\omega$  scans for the GaN (0002) and GaN (20 $\bar{2}$ 1) reflections are also presented.**

Structure	$\text{In}_x\text{Al}_{1-x}\text{N}$ Barrier				GaN (0002)	GaN (20 $\bar{2}$ 1)
	$x$	$t$ (nm)	GaN IL (nm)	AlN IL (nm)	$\Delta\omega$ (arcsec)	$\Delta\omega$ (arcsec)
i	0.170	32	0	0	355	421
ii	0.171	31	0	~1.5	357	398
iii	0.174	33	0	~3	371	397
iv	0.169	32	~2	~3	348	418
v	0.175	32	~4	~3	359	397

### 8.3.2 In-plane Compositional Homogeneity of InAlN

An HAADF-STEM image taken in the [0001] zone axis projection of the  $\text{In}_{0.175}\text{Al}_{0.825}\text{N}$  barrier in Structure v is presented in Fig. 8.4.

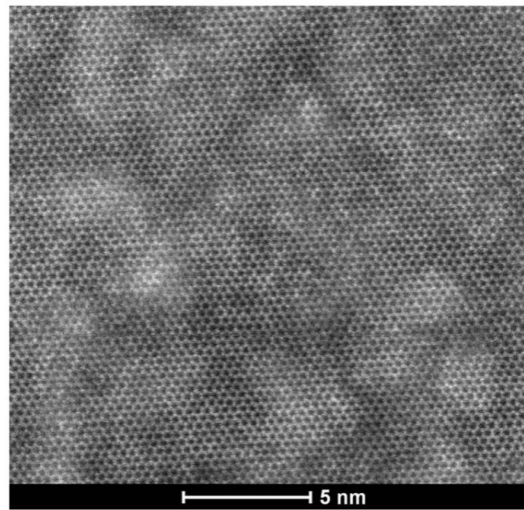


**Figure 8.4: Plan-view HAADF-STEM image taken in the [0001] zone axis projection of a metal-polar  $\text{In}_{0.175}\text{Al}_{0.825}\text{N}$  layer grown with  $F_{\text{III}}/F_{\text{V}} = 0.25$ ,  $F_{\text{In}}/F_{\text{Al}} = 1$ , and  $T_{\text{sub}} = 550$  °C. HAADF-STEM was performed by Feng Wu.**

Since HAADF-STEM image intensity depends on the atomic number of the elements present, lighter contrast (higher intensity) indicates a higher InN mole fraction. As there was no discernible pattern of lighter regions, the InAlN barrier appeared to be compositionally homogeneous. All InAlN barriers were grown under roughly the same conditions, so it can be assumed that each structure had a homogeneous InAlN barrier.

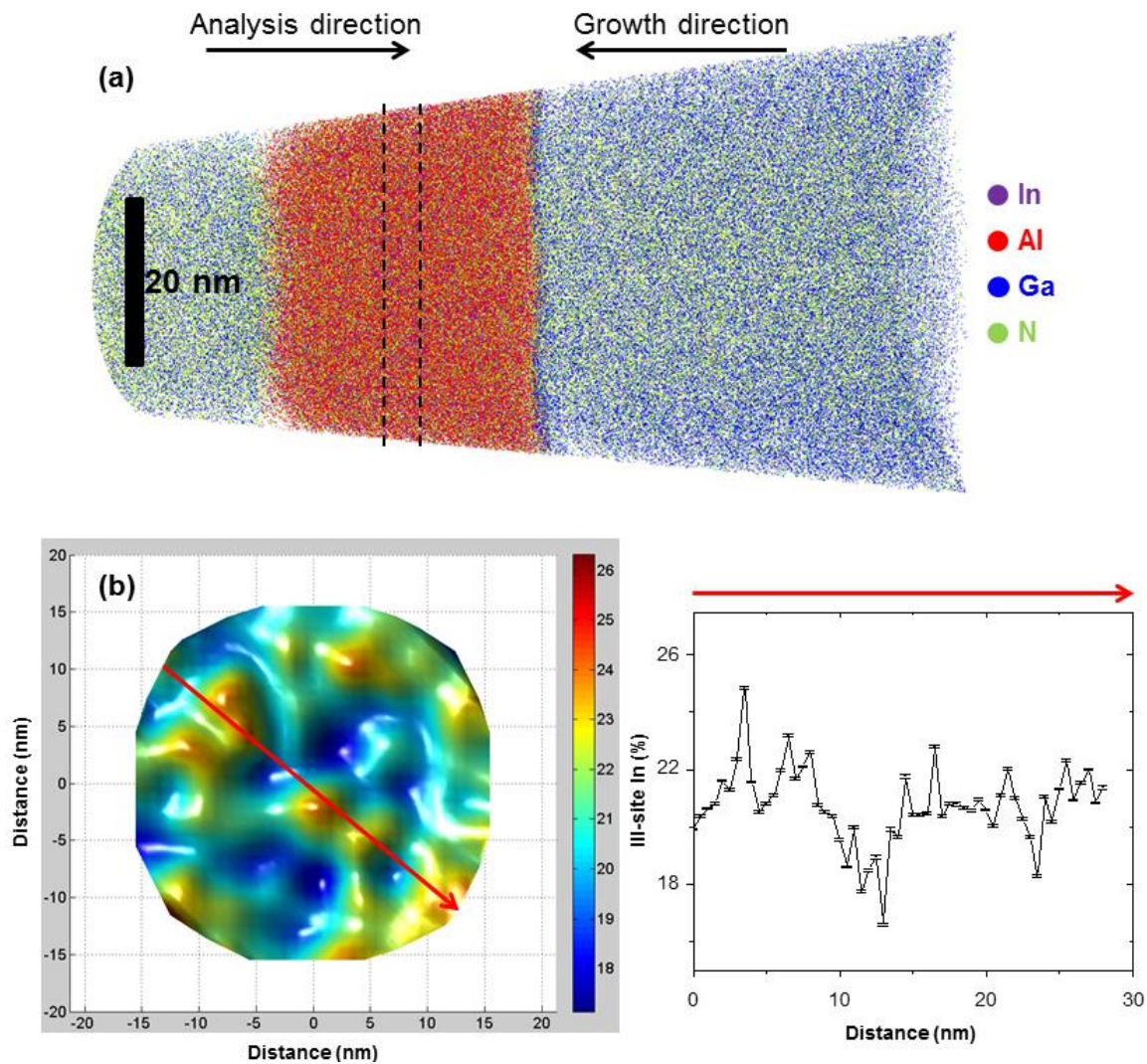


**Figure 8.5:** (a) 3D APT reconstruction of a metal-polar GaN/In<sub>0.171</sub>Al<sub>0.829</sub>N/GaN specimen. (b) APT map of the III-site In concentration in the *c*-plane (averaged over a thickness of 5 nm) of a metal-polar In<sub>0.171</sub>Al<sub>0.829</sub>N barrier grown with  $F_{\text{III}}/F_{\text{V}} = 0.25$ ,  $F_{\text{In}}/F_{\text{Al}} = 1$ , and  $T_{\text{sub}} = 550$  °C. APT performed by Baishakhi Mazumder.

From the 3D APT reconstruction of a metal-polar GaN/In<sub>0.171</sub>Al<sub>0.829</sub>N/GaN specimen (Fig. 8.5(a)), the In distribution in the In<sub>0.171</sub>Al<sub>0.829</sub>N appeared to be random. The In III-site distribution in the *c*-plane (perpendicular to the growth direction) for the In<sub>0.171</sub>Al<sub>0.829</sub>N barrier was quantified (Fig. 8.5(b)). Averaging over a thickness of 5 nm, the InN mole fraction within a 30- nm- wide disc did not drop below 0.17 and did not exceed 0.26. The integrated InN mole fraction of the APT disc was 0.2; thus, HRXRD underestimated the InN mole fraction. This may point to shortcomings in the HRXRD simulation, since perfect uniformity of the InAlN was assumed, and bowing parameters for lattice constants (i.e., deviation from Vegard's law) are unknown. Regardless, HRXRD was the only practical method for determining the In content of the InAlN barrier, and all compositions stated in this study were determined through HRXRD, assuming Vegard's law for the InAlN lattice constants.

Growth of InAlN by PAMBE is generally performed in the In-rich regime to ensure step-flow growth. Though the presence of an In adlayer enhances the surface diffusion of the group-III adatoms, the In adlayer and droplets tend to solidify, leaving clusters on the surface that cannot be removed with HCl [104,106]. Additionally, lateral compositional inhomogeneity has been identified in InAlN layers grown In-rich [103]. This inhomogeneity manifests itself as a “honeycomb” of AlN-rich domains (5-10 nm wide) with InN-rich peripheries and is most likely the result of kinetic constraints [103]. Under In-rich conditions, the growth rate is N-limited, and the lowest active N BEP that can be maintained with a stable RF plasma is  $\sim 10^7$  Torr. As such, relatively high metal-rich growth rates ( $> 2$  nm/min), combined with poor Al adatom mobility at low growth

temperatures (500-600 °C), yield faceted AlN-rich platelets upon InAlN growth initiation [102]. These kinetic limitations are partially alleviated by N-rich growth since lower growth rates, allowing more time for adatom diffusion, can be achieved with a low group-III BEP. N-rich growth, however, further reduces the Al adatom diffusivity.

From the work of Choi *et al.* [104], the same “honeycomb” microstructure was seen when metal-polar InAlN was grown N-rich ( $F_{\text{III}}/F_{\text{V}} = 0.3$ ) at a very low growth rate ( $\sim 1$  nm/min) with a  $F_{\text{In}}/F_{\text{Al}}$  of 0.19. With this low  $F_{\text{In}}/F_{\text{Al}}$ , most of the impinging In flux had to be incorporated to yield a lattice-matched alloy, so a  $T_{\text{sub}}$  of 480 °C was employed. In the study presented here, we eliminated the “honeycomb” microstructure by enhancing the Al adatom mobility through increases in  $F_{\text{In}}/F_{\text{Al}}$  (1) and  $T_{\text{s}}$  (550 °C), while maintaining a low growth rate (1.2 nm/min) in the N-rich regime. To the best of our knowledge, this is the first demonstration of compositional homogeneity in metal-polar InAlN grown by PAMBE. Similar growth parameters were employed by Schmult *et al.* [107], but in-depth microstructure analyses were not presented.

### 8.3.3 Verification of Interlayer Thickness and Purity

To confirm the IL thicknesses determined by HRXRD simulations and examine the interfacial quality of the IL series, cross-sectional HAADF-STEM was performed on Structure v (Fig. 8.6). The interfaces were highly abrupt, and the thicknesses of the AlN and GaN ILs were approximately 3 and 4 nm, respectively, which agreed with the HRXRD simulations. These were the intended IL thicknesses, so the N-limited growth rate and  $F_{\text{Al}}/F_{\text{N}}$  were effectively calibrated.

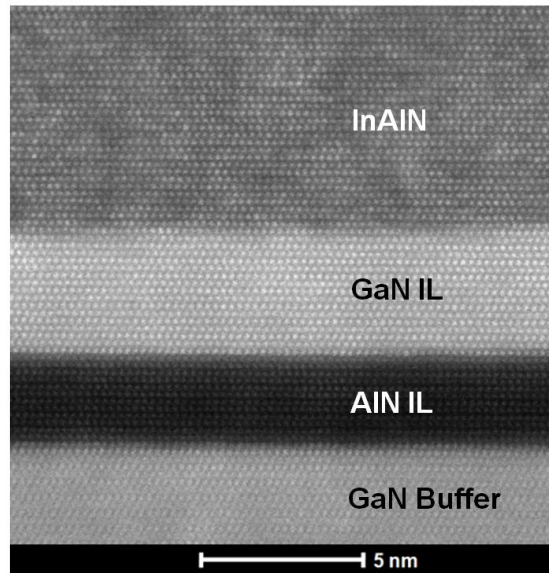


**Figure 8.6:** Cross-sectional HAADF-STEM image taken in the  $[11\bar{2}0]$  zone axis projection of a metal-polar  $\text{In}_{0.175}\text{Al}_{0.825}\text{N}/\text{GaN}(4\text{ nm})/\text{AlN}(3\text{ nm})/\text{GaN}$  structure (Structure v). HAADF-STEM was performed by Feng Wu.

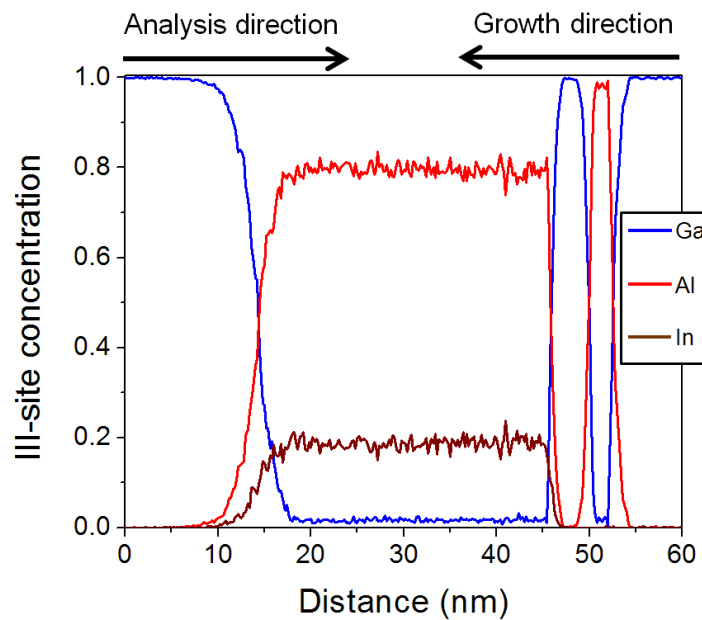


**Figure 8.7:** 1D APT III-site concentration profile of a  $\text{GaN}/\text{In}_{0.168}\text{Al}_{0.832}\text{N}/\text{GaN}(4\text{ nm})/\text{AlN}(3\text{ nm})/\text{GaN}$  structure (similar to Structure v), displaying abrupt interfaces near the channel and pure AlN/GaN ILs. APT was performed by Baishakhi Mazumder.

Quantification of the purity of the AlN/GaN ILs was determined through APT of a GaN/In<sub>0.168</sub>Al<sub>0.832</sub>N/GaN(4 nm)/AlN(3 nm)/GaN specimen, similar to Structure v (Fig. 8.7). The AlN/GaN ILs were effectually pure, and the interfaces near the channel were abrupt. The top GaN/In<sub>0.168</sub>Al<sub>0.832</sub>N interface was very diffuse, however, with compositional grading over thickness of ~5 nm.

An important advantage of PAMBE over MOCVD in the epitaxy of HEMT structures is the superior quality of the ILs [108]. Although pure ILs with abrupt interfaces were shown with the metal-polar GaN/In<sub>0.168</sub>Al<sub>0.832</sub>N/GaN(4 nm)/AlN(3 nm)/GaN APT specimen, the net negative polarization interface of the InAlN barrier was diffuse. This could be a consequence of decomposition of the InAlN layer as the substrate was heated to 720 °C, even though a thin GaN layer was deposited at low temperature to prevent decomposition of the underlying layers. This diffuseness could also be symptomatic of the reconstruction that takes place at the negative polarization interface of nitride barriers when a thick GaN cap is deposited. In a previous study, chemically diffuse net-negative-polarization interfaces of GaN/AlGaIn/GaN heterostructures were identified with APT [109]. Theoretically, the charge at these interfaces should be balanced by a significant hole concentration or a two-dimensional hole gas (2DHG). But, without a sufficient source of holes, atomic rearrangements may also result [110]. The mechanism for these rearrangements requires further investigation. It is unlikely that the grading of the upper GaN/InAlN interface was caused by roughness since the parameters applied yielded step-flow growth and very smooth surface morphology (shown in the next section).



The background impurity concentrations in GaN/In<sub>0.171</sub>Al<sub>0.829</sub>N/GaN and GaN/In<sub>0.168</sub>Al<sub>0.832</sub>N/GaN(4 nm)/AlN(3 nm)/GaN specimens were analyzed with APT. GIs are generally avoided during device epitaxy because they often result in a higher background impurity concentration at the GI interface. Since the GI included a large drop in substrate temperature, maintaining the liquid Ga bilayer as a protective coating [61] was not possible. The sticking coefficient of Ga below 600 °C is too high for a thermal desorption period of reasonable length. As such, the growth surface was “dry” during the GI for better control of the structure. If liquid Ga was present on the surface upon the initialization of InAlN barrier growth, a poor-quality GaN layer of indeterminate thickness would be grown. Surprisingly, the monolayer of material that comprised the exposed surface during the GI did not contain impurity (Si, O, and C) concentrations above 10<sup>18</sup> cm<sup>-3</sup>. The overall impurity concentration of the layers of interest was in the low 10<sup>17</sup> cm<sup>-3</sup> range, which is the detection limit of APT.

### **8.3.4 Surface Morphologies of Interlayer Series**

The surface morphologies of the IL Series, determined by AFM (Fig. 8.8), displayed the step-terrace structure, which is associated with step-flow growth. The surface morphologies of each structure in the IL Series were very similar, but the step density and rms roughness of Structure ii (0.575 nm) and Structure iii (0.627 nm) were slightly higher than those of the other structures. Structure iv had an rms roughness of 0.362 nm, which was the lowest of the IL Series.

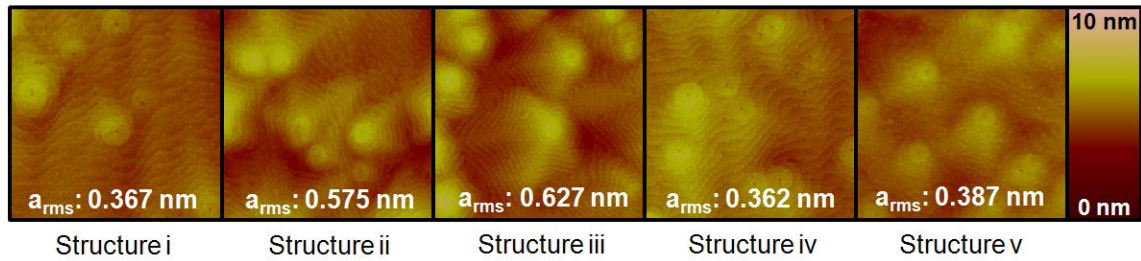


**Figure 8.8:  $2 \times 2 \mu\text{m}^2$  AFM micrographs of the InAlN surfaces in the IL series, including rms roughness ( $a_{\text{rms}}$ ) values.**

The surfaces of the IL Series were dominated by dislocation-mediated features – spiral hillocks and surface depressions. From previous studies, it can be assumed that spiral hillocks formed during the growth of the GaN buffer layer [40], and the surface depressions formed under the low driving force conditions of InAlN barrier growth. When the growth of the InAlN barrier was initiated on an AlN layer (Structure ii and Structure iii), the step density and rms roughness were slightly higher. Higher step density is connected to higher step-line curvature, which has been correlated to a higher driving force [40]. The growth rates of the InAlN barriers were very similar for all structures in the IL Series so the origin of the increased step density with only an AlN IL is unclear.

### 8.3.5 Temperature-dependent Mobility of Interlayer Series

The 2DEG sheet densities, mobilities, and sheet resistances of the IL Series, determined through Hall measurements at RT and 77 K, are reported in Table 8.2. The 2DEG characteristics from the Hall patterns that yielded the lowest RT sheet resistances are presented. Whereas there was little deviation in the 2DEG characteristics from different Hall patterns across Structures ii-v, there was significant deviation across

Structure i. Several Hall patterns on Structure i yielded RT sheet densities below  $1 \times 10^{12} \text{ cm}^{-2}$ .

**Table 8.2: Hall measurements performed at RT and 77 K on the IL Series, including the 2DEG sheet density ( $n_s$ ), mobility ( $\mu$ ), and sheet resistance ( $R_{sh}$ ).**

Structure	RT			77 K		
	$n_s$ ( $10^{13} \text{ cm}^{-2}$ )	$\mu$ ( $\text{cm}^2/\text{Vs}$ )	$R_{sh}$ ( $\Omega/\square$ )	$n_s$ ( $10^{13} \text{ cm}^{-2}$ )	$\mu$ ( $\text{cm}^2/\text{Vs}$ )	$R_{sh}$ ( $\Omega/\square$ )
i	0.3090	394	5321	0.3163	374	5476
ii	1.358	822	559	1.372	1437	316
iii	1.308	1975	241	1.350	8376	55
iv	2.274	1684	163	2.298	5885	46
v	2.029	1693	181	2.081	5592	53

Considering the trade-off between sheet density and mobility, the low RT sheet density of Structure i was expected to correlate to a high mobility. However, Structure i yielded the lowest RT mobility ( $394 \text{ cm}^2/\text{Vs}$ ) of the IL Series. The RT mobility of Structure ii was also rather low at  $822 \text{ cm}^2/\text{Vs}$ . The highest RT mobility ( $1975 \text{ cm}^2/\text{Vs}$ ) in the IL Series was measured on Structure iii. Although the RT mobility of Structure iv ( $1684 \text{ cm}^2/\text{Vs}$ ) was lower than that of Structure iii, Structure iv yielded the lowest RT sheet resistance ( $163 \Omega/\square$ ) in the IL Series because of its large sheet density. Thus, the AlN/GaN IL thicknesses of  $3/2 \text{ nm}$  included in Structure iv were determined to be the optimal IL thicknesses. Structure v, which had AlN/GaN IL thicknesses of  $3/4 \text{ nm}$ , yielded a sheet density and mobility slightly lower than those of Structure iv, resulting in a RT sheet resistance of  $181 \Omega/\square$ .

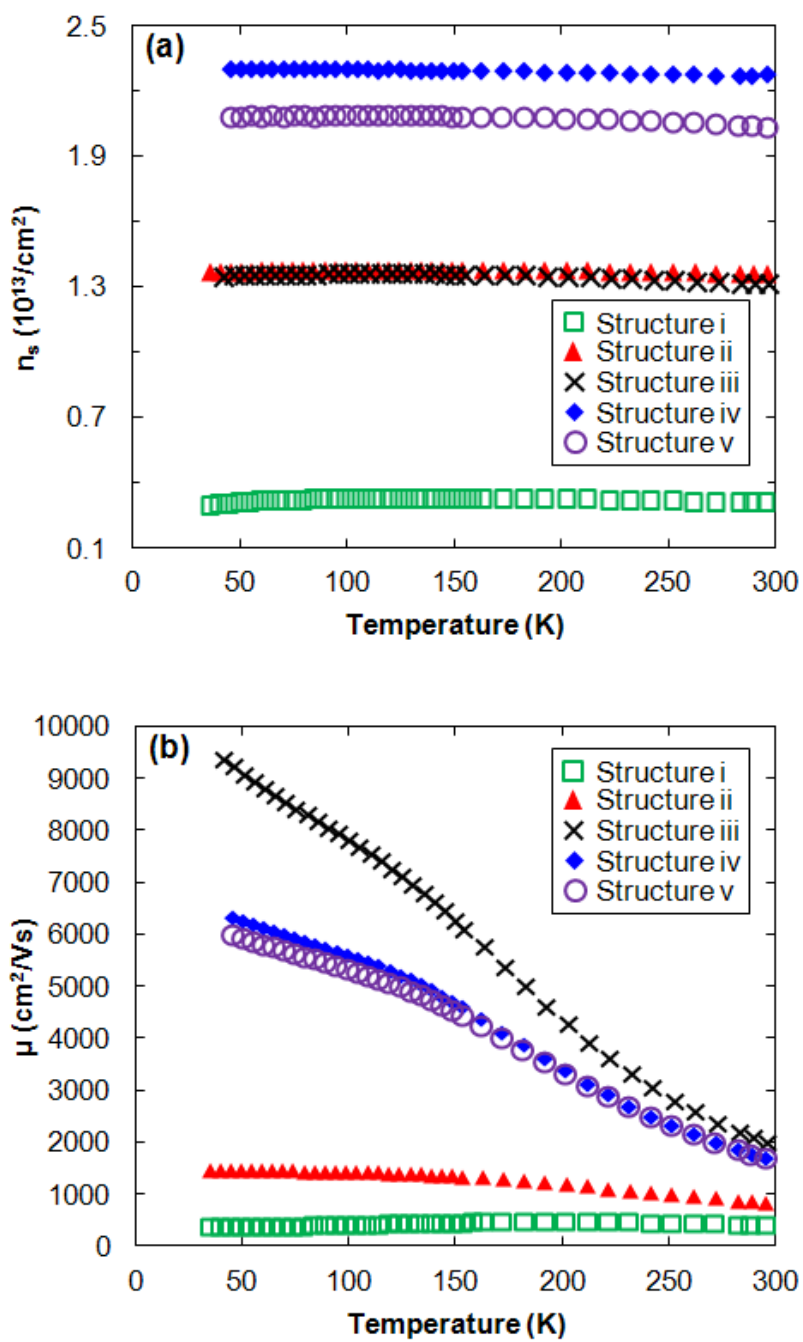


**Figure 8.9: Hall measurements showing (a) sheet density ( $n_s$ ) with respect to temperature and (b) mobility ( $\mu$ ) with respect to temperature for the IL series.**

The increase in mobility shown in Table 8.2 for Structures ii-v at 77 K can be largely attributed to a decrease in OP scattering. To further understand the scattering

mechanisms limiting the 2DEG mobility of the IL Series, temperature-dependent Hall measurements (Fig. 8.9) were performed. 2DEGs are highly degenerate, and their sheet densities show little temperature-dependence. As shown in Fig. 8.9(a), the sheet densities of Structures i-v were constant as temperature decreased. The mobility of Structure i was also constant with temperature, and the mobility of Structure ii increased only slightly as temperature decreased. The mobilities of Structures iii-v, on the other hand, increased dramatically as temperature was reduced.

The 2DEG characteristics of the structures in the IL Series were surprisingly different. The differences in sheet density will be discussed first, followed by the differences in mobility.

The sheet density of Structure i was exceptionally low. Through a band simulation of Structure i with a 1D self-consistent Schrödinger-Poisson solver [89] (Fig. 8.10(a)), a sheet density of  $2.4 \times 10^{13} \text{ cm}^{-2}$  was predicted with a surface barrier height of 3 eV [111]. The measured RT sheet density ( $3.09 \times 10^{12} \text{ cm}^{-2}$ ) of Structure i was almost an order of magnitude lower than what was predicted. There are currently no other reports of Hall characteristics for metal-polar InAlN/GaN structures grown by PAMBE. Katzer *et al.* [101] grew a metal-polar  $\text{In}_{0.175}\text{Al}_{0.825}\text{N}$  barrier by In-rich PAMBE on GaN after a GI, and the sheet resistance was too high to be measured through contactless resistivity methods. This may have been a consequence of barrier inhomogeneity, though, so it is difficult to compare the results of Katzer *et al.* to those presented in this study. However, it should be noted that with an N-polar GaN/ $\text{In}_{0.18}\text{Al}_{0.82}\text{N}$  structure grown by In-rich PAMBE, which was also plagued by barrier inhomogeneity, Dasgupta *et al.* [112]

achieved a RT sheet density of  $2.1 \times 10^{13} \text{ cm}^{-2}$ . But, in the case of N-polar GaN/InAlN structures, the 2DEG is formed at low-temperature before the substrate is heated to complete the rest of the GaN channel.

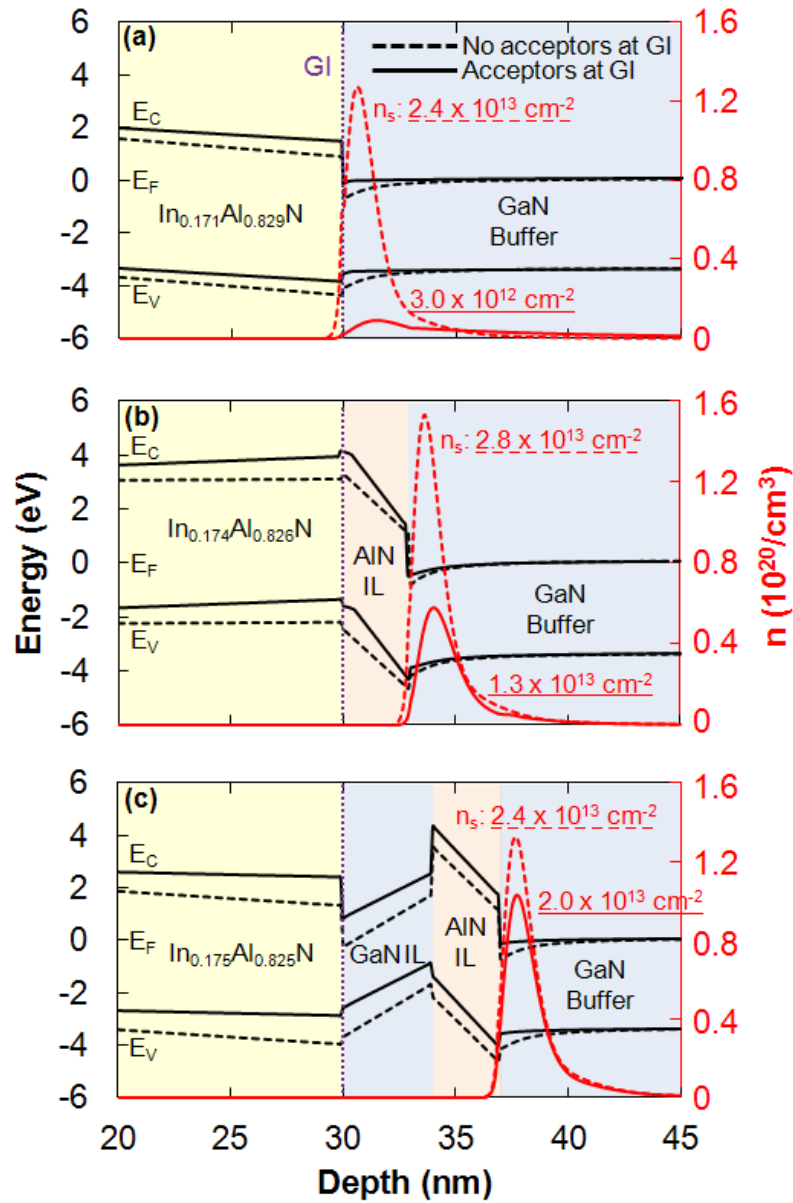


**Figure 8.10:** Band diagrams, including the sheet density ( $n_s$ ) values with and without acceptors in the monolayer exposed during the GI, for (a) Structure i, (b) Structure iii, and (c) Structure v.

Through the work of Gonshorek *et al.* [113], MOCVD produced a metal-polar  $\text{In}_{0.185}\text{Al}_{0.815}\text{N}/\text{GaN}$  structure with a RT sheet density of  $2.49 \times 10^{13} \text{ cm}^{-2}$ . Much like PAMBE, MOCVD requires a GI between the deposition of the GaN buffer and InAlN barrier for substrate cooling, so system conditions (ultrahigh vacuum, etc.) may be an important factor in the poor sheet density realized with PAMBE. The end point of the drop in  $T_{\text{sub}}$  may also be crucial to defect formation at the GI interface. During the GI, a drop in  $T_{\text{sub}}$  from  $\sim 1000 \text{ }^\circ\text{C}$  to  $\sim 850 \text{ }^\circ\text{C}$  has been used in many MOCVD studies [114], whereas in this study, the  $T_{\text{sub}}$  was lowered from  $720 \text{ }^\circ\text{C}$  to  $550 \text{ }^\circ\text{C}$ . We speculate that the conditions of the GI allowed a high density of acceptors to form at the GI interface of Structure i. To attain the measured sheet density of Structure i with the Schrödinger-Poisson solver (Fig. 8.10(a)), an acceptor concentration of  $5 \times 10^{20} \text{ cm}^{-3}$  was included in the monolayer of GaN that was exposed during the GI. Since an increased impurity concentration at the GI was not identified by APT, it is likely that these acceptor states are correlated to intrinsic defects – possibly Ga vacancies.

The majority of reports concerning metal-polar heterostructures with InAlN barriers include an AlN IL. The AlN IL is necessary to “protect” the GaN channel during the GI, as well as improve the sheet density. Inclusion of an AlN IL increases the polarization discontinuity between the barrier and the channel. Structure ii and Structure iii, which had only AlN ILs, displayed a marked improvement in sheet density over Structure i, though a much higher sheet density was predicted by the Schrödinger-Poisson solver. For the calculated sheet density ( $2.8 \times 10^{13} \text{ cm}^{-2}$ ) of Structure iii to equal that which was measured ( $1.30 \times 10^{13} \text{ cm}^{-2}$ ), an acceptor concentration of  $4 \times 10^{20} \text{ cm}^{-3}$  was

included in the monolayer of AlN that was grown before the GI (Fig. 8.10(b)). Though an increase in the AlN IL thickness from 1.5 to 3 nm should entail an increase in sheet density, the sheet densities of Structure ii and Structure iii were roughly the same.

The RT sheet densities measured on Structure ii and Structure iii were substantially less than those from a similar structure in the literature that was grown by PAMBE. K. Jeganathan *et al.* [115] demonstrated a RT sheet density of  $2.68 \times 10^{13} \text{ cm}^{-2}$  in a metal-polar  $\text{In}_{0.17}\text{Al}_{0.83}\text{N}/\text{AlN}(1 \text{ nm})/\text{GaN}$  structure with N-rich AlN and In-rich InAlN. The growth conditions of the AlN IL may be the source of the discrepancy in sheet density. The AlN ILs in this study were grown Ga-rich to improve adatom diffusion and realize high-quality AlN ILs with thicknesses beyond 1 nm.

The addition of a GaN IL (Structure iv and Structure v) unexpectedly enhanced the sheet density. With the inclusion of a GaN IL, the polarization discontinuity between the barrier and channel should be lowered as long as a high acceptor concentration is present at the GI interface. The surfaces exposed during the GI of Structure iv and Structure v were chemically identical to the surface exposed during the GI of Structure i, yet the RT sheet densities of Structure iv and Structure v were greater than  $2 \times 10^{13} \text{ cm}^{-2}$ . The GI of Structure i occurred at a neutral interface, whereas the GI of Structure ii and Structure iii occurred at a positive polarization interface. This may have influenced the formation of acceptors. The RT sheet density of Structure v ( $2.029 \times 10^{13} \text{ cm}^{-2}$ ) was similar to that predicted by the Schrödinger-Poisson solver ( $2.4 \times 10^{13} \text{ cm}^{-2}$ ), but an acceptor concentration of  $1 \times 10^{20} \text{ cm}^{-3}$  was included in the monolayer of GaN before the GI to make the values match (Fig. 8.10(c)). The larger sheet density of Structure iv



( $2.274 \times 10^{13} \text{ cm}^{-2}$ ), compared to that of Structure v ( $2.029 \times 10^{13} \text{ cm}^{-2}$ ), can be attributed to an increase in the polarization discontinuity between the barrier and channel with a thinner GaN IL.

The impact of dislocation scattering on the 2DEG mobility was invariant between structures in the IL Series. PE and DP scattering were virtually invariant between Structures i-v, as well. AD scattering was only considered for Structure i since the calculated 2DEG wavefunctions of Structures ii-v were blocked from the InAlN barriers by pure AlN interlayers. Yet, AD scattering cannot possibly explain the low 2DEG mobility of Structure i at RT and low-T. According to Schrödinger-Poisson simulations, less than 1% of the 2DEG resides in the InAlN barrier of Structure i. It is more likely that the 2DEG mobility of Structure i was limited by Coulombic scattering from charged defects at the GI interface. Since the sheet density of Structure i was extremely low, screening of charged defects was severely inhibited. Similar charged defects appeared to suppress the mobility of Structure ii since the GI interface was only 1.5 nm away from the 2DEG. When the AlN IL thickness and distance from the channel to the GI interface was increased to 3 nm (Structure iii), the 2DEG mobility increased dramatically at RT and low-T. Increasing the distance between the 2DEG and the alloy barrier would also aid the screening of potential fluctuations from the alloy, which could reduce alloy-related IR scattering.

By including GaN ILs (Structures iv and Structure v), the separation between the 2DEG and the InAlN alloy was further increased, and the sheet density increased greatly. This improved both the screening of charged defects and, presumably, the random alloy

potential. However, the RT and low-T mobility of Structure iv and Structure v were lower than that of Structure iii. This decrease in mobility was possibly the result of increased IR scattering since the centroid of the 2DEG wavefunction is closer to the AlN/GaN interface with higher sheet density. Regardless, the increase in sheet density by including a GaN IL outweighed the decrease in mobility toward the end of achieving a low sheet resistance.

### **8.3.6 Structural Properties of InAlN/GaN/AlN/GaN HEMT on FS GaN**

Symmetric HRXRD  $\omega$ - $2\theta$  scans, directed at the areas where Hall dies were fabricated on the InAlN/GaN/AlN/GaN heterostructure on FS GaN (Structure vi), are shown in Fig. 8.11. As determined through Rigaku Globalfit simulations, the InAlN barrier on which Hall Die 3 was fabricated had a lower InN mole fraction (0.145) than the barriers on which Hall Die 1 and Hall 2 were fabricated (0.169). Since the sticking coefficient of the In adatoms is exponentially reduced with an increase in temperature, the InAlN barrier grown at 555-560 °C (Fig. 8.2(b)) had lower In content. For the three areas scanned on Structure vi, AlN/GaN IL thicknesses of ~2/~3 nm and InAlN barrier thicknesses of 11 nm were determined (Table 8.3). The FWHMs of HRXRD  $\omega$  rocking curves for the GaN (0002) and GaN (20 $\bar{2}$ 1) reflections of Structure vi agree with those previously measured for heterostructures with TDDs of  $\sim 5 \times 10^7 \text{ cm}^{-2}$ .

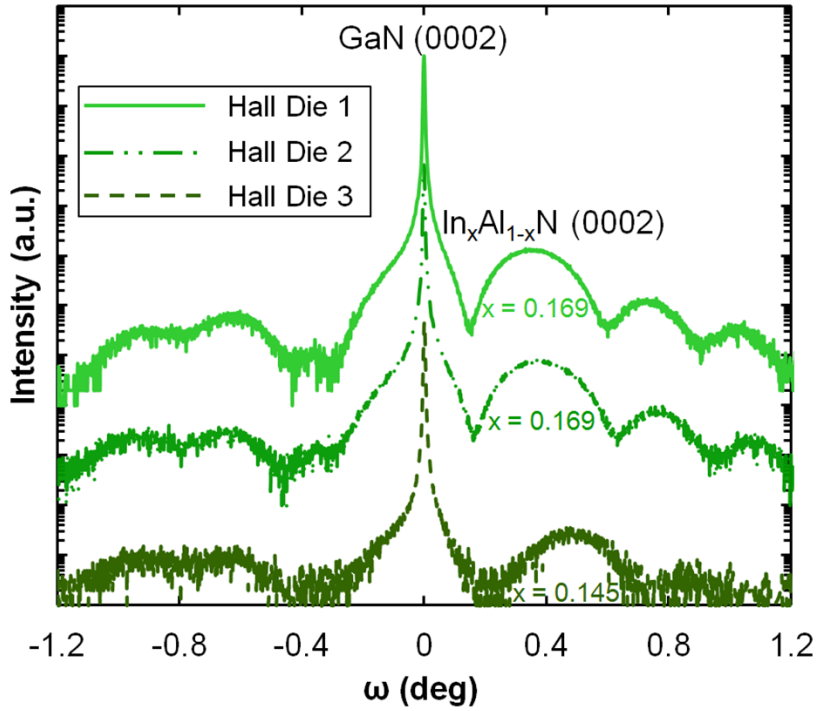


**Figure 8.11: Symmetric HRXRD  $\omega$ - $2\theta$  scans around the GaN (0002) reflection directed at the areas where Hall dies were fabricated on the InAlN/GaN/AlN/GaN heterostructure on FS GaN.**

**Table 8.3: Relevant structural parameters of the areas where Hall dies were fabricated on the InAlN/GaN/AlN/GaN heterostructure on FS GaN, including the In mole fraction ( $x$ ) and thickness ( $t$ ) of the  $\text{In}_x\text{Al}_{1-x}\text{N}$  barrier.**

Hall Die	$\text{In}_x\text{Al}_{1-x}\text{N}$ Barrier				GaN (0002)	GaN (20 $\bar{2}$ 1)
	$x$	$t$ (nm)	GaN IL (nm)	AlN IL (nm)	$\Delta\omega$ (arcsec)	$\Delta\omega$ (arcsec)
1	0.169	11	~2	~3	161	213
2	0.169	11	~2	~3	159	208
3	0.145	11	~2	~3	162	210

### 8.3.7 Surface morphology of InAlN/GaN/AlN/GaN HEMT Structure on FS GaN

Unlike the surface morphologies of the IL Series, only meandering step edges were identified on the InAlN/GaN/AlN/GaN heterostructure on FS GaN (Fig. 8.12). This heterostructure had an rms roughness of 0.308 nm, which was slightly lower than the lowest rms roughness measured on the IL Series. Structure vi exhibited no dislocation-mediated surface features since it was regrown on a low-TDD FS GaN template. The meandering step edges were similar to those identified on AlGaN barriers grown Ga-rich on FS GaN [62]. The absence of dislocation-mediated surface features, which often lead to higher roughness, is an advantage of regrowth on FS GaN.

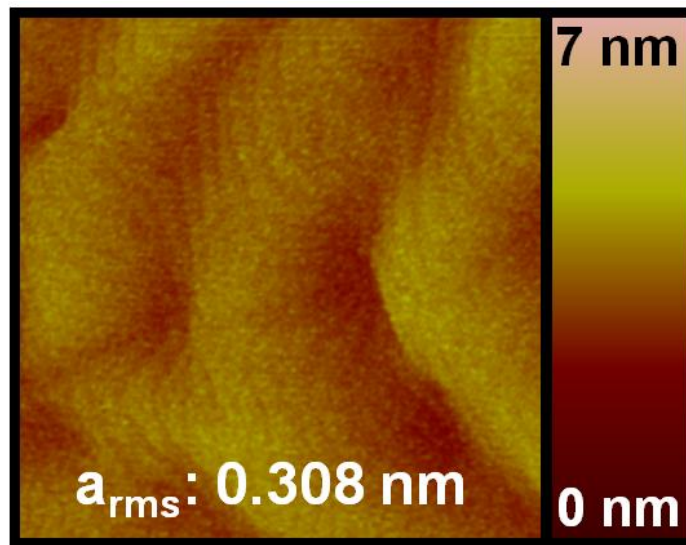


Figure 8.12:  $2 \times 2 \mu\text{m}^2$  AFM micrograph displaying the surface morphology of the InAlN/GaN/AlN/GaN heterostructure on FS GaN, noting the rms roughness ( $a_{\text{rms}}$ ).

### 8.3.8 Temperature-dependent Mobility of InAlN/GaN/AlN/GaN HEMT on FS GaN

Table 8.4 shows the 2DEG sheet densities, mobilities, and sheet resistances of the three Hall dies fabricated on Structure vi at RT and 77 K. Even though the InAlN barrier of Structure vi was thinner than that of Structure iv, Structure vi yielded higher RT sheet densities.

**Table 8.4: Hall measurements performed at RT and 77 K on the three Hall dies fabricated on the InAlN/GaN/AlN/GaN heterostructure on FS GaN, including the 2DEG sheet density ( $n_s$ ), mobility ( $\mu$ ), and sheet resistance ( $R_{SH}$ ).**

Hall Die	RT			77 K		
	$n_s$ ( $10^{13} \text{ cm}^{-2}$ )	$\mu$ ( $\text{cm}^2/\text{Vs}$ )	$R_{sh}$ ( $\Omega/\square$ )	$n_s$ ( $10^{13} \text{ cm}^{-2}$ )	$\mu$ ( $\text{cm}^2/\text{Vs}$ )	$R_{sh}$ ( $\Omega/\square$ )
1	2.338	1822	146	2.476	7187	35
2	2.659	1612	145	2.717	5766	40
3	4.766	1068	123	4.748	4361	30

Hall Die 1 and Hall Die 2 were fabricated on heterostructures with lattice-matched InAlN barriers and achieved 2DEG sheet densities greater than  $2.3 \times 10^{13} \text{ cm}^{-2}$ . The heterostructure on which Hall Die 3 was fabricated had an  $\text{In}_{0.145}\text{Al}_{0.855}\text{N}$  barrier. Since this InAlN barrier was tensilely strained, the total polarization charge was determined by spontaneous and piezoelectric polarization, and a RT sheet density of  $4.76 \times 10^{13} \text{ cm}^{-2}$  was measured. Hall Die 1 and Hall Die 2 yielded high RT mobilities of 1822 and  $1612 \text{ cm}^2/\text{Vs}$ , respectively, resulting in RT sheet resistances below  $150 \Omega/\square$ . Hall Die 3 achieved a mobility of  $1068 \text{ cm}^2/\text{Vs}$ , resulting in a low RT sheet resistance of  $123 \Omega/\square$ . Figure 8.13 displays the temperature-dependent Hall measurements performed on

Structure vi. As the temperature was decreased, the sheet densities measured on Hall Dies 1-3 were constant, and the mobilities increased.

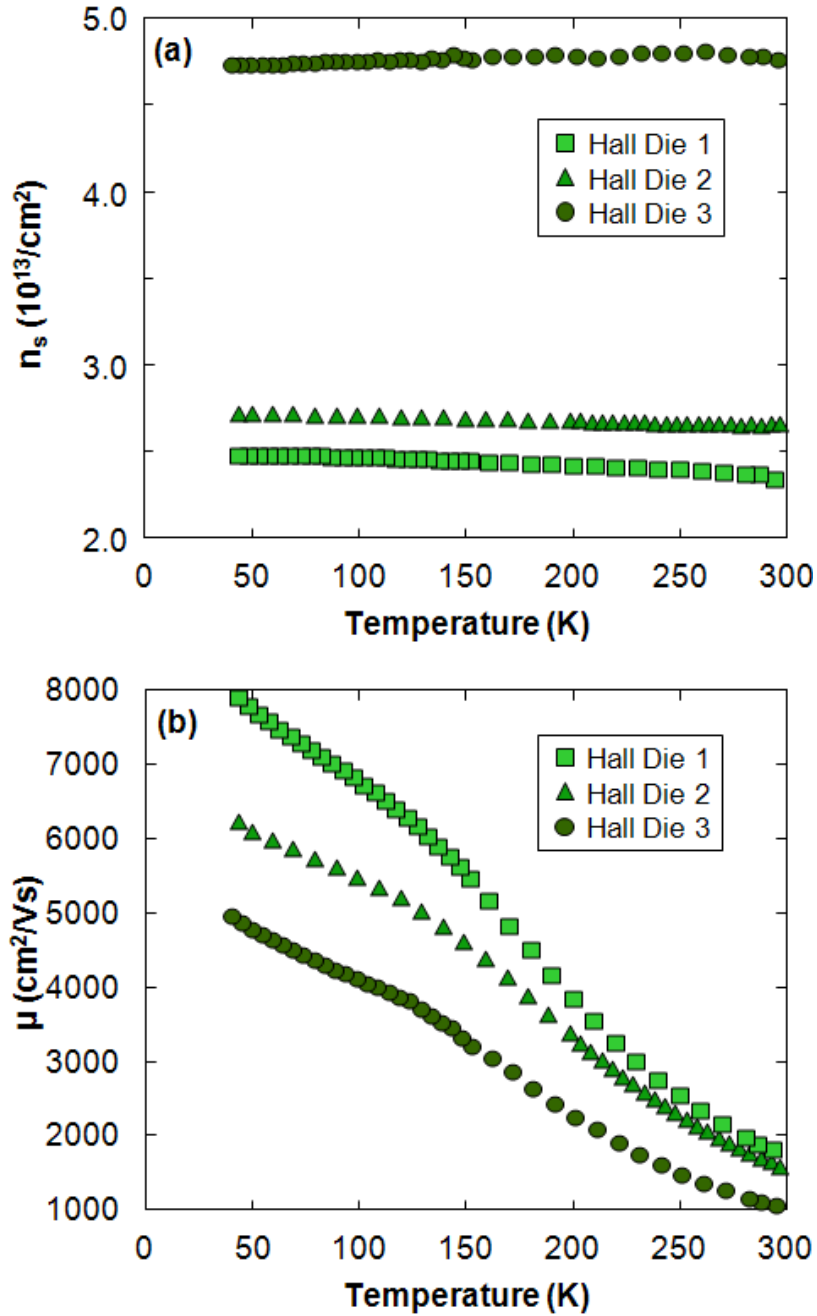


**Figure 8.13: Hall measurements showing (a) sheet density ( $n_s$ ) with respect to temperature and (b) mobility ( $\mu$ ) with respect to temperature for Hall Dies 1-3 on the InAlN/GaN/AlN/GaN heterostructure on FS GaN.**

Below 15 nm, InAlN thickness variations of +/- 0.5 nm can have a large impact on the sheet density [99]. This is likely the source of the discrepancy between the RT sheet densities of Hall Die 1 and Hall Die 2 on Structure vi. A slight increase in the AlN IL thickness or decrease in the GaN IL thickness, which are difficult to identify with HRXRD, may have also contributed to the higher sheet density of Hall Die 2 in comparison with Hall Die 1.

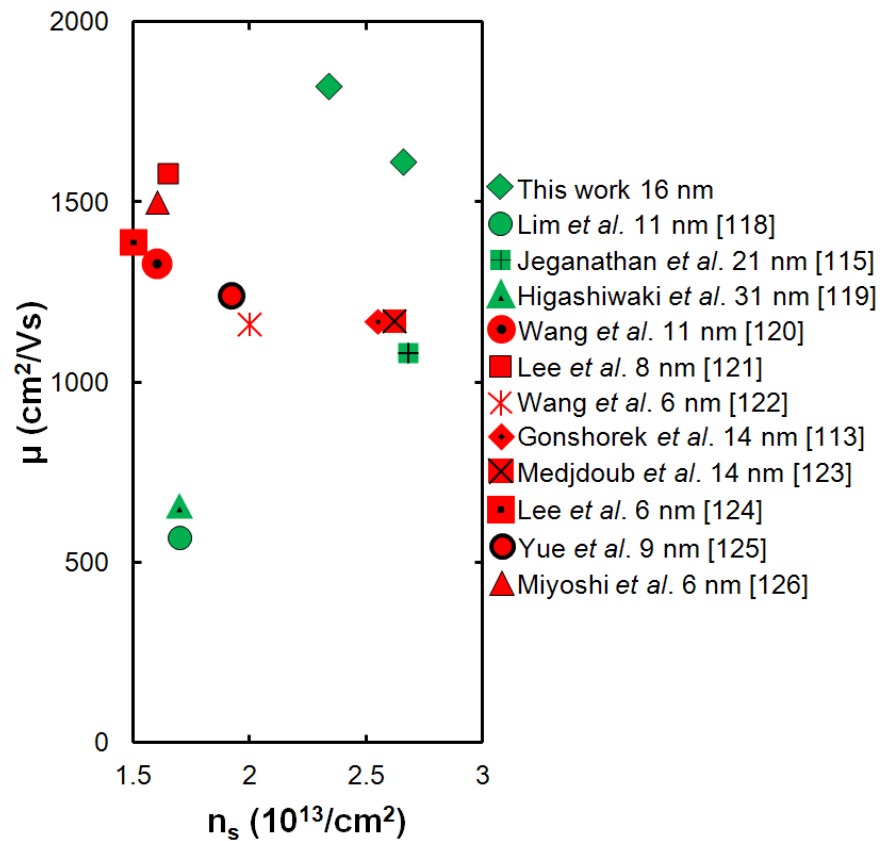


**Figure 8.14: Compilation of sheet density ( $n_s$ ) and mobility ( $\mu$ ) values from the literature for metal-polar heterostructures with nominally lattice-matched InAlN barriers. Green markers indicate growth by PAMBE, and red markers indicate growth by MOCVD. The total  $t_b$  is noted in the legend.**

The separation between the temperature-dependent mobility curves for Hall Dies 1-3 on Structure vi (Fig. 8.13(b)) was likely caused by an increase of IR with higher sheet

density. In comparison with Structure iv, regrowth of the optimal structure on a low-TDD FS GaN template yielded a much higher RT mobility with a similar sheet density, due to a reduction in DIS and IR scattering (reduced rms roughness) [62,116]. To the best of our knowledge, Structure vi realized a lower RT sheet resistance ( $145 \Omega/\square$ ) and higher RT mobility ( $1822 \text{ cm}^2/\text{Vs}$ ) than any previously reported for a single-channel heterostructure with an InAlN barrier, lattice-matched or otherwise [90,117]. Figure 8.14 presents a compilation of the highest RT 2DEG sheet densities and mobilities from the literature for metal-polar structures with nominally lattice-matched InAlN barriers [113,115,118–126]. Hall Die 3, fabricated on strained InAlN barrier, produced a RT sheet resistance of  $123 \Omega/\square$ , which is lower than any previously reported RT sheet resistance for a single-channel III-Nitride heterostructure [83].

### **8.3.9 DC-IV Measurements of InAlN/GaN/AlN/GaN HEMT on FS GaN**

As shown in Fig. 8.15(a), a TLM pattern in proximity to Hall Die 1 yielded a similar RT sheet resistance ( $148 \Omega/\square$ ) to that from Hall measurements and a relatively high contact resistance of  $0.928 \Omega\text{-mm}$ . The DC-IV curves of an unpassivated HEMT from the same die as the TLM pattern are shown in Fig. 8.15(b). With this HEMT, a peak drain current ( $I_{\text{DS,max}}$ ) of  $1.05 \text{ A/mm}$  was produced with a  $V_{\text{GS}}$  of  $0 \text{ V}$  at a  $V_{\text{DS}}$  of  $10 \text{ V}$ . Leakage currents were negligible, as the HEMT displayed sharp pinch-off at  $V_{\text{GS}} = -6.5 \text{ V}$ . At  $V_{\text{GS}} = -7 \text{ V}$  and  $V_{\text{DS}} = 10 \text{ V}$ , a gate current ( $I_{\text{G}}$ ) of  $0.625 \text{ mA/mm}$  dominated the OFF-state drain current. An ON/OFF drain current ratio of 1515 at  $V_{\text{DS}} = 10 \text{ V}$  was determined for the HEMT in Fig. 8.15(b). There was little variation in HEMT



characteristics across the InAlN/GaN/AlN/GaN heterostructure, and buffer breakdown voltages in excess of 50 V were measured.

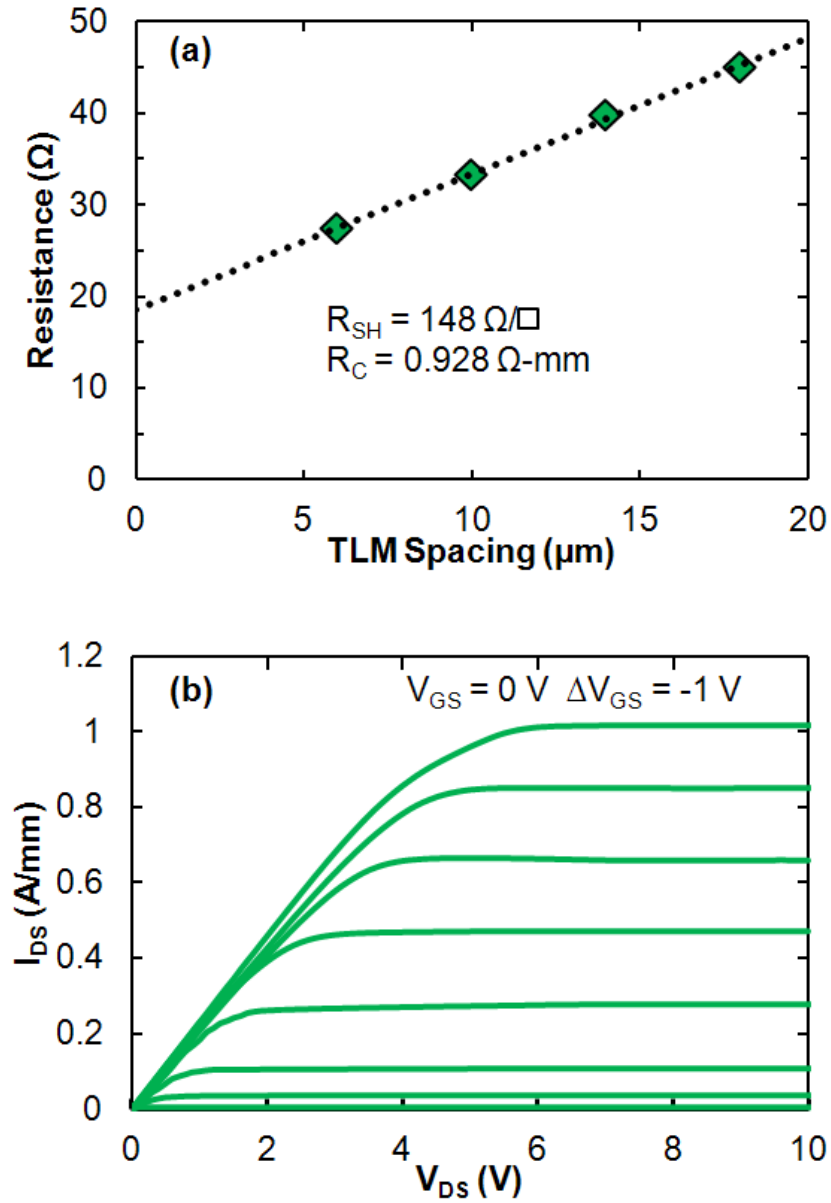


**Figure 8.15: (a) TLM performed in close proximity to Hall Die 1 on the InAlN/GaN/AlN/GaN heterostructure regrown on FS GaN. (b) DC-IV curves for an unpassivated HEMT near Hall Die 1 on the InAlN/GaN/AlN/GaN heterostructure.**

Even though the 2DEG sheet resistance of InAlN/GaN/AlN/GaN heterostructure on FS GaN was exceptionally low, the  $I_{DS,max}$  of the HEMT fabricated on Structure vi with  $V_{GS} = 0$  V was barely above 1 A/mm. Considering the geometry of the HEMTs, the contact resistance dominated the overall parasitic resistance. In Chapter 2, HEMTs with the same geometry, higher sheet resistance ( $\sim 400 \text{ } \Omega/\square$ ), and lower contact resistance ( $\sim 0.7 \text{ } \Omega\text{-mm}$ ) produced a similar  $I_{DS,max}$  with  $V_{GS} = 0$  V [59]. The contact resistance needs to be reduced through plasma treatments [127] or contact regrowth [128,129] to yield metal-polar InAlN/GaN/AlN/GaN HEMTs with extremely low parasitic resistance. With C-related traps in close proximity to the channel because of the low UID GaN buffer thickness, there is increased likelihood for back-gating through trapping of hot electrons under high-power operation [23,60]. To make these low-TDD HEMTs suitable for high-frequency, high-power operation, back barriers need to be included [60].

## Chapter 9. Summary and Future Work

Threading dislocations were found to facilitate vertical leakage in Ga-rich PAMBE-grown HEMTs, but their effect on the leakage of NH<sub>3</sub>-MBE HEMTs was unclear. High TDD was consistently shown to degrade the 2DEG mobility and sheet resistance of AlGaN/GaN heterostructures, regardless of the 2DEG density or whether an AlN IL was included. However, degradation of the 2DEG mobility with high TDD was more pronounced in AlGaN/AlN/GaN for which the impact of alloy-related scattering mechanisms was reduced.

Pure AlN ILs in Ga-rich PAMBE-grown heterostructures were identified by APT, but a high concentration of Ga impurities was seen in AlN ILs grown by NH<sub>3</sub>-MBE. Studies then pointed to the decomposition of underlying GaN layers as the source of the Ga impurities, seeing that the standard NH<sub>3</sub>-MBE growth temperatures (~820 °C) are far greater than the GaN decomposition temperature (~745 °C in vacuum). Although low-temperature growth improved the purity of the AlN ILs, the 2DEG mobility, presumably affected by the N-rich conditions of NH<sub>3</sub>-MBE, did not surpass 1300 cm<sup>2</sup>/Vs. Under N-rich conditions, the diffusion of Group III adatoms is severely limited by low growth temperature, and surface/interface roughness increases. Applying an In surfactant was shown to improve the surface roughness of low-temperature AlN, but the 2DEG characteristics were only marginally improved.

The dominant scattering mechanisms with low-temperature NH<sub>3</sub>-MBE growth need to be identified before low sheet resistances (similar to those in Ga-rich PAMBE-grown heterostructures) can be achieved. The N-rich growth conditions present a

significant opportunity for Group III flux optimization. The growth rate is easily tuned in an N-rich environment. The trends of 2DEG mobility with Al and Ga flux at high and low temperature, as well as trends with In surfactant flux at high and low temperature, should be established. Once the 2DEG properties are improved, SOA HEMTs should be fabricated. It was shown that high-TDD heterostructures are far less leaky through  $\text{NH}_3$ -MBE growth in comparison with Ga-rich growth. Yet, e-beam gates, gate dielectrics, regrown contacts, and structural modification (thin/thick GaN caps) have not been applied to  $\text{NH}_3$ -MBE-grown HEMTs. With SOA fabrication techniques, the performance limits of HEMTs with the different MBE growth techniques can be defined.

The source of poor sheet resistance in  $\text{In}_{0.17}\text{Al}_{0.83}\text{N}/\text{GaN}$  heterostructures grown by PAMBE also needs to be identified. It was unclear how the inclusion AlN and GaN ILs in these structures had such a great impact on 2DEG characteristics. Nevertheless,  $\text{In}_{0.17}\text{Al}_{0.83}\text{N}/\text{GaN}/\text{AlN}/\text{GaN}$  heterostructures with homogeneous barriers grown by PAMBE yielded world-class sheet resistances. If these heterostructures are to be used in high-power high-frequency HEMTs, contact issues need to be resolved (regrown contacts), and the buffer structure needs to be optimized. Ironically, the poor  $\text{In}_{0.17}\text{Al}_{0.83}\text{N}/\text{GaN}$  interface may aid in  $\text{In}_{0.17}\text{Al}_{0.83}\text{N}$ 's use as a back barrier in HEMTs grown by Ga-rich PAMBE on FS GaN. Focusing on reliability, a potential deep-recess depletion-mode HEMT structure (Fig. 9.1) by PAMBE would be regrown on semi-insulating FS GaN to essentially eliminate parasitic pad capacitance. This potential HEMT structure would also include an  $\text{In}_{0.17}\text{Al}_{0.83}\text{N}$  back barrier and a thin (<5 nm) gate dielectric to improve PAE. In addition to optimizing the back barriers in HEMTs on FS GaN, polarization

engineering of the buffer layers to remove C-doping altogether should be considered. Thick UID  $\text{Al}_{0.04}\text{Ga}_{0.96}\text{N}$  buffers may be far less leaky than UID GaN buffers grown by Ga-rich PAMBE on low-TDD templates.

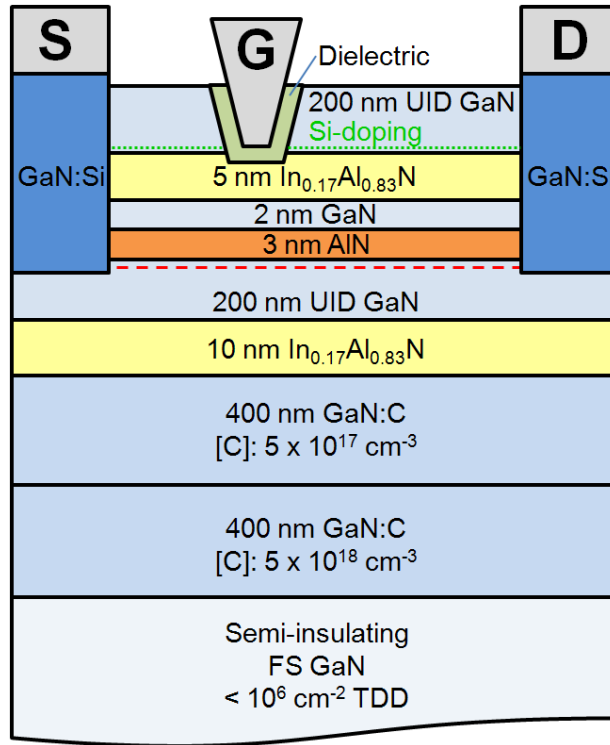


**Figure 9.1: Schematic of potential deep-recess HEMT structure grown by PAMBE on FS GaN with an  $\text{In}_{0.17}\text{Al}_{0.83}\text{N}$  back barrier.**

Although digital alloy barriers were not grown in this thesis, they may prove to be valuable for future HEMT designs. Digital AlGa<sub>N</sub> blocks a percolative transport pathway [94] that may facilitate high gate leakage currents and charge accumulation under a gate dielectric. Digital AlGa<sub>N</sub> also removes the barrier potential fluctuations associated with clustering in a random alloy. In Chapter 4 and Chapter 8, thicker ILs and further separation of the random alloy barrier from the 2DEG yielded an increase in

mobility. Though it was previously assumed that the increased mobility was a result of reduced 2DEG wavefunction overlap with the random alloy, increased shielding of the 2DEG from clustering in the alloy barrier may have been far more important. Since we now have accurate 3D composition data from APT, we can improve previous scattering models where compositions were mainly determined by HRXRD. Quantification of in-plane clustering, combined with modeling, will help determine the dominant scattering mechanisms. If scattering from alloy clustering is an important mechanism, it can essentially be eliminated with a digital alloy barrier. But, the benefits of including a digital alloy barrier may be outweighed by its effects on the reliability of the device. Strain-free structures have been recently favored to reduce the likelihood of crystal defect formation under high negative biases.

The future of GaN-based electron device research will likely be dominated by vertical and normally-off (enhancement-mode) devices. In vertical devices, the peak electric field under the gate is reduced in comparison with lateral devices, and gate shaping is not as important. In normally-off devices, control circuitry is simplified because a constant gate bias is not required. Although this thesis focused on normally-on lateral devices, the growth optimization studies may be valuable for reducing gate leakage and access resistances in vertical and normally-off devices. The growth study in Chapter 8 may also act as a starting point for the PAMBE growth of polarization-matched  $\text{In}_{\sim 0.4}\text{Al}_{\sim 0.6}\text{N}/\text{GaN}$  heterostructures. Polarization-matched heterostructures may find application in normally-off devices since they do not have a 2DEG at the heterointerface.

## References

- [1] Johnson E 1965 Physical Limitations on Frequency and Power Parameters of Transistors *RCA Rev.* 163–77
- [2] Baliga B J 1982 Semiconductors for high-voltage, vertical channel field-effect transistors *J. Appl. Phys.* **53** 1759
- [3] Shen L 2004 *Advanced Polarization-Based Design of AlGaN/GaN HEMTs* (University of California, Santa Barbara)
- [4] Mishra U K and Kazior T E 2008 GaN-Based RF Power Devices and Amplifiers *Proc. IEEE* **96** 287–305
- [5] Huang A 2004 New Unipolar Switching Power Device Figures of Merit *IEEE Electron Device Lett.* **25** 298–301
- [6] Clarke R C and Palmour J W 2002 SiC Microwave Power Technologies *Proc. IEEE* **90** 987–92
- [7] Dimitrijević S and Jamet P 2003 Advances in SiC power MOSFET technology *Microelectron. Reliab.* **43** 225–33
- [8] Yu E T, Dang X Z, Asbeck P M, Lau S S and Sullivan G J 1999 Spontaneous and piezoelectric polarization effects in III–V nitride heterostructures *J. Vac. Sci. Technol. B Microelectron. Nanom. Struct.* **17** 1742–9
- [9] Jiménez-Riobóo R J, Cuscó R, Domènech-Amador N, Prieto C, Yamaguchi T, Nanishi Y and Artús L 2012 Surface acoustic waves and elastic constants of InN epilayers determined by Brillouin scattering *Phys. status solidi - Rapid Res. Lett.* **6** 256–8
- [10] Ibbetson J P, Fini P T, Ness K D, Denbaars S P, Speck J S and Mishra U K 2000 Polarization effects, surface states, and the source of electrons in AlGaIn/GaN heterostructure field effect transistors *Appl. Phys. Lett.* **77** 250–2
- [11] Higashiwaki M, Chowdhury S, Swenson B L and Mishra U K 2010 Effects of oxidation on surface chemical states and barrier height of AlGaIn/GaN heterostructures *Appl. Phys. Lett.* **97** 222104
- [12] Palacios T 2009 Beyond the AlGaIn/GaN HEMT: new concepts for high-speed transistors *Phys. Status Solidi* **206** 1145–8

- [13] Shen L, Palacios T, Poblencz C, Corrion A, Chakraborty A, Fichtenbaum N, Keller S, Denbaars S P, Speck J S and Mishra U K 2006 Unpassivated high power deeply recessed GaN HEMTs with fluorine-plasma surface treatment *IEEE Electron Device Lett.* **27** 214–6
- [14] Palacios T, Chakraborty A, Rajan S, Poblencz C, Keller S, Denbaars S, Speck J and Mishra U 2005 High-Power AlGaIn/GaN HEMTs for Ka-Band Applications *IEEE Electron Device Lett.* **26** 781–3
- [15] Palacios T, Chakraborty A, Heikman S, Keller S, Denbaars S P and Mishra U 2006 AlGaIn/GaN High Electron Mobility Transistors With InGaIn Back-Barriers *IEEE Electron Device Lett.* **27** 2005–7
- [16] Fernández-Garrido S, Koblmüller G, Calleja E and Speck J S 2008 In situ GaN decomposition analysis by quadrupole mass spectrometry and reflection high-energy electron diffraction *J. Appl. Phys.* **104** 033541
- [17] Koblmüller G, Pongratz P, Averbeck R and Riechert H 2002 Nucleation Phenomena during Molecular Beam Epitaxy of GaN Observed by Line-of-Sight Quadrupole Mass Spectrometry *Phys. Status Solidi* **194** 515–9
- [18] Koblmüller G, Chu R M, Raman a., Mishra U K and Speck J S 2010 High-temperature molecular beam epitaxial growth of AlGaIn/GaN on GaN templates with reduced interface impurity levels *J. Appl. Phys.* **107** 043527
- [19] Denninghoff D J, Dasgupta S, Lu J, Keller S and Mishra U K 2012 Design of High-Aspect-Ratio T-Gates on N-Polar GaN/AlGaIn MIS-HEMTs for High f(max) *IEEE Electron Device Lett.* **33** 785–7
- [20] Pei Y, Chen Z, Brown D, Keller S, Denbaars S P and Mishra U K 2009 Deep-Submicrometer AlGaIn/GaN HEMTs With Slant Field Plates *IEEE Electron Device Lett.* **30** 328–30
- [21] Wu Y, Saxler A, Moore M, Smith R P, Sheppard S, Chavarkar P M, Wisleder T, Mishra U K and Parikh P 2004 30-W/mm GaN HEMTs by Field Plate Optimization *IEEE Electron Device Lett.* **25** 2003–5
- [22] Green D S, Gibb S R, Hosse B, Vetury R, Grider D E and Smart J A 2004 Control of epitaxial defects for optimal AlGaIn/GaN HEMT performance and reliability *J. Cryst. Growth* **272** 285–92
- [23] Uren M J, Möreke J and Kuball M 2012 Buffer Design to Minimize Current Collapse in GaN/AlGaIn HFETs *IEEE Trans. Electron Devices* **59** 3327–33



- [24] Vetury R, Zhang N Q, Keller S and Mishra U K 2001 The impact of surface states on the DC and RF characteristics of AlGaIn/GaN HFETs *IEEE Trans. Electron Devices* **48** 560–6
- [25] Rajan S 2006 *Advanced Polarization Engineering for GaN-based Transistors* (University of California, Santa Barbara)
- [26] Zou J, Kotchetkov D, Balandin A, Florescu D and Pollak F 2002 Thermal conductivity of GaN films: Effects of impurities and dislocations *J. Appl. Phys.* **92** 2534–9
- [27] Kotchetkov D, Zou J, Balandin A, Florescu D and Pollak F 2001 Effect of dislocations on thermal conductivity of GaN layers *Appl. Phys. Lett.* **79** 4316–8
- [28] Wu X, Fini P, Tarsa E, Heying B, Keller S, Mishra U, DenBaars S and Speck J 1998 Dislocation generation in GaN heteroepitaxy *J. Cryst. Growth* **189-190** 231–43
- [29] Lahreche H, Vennéguès P, Vaille M, Beaumont B, Laugt M, Lorenzini P and Gibart P 1999 Comparative study of GaN layers grown on insulating AlN and conductive AlGaIn buffer layers *Semicond. Sci. Technol.* **14** L33–L36
- [30] Moran B, Wu F, Romanov A E, Mishra U K, Denbaars S P and Speck J S 2004 Structural and morphological evolution of GaN grown by metalorganic chemical vapor deposition on SiC substrates using an AlN initial layer *J. Cryst. Growth* **273** 38–47
- [31] Waltereit P, Poblenz C, Rajan S, Wu F, Mishra U K and Speck J S 2004 Structural Properties of GaN Buffer Layers on 4H-SiC(0001) Grown by Plasma-Assisted Molecular Beam Epitaxy for High Electron Mobility Transistors *Jpn. J. Appl. Phys.* **43** L1520–L1523
- [32] Poblenz C, Waltereit P, Rajan S, Heikman S, Mishra U K and Speck J S 2004 Effect of carbon doping on buffer leakage in AlGaIn/GaN high electron mobility transistors *J. Vac. Sci. Technol. B Microelectron. Nanom. Struct.* **22** 1145
- [33] Poblenz C, Waltereit P, Rajan S, Mishra U, Speck J, Chin P, Smorchkova I and Heying B 2005 Effect of AlN nucleation layer growth conditions on buffer leakage in AlGaIn/GaN high electron mobility transistors grown by molecular beam epitaxy (MBE) *J. Vac. Sci. Technol. B Microelectron. Nanom. Struct.* **23** 1562–7
- [34] Koblmüller G, Fernández-Garrido S, Calleja E and Speck J 2007 In situ investigation of growth modes during plasma-assisted molecular beam epitaxy of (0001) GaN *Appl. Phys. Lett.* **91** 161904

- [35] Heying B, Averbek R, Chen L, Haus E, Riechert H and Speck J 2000 Control of GaN surface morphologies using plasma-assisted molecular beam epitaxy *J. Appl. Phys.* **88** 1855–60
- [36] Poblenz C 2005 *Growth of (In,Al)GaN alloys by RF-plasma assisted molecular beam epitaxy for application in high electron mobility transistor structures* (University of California, Santa Barbara)
- [37] Romanov A, Beltz G, Cantu P, Wu F, Keller S, DenBaars S and Speck J 2006 Cracking of III-nitride layers with strain gradients *Appl. Phys. Lett.* **89** 161922
- [38] Kaun S W, Ahmadi E, Mazumder B, Wu F, Kyle E C H, Burke P G, Mishra U K and Speck J S 2014 GaN-based high-electron-mobility transistor structures with homogeneous lattice-matched InAlN barriers grown by plasma-assisted molecular beam epitaxy *Semicond. Sci. Technol.* **29** 045011
- [39] Ahmadi E, Shivaraman R, Wu F, Wienecke S, Kaun S W, Keller S, Speck J S and Mishra U K 2014 Elimination of columnar microstructure in N-face InAlN, lattice-matched to GaN, grown by plasma-assisted molecular beam epitaxy in the N-rich regime *Appl. Phys. Lett.* **104** 072107
- [40] Heying B, Tarsa E J, Elsass C R, Fini P, DenBaars S P and Speck J S 1999 Dislocation mediated surface morphology of GaN *J. Appl. Phys.* **85** 6470–6
- [41] Look D and Sizelove J 1999 Dislocation Scattering in GaN *Phys. Rev. Lett.* **82** 1237–40
- [42] Shi J and Eastman L F 2011 Correlation Between AlGaIn/GaN MISHFET Performance and HfO<sub>2</sub> Insulation Layer Quality *IEEE Electron Device Lett.* **32** 312–4
- [43] Liu X, Yeluri R, Lu J and Mishra U K 2012 Effects of H<sub>2</sub>O Pretreatment on the Capacitance–Voltage Characteristics of Atomic-Layer-Deposited Al<sub>2</sub>O<sub>3</sub> on Ga-Face GaN Metal–Oxide–Semiconductor Capacitors *J. Electron. Mater.* **42** 33–9
- [44] Gao F, Lu B, Li L, Kaun S, Speck J S, Thompson C V. and Palacios T 2011 Role of oxygen in the OFF-state degradation of AlGaIn/GaN high electron mobility transistors *Appl. Phys. Lett.* **99** 223506
- [45] Makaram P, Joh J, del Alamo J A, Palacios T and Thompson C V. 2010 Evolution of structural defects associated with electrical degradation in AlGaIn/GaN high electron mobility transistors *Appl. Phys. Lett.* **96** 233509

- [46] Gao F, Chen D, Lu B, Tuller H L, Thompson C V, Keller S, Mishra U K and Palacios T 2012 Impact of Moisture and Fluorocarbon Passivation on the Current Collapse of AlGaIn/GaN HEMTs *IEEE Electron Device Lett.* **33** 1378–80
- [47] Heikman S, Keller S, Wu Y, Speck J S, DenBaars S P and Mishra U K 2003 Polarization effects in AlGaIn/GaN and GaN/AlGaIn/GaN heterostructures *J. Appl. Phys.* **93** 10114
- [48] Pearton S J, Zolper J C, Shul R J and Ren F 1999 GaN: Processing, defects, and devices *J. Appl. Phys.* **86** 1–78
- [49] Lahreche H, Vennéguès P, Tottereau O, Laugt M, Lorenzini P, Leroux M, Beaumont B and Gibart P 2000 Optimisation of AlN and GaN growth by metalorganic vapour-phase epitaxy (MOVPE) on Si (111) *J. Cryst. Growth* **217** 13–25
- [50] Krost A, Dadgar A, Strassburger G and Clos R 2003 GaN-based epitaxy on silicon: stress measurements *Phys. Status Solidi* **200** 26–35
- [51] Krost A, Dadgar A, Bläsing J, Diez A, Hempel T, Petzold S, Christen J and Clos R 2004 Evolution of stress in GaN heteroepitaxy on AlN/Si(111): From hydrostatic compressive to biaxial tensile *Appl. Phys. Lett.* **85** 3441
- [52] Manuel J M, Morales F M, García R, Aidam R, Kirste L and Ambacher O 2012 Threading dislocation propagation in AlGaIn/GaN based HEMT structures grown on Si (111) by plasma assisted molecular beam epitaxy *J. Cryst. Growth* **357** 35–41
- [53] Avrutin V, Silversmith D J, Mori Y, Kawamura F, Kitaoka Y and Morkoc H 2010 Growth of Bulk GaN and AlN: Progress and Challenges *Proc. IEEE* **98** 1302–15
- [54] Corrion A L, Poblenz C, Wu F and Speck J S 2008 Structural and morphological properties of GaN buffer layers grown by ammonia molecular beam epitaxy on SiC substrates for AlGaIn/GaN high electron mobility transistors *J. Appl. Phys.* **103** 093529
- [55] Tang H, Fang Z Q, Rolfe S, Bardwell J A and Raymond S 2010 Growth kinetics and electronic properties of unintentionally doped semi-insulating GaN on SiC and high-resistivity GaN on sapphire grown by ammonia molecular-beam epitaxy *J. Appl. Phys.* **107** 103701
- [56] Corrion A L, Wu F and Speck J S 2012 Growth regimes during homoepitaxial growth of GaN by ammonia molecular beam epitaxy *J. Appl. Phys.* **112** 054903

- [57] Dharmarasu N, Radhakrishnan K, Agrawal M, Ravikiran L, Arulkumaran S, Lee K E and Ing N G 2012 Demonstration of AlGa<sub>N</sub>/Ga<sub>N</sub> High-Electron-Mobility Transistors on 100-mm-Diameter Si(111) by Ammonia Molecular Beam Epitaxy *Appl. Phys. Express* **5** 091003
- [58] Kaun S W, Wong M H, Mishra U K and Speck J S 2013 Molecular beam epitaxy for high-performance Ga-face Ga<sub>N</sub> electron devices *Semicond. Sci. Technol.* **28** 074001
- [59] Kaun S, Wong M, Dasgupta S, Choi S, Chung R, Mishra U and Speck J 2011 Effects of Threading Dislocation Density on the Gate Leakage of AlGa<sub>N</sub>/Ga<sub>N</sub> Heterostructures for High Electron Mobility Transistors *Appl. Phys. Express* **4** 024101
- [60] Kaun S W, Lu J, Speck J S, Wong M H and Mishra U K 2013 Reduction of carbon proximity effects by including AlGa<sub>N</sub> back barriers in HEMTs on free-standing Ga<sub>N</sub> *Electron. Lett.* **49** 893–5
- [61] Kaun S W, Wong M H, Mishra U K and Speck J S 2012 Correlation between threading dislocation density and sheet resistance of AlGa<sub>N</sub>/Al<sub>N</sub>/Ga<sub>N</sub> heterostructures grown by plasma-assisted molecular beam epitaxy *Appl. Phys. Lett.* **100** 262102
- [62] Kaun S W, Burke P G, Hoi Wong M, Kyle E C H, Mishra U K and Speck J S 2012 Effect of dislocations on electron mobility in AlGa<sub>N</sub>/Ga<sub>N</sub> and AlGa<sub>N</sub>/Al<sub>N</sub>/Ga<sub>N</sub> heterostructures *Appl. Phys. Lett.* **101** 262102
- [63] Kozodoy P, Ibbetson J P, Marchand H, Fini P T, Keller S, Speck J S, DenBaars S P and Mishra U K 1998 Electrical characterization of Ga<sub>N</sub> p-n junctions with and without threading dislocations *Appl. Phys. Lett.* **73** 975–7
- [64] Hsu J W P, Manfra M J, Molnar R J, Heying B and Speck J S 2002 Direct imaging of reverse-bias leakage through pure screw dislocations in Ga<sub>N</sub> films grown by molecular beam epitaxy on Ga<sub>N</sub> templates *Appl. Phys. Lett.* **81** 79
- [65] Northrup J E 2001 Screw dislocations in Ga<sub>N</sub>: The Ga-filled core model *Appl. Phys. Lett.* **78** 22882290
- [66] Law J J M, Yu E T, Koblmüller G, Wu F and Speck J S 2010 Low defect-mediated reverse-bias leakage in (0001) Ga<sub>N</sub> via high-temperature molecular beam epitaxy *Appl. Phys. Lett.* **96** 102111
- [67] Wong Y-Y, Huang W-C, Trinh H-D, Yang T-H, Chang J-R, Chen M and Chang E Y 2012 Effect of Nitridation on the Regrowth Interface of AlGa<sub>N</sub>/Ga<sub>N</sub> Structures

Grown by Molecular Beam Epitaxy on GaN Templates *J. Electron. Mater.* **41** 2139–44

- [68] Cao Y, Zimmermann T, Xing H and Jena D 2010 Polarization-engineered removal of buffer leakage for GaN transistors *Appl. Phys. Lett.* **96** 042102
- [69] Heikman S 2002 *MOCVD Growth Technologies for Applications in AlGaIn/GaN High Electron Mobility Transistors* (University of California, Santa Barbara)
- [70] Corrion A, Wu F, Mates T, Gallinat C S, Poblenz C and Speck J S 2006 Growth of Fe-doped GaN by RF plasma-assisted molecular beam epitaxy *J. Cryst. Growth* **289** 587–95
- [71] Green D S, Mishra U K and Speck J S 2004 Carbon doping of GaN with CBr<sub>4</sub> in radio-frequency plasma-assisted molecular beam epitaxy *J. Appl. Phys.* **95** 8456–62
- [72] Armstrong A, Arehart A R, Green D, Mishra U K, Speck J S and Ringel S A 2005 Impact of deep levels on the electrical conductivity and luminescence of gallium nitride codoped with carbon and silicon *J. Appl. Phys.* **98** 053704
- [73] Lyons J L, Janotti A and Van de Walle C G 2010 Carbon impurities and the yellow luminescence in GaN *Appl. Phys. Lett.* **97** 152108
- [74] Dora Y, Chakraborty a., McCarthy L, Keller S, Denbaars S P and Mishra U K 2006 High Breakdown Voltage Achieved on AlGaIn/GaN HEMTs With Integrated Slant Field Plates *IEEE Electron Device Lett.* **27** 713–5
- [75] Sun Y J, Brandt O, Liu T Y, Trampert A, Ploog K H, Bläsing J and Krost A 2002 Determination of the azimuthal orientational spread of GaN films by x-ray diffraction *Appl. Phys. Lett.* **81** 4928–30
- [76] Moram M A and Vickers M E 2009 X-ray diffraction of III-nitrides *Reports Prog. Phys.* **72** 036502
- [77] Waltreit P, Lim S-H, McLaurin M and Speck J S 2002 Heteroepitaxial Growth of GaN on 6H-SiC(0001) by Plasma-Assisted Molecular Beam Epitaxy *Phys. Status Solidi* **194** 524–7
- [78] Storm D F, Roussos J A, Katzer D S, Mittereder J A, Bass R, Binari S C, Hanser D, Preble E A and Evans K 2006 Microwave power performance of MBE-grown AlGaIn/GaN HEMTs on HVPE GaN substrates *Electron. Lett.* **42** 9–10

- [79] Storm D F, Katzer D S, Deen D A, Bass R, Meyer D J, Roussos J A, Binari S C, Paskova T, Preble E A and Evans K R 2010 Proximity effects of beryllium-doped GaN buffer layers on the electronic properties of epitaxial AlGaN/GaN heterostructures *Solid. State. Electron.* **54** 1470–3
- [80] Miyoshi M, Ishikawa H, Egawa T, Asai K, Mouri M, Shibata T, Tanaka M and Oda O 2004 High-electron-mobility AlGaN/AlN/GaN heterostructures grown on 100-mm-diam epitaxial AlN/sapphire templates by metalorganic vapor phase epitaxy *Appl. Phys. Lett.* **85** 1710–2
- [81] Smorchkova I P, Chen L, Mates T, Shen L, Heikman S, Moran B, Keller S, DenBaars S P, Speck J S and Mishra U K 2001 AlN/GaN and (Al,Ga)N/AlN/GaN two-dimensional electron gas structures grown by plasma-assisted molecular-beam epitaxy *J. Appl. Phys.* **90** 5196–201
- [82] Cao Y and Jena D 2007 High-mobility window for two-dimensional electron gases at ultrathin AlN/GaN heterojunctions *Appl. Phys. Lett.* **90** 182112
- [83] Cao Y, Wang K, Li G, Kosel T, Xing H and Jena D 2011 MBE growth of high conductivity single and multiple AlN/GaN heterojunctions *J. Cryst. Growth* **323** 529–33
- [84] Jena D, Gossard A C and Mishra U K 2000 Dislocation scattering in a two-dimensional electron gas *Appl. Phys. Lett.* **76** 1707
- [85] Jena D and Mishra U K 2002 Effect of scattering by strain fields surrounding edge dislocations on electron transport in two-dimensional electron gases *Appl. Phys. Lett.* **80** 64
- [86] Jena D, Smorchkova I, Gossard A C and Mishra U K 2001 Electron Transport in III-V Nitride Two-Dimensional Electron Gases *Phys. Status Solidi* **228** 617–9
- [87] Gurusinge M, Davidsson S and Andersson T 2005 Two-dimensional electron mobility limitation mechanisms in  $\text{Al}_x\text{Ga}_{1-x}\text{N}/\text{GaN}$  heterostructures *Phys. Rev. B* **72** 045316
- [88] Asgari A, Babanejad S and Faraone L 2011 Electron mobility, Hall scattering factor, and sheet conductivity in AlGaN/AlN/GaN heterostructures *J. Appl. Phys.* **110** 113713
- [89] Grundmann M BandEng <http://my.ece.ucsb.edu/mgrundmann/>
- [90] Tülek R, Ilgaz A, Gökden S, Teke A, Öztürk M K, Kasap M, Özçelik S, Arslan E and Özbay E 2009 Comparison of the transport properties of high quality

AlGaN/AlN/GaN and AlInN/AlN/GaN two-dimensional electron gas heterostructures *J. Appl. Phys.* **105** 013707

- [91] Jena D, Simon J, Wang A K, Cao Y, Goodman K, Verma J, Ganguly S, Li G, Karda K, Protasenko V, Lian C, Kosel T, Fay P and Xing H 2011 Polarization-engineering in group III-nitride heterostructures: New opportunities for device design *Phys. Status Solidi* **208** 1511–6
- [92] Joshi R P, Viswanadha S, Jogai B, Shah P and del Rosario R D 2003 Analysis of dislocation scattering on electron mobility in GaN high electron mobility transistors *J. Appl. Phys.* **93** 10046–52
- [93] Tang H, Fang Z Q, Rolfe S, Bardwell J A and Raymond S 2010 Growth kinetics and electronic properties of unintentionally doped semi-insulating GaN on SiC and high-resistivity GaN on sapphire grown by ammonia molecular-beam epitaxy *J. Appl. Phys.* **107** 103701
- [94] Nath D N, Yang Z C, Lee C-Y, Park P S, Wu Y-R and Rajan S 2013 Unipolar vertical transport in GaN/AlGaIn/GaN heterostructures *Appl. Phys. Lett.* **103** 022102
- [95] Wu Y-R, Singh M and Singh J 2006 Device scaling physics and channel velocities in AlGaIn/GaN HFETs: velocities and effective gate length *IEEE Trans. Electron Devices* **53** 588–93
- [96] Jessen G H, Fitch R C, Gillespie J K, Via G, Crespo A, Langley D, Denninghoff D J, Trejo M and Heller E R 2007 Short-Channel Effect Limitations on High-Frequency Operation of AlGaIn/GaN HEMTs for T-Gate Devices *IEEE Trans. Electron Devices* **54** 2589–97
- [97] Del Alamo J A and Joh J 2009 GaN HEMT reliability *Microelectron. Reliab.* **49** 1200–6
- [98] Kuzmík J 2001 Power Electronics on InAlN/(In)GaIn: Prospect for a Record Performance *IEEE Electron Device Lett.* **22** 510–2
- [99] Gonschorek M, Carlin J-F, Feltin E, Py M A, Grandjean N, Darakchieva V, Monemar B, Lorenz M and Ramm G 2008 Two-dimensional electron gas density in  $\text{Al}_{1-x}\text{In}_x\text{N}/\text{AlN}/\text{GaIn}$  heterostructures ( $0.03 \leq x \leq 0.23$ ) *J. Appl. Phys.* **103** 093714
- [100] Yue Y, Hu Z, Guo J, Sensale-Rodriguez B, Li G, Wang R, Faria F, Song B, Gao X, Guo S, Kosel T, Snider G, Fay P, Jena D and Xing H 2013 Ultrascaled InAlN/GaN High Electron Mobility Transistors with Cutoff Frequency of 400 GHz *Jpn. J. Appl. Phys.* **52** 08JN14

- [101] Katzer D S, Storm D F, Binari S C, Shanabrook B V, Torabi A, Zhou L and Smith D J 2005 Molecular beam epitaxy of InAlN/GaN heterostructures for high electron mobility transistors *J. Vac. Sci. Technol. B Microelectron. Nanom. Struct.* **23** 1204–8
- [102] Sahonta S-L, Dimitrakopoulos G P, Kehagias T, Kioseoglou J, Adikimenakis A, Iliopoulos E, Georgakilas a., Kirmse H, Neumann W and Komninou P 2009 Mechanism of compositional modulations in epitaxial InAlN films grown by molecular beam epitaxy *Appl. Phys. Lett.* **95** 021913
- [103] Zhou L, Smith D J, McCartney M R, Katzer D S and Storm D F 2007 Observation of vertical honeycomb structure in InAlN/GaN heterostructures due to lateral phase separation *Appl. Phys. Lett.* **90** 081917
- [104] Choi S, Wu F, Shivaraman R, Young E C and Speck J S 2012 Observation of columnar microstructure in lattice-matched InAlN/GaN grown by plasma assisted molecular beam epitaxy *Appl. Phys. Lett.* **100** 232102
- [105] Lorenz K, Franco N, Alves E, Watson I M, Martin R W and O'Donnell K P 2006 Anomalous Ion Channeling in AlInN/GaN Bilayers: Determination of the Strain State *Phys. Rev. Lett.* **97** 085501
- [106] Fernández-Garrido S, Gačević Ž and Calleja E 2008 A comprehensive diagram to grow InAlN alloys by plasma-assisted molecular beam epitaxy *Appl. Phys. Lett.* **93** 191907
- [107] Schmult S, Siegrist T, Sergent a. M, Manfra M J and Molnar R J 2007 Optimized growth of lattice-matched  $\text{In}_x\text{Al}_{1-x}\text{N}/\text{GaN}$  heterostructures by molecular beam epitaxy *Appl. Phys. Lett.* **90** 021922
- [108] Mazumder B, Kaun S W, Lu J, Keller S, Mishra U K and Speck J S 2013 Atom probe analysis of AlN interlayers in AlGaN/AlN/GaN heterostructures *Appl. Phys. Lett.* **102** 111603
- [109] Mazumder B, Wong M H, Hurni C A, Zhang J Y, Mishra U K and Speck J S 2012 Asymmetric interfacial abruptness in N-polar and Ga-polar GaN/AlN/GaN heterostructures *Appl. Phys. Lett.* **101** 091601
- [110] Harrison W A, Kraut E A, Waldrop J R and Grant R W 1978 Polar heterojunction interfaces *Phys. Rev. B* **18** 4402–10
- [111] Gonschorek M, Carlin J-F, Feltin E, Py M and Grandjean N 2010 Exact determination of electrical properties of wurtzite  $\text{Al}_{1-x}\text{In}_x\text{N}/(\text{AlN})/\text{GaN}$



heterostructures ( $0.07 \leq x \leq 0.21$ ) by means of a detailed charge balance equation  
*Int. J. Microw. Wirel. Technol.* **2** 13–20

- [112] Dasgupta S, Nidhi, Choi S, Wu F, Speck J S and Mishra U K 2011 Growth, Structural, and Electrical Characterizations of N-Polar InAlN by Plasma-Assisted Molecular Beam Epitaxy *Appl. Phys. Express* **4** 045502
- [113] Gonschorek M, Carlin J-F, Feltin E, Py M A and Grandjean N 2006 High electron mobility lattice-matched AlInN/GaN field-effect transistor heterostructures *Appl. Phys. Lett.* **89** 062106
- [114] Dadgar A, Neuburger M, Schulze F, Bläsing J, Krtschil A, Daumiller I, Kunze M, Günther K-M, Witte H, Diez A, Kohn E and Krost A 2005 High-current AlInN/GaN field effect transistors *Phys. Status Solidi* **202** 832–6
- [115] Jeganathan K, Shimizu M, Yano Y, Akutsu N and Okumura H 2007 Lattice-matched InAlN/GaN two-dimensional electron gas with high mobility and sheet carrier density by plasma-assisted molecular beam epitaxy *J. Cryst. Growth* **304** 342–5
- [116] Lugani L, Carlin J-F, Py M A, Martin D, Rossi F, Salviati G, Herfurth P, Kohn E, Bläsing J, Krost A and Grandjean N 2013 Ultrathin InAlN/GaN heterostructures on sapphire for high on/off current ratio high electron mobility transistors *J. Appl. Phys.* **113** 214503
- [117] Lee D S, Gao X, Guo S and Palacios T 2011 InAlN/GaN HEMTs With AlGaN Back Barriers *IEEE Electron Device Lett.* **32** 617–9
- [118] Lim T, Aidam R, Kirste L, Waltereit P, Quay R, Müller S and Ambacher O 2010 Compositional variation of nearly lattice-matched InAlGaN alloys for high electron mobility transistors *Appl. Phys. Lett.* **96** 252108
- [119] Higashiwaki M and Matsui T 2004 InAlN/GaN Heterostructure Field-Effect Transistors Grown by Plasma-Assisted Molecular-Beam Epitaxy *Jpn. J. Appl. Phys.* **43** L768–L770
- [120] Wang R, Li G, Laboutin O, Cao Y, Johnson W, Snider G, Fay P, Jena D and Xing H G 2011 210-GHz InAlN/GaN HEMTs With *IEEE Electron Device Lett.* **32** 892–4
- [121] Lee D S, Gao X, Guo S, Kopp D, Fay P and Palacios T 2011 300-GHz InAlN/GaN HEMTs With *IEEE Electron Device Lett.* **32** 1525–7

- [122] Wang R, Saunier P, Xing X, Lian C, Gao X, Guo S, Snider G, Fay P, Jena D and Xing H 2010 Gate-Recessed Enhancement-Mode InAlN/AlN/GaN *IEEE Electron Device Lett.* **31** 1383–5
- [123] Medjdoub F, Carlin J, Gonschorek M, Py M A, Grandjean N, Vandenbrouck S, Gaquiere C, Dejaeger J C and Kohn E 2006 Small-signal characteristics of AlInN/GaN HEMTs *Electron. Lett.* **42** 13–4
- [124] Lee H, Piedra D, Sun M, Gao X, Guo S and Palacios T 2012 3000-V 4.3-m $\Omega$ ·cm<sup>2</sup> InAlN/GaN MOSHEMTs With AlGaN Back Barrier *IEEE Electron Device Lett.* **33** 982–4
- [125] Yue Y, Hu Z, Guo J, Sensale-Rodriguez B, Li G, Wang R, Faria F, Fang T, Song B, Gao X, Guo S, Kosel T, Snider G, Fay P, Jena D and Xing H 2012 InAlN/AlN/GaN HEMTs With Regrown Ohmic Contacts and  $f_T$  of 370 GHz *IEEE Electron Device Lett.* **33** 988–90
- [126] Miyoshi M, Kuraoka Y, Tanaka M and Egawa T 2008 Metalorganic chemical vapor deposition and material characterization of lattice-matched InAlN/GaN two-dimensional electron gas heterostructures *Appl. Phys. Express* **1** 081102
- [127] Fujishima T, Joglekar S, Piedra D, Lee H-S, Zhang Y, Uedono A and Palacios T 2013 Formation of low resistance ohmic contacts in GaN-based high electron mobility transistors with BCl<sub>3</sub> surface plasma treatment *Appl. Phys. Lett.* **103** 083508
- [128] Guo J, Li G, Faria F, Cao Y, Wang R, Verma J, Gao X, Guo S, Beam E, Ketterson A, Schuette M, Saunier P, Wistey M, Jena D and Xing H 2012 MBE-Regrown Ohmics in InAlN HEMTs With a Regrowth Interface Resistance of 0.05  $\Omega$  · mm *IEEE Electron Device Lett.* **33** 525–7
- [129] Pang L, Seo H-C, Chapman P, Adesida I and Kim K 2010 Breakdown Voltage Enhancement of AlGaN/GaN High-Electron-Mobility Transistors via Selective-Area Growth for Ohmic Contacts over Ion Implantation *J. Electron. Mater.* **39** 499–503

## Appendix A. Metal-polar HEMT Fabrication

Fully processed quarter 2" AlGaIn/GaN HEMT structures have been delivered to collaborators with the die layout shown in Fig. A.1. The HEMTs defined by the lower middle section of the CHU\_V01 mask were the most reliable, as HEMT #2 was commonly used for large-signal measurements. The shorter gate lengths in other sections of the mask were often poorly defined. A step-by-step procedure for fabricating unpassivated rectangular-gate HEMTs, passivated rectangular-gate HEMTs, and passivated slant-gate HEMTs is presented below.

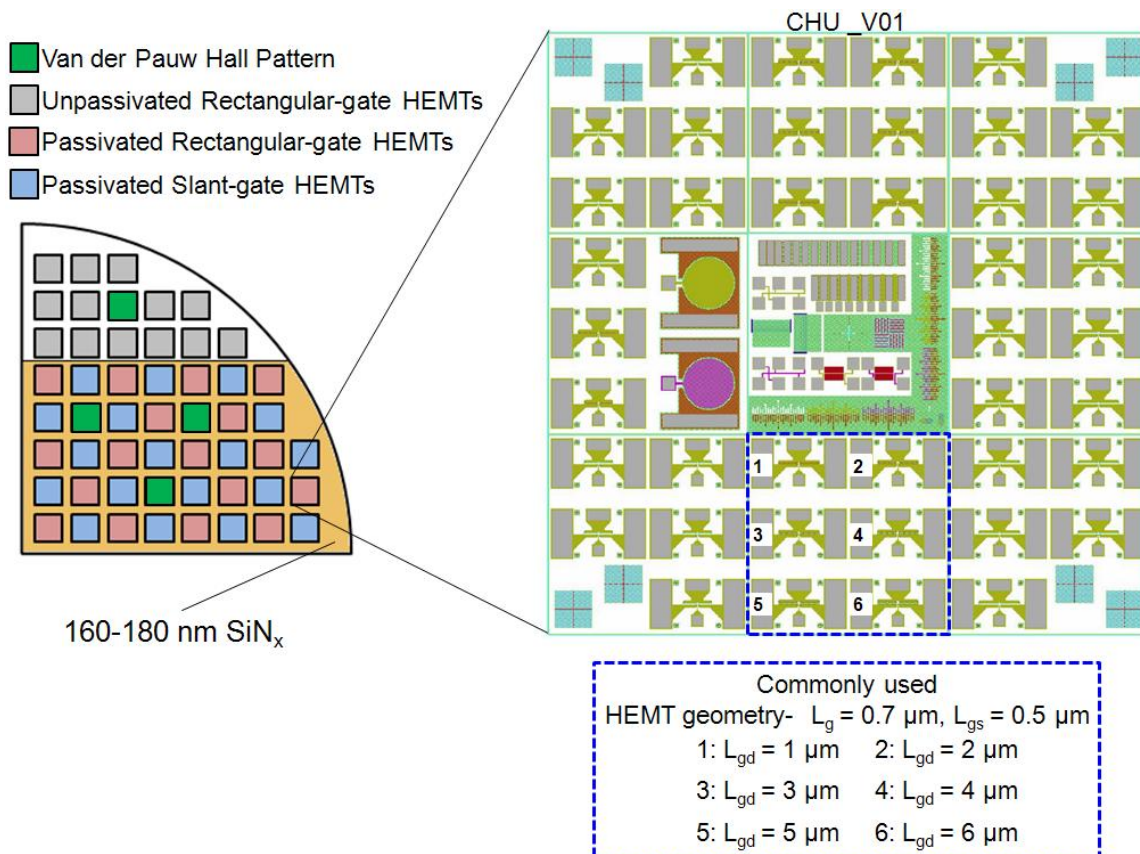


**Figure A.1: Die layout for HEMTs on quarter 2" substrates and the layout of the CHU\_V01 mask.**

### **Removal of Backside Metallization:**

- HNO<sub>3</sub>:HF 1:1 30 s (or until metal completely dissolves)
- DI rinse >2 min
- N<sub>2</sub> blow dry

### **Ohmic Contacts (first step for all HEMTs):**

Clean:

- Acetone ultrasonicate 3 min
- Isopropanol ultrasonicate 3 min
- DI rinse >2 min
- N<sub>2</sub> blow dry

Double-layer Photoresist (PR):

- Dehydration bake 120 °C 3 min
- Cool down >5 min
- Spin 825 PR 5 krpm 30s
- Bake 95 °C 1 min
- Cool down >30 s
- Spin 950 PR 3.5 krpm 30s
- Bake 90 °C 1 min
- Cool down >30 s
- Expose 2.0 s
- Postbake 100 °C 2 min
- Cool down >30 s
- Develop in AZ300K:DI 2:1 1'40" (gently spin wafer carrier)
- DI rinse >2 min
- N<sub>2</sub> blow dry
- Optical microscope inspection

If HTCVD SiN<sub>x</sub> is included, add a SiN<sub>x</sub> etch step (follow procedure for RIE #3 in the slant gate deposition section)

Contact Metal Deposition:

- O<sub>2</sub> descum 300 mT 100W 15 s (Asher #1)
- HCl:DI 1:3 dip 30s

- DI rinse >1 min
- N<sub>2</sub> blow dry
- Load sample in E-beam #4 or E-beam #1 (direct path from metal source to sample)
- Load Speck Group source material
- Check quartz crystal
- Evaporate Ti/Al/Ni/Au (200 Å/1200 Å/300 Å/500Å)

Liftoff:

- Leave sample in 1165 (closed container) until most of the metal comes off
- 1165 heated bath ultrasonicate 3 min
- Isopropanol ultrasonicate 2 min
- Acetone ultrasonicate 2 min
- Isopropanol ultrasonicate 2 min
- DI rinse >2 min
- N<sub>2</sub> blow dry
- Optical microscope inspection

Contact Anneal:

- Load personal SiO<sub>2</sub>/Si carrier wafer in AET RX6
- Before loading sample, RTA at 820°C in N<sub>2</sub> for 30s at least 2 times
- After loading sample, RTA at 820°C in N<sub>2</sub> for 30s
- Optical microscope inspection (typically dark bubbled alloy contacts)
- Check the linearity of TLMs with curve tracer

**Mesa Isolation (all HEMTs - sometimes performed after SiN<sub>x</sub> deposition for passivated devices):**

Clean:

- Acetone ultrasonicate 3 min
- Isopropanol ultrasonicate 3 min
- DI rinse >2 min
- N<sub>2</sub> blow dry

Single-layer Photoresist:

- Dehydration bake 120°C 3 min
- Cool down >5 min
- Spin 950 PR 3.5 krpm 30s
- Bake 90°C 1 min
- Cool down >30 s
- Expose 2.0 s
- Postbake 100 °C 2 min
- Cool down >30 s
- Develop AZ300K 2'20"
- DI rinse >2 min
- N<sub>2</sub> blow dry
- Optical microscope inspection

#### AlGaIn/GaN Etch in RIE #5:

- Descum O<sub>2</sub> 300 mT 100 W 15 s (Asher #1) - no need for HCl dip
- DI rinse >1 min
- N<sub>2</sub> blow dry
- Load sample in RIE #5
- Descum in RIE #5 O<sub>2</sub> 50 mT 50 SCCM 50 W 20 s (if descum is not done prior to loading)
- Oxide etch in RIE #5 BCl<sub>3</sub> 10 mT 10 SCCM 100 W 1 min
- AlGaIn/GaN etch Cl<sub>2</sub> 10 mT 10 SCCM 100W 2'30" (60 nm/min)

#### Clean:

- Acetone ultrasonicate 3 min
- Isopropanol ultrasonicate 3 min
- DI rinse >2 min
- N<sub>2</sub> blow dry
- Optical microscope inspection
- Check isolation with curve tracer
  - Go to an unetched channel device. Place 'collector' probe on drain, 'source' probe on source. Check IV curve and note the maximum current density =  $I_0/75$  A/mm
  - Go to an etched channel device. Apply voltage between S/D (1 μm separation) and check for buffer leakage. Take IV data points at 20V, 1 mA/mm (75 μA/75 μm), and 4 mA/mm (300 μA/75 μm). Resistive buffers need >60 V to reach 1 mA/mm.

### Gate Contact (Rectangular):

Clean:

- Acetone ultrasonicate 3 min
- Isopropanol ultrasonicate 3 min
- DI rinse >2 min
- N<sub>2</sub> blow dry

Double-layer Photoresist:

- Dehydration bake 120 °C 3 min
- Cool down >5 min
- Spin 825 PR 5 krpm 30s
- Bake 95 °C 1 min
- Cool down >30 s
- Spin 950 PR 3.5 krpm 30s
- Bake 90 °C 1 min
- Cool down >30 s
- Expose 2.8 s
- Postbake 100 °C 2 min
- Cool down >30 s
- Develop in AZ300K:DI 2:1 1'40" (gently spin wafer carrier)
- DI rinse >2 min
- N<sub>2</sub> blow dry
- Optical microscope inspection

Gate Metal Deposition:

- O<sub>2</sub> descum 300 mT 100W 15 s (Asher #1)
- HCl:DI 1:3 dip 30s
- DI rinse >1 min
- N<sub>2</sub> blow dry
- Load sample in E-beam #4 or E-beam #1 (direct path from metal source to sample)
- Load Speck Group source material
- Check quartz crystal
- Evaporate Ni/Au/Ni (300 Å/2500 Å/300 Å) – top layer of Ni protects Au from subsequent processing steps

Liftoff:

- Leave sample in 1165 (closed container) until most of the metal comes off
- 1165 heated bath ultrasonicate 3 min
- Isopropanol ultrasonicate 2 min
- Acetone ultrasonicate 2 min
- Isopropanol ultrasonicate 2 min
- DI rinse >2 min
- N<sub>2</sub> blow dry
- Optical microscope inspection

### SiN<sub>x</sub> PECVD Passivation:

PECVD Chamber Clean:

- Check chamber, clean walls with Isopropanol, then close chamber
- Load and run cleaning program \_30CLNSN.PRC [30 min clean]
- Solvent clean while CF<sub>4</sub> is flowing
  - Acetone ultrasonicate 3 min
  - Isopropanol ultrasonicate 3 min
  - DI rinse >2 min
  - N<sub>2</sub> blow dry
- After 30 min of CF<sub>4</sub>, some SiN<sub>x</sub> is deposited. Watch the 'voltage' during SiN<sub>x</sub> deposition. After 30 s it should be within 54-57 V. If lower, clean the chamber again. If higher by 1-2 V, it is OK. If more, something is wrong.
- Once the voltage of the SiN<sub>x</sub> deposition is checked and OK, proceed with descum and HCl dip.

SiN<sub>x</sub> PECVD Deposition:

- O<sub>2</sub> descum 300 mT 100W 15 s (Asher #1)
- HCl:DI 1:3 dip 30s
- DI rinse >1 min
- N<sub>2</sub> blow dry
- Load sample in PECVD chamber
- Load and run deposition program \_SIN16.PRC. SiN<sub>x</sub> thickness ~1600-1700 Å - should look yellowish-orange



### **SiN<sub>x</sub> Etching and Bond Pads (Passivated Rectangular Gate):**

Clean:

- Acetone ultrasonicate 3 min
- Isopropanol ultrasonicate 3 min
- DI rinse >2 min
- N<sub>2</sub> blow dry

Double-layer Photoresist (PR):

- Dehydration bake 120 °C 3 min
- Cool down >5 min
- Spin 825 PR 5 krpm 30s
- Bake 95 °C 1 min
- Cool down >30 s
- Spin 950 PR 3.5 krpm 30s
- Bake 90 °C 1 min
- Cool down >30 s
- Expose 2.0 s
- Postbake 100 °C 2 min
- Cool down >30 s
- Develop in AZ300K:DI 2:1 1'40" (gently spin wafer carrier)
- DI rinse >2 min
- N<sub>2</sub> blow dry
- Optical microscope inspection

SiN<sub>x</sub> etch in Asher #2:

- Clean chamber O<sub>2</sub> 300 mT 300 W 2 min (sample out)
- Etch CF<sub>4</sub> 300 mT 200 W 2 min (sample in)
- Clean chamber O<sub>2</sub> 300 mT 300 W 10 min (sample out)
- Cl<sub>2</sub> etch in RIE#5 10 mT 10 SCCM 1 min

Bond Pad Deposition:

- O<sub>2</sub> descum 300 mT 100W 15 s (Asher #1)
- HCl:DI 1:3 dip 30s
- DI rinse >1 min
- N<sub>2</sub> blow dry

- Load sample in E-beam #3 (direct path from source to substrate unnecessary, large room for error in bond pad placement)
- Evaporate Ti/Au (300 Å/3000 Å)

Liftoff:

- Leave sample in 1165 (closed container) until most of the metal comes off
- 1165 heated bath ultrasonicate 3 min
- Isopropanol ultrasonicate 2 min
- Acetone ultrasonicate 2 min
- Isopropanol ultrasonicate 2 min
- DI rinse >2 min
- N<sub>2</sub> blow dry
- Optical microscope inspection

#### **SiN<sub>x</sub> Etching and Gate Contacts/Bond Pads (Passivated Slant Gate):**

Clean:

- Acetone ultrasonicate 3 min
- Isopropanol ultrasonicate 3 min
- DI rinse >2 min
- N<sub>2</sub> blow dry

Double-layer Photoresist (PR):

- Dehydration bake 120 °C 3 min
- Cool down >5 min
- Spin 825 PR 5 krpm 30s
- Bake 95 °C 1 min
- Cool down >30 s
- Spin 950 PR 3.5 krpm 30s
- Bake 90 °C 1 min
- Cool down >30 s
- Expose 2.8 s
- Postbake 100 °C 2 min
- Cool down >30 s
- Develop in AZ300K:DI 2:1 1'40" (gently spin wafer carrier)
- DI rinse >2 min

- N<sub>2</sub> blow dry
- Optical microscope inspection

SiN<sub>x</sub> etch in RIE #3:

- Clean chamber O<sub>2</sub> 50 mT 20 SCCM 300 V (~15-20 W) 30 min (sample out)
- Etch CF<sub>4</sub>/O<sub>2</sub> 50 mT 20/2 SCCM 100 V (~5 W) 20 min (sample in) - ~10 nm/min slight over etch to make sure AlGaN is exposed

AlGaN Recess Etch in RIE #5 (if required):

- Low-power oxide etch BCl<sub>3</sub> 10 mT 10 SCCM 15 W 2'30"
- Low-power AlGaN/GaN etch BCl<sub>3</sub>/Cl<sub>2</sub> 10 mT 20/5 SCCM 15 W 30" for 3 nm recess (~6 nm/min)

Slant Gate/Bond Pad Deposition:

- Load sample in E-beam #1 on rotation arm
- Angle the sample 15-20 deg from normal to the source (facilitates sidewall deposition)
- Connect rotation arm to power supply and turn on power supply
- Load Speck Group source material
- Check quartz crystal
- Evaporate Ni/Au (300 Å/3000 Å)

Liftoff:

- Leave sample in 1165 (closed container) until most of the metal comes off
- 1165 heated bath ultrasonicate 3 min
- Isopropanol ultrasonicate 2 min
- Acetone ultrasonicate 2 min
- Isopropanol ultrasonicate 2 min
- DI rinse >2 min
- N<sub>2</sub> blow dry
- Optical microscope inspection

## Appendix B. OFF-State Stress Tests on Passivated Slant-gate and Passivated Rectangular-gate HEMTs

Passivated slant-gate and rectangular-gate HEMTs were fabricated on  $\text{Al}_{0.3}\text{Ga}_{0.7}\text{N}/\text{GaN}$  heterostructures grown by Ga-rich PAMBE directly on 4H-SiC. These HEMTs were then subjected to various OFF-state ( $V_{\text{GS}} = -7 \text{ V}$ , variable  $V_{\text{DS}}$ ) stresses with the peak electric field on the drain-side of the gate. The post-stress DC-IV curves were remarkably different between the two gate structures. The slant-gate HEMTs consistently developed higher gate leakage currents and a greater degree of current collapse than the rectangular-gate HEMTs (Fig. B.1).

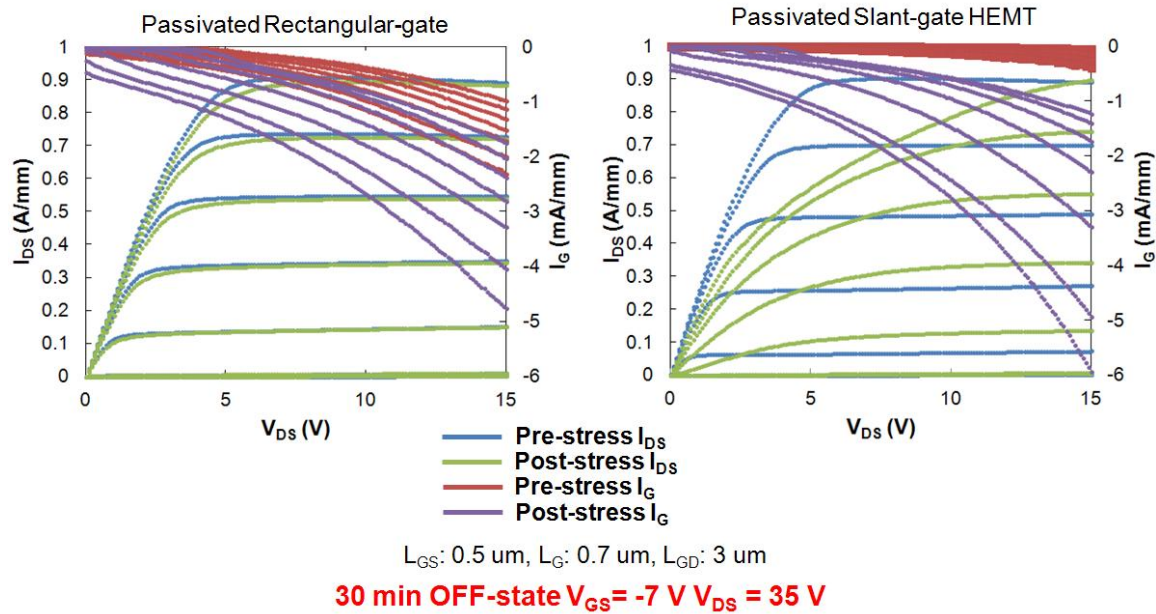


**Figure B.1. 30 min OFF-state stress ( $V_{\text{GS}} = -7 \text{ V}$ ,  $V_{\text{DS}} = 35 \text{ V}$ ) of passivated rectangular-gate and passivated slant-gate HEMTs directly grown on 4H-SiC.**

Slant-gates reduce the peak electric field at the drain-side of the gate and improve breakdown voltage. As shown in Fig. B.1, the pre-stress  $I_G$  of the slant-gate HEMT was lower than the pre-stress  $I_G$  of the rectangular-gate HEMT, as expected. After OFF-state stress, the gate current increased drastically in the slant-gate HEMT. This increased gate current after OFF-state stressing was likely result of specific processing steps (Fig. B.2).

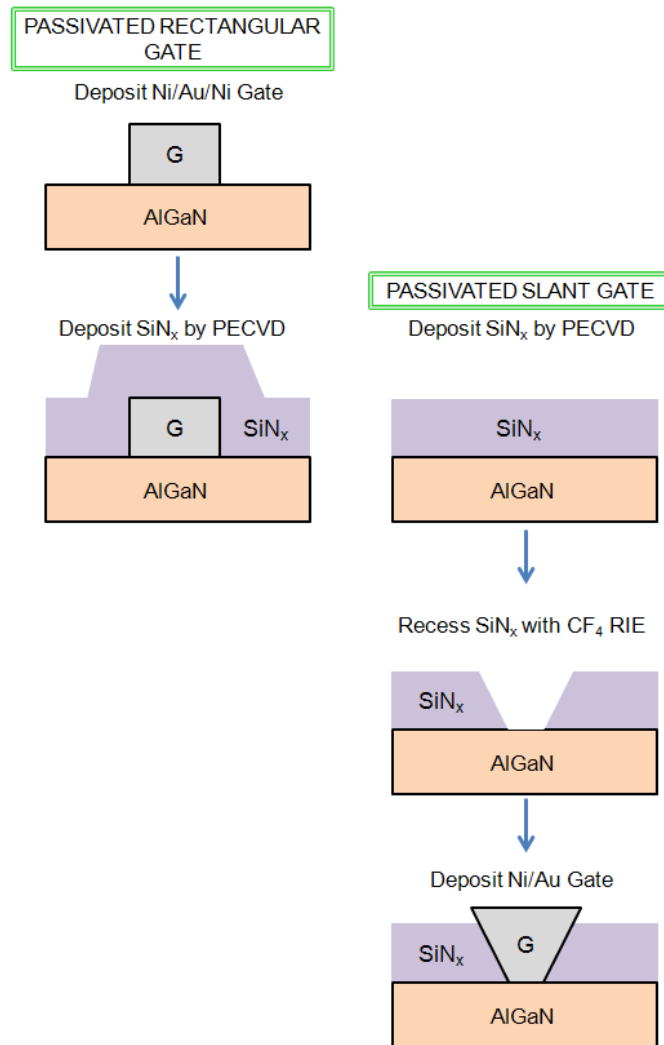


**Figure B.2: Simplified flow chart of processing steps for passivated rectangular-gate and passivated slant-gate HEMTs.**

The AlGaIn surface in the slant-gate HEMTs was exposed to a low-power CF<sub>4</sub> plasma before gate metal deposition (“over-etch” of SiN<sub>x</sub>). Exposure to CF<sub>4</sub> plasma is thought to introduce deep-level F-related traps in the AlGaIn, which reduce gate leakage. It appears that in the presence of a high electric field for a long duration, these deep-level traps facilitate a leakage path. To verify if exposure to CF<sub>4</sub> plasma is detrimental to OFF-state gate leakage, a series of unpassivated rectangular-gate HEMTs should be fabricated with various CF<sub>4</sub> plasma powers and exposure times before gate deposition.

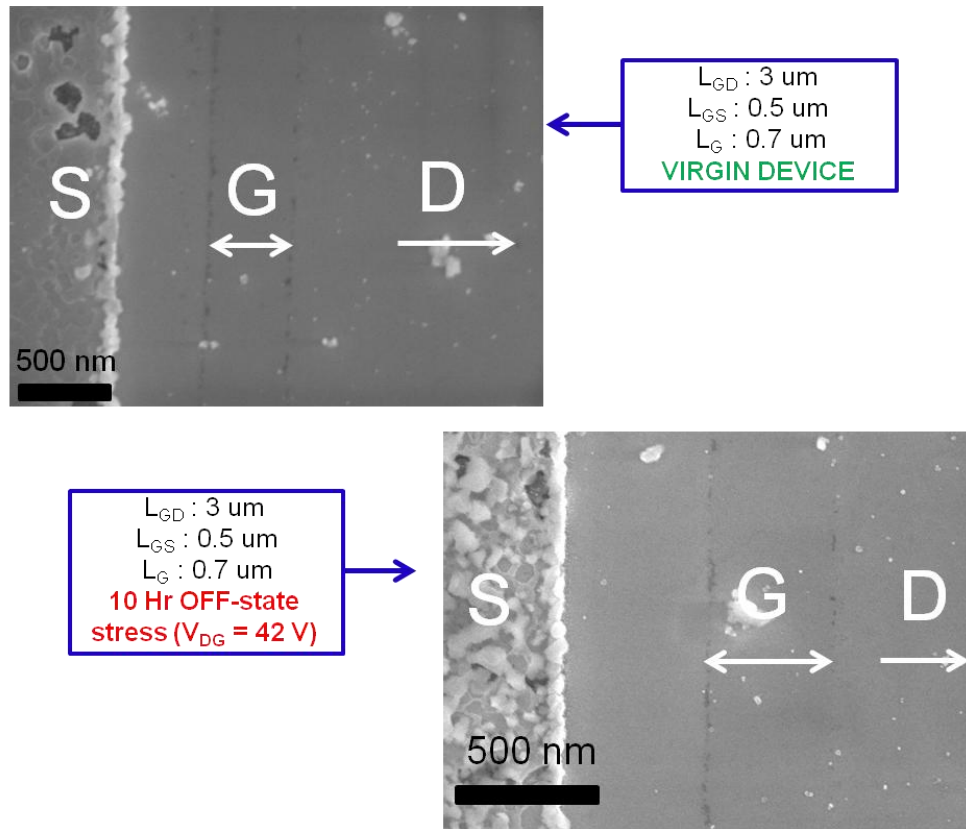


**Figure B.3: SEM images of etched passivated rectangular-gate HEMTs before and after OFF-state stress.**

This OFF-state stress study was initially intended to introduce pits on the drain-side of the gate (described in Chapter 1) that would then be analyzed by HAADF-STEM. However, no pits were identified after the passivation layers and metals were etched with HF, piranha, and aqua regia, respectively. The SEM images in Fig. B.3 show similar discolorations on both sides of the gate before and after stressing. The discolorations on the post-stress HEMT of Fig. B.3 were not pits, but rather bumps, as identified by AFM (Fig. B.4). Refinement of the etching process will presumably eliminate these bumps. Additionally, HAADF-STEM (Fig. B.5) was used to analyze the heterostructure under the drain-side of the rectangular gate after OFF-state stress ( $V_{GS} = -7$  V,  $V_{DS} = 45$  V, 2 hr), and no pitting was seen.

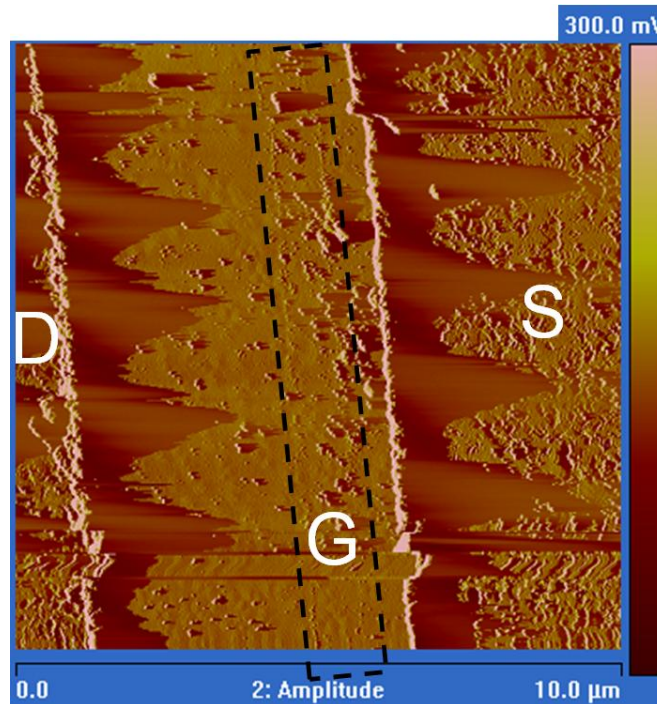


**Figure B.4:**  $10 \times 10 \mu\text{m}^2$  AFM micrograph of an etched rectangular-gate HEMT post-stress ( $V_{GS} = -7$  V,  $V_{DS} = 35$  V, 10 hr).

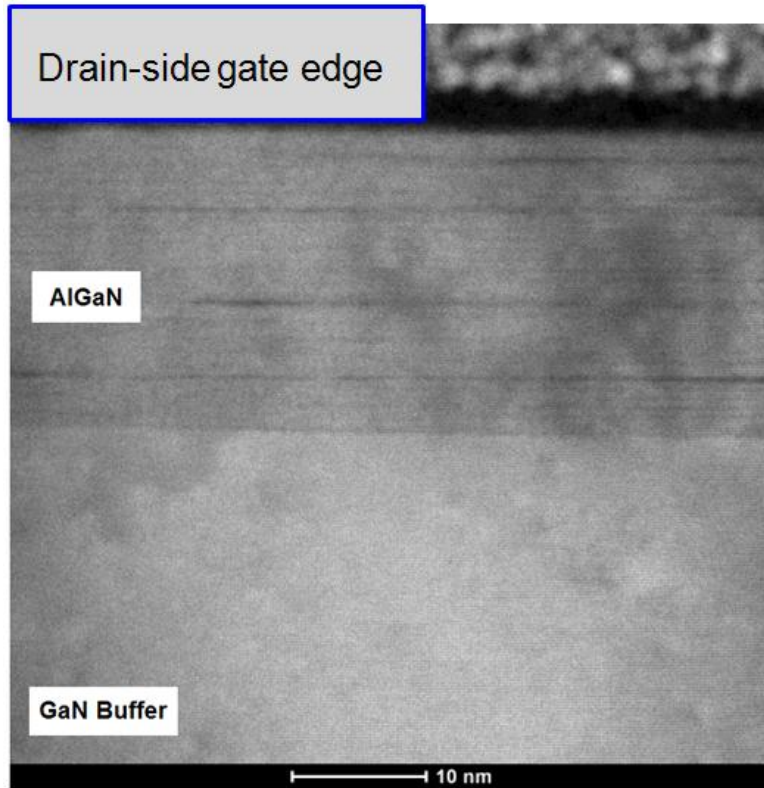


**Figure B.5:** Cross-sectional HAADF-STEM image under the drain-side of the gate in a post-stress AlGaIn/GaN HEMT (passivated rectangular gate,  $V_{GS} = -7$  V,  $V_{DS} = 45$  V, 2 hr). HAADF-STEM was performed by Yan-Ling Hu.